

UC Berkeley

UC Berkeley Electronic Theses and Dissertations

Title

Critical Zone Ecohydrology of the Northern California Coast Ranges

Permalink

<https://escholarship.org/uc/item/9g8492jx>

Author

Hahm, William Jesse

Publication Date

2019

Peer reviewed|Thesis/dissertation

Critical Zone Ecohydrology of the Northern California Coast Ranges

by

William J Hahm

A dissertation submitted in partial satisfaction of the
requirements for the degree of
Doctor of Philosophy

in

Earth and Planetary Science

in the

Graduate Division

of the

University of California, Berkeley

Committee in charge:

Professor William E. Dietrich, Chair
Professor Todd E. Dawson
Professor Michael Manga
Assistant Professor Nicholas Swanson-Hysell
Assistant Professor Daniella M. Rempe

Summer 2019

Critical Zone Ecohydrology of the Northern California Coast Ranges

Copyright 2019
by
William J Hahm

Abstract

Critical Zone Ecohydrology of the Northern California Coast Ranges

by

William J Hahm

Doctor of Philosophy in Earth and Planetary Science

University of California, Berkeley

Professor William E. Dietrich, Chair

Earth's critical zone includes plants as well as the heterogeneous near-surface layers into which they are rooted: the soil, saprolite, and weathered bedrock. It is within the critical zone (CZ) that water is stored and then released to streams and withdrawn by vegetation, highlighting its importance to humans, ecosystems, and the functioning of the Earth system in general. The research presented here is motivated by the global-scale challenges of mapping and predicting subsurface critical zone structure and understanding how that structure impacts water routing and storage for terrestrial ecosystems. It addresses these challenges by shedding light on inter-related ecohydrologic puzzles presented at the regional-scale across natural landscapes in the Eel River watershed: What explains the persistence and dominance of a particular species of oak, *Quercus garryana*, across savannas typified in the dry season by rolling golden hills mantled by senesced annual grasses? What explains the sharp ecotone that extends for hundreds of kilometers between this oak savanna community and a dense evergreen forest in a region of similar climate? Why did plant communities in this region fare better than others in the face of recent extreme drought?

By studying *Quercus garryana*'s ecophysiology, I show that the oak is extremely water-limitation tolerant, which explains its ability to persist where a thin subsurface critical zone provides limited water storage capacity. Through sapflow monitoring on mature trees inhabiting an upslope position in the Central belt melange of the Franciscan, I reveal that the oaks maintain high rates of transpiration throughout the summer dry season, even as pre-dawn water potentials dropped to very low levels (below -3 MPa). At this site, Douglas fir has not encroached upon the oak groves like it has elsewhere throughout their mutual range. This is presumably due to Douglas fir's lower water limitation tolerance, and anticipates *Quercus garryana*'s likely persistence in a warmer, drier future along western North America.

Through geospatial analysis coupled with intensive hillslope- and catchment-scale hydrological observation, I show that under a similar climate, adjacent landscapes across an extensive region of the Northern California Coast Ranges are either evergreen forest or deciduous oak savannah depending on their subsurface lithology. This is due to lithologically controlled contrasts in the extent of bedrock weathering and water storage capacity and

thereby plant-available moisture in the summer dry season: a thick subsurface critical zone stores ample moisture and supports evergreen forest, whereas an adjacent thin subsurface critical zone sheds wet season rains and sustains savannah. The thick subsurface critical zone occurs in the modestly deformed shales and sandstones of the Coastal belt of the Franciscan; the thin subsurface critical zone occurs in the intensely deformed mud-matrix melange of the Central belt of the Franciscan. An important difference between the rock types is the thickness of the weathered bedrock layer; in contrast, the soil layer is of similar thickness. The thicker weathered bedrock at the Coastal belt site results in a larger rock moisture reservoir, i.e., unsaturated water residing within the weathered bedrock, which is primarily responsible for sustaining summer transpiration after shallow soils have dried. Extensive drilling was used to characterize the subsurface weathering extent and water storage dynamics, and was complemented by point-scale precipitation monitoring, catchment-wide remotely sensed evapotranspiration, and stream gauging to determine annual water budgets. Finally, late-summer dry season pre-dawn water potential observations in the dominant trees at both sites were used to compare subsurface water availability and show that where the weathered bedrock was thicker and hosted more rock moisture, the forest was less water stressed.

The observation of plant-available water in the dry season being mediated by the water storage capacity of the critical zone motivated a new hypothesis for how the subsurface can regulate plant response to drought: where annual rainfall reliably exceeds subsurface storage capacity, plant productivity and water use in summer should be insensitive to winter rainfall variability, because the subsurface water storage is replenished in wet and dry years alike. A simple ecohydrologic model for water storage in seasonally dry, Mediterranean climates predicts that storage will be replenished most reliably where the average precipitation is high relative to the subsurface storage capacity and winter evapotranspiration, and where year-to-year variability in precipitation is low. In order to test whether this storage-capacity limited behavior indeed decouples plants from inter-annual rainfall variability, running winter water balances were calculated for all unimpaired and generally undisturbed rain-dominated Mediterranean USGS catchments, using runoff, gridded precipitation and remotely sensed evapotranspiration as input data. These water balances revealed that sites in the Northern California Coast Ranges exhibited storage-capacity limitation, unlike most of the rest of the state. At all of the sites in the Northern California Coast Ranges, the consistent summer plant water supply resulted in plant insensitivity to rainfall variability, as revealed by remotely sensed summer plant greenness. Such sites are inherently resilient to meteorological drought, helping to explain the lack of mortality in the region in the extreme 2011-2016 drought.

Contents

Contents	i
List of Figures	iii
List of Tables	xii
1 Introduction	1
2 Oak's response to water limitation	12
2.1 Abstract	12
2.2 Introduction	13
2.3 Methods	16
2.4 Results	24
2.5 Discussion	34
2.6 Conclusions	45
2.7 Acknowledgements	46
3 Critical zone water storage capacity controls plant distribution	47
3.1 Abstract	47
3.2 Introduction	48
3.3 Site description	54
3.4 Methods	62
3.5 Results	68
3.6 Discussion	85
3.7 Conclusions	91
3.8 Acknowledgements	94
4 Water storage capacity and drought response	96
4.1 Abstract	96
4.2 Introduction	97
4.3 Model development and catchment water balance methodology	99
4.4 Winter water balance and summer plant sensitivity to variable precipitation	108
4.5 Discussion	110

4.6	Conclusions	116
4.7	Acknowledgements	116
	Bibliography	117

List of Figures

1.1	A pair of Oregon white (Garry) oaks thrive in a harsh savanna environment in the Central Belt mélange in the Northern California Coast Ranges. Photo courtesy of Wendy Baxter.	4
1.2	Oblique birds-eye view looking north along the Northern California Coast Ranges reveals a sharp ecotone separating a evergreen mixed broadleaf-needleleaf forest (to the west) from a deciduous oak savanna-woodland (to the east). Yellow line is the geologic contact separating the Coastal belt (west) from the Central belt (east) of the Franciscan complex, after Langenheim et al. [2013]. Google Earth image taken by David Dralle.	5
1.3	Widespread tree die-off in the Sierra Nevada (top, photo credit US Forest Service) contrasted with healthy mixed conifer-broadleaf forest at the Angelo Coast Range Reserve (bottom, photo credit Collin Bode) in the recent extreme California drought.	7
1.4	Vertical profiles of rock moisture expressed as volumetric water content, θ , in a subset of wells at the Angelo Coast Range Reserve show that similar minimum (red) and maximum (blue) θ is reached in different years. Seasonal cumulative precipitation at the time of the wet-season measurement is shown in parentheses in the legend. Colored vertical bars on the right of each graph illustrate the zone of water table fluctuation identified via groundwater monitoring (left bars) and the weathering profile characteristics identified during drilling (right bars). Caption and figure adapted from Rempe and Dietrich [2018].	8
1.5	End-of-summer site-wide average and standard error tree pre-dawn water potential, a metric of relative plant water availability in the subsurface and internal plant water stress. Although the two sites are different (see details in Chapter 3), no detectable difference exists between years with very different total winter precipitation (2015: approximately 1600 mm; 2017: approximately 3500 mm).	9
1.6	Cartoon depicting a relatively small subsurface water storage capacity, in the form of the cups below, which will be filled in both dry (left) and wet (right) years, because the average rainfall (above) is so much larger.	10

2.1	(a) Map showing distribution of <i>Quercus garryana</i> and <i>Pseudotsuga menziesii</i> in western North America and study area (black triangle). The <i>Q. garryana</i> range is almost entirely subsumed by <i>P. menziesii</i> , except at its western- and southern-most margins. Range maps were generated from the union of Little [1971] shapefiles provided by the USGS and scanned, georeferenced, and digitized maps by Griffin and Critchfield [1972] of the state of California, which include smaller, geographically isolated populations at higher spatial resolution. Study area map (b) created from semi-transparent canopy height raster draped over hillshade derived from first return lidar elevations. Elevation contour labels in meters above sea level; white-outlined numbers show the location of study trees (see Table 2.1)	15
2.2	Perspective view of south-facing slope study trees, illustrating their geomorphic context (above first-order channel head) and savanna setting. First-return lidar point cloud above bare-earth hillshade shows density of data used to create canopy height in Figure 2.1. Points were clipped to include only those >1 m above the ground, brown-beige-green color scale shows increasing height above ground surface. Scale varies in this perspective view; Tree #1 is approximately 13 m tall.	20
2.3	Time series of (a) pre-dawn and mid-day shoot Ψ , (b, c) climate, and (d) sap flow in mature <i>Quercus garryana</i> . Sap flow remains high in late summer (d) in spite of low subsurface water availability (low pre-dawn Ψ in a), and lack of summer precipitation (b). In (d), slight transparencies highlight the density of data. Cumulative water year precipitation in (b) is missing for 2015 due to incomplete record. Non-zero sap flow during winter when <i>Q. garryana</i> lacks leaves in (d) is attributable to evergreen mistletoe.	25
2.4	Pre-dawn vs. mid-day shoot Ψ of individual mature <i>Quercus garryana</i> , color-coded by measurement month in the 2015 and 2016 growing seasons. November measurements taken after return of wet-season rains in 2016. The diagonal dashed lines show -1 , -2 , and -3 MPa isopotential gradients for reference.	27
2.5	Comparison of stem and leaf Ψ from the same shoot at mid-day across two summer days shows consistent >1 MPa hydraulic gradient from stem to leaf. Numbers on horizontal axis refer to tree ID (see Table 2.1 and site map in Figure 2.1). . .	28
2.6	Example pressure-volume (PV) curve from a rehydrated <i>Q. garryana</i> leaf collected from tree #5 on September 17, 2016, showing pre- (filled) and post- (empty) turgor loss points. Plots (a)–(c) show graphical derivation of important leaf water relations metrics: the turgor loss point (TLP), cell wall symplastic modulus of elasticity (ϵ) and relative symplastic water content at turgor loss ($RWC_{\text{sym}} @ \text{TLP}$), the osmotic potential at full turgor (Ψ_{S100}), and the apoplastic water fraction (AWF). All lines (grey) are determined with standardized major axis fitting.	29
2.7	Leaf hydraulic vulnerability curve shows decline in the leaf hydraulic conductance (K) as leaf water potential (Ψ) declines.	31

2.8	Average diurnal sap flow pattern across each month of the 2016 growing season. Sap flow is high in the dry-season summer months, continues at night, and exhibits a mid-day depression. Closer to the solstice, the onset of sap flow in the morning occurs earlier and the evening decline occurs later. Curves do not reach 0% or 100% as the monthly averaged behavior shown here averages across multiple trees and includes days when sap flow did not reach the minimum or maximum recorded.	32
2.9	Total integrated sap flow per month, normalized to the maximum month recorded by each sensor. Sap flow peaks during the summer months with greatest insolation in spite of negligible precipitation.	33
2.10	Radial displacement of sapwood, cambium, and inner bark away from the trunk in the 2016 growing season. Early growing season increase reflects sapwood growth. Smaller amplitude oscillations (see Figure 2.11) reflect diurnal water storage and release. Abrupt increases that decay after a period of days reflect rehydration of inner bark and sapwood due to rain (vertical gray lines, right y -axis).	34
2.11	Average daily displacement of sapwood, cambium, and inner bark away from the trunk in a heartwood reference frame (positive is radially outward) across all instrumented trees each month of the 2016 growing season. The start of each 24-h period is fixed to zero to highlight inter-month dynamics. Spring-early summer months exhibit net positive daily displacement, reflecting sapwood growth, and the amplitude of displacement is highest in midsummer, reflecting greatest daily uptake and release of stored water.	35
2.12	The turgor loss point (TLP; labeled contours) as a function of Ψ_{S100} and ϵ , based on the analytical formulation of Bartlett et al. [2012]. The TLP is more sensitive to Ψ_{S100} than ϵ for a given 1 MPa change in either term, but ϵ varies much more than Ψ_{S100} , and is lower for non-rehydrated leaves, illustrating a potential mechanism for TLP depression in leaves experiencing low Ψ . Inset shows TLP (x -axis) inferred as described in the <i>Methods</i> section and illustrated in Figure 2.6 compared to analytical prediction of Bartlett et al. [2012] as a function of Ψ_{S100} and ϵ .	38
2.13	End-of-summer (mid-September) <i>Q. garryana</i> foliage and acorns, seen from below. Photo by Wendy Baxter.	40
3.1	Comparison of land cover (a; 2011 National Land Cover Database [Homer et al., 2015]) and Franciscan bedrock geology (b; Langenheim et al. [2013]). Blue lines in (a) show primary forks of the Eel River. Map inspired by Figure 2 of Lovill et al. [2018].	50

3.2	Tree canopy cover map of the field area shows the abrupt change in tree canopy cover at the geologic contact (white bold line) that separates the Coastal Belt (west) from the Central Belt (east) in the study area. Green (forested) patches in mélangé are primarily on sandstone blocks. Study watersheds in each rock type are demarcated with dashed lines; gray = 0% canopy cover, darkest green = 100% canopy cover. Coordinates in WGS84; geologic contact after Jayko et al. [1989]. Canopy cover from the 2011 National Land Cover Database. Map inspired by Figure 2 of Dralle et al. [2018].	51
3.3	(a) Photo from headwaters of Elder Creek in the Coastal Belt, looking west, shows mixed broadleaf-needleleaf evergreen forest grading to chaparral on higher elevation, south-facing steep slopes. (b) Photo from northern ridge of Dry Creek watershed, looking north, shows annual-grass dominated, low-gradient hillslopes, with leafless winter-deciduous mistletoe-infested <i>Q. garryana</i> in foreground. The lumpy topography records relict earthflows. (c) Photo of south-facing tributary of Dry Creek during rainstorm (10 January 2017), showing extent of wetted channels and widespread saturation overland flow. Person for scale (170 cm tall); point in lower-right drains area of approximately 2 ha. (d) Panoramic photo between wells 503 and 500 at the Sagehorn Central Belt site along ridgetop on northern boundary of the Dry Creek catchment, showing complete saturation of the subsurface and overland flow in a winter rainstorm (190 cm tall person in yellow jacket for scale).	52
3.4	Global delineation of biome type as a function of mean annual precipitation and temperature. The average climate of the Coastal Belt (Angelo; blue circle) and Central Belt (Sagehorn; red triangle) study sites is associated with temperate forests, consistent with the ecosystem inhabiting the Coastal Belt. In contrast, the actual Central Belt biome is woodland/shrubland/grassland, denoted with the lower red triangle. Biome delineations based on Ricklefs [2008]; Whittaker [1975]. Greater interception at the Coastal Belt results in nearly identical precipitation at the ground surface, as discussed in text.	53
3.5	Map of study area in the Coastal Belt (‘Angelo’) highlighting evergreen forest community. Inset box shows expanded view of topography along intensively-studied hillslope (‘Rivendell’). Here only the location of wells drilled down to fresh bedrock are shown. Coordinates provided in NAD83/UTM Zone 10N. 1 (grey) and 5 (black) m ground surface elevation contours from 2014 lidar collected by NCALM. Background NAIP air photo from June 7, 2014	55
3.6	Map of study area in the Central Belt mélangé (‘Sagehorn’), highlighting mixed woodland and savanna vegetation communities. Inset box shows expanded view of topography along intensively-studied hillslope. Coordinates provided in NAD83/UTM Zone 10N. 1 (grey) and 5 (black) m ground surface elevation contours from 2015 lidar collected by NCALM. Background NAIP air photo from May 29, 2012. . .	57

- 3.7 Schematic cross sections of hillslopes in the Coastal Belt (left) and Central Belt (right) of the Franciscan complex, highlighting contrasting critical zone structure, runoff pathways, vegetation distribution, and topography. End-of-winter and end-of-summer water table positions shown with inverted blue and red triangles, respectively. Runoff in Coastal Belt is generated from saturated flow through fractures in the deep, weathered rock zone that thickens toward the topographic divide. In the Central Belt, the subsurface CZ is approximately tenfold thinner at the topographic divide. Many winter storms completely saturate the subsurface, resulting in quick shallow subsurface storm flow through macropores and widespread saturation overland flow. Figure not to scale. 69
- 3.8 Timeseries of groundwater behavior inferred from pressure transducers in continuously slotted monitoring wells at Sagehorn (upper panel, Central Belt mélange site) and Rivendell (lower panel, Coastal Belt site). Groundwater elevation is referenced to the ground surface elevation at the location of each well. At Sagehorn, wells drilled into primarily mélange matrix (500, 502, 506, 507, 508, MN-1, and MS-4) exhibit flashy responses to winter rain events and rise to the ground surface frequently throughout the winter, receding to relatively shallow depths over the course of the dry season. Wells 501 and 503 are drilled into a crystalline-block complex and sandstone block, respectively, and have a deeper water table. Wells 500, 501, 502, and 503 are located along a topographic divide, wells 506, 507, and 508 along a slight topographic saddle, well MS-4 in the axis of a colluvial hollow, and well MN-1 along the side slope of a colluvial hollow (see Figure 3.6). Horizontal summer groundwater lines in wells 508, MN-1, and MS-4 reflect groundwater recession below pressure transducer depth. See Rivendell well locations in Figure 3.5. In all wells at both sites, periodic vertical negative excursions in summer reflect groundwater sampling events. Times when pressure transducers were removed for sampling were filtered from the timeseries with a median rolling filter with a 0.25 m threshold and 12 hour window, and gap-filled with linear interpolation. Straight lines in Feb., 2017, reflect missing, interpolated data. 71
- 3.9 Contrasting groundwater (a, b) and stream (c) responses across sites with different depths to fresh bedrock, Z_b (blue = Coastal Belt; red = Central Belt) to similar precipitation input (d) in 2016. (a) Long dry season recession of groundwater at ridge after last winter rains to contrasting depths. (b) Expanded time series from (a) shows response of groundwater to first rains of wet season. Groundwater in Coastal Belt does not respond until ~ 700 mm of cumulative precipitation, whereas groundwater in Well 507 rises rapidly to ground surface in first major winter storm, indicating complete saturation of CZ in Central Belt, driving flashy runoff in Dry Creek (c). Variable maximum runoff in Dry Creek with saturated CZ indicates importance of saturation overland flow. Elder Creek response is muted in comparison, with longer recession. 72

- 3.10 Cumulative precipitation (P), runoff (Q), potential evapotranspiration (PET), and inferred catchment-wide dynamic storage (S) in the 2017 water year. The Dry Creek watershed has a factor of approximately four lower catchment-wide dynamic storage than the Elder Creek watershed and reaches a maximum storage sooner into the wet season, resulting in a much higher runoff ratio. 73
- 3.11 Depth profiles of XRD-determined mineral phases. Horizontal dashed lines indicate drilling-inferred transition to fresh bedrock (Z_b) at each borehole (14, blue, Coastal Belt; 506, red, Central Belt). Illite and smectite were separately estimated and not included in the normalization, resulting in some sums exceeding 100% (see section 3.4). Their concentrations are presented as likely ranges, as denoted by the horizontal lines. 74
- 3.12 Depth-profiles of dissolved oxygen within groundwater in the Central Belt mélange in the 2017 water year. Measurements were made from the top of the groundwater table downward, in continuously slotted boreholes. 76
- 3.13 Scanning electron microscope images taken at increasing levels of magnification of fresh mélange matrix. The uppermost image (a, low magnification), shows scattered larger (sand size) particles (mineral and rock fragments) that are suspended in a fine-grained matrix. At intermediate magnification (b), we see larger silt-size particles (also mineral and rock fragments) in a finer matrix. The larger particles may show intraparticle pores (yellow arrow). At highest magnification (c), the intraparticle matrix resolves as a felted mass of phyllosilicates (likely chlorite). This phyllosilicate matrix has some intrinsic porosity (interparticle framework pores, yellow arrow), but pores are small ($\sim 10\text{--}20$ nm) and not abundant, and thus permeability is low. Larger open spaces between phyllosilicate matrix and mineral grains are not pores but rather artifacts of sample preparation (beam heating causes shrinkage of phyllosilicate matrix). 77
- 3.14 Perspective view near the mouth of Dry Creek at the Central Belt site. Red line denotes contact between sandstone block (covered with mixed broadleaf-needleleaf evergreen forest) and mélange matrix (with primarily annual herbaceous ground cover) from reconnaissance geologic mapping. Scale varies in this west-looking view; sandstone block is ~ 750 m across in W–E direction. Google Earth imagery date 30 May 2014, eye-altitude 1.5 km, $1.5\times$ vertical exaggeration. 79

- 3.15 Time series of air photos of the Central Belt mélange site (groundwater monitoring wells are distributed along WSW–ENE running road in SE portion of photo; Dry Creek runs approximately NE from ‘459500’ to ‘4380000’ m UTM grid zone marks). The boundary between forest and grassland has remained essentially fixed in space for more than seven decades. The 1952 image shows the large reduction in woody canopy cover in aftermath of selective logging of *P. menziesii* and a large fire. Forested areas have regrown in the same locations, which coincide with the location of large sandstone blocks or north-facing hillslopes. The photo name is provided below the date each photo was taken; 1941 and 1952 photos provided by the Map and Imagery Laboratory at UC Santa Barbara; 2012 image from the USDA National Agriculture Imagery Program. 81
- 3.16 Composite annual time series of (a) energy (radiation measured at Angelo in the Coastal Belt) and water delivery reveal that in spite of similar climate, distinct subsurface CZ water storage capacity, and plant water availability result in distinct annual phenological trends, as shown via the enhanced vegetation index (EVI; b) from MODIS within the Elder Creek (Coastal Belt) and Dry Creek (Central Belt) watersheds. Vertical bars = 1 standard deviation. 83
- 3.17 Energy and water balances of each site depicted within the traditional Budyko framework indicate that the Elder Creek catchment partitions more incoming precipitation into evapotranspiration (*ET*; remotely sensed, and including interception losses; see Ryu et al., 2011) than Dry Creek, in spite of similar *P* and potential evapotranspiration (*PET*) between the sites. Each point (a) and horizontal line (b) represent a single water year, from 2002–2015. Lines fit (and reported parameter *n*) according to equation described in Yang et al. [2008]. . . 84
- 3.18 Conceptual cross section illustrating the hypothetical role of critical zone structure in governing water storage and ecosystem composition in the seasonally dry, Northern California Coast Ranges. Topographic position, rainfall, and evaporative demand are assumed constant: only the thickness and corresponding water storage capacity changes from left to right. Although shown as a horizontal surface, this analysis applies to well-drained hillslopes underlain by bedrock, not valley flats where thick colluvium or alluvium may accumulate and seasonal drainage may be poor. Plant variation at far right illustrates possible role of fire exclusion in promoting pure stands of Douglas fir [e.g., Schriver et al., 2018]. 89
- 3.19 Lidar-derived shaded relief map of the Central Belt mélange Sagehorn study site, in which the incised channel network has resulted in the development of both convex-up hillslopes (seen in the vertical elevation profile A–A’) and gently undulating earthflow topography (B–B’). Also visible are prominent blocks within the mélange matrix that disrupt the otherwise smooth, soil-mantled topography. 92
- 3.20 Photo of disaggregating shale cobble (approximately 20 cm across) resting on sandstone and conglomerate boulders in active stream bed, illustrating effect of wetting and drying cycles on the bedrock of the Coastal Belt. Photo courtesy Mary E. Power. 93

- 4.1 The critical zone (CZ) extends from treetops to the base of weathered bedrock. Channel incision and erosion bring fresh, low permeability bedrock into the near surface. Fresh bedrock can then be weathered to generate porosity and permeability, which mediate the partitioning of precipitation (P) into storage (S), evapotranspiration (ET) and runoff (Q). 98
- 4.2 Conceptual diagram illustrating how the start-of-summer dynamic water storage (S), depends on winter precipitation (P) and subsurface critical zone water storage capacity (S_{\max}). Evapotranspiration (ET) is winter evapotranspiration (assumed constant here) and Q is the winter runoff. The three rows (a–c) show, for an increase in S_{\max} : (left column) the probability distribution of annual precipitation (P) relative to S_{\max} , and the resultant S distribution, shifted left due to ET ; (middle column) corresponding scatter plots of S versus P for five hypothetical years, along with the Spearman rank correlation coefficient (ρ) expressing the dependence of S on P ; (right column) relative water volumes, stylized as columns, of S , P , ET , and Q for an exemplary dry (left) and wet (right) year. In cases when $P < S_{\max} - ET$, the volume of S (colored red) is less than S_{\max} (the column’s wire frame). 101
- 4.3 Storage sensitivity to precipitation depends on the coefficient of variation of winter precipitation and the ratio between average precipitation and storage capacity plus winter evapotranspiration. Contours represent the expected strength of correlation between stored water at the start of summer (S) and (gamma-distributed) cumulative winter precipitation (P) for varying S_{\max} , CV of P , and \bar{P} 103
- 4.4 Plots of S and Q vs. winter P (top row) and mean summer EVI vs. winter P (bottom row) for all sites. In the top row, lines trace the seasonal evolution of both the dynamic storage (S , grey) and the cumulative winter runoff (Q , blue). Sites are arranged along a spectrum of behavior: storage-capacity limited (left) to precipitation limited (right). Points at the termini of the S traces are colored by the water year, and paired with the summer EVI in the bottom row. Storage-capacity-limited sites tend to have higher rainfall. 107
- 4.5 Winter storage (S) and the summer enhanced vegetation index as a function of winter precipitation (P). Plots (a–c) track the running catchment-wide S water balance (grey line traces) for each water year as a function of cumulative winter precipitation (up to 1 April). The dashed 1:1 lines reflect a reference case of no runoff (Q) or evapotranspiration. Plots (d–f) plot mean-normalized summer enhanced vegetation index between 1 April and 30 September, also as a function of total winter precipitation (P). ρ denotes the Spearman rank correlation for each scatter plot; asterisks denote significance at $p < 0.05$ 109

4.6	Winter storage and summer enhanced vegetation index (EVI) sensitivity to winter P . Spearman rank correlations between (a) S and winter precipitation and (b) summer EVI and winter precipitation. The filled symbols denote significance at $p < 0.05$. The grey-shaded vertical bars connect storage-capacity-limited sites between (a) and (b). Dry Creek lacks complete runoff record but is inferred to be storage-capacity-limited based on intensive hillslope-scale monitoring.	110
4.7	Distribution of mean canopy cover (jittered) by limitation category.	111
4.8	Distribution of mean annual precipitation (jittered) by limitation category.	112
4.9	Winter storage sensitivity to P and summer EVI sensitivity to summer PET . Spearman rank correlations between S and winter precipitation (a), and summer EVI and summer PET (b), are shown for the 2002–2013 water years. Filled symbols denote significance at $p < 0.05$. Grey-shaded vertical bars connect storage-capacity-limited sites between (a) and (b).	113
4.10	Plots of S and Q vs. winter P (top row) and mean summer EVI vs. winter P (bottom row), including extreme drought years, for sites classified as storage-capacity limited for the years 2002 to 2013. In the top row, lines trace the seasonal evolution of both the dynamic storage (S , grey) and the cumulative winter runoff (Q , blue). Points at the termini of the S traces are colored by the water year and are paired with the summer EVI in the bottom row. Squares denote water years after the start of extreme drought (2014, 2015, 2016, and 2017).	115

List of Tables

2.1	Study tree characteristics.	19
2.2	Symbols, units, and terms.	24
2.3	Comparison of Ψ along the subsurface-plant-atmosphere continuum on two dry-growing season days.	26
2.4	Leaf metrics derived from pressure-volume (PV) curve experiments on mature <i>Quercus garryana</i> individuals, across sampling days and hydration status.	30
3.1	Catchment physiographic and vegetation characteristics	56
3.2	Historical climate	58
3.3	Franciscan geology of the Northern California Coast Ranges	59
3.4	Fresh rock bulk geochemistry	82
4.1	USGS Basin Filtering Criteria.	106

Acknowledgments

One of the largest shifts in perspective that occurred in my time as a graduate student was the recognition that science, in spite of being grounded in a set of objective approaches for exploring the workings of the physical universe, is also very much a human endeavour—a *duh* moment insight that went under-appreciated in earlier years learning from textbooks. This new worldview comes, in part, from participating in the projection of ideas into the world and witnessing how scientific consensus emerges. But, perhaps more importantly, it also comes from the day-to-day interactions with inspiring, funny and passionate people. I have a welcome opportunity here to reflect on those individuals who elevated my experience the last five years.

This dissertation is dedicated to my wife, Claire Wilkin, who is the rock that sustains and supports me, and without whom I would not have achieved what I have. This work is also only possible due to the tremendous and continued support of my parents who have encouraged and enabled my pursuit of education throughout my life. Thank you!

Bill Dietrich—

A topoholic

And at the end of the day

Avocado, cheese

—is responsible for giving me a new set of critical zone-colored glasses to look at the world with. I was initially attracted to Berkeley by a suite of papers from Bill's group that tested and expanded upon G.K. Gilbert's ideas about landscape evolution. I was fascinated by the notion that the shape of hilly, upland landscapes could be explained by a few elegant equations describing soil production and transport. At Berkeley, Bill pushed me in new directions, spurred by compelling ecohydrological puzzles in Northern California Coast Ranges. On our first trips—and to this day—he challenged me to think hard about what lies below the soil, a largely unmeasured zone that he and Gordon Grant have referred to as the 'frontier beneath our feet'. What drives the evolution of weathered bedrock? How is water stored in this zone? How does variation in water storage capacity below the soil impact plant water availability and streamflow? If I have made any progress in thinking about these questions it is thanks first and foremost to Bill, who has been a constant font of ideas and energy. As the creator and leader of the Eel River Critical Zone Observatory he brought together a diverse cast of scientists—the academic village in which I was raised. Bill found ample opportunities to create teaching moments, while also giving me and others the chance to teach. He engages in countless hours of hiking and debating and brainstorming over the landscape, and can then somehow stay up till the wee hours of the morning to provide constructive criticism to ideas and writing, typically cutting right to the heart of the matter. He is also an eager sharer of food—and, more recently—a roof. The list goes on. Thanks very much Bill for providing me with so many opportunities. Mary Power has also played no small role in inspiring my love for natural history, and showing how much hard work and dedication is required to protect and maintain wild lands that can also be carefully studied.

My immediate academic ‘family’ at Berkeley has had an outsized impact on my happiness as a graduate student and growth as a scientist. Diverse escapades with Sky Lovill taught me the importance of covering ground and getting in close with all aspects of the landscape. His parents, Hope and Jim, frequently invited me into their home in Marin for rest and recuperation and helped solidify an appreciation for one of the enduring Bay area scenes: the Grateful Dead. Daniella Rempe knows quite a bit about the exciting field of critical zone science, and has become a friend, life-coach, and scientific sounding board. She is typically a step ahead of me in the planning and execution of field campaigns; whenever it dawned on me that something needed to be done, she had already thought about three ways to accomplish the task. It is an unbelievable honor to be invited to join the team at Rempe Global this fall in Texas. David “Round Boy” Dralle—the hot dog eater’s hot dog eater—knows a thing or two about hydrology, especially stochastic hydrology, and showed me how a PhD-level understanding of recession limbs could be used to execute harrowing white water tubing trips, amongst so many other things. Alex, my stalwart fellow Midwesterner, grounds the lab and is always there to lend a hand, a whiskey, or a futon, as the case may be. I have rarely laughed so hard as when in Sky, Daniella, David, and Alex’s company, and I hope that our collaborative enterprise continues. Mariel Nelson participated in endless field campaigns with dedication and healthy bemusement, and has become a role model in how to make field work efficient, rigorous and fun. Runze “Rowdy” Miao is one of the kindest, goofiest, and most generous labmates one could hope for. Jill Marshall, Dino Bellugi, Christian Braudrick, and Jasper Oshun all served as warm and enlightened mentors. Jen Natali—honorary lab member extraordinaire—is a superstar nonpareil, a shining exemplar of kindness, good design, field grit, humor, and level-headedness.

The Dawson lab constituted a second home at Berkeley, where I could absorb new information about all-things-plants at an astounding rate. Todd is to be credited with championing my scientific pursuits through an indefatigable positivity and engendering a lab atmosphere and dynamic that is at once supportive, fun, engaged in cutting-edge research and, importantly, tasty-snack-fueled. Todd and the members of his lab created countless opportunities for me to pursue research in plant ecophysiology and water isotopes. Among so many other things, Cameron Williams and Rikke Naesborg taught me how to circumnavigate the canopy of an oak, Wendy Baxter and Anthony Ambrose got me up into a giant sequoia, Wenbo Yang and Stefania Mambelli patiently explained basic lab procedures to a primarily field scientist, Todd took me on a trip with Claire Willing and Roxy Cruz to Switzerland to ponder isotopes, Kelsey Crutchfield-Peters schemed through a rather involved deuterium experiment, and not least, Chris Wong, cheerfully explained to me over and over again that our sensors would be fine and produce good data just as long I was sure to not **** anything up.

I had the pleasure of accompanying Nick Swanson-Hysell on numerous field trips across California, picking up bits here and there of his deep-time geologic wisdom and trying to emulate his sharp eye for interpreting rock relations in the field. He is a superlative teacher and I am fortunate to have been able to pursue a project in paleomagnetism with him and to have him sit on my dissertation committee. Michael Manga, who also participates in this

dissertation and currently leads the department with great efficiency, has similarly been a role model for clear thinking and exposition of fundamental earth science concepts. He has a beautiful knack for reducing seemingly complex problems to their essential components, something I aspire to. Cliff Riebe, my MSc advisor at Wyoming, continued to mentor me, lending a helpful ear at numerous junctions in my PhD experience. Sally Thompson and Jenny Druhan held me to rigorous ecohydrological and geochemical standards while also helping me to not take myself too seriously.

Few are the streams into which I will cup my hands and drink deeply. The Angelo Coast Range Reserve is a magical place that hosts several wild rivers that are now, sadly, vestiges of a once great coastal ecosystem. The area was protected by many generations of indigenous people who lived lightly on the land, and more recently saved from logging and development thanks to the longsighted vision of the Angelo family, the Nature Conservancy, the University of California, and Peter Steel and Mary Power, who have shepherded the Reserve into the 21st century. I am extremely fortunate to have been able to spend so much time living and researching under the canopy of towering fir, redwood, oak, madrone and bay, and thank all those who have protected this forest.

Marilyn Russell is an inspirational conservationist, naturalist and educator who enabled and promoted research on her beautiful ranch, Sagehorn, where much of my dissertation work took place. Sagehorn is on the Central belt melange of the Franciscan, and served as a counterpoint to Angelo—the nucleus of the Eel River Critical Zone Observatory—which lies on the Coastal belt. Without the stark contrasts presented by the two sites we would not have fully appreciated the importance of differences in subsurface weathering and water storage capacity in mediating the hydrologic cycle in the Eel River watershed. Much of our ecohydrologic framework for the region came into focus after drilling and monitoring at Sagehorn, with disparate clues from the plants, streams, and land surface topography eventually coalescing into a unified story. I am forever thankful for Marilyn's vision and enthusiasm, and have fond memories of watching her approach over the horizon on horseback to chat science and teach us about the landscape she grew up on and so adores. The Holleman family has also played an integral role in research efforts at the ranch. Renee in particular has carefully collected crucial water samples now for nearly half a decade, often in challenging conditions.

Farther afield, where the Northern California Coast Range meets the Great Valley, I have found new friends with a passion for land and water in Rhonda Gruber and Greg Hemmi, as well as a fellow ecohydrology enthusiast in Jerry Brown. Along with Anne Gust Brown, Rhonda, Greg, and Jerry have unhesitatingly welcomed us into their homes for meals, provided warm beds in inclement weather, and created incredible research opportunities in the magnificently upturned Great Valley Sequence. Thanks to the discovery and investment by Kristen Fauria, Mong-Han Huang, Alex Bryk, and Mariel Nelson, this new field area creates—in Bill's words—a 'string of pearls' across shale-based lithologies that will continue to shape our understanding of the interactions amongst weathering, erosion, and ecohydrology.

I am fortunate to have interacted with Kat Quigley, Tim Bailey, Jeff Hedin, Richard

Gienger, Jeff Garberson, Bob Sanders and Barbara Domanchuk, who have all translated the science at the Eel River CZO into exciting and accessible words and videos for wider audiences.

Numerous individuals have helped to advance research and keep things running behind the scenes. I thank Jen Hunter and Sarah Roy in particular for keeping my personal finance and healthcare ship afloat, with humor and tenacity, in the challenging seas of the UC Berkeley bureaucratic complex. Collin Bode created an amazing sensor database that made accessing datastreams a cinch while also making sure sensors could talk to dataloggers which could in turn talk to radios and servers back in Berkeley. Peter Steel turned daunting field objectives into fun, tractable problems. Without Steve Taber, the drilling wizard, we would not have the invaluable portrait of the subsurface structure and hydrology that has formed the basis of so much of our understanding. Ilana Stein and Cameron Williams selflessly helped design and implement piston dendrometer and sapflow sensor networks. Jen Rose helped map trees and watersheds. Jia Wang helped to make solute geochemistry measurements. Sami Cargill, Marshall Wolf, Will Speiser, and Gunnar Rieth, assisted by many intrepid Berkeley undergrads, including Quinn Miller, Karina Redding, Maryn Sanders, Hunter Jamison, and Benjamin Purcell, collected thousands of samples for the collective ERCZO effort. Colleen Murphy, among that group, was inspiring to watch as she undertook a field mapping project in the chaos of the melange. Owen Nelson—jack of all trades—appeared in the field at important junctures, fixing gear, collecting samples, and providing a level head. He is also to be endlessly thanked for the difficult task of formatting this dissertation in LaTeX. The crew at the Wyoming Center for Environmental Hydrology and Geophysics, led on the ground by Matt Provart and envisioned by Steve Holbrook, mounted two massive geophysics campaigns at Angelo and Sagehorn. Anya Mikheicheva, Zhiyang Li, Dave Bish and Juergen Schieber made crucial lab analyses and images. The Texan bunch—Shawn, Logan, Brandon, Michelle, and Alison—simply made fieldwork fun. Thanks y’all.

A close cohort and group of friends saw me through. Felipe “con grillo” Orellana Roviroso was assigned to be my graduate student mentor when I entered the Earth and Planetary Science department at Berkeley, and boy, he took the job seriously. Much of my experience of Oakland comes from Felipe, who could typically be found at First Fridays, posted up on a street corner or lurking in one of his many haunts: Chinese restaurants, dives, death metal venues, and public swimming pools. Thank you Felipe for being there and introducing me to so many people and parts of the Bay, where it turned out I was very much the foreigner. I also identify many parts of my experience in the Bay with Seth Saltiel—another close friend, and of California at large with John Krueger and Claire Landowski. There are too many other great people at Berkeley that I need to list... Sean, Brent, Chelsea, Kristen, Mong-Han, Anneliese, David, Ian, Gopal, and more that I forget now. I learned so much from the community of graduate students working at the Angelo Coast Range Reserve. I thank Phil, Keith, Kelsey, and Gabe in particular for enlivening the scene at the Eel.

Finally, I am extremely grateful for the funding that enabled all of this work. This includes the National Science Foundation-supported Critical Zone Observatory program, as

well as the Mildred E. Mathias Graduate Student Research Grant, the Carol Baird Fund for Graduate Field Science, and the Institute for the Study of Ecological and Evolutionary Climate Impacts.

Chapter 1

Introduction

When vascular plants transpire, returning moisture to the atmosphere through leaf stomata, they act as low resistance pathways for water between the relatively wet, high water potential subsurface and the often desiccating, low water potential atmosphere. Transpiration plays a central role in the terrestrial hydrologic cycle and, via feedbacks with the carbon cycle, is a crucial process in the functioning of the Earth system as a whole. Our understanding of the controls on transpiration—including controls on the distribution, function and sensitivity to global change of vascular plants—remains incomplete, and has been identified as an important research priority in the United States [National Research Council, 2012]. In general, where disturbance and land use can be discounted, climate patterns offer the best explanation for present-day global plant biome distribution and function [Holdridge, 1947; Woodward, 1987; Whittaker, 1975; Stephenson, 1990]. Shifts in climate are similarly expected to drive shifts in plant communities [Kelly and Goulden, 2008; Loarie et al., 2009], provided dispersal can keep pace with migrating temperature and precipitation zones. Nevertheless, significant uncertainty exists in our ability to predict and explain the existing distribution of plants. Plant response to environmental change, including higher temperatures, higher atmospheric carbon dioxide concentrations, and increasingly variable precipitation [Swain et al., 2018], is also incompletely understood. This knowledge gap has resulted in parallel efforts to better understand the physiology of plants as well as the aspects of their physical environment that impact their function, including the supply of energy, nutrients and, not least, water. The controls on subsurface water supply and their interaction with plants are the primary focus of this dissertation.

The subsurface is structured, and can be divided into different zones where water storage occurs. In most landscapes, the thickness of the soil—the uppermost layer—is generally less than one meter, and in many uplands less than half a meter [Amundson et al., 2015]. Trees are commonly rooted directly into the weathered bedrock that underlies soil (e.g., Hellmers et al. [1955]; Scholl [1976]), which retains relict bedrock structures like sedimentary bedding. During dry periods, thin soils desiccate via drainage and evapotranspiration, and plant transpiration may be sustained by deeper water sources (e.g., Mooney et al. [1974]; Schwinning [2010]). Although porosity is typically lower in the underlying highly weathered

saprolite and weathered bedrock than in soil, the depth to fresh bedrock is commonly many meters below the ground surface in upland areas, resulting in a weathered bedrock water storage reservoir (containing both unsaturated and saturated zones) that is potentially larger than the soil water reservoir [Graham et al., 2010]. Indeed, many studies in winter-wet, summer-dry Mediterranean climates have highlighted the ecological significance of water sourced from weathered bedrock by arguing for tree water extraction from this deeper zone in the dry summer [Lewis and Burgy, 1964; Anderson et al., 1995; Arkley, 1981; Zwieniecki and Newton, 1996; Rose et al., 2003; Baldocchi et al., 2004; Miller et al., 2010; Bales et al., 2011; Salve et al., 2012; Rempe and Dietrich, 2018; Eliades et al., 2018; Zunzunegui et al., 2018].

In spite of the studies listed above, near-surface, typically shallow soils, like those mapped by US Natural Resources Conservation Service (NRCS), have historically been—and continue to be—the focus of efforts to understand plants’ belowground physical environment. The US National Science Foundation supported Critical Zone (CZ) Observatory Program has for the past decade, however, placed an emphasis on understanding the entire zone of weathered material near Earth’s surface—including bedrock beneath the soil—and its connection to the biosphere [Anderson et al., 2004]. This perspective is a geological one, in which uplift and erosion bring bedrock towards Earth’s surface while channels incise and drive the development of topographic gradients for the transport of soil. Over geologic timescales this soil works its way down slopes and into channels. Collectively, these processes result in landscape evolution, carving hillslopes and valleys out of the Earth. The Earth’s land surface has been mapped extensively—first by boots-on-the-ground surveying, and subsequently by aerial orthophotos, satellite interferometry, and more recently, at high resolution with airborne laser imaging. Although out of sight compared to the land surface, and therefore poorly mapped, a no less important surface—the weathering front—takes shape *beneath* hillslopes. As rocks are exhumed, they encounter new thermal, chemical, biological, and pressure conditions in the near surface, causing fractures to open and minerals to chemically transform. Beneath the soil, Earth’s weathering engine is at work liberating nutrients and generating porosity for water storage within the bedrock Graham et al. [2010]. Various weathering fronts can exist, defined by, for example, the inception of alteration or dissolution of particular minerals. In general, the lowest boundary, defined by as a low permeability boundary of unweathered bedrock, sets the bottom of the critical zone. Direct glimpses into the fracturing and chemical alteration of bedrock are generally limited to road cuts, quarries, and boreholes; the general difficulty of characterizing and observing this zone is largely responsible for our limited understanding of its role in impacting plant function, distribution, and sensitivity to global change. This is one of the reasons the deep critical zone has recently been referred to as the “frontier beneath our feet” [Grant and Dietrich, 2017]. Importantly, very little work exists that has directly focused on plant physiology and how it interacts with the subsurface weathering structure that directly impacts water storage dynamics.

Differences in terminology exist across disciplines when categorizing the subsurface pools of water that supply transpiration. Here I divide these pools into three groups, in a way that captures both saturation state and the physical (or geomorphic) state of the material: (i)

soil moisture, which occurs as unsaturated water from the ground surface to the base of the physically mobile regolith. Soil moisture has commonly been used to describe all unsaturated zone moisture, and sometimes all subsurface water (both saturated and unsaturated), but here I separate it from (ii) rock moisture (*sensu* Salve et al. [2012]; Rempe and Dietrich [2018], see also Schwinning [2010]), which is similarly unsaturated, but found below the soil, within the saprolite (which has soil-like texture but is physically immobile and retains relict bedrock structure) and the fractures and matrix of deeper weathered bedrock (the weathered zone bedrock zone including saprolite is referred to as the C horizon in pedologic studies), and (iii) groundwater, which completely fills pore spaces regardless of the material it occupies. Groundwater is typically below soil and rock moisture but occasionally intrudes upon these layers due to water table perching or complete saturation of the subsurface. Thus, soil moisture is distinguished from rock moisture by the material in which it resides (a spatial, material-based distinction); and groundwater is distinguished from soil and rock moisture by saturation state (which may change in time at any given location). Together these sources constitute the subsurface water of Earth's critical zone—the near-surface, life-sustaining layer extending from fresh bedrock at depth upwards to the top of the vegetation canopy.

Here, I build on previous work at the Eel River Critical Zone Observatory (ERCZO) in Mendocino County, California, and present three case studies of how the interaction of plants and their subsurface physical environment govern regional-scale ecohydrological patterns. These studies are spatially nested, ranging in scale across Chapters 2 through 4 from individual leaves and trees to hillslopes and watersheds to entire landscapes.

The first study presented here (in Chapter 2) was originally motivated by the striking distribution of a particular tree species, commonly the only woody plant found growing in a sea of herbaceous groundcover in Mendocino County, California (Figure 1.1). Eventually, observation expanded into a detailed study of the species, *Quercus garryana* (Oregon white oak, also called Garry oak), one of Western North America's most culturally and ecologically significant oaks. Chapter 2 weaves together the historical fire ecology of *Q. garryana* with a suite of new intensive field-based ecophysiological measurements of its water relations. *Q. garryana* has experienced radical habitat reduction associated with Euro-American fire exclusion over the past century, leading to widespread conifer encroachment and the endangerment of biodiverse oak savanna ecosystems. The study is framed in light of anticipated warming in the coming century, and asks how the oak will fare in a warmer future. It provides a comprehensive process-level portrait of the oak's water use, water potential dynamics, and sensitivity to hydraulic stress. These details can be used to explain extant biogeographic patterns and can be incorporated into land-plant-atmosphere models. The new ecophysiological observations indicate that the oak is extremely water-limitation tolerant, and therefore suggests that it may be resilient to further encroachment by more easily water stressed conifers. A novelty of this study is the union of two important threads in the literature that have rarely been brought together: conservation and biodiversity of oak savanna ecosystems and process-level ecophysiological water relations of trees.

The second study presented here (Chapter 3) is motivated by a puzzling juxtaposition



Figure 1.1: A pair of Oregon white (Garry) oaks thrive in a harsh savanna environment in the Central Belt *mélange* in the Northern California Coast Ranges. Photo courtesy of Wendy Baxter.

of radically different plant communities that border one another for a significant portion of the Northern California Coast Ranges (Figure 1.2). From west to east, as one moves across the landscape inland from the Pacific coast in Mendocino County, the towering evergreen forest abruptly gives way to a sparse deciduous oak savanna-woodland. Although rainfall generally decreases inland, it does not decrease quickly enough to explain this sudden vegetation transition, and the savanna-woodland receives 1800 mm of rain on average each year, compared to the 2000 mm a year in the evergreen forest to the west. Instead, the ecotone separating the plant communities coincides with a geologic contact separating different belts of the Franciscan. The fact that globally the savanna-woodland plant community is more commonly found in environments that receive approximately five times less rainfall hinted to us early on that a subsurface water supply limitation may explain the existence of the savanna-woodland. Chapter 3 summarizes findings from extensive drilling and intensive hydrologic observations at two hillslopes and catchments that lie opposite one another on either side of the geologic contact. These investigations revealed how the subsurface structure of the critical zone determines how water is shed from landscapes and how much water can be seasonally stored. The densely forested site had a thicker subsurface critical zone which results in higher water storage capacity, more productive ecosystems, runoff generation from deeper groundwater, and greater summer streamflow. Where the subsurface critical zone is



Figure 1.2: Oblique birds-eye view looking north along the Northern California Coast Ranges reveals a sharp ecotone separating a evergreen mixed broadleaf-needleleaf forest (to the west) from a deciduous oak savanna-woodland (to the east). Yellow line is the geologic contact separating the Coastal belt (west) from the Central belt (east) of the Franciscan complex, after Langenheim et al. [2013]. Google Earth image taken by David Dralle.

thin and storage capacity is limited, the subsurface completely saturates, and the landscape sheds incoming rain via surface runoff. This lithologically driven water storage limitation therefore explains the presence of an oak-savannawoodland in the Northern California Coast Ranges where rainfall is ample.

The final study presented here (Chapter 4) is primarily motivated by diverse plant community responses to drought. Much has been written about the physiological response of plants to water stress, and a paradigm of how trees die in drought has existed for more than a decade [McDowell et al., 2008]. The basic framework is that two fundamental mechanisms kill trees when water supply declines, with the particular mode of mortality depending on

plant behavior. One strategy in drought, referred to as anisohydricity, is for trees to keep their stomata open in order to continue fixing carbon. Although this maintains the plant's energy supply it provokes sustained water loss and subsurface drying, resulting in a harder "pull" (greater negative pressure) on the continuous water column that extends through the xylem from the subsurface to the leaf. Excessive tension in this column can result in cavitation and abrupt hydraulic failure. The second strategy, referred to as isohydricity, is for trees to close their stomata to prevent water loss and excessive tension in their vascular network. However, this strategy prevents carbon from entering the leaf, leading to starvation. The first mode of mortality can be discrete and sudden, and is likely a function of the severity of the drought; the second mode is prolonged, and can be more a function of the duration of the drought. This paradigm provides a useful physiologic framework for interpreting how low water availability mechanistically leads to tree death, but it does not fundamentally address the conditions required for a decline in precipitation to actually become a shortage of water supply—in other words, when and why a meteorological drought becomes hydrological drought. That depends on the interactions between precipitation patterns and subsurface water storage dynamics, and is the subject of Chapter 4.

The stage for Chapter 4 was set when a period of low precipitation and high temperatures began in 2011, peaking in 2014, across the state of California. It was, according to various historical and proxy records, the most severe drought in more than a thousand years [Griffin and Anchukaitis, 2014]. Accompanying concerns for municipal and agricultural water supplies—and the first state-wide water conservation mandates [Office of Governor, California, 2015]—more than a hundred million mature trees died [US Forest Service, 2016a]. This tree mortality was presumably due to the combined effects of steep declines in precipitation, increases in temperature, and acute pest-related pressures. The drought provided a stark backdrop to efforts by those of us working at the ERCZO in the Northern California Coast Ranges, where very few trees appeared to be dying (Figure 1.3), to understand how the subsurface critical zone structure mediates subsurface water storage and supply to plant communities. Over the course of several years a variety of clues emerged from tree-, hillslope- and catchment-scale observations, explaining why diverse plant communities along the North Coast—spanning oak woodland to dense old growth Douglas fir—generally survived the drought, unlike other areas in the state. These observations were collected at Rivendell, the intensively monitored hillslope at the Angelo Coast Range Reserve in the dense conifer forest along the south fork of the Eel River, and Sagehorn Ranch, the nearby intensively monitored oak woodland site in the Central Belt of the *mélange*, both part of the ERCZO.

One of the first key observations came from repeat down-borehole neutron probe surveys at Rivendell. These measurements enabled detection of changes in water content in the vadose zone. Rempe and Dietrich [2018] observed that the tens-of-meters thick unsaturated (soil and rock moisture) zone exhibits a common wet-up and dry-down cycle year after year. A maximum moisture content is reached, akin to field capacity, relatively early (in terms of the cumulative precipitation) in the wet season (Figure 1.4); subsequent rains do not further elevate the water content, but instead water passes to the groundwater table, where rising



Figure 1.3: Widespread tree die-off in the Sierra Nevada (top, photo credit US Forest Service) contrasted with healthy mixed conifer-broadleaf forest at the Angelo Coast Range Reserve (bottom, photo credit Collin Bode) in the recent extreme California drought.

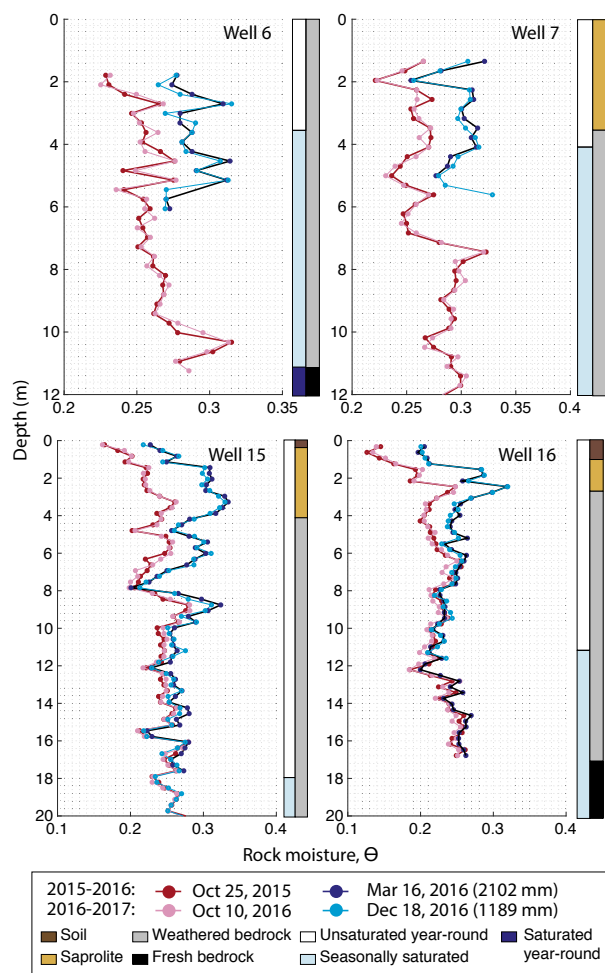


Figure 1.4: Vertical profiles of rock moisture expressed as volumetric water content, θ , in a subset of wells at the Angelo Coast Range Reserve show that similar minimum (red) and maximum (blue) θ is reached in different years. Seasonal cumulative precipitation at the time of the wet-season measurement is shown in parentheses in the legend. Colored vertical bars on the right of each graph illustrate the zone of water table fluctuation identified via groundwater monitoring (left bars) and the weathering profile characteristics identified during drilling (right bars). Caption and figure adapted from Rempe and Dietrich [2018].

water levels drive increased runoff and streamflow.

A distinct but related hydrological behavior is observed at Sagehorn in the *mélange*, where the weathered zone is much thinner. After the first 100–200 mm of rain in the wet season, the entire subsurface saturates, resulting in saturation overland flow as Dralle et al. [2018] and Hahm et al. [2019b] observed. Thus, the saturated zone storage reaches a common maximum value at various times throughout a particular wet season, and further rain does

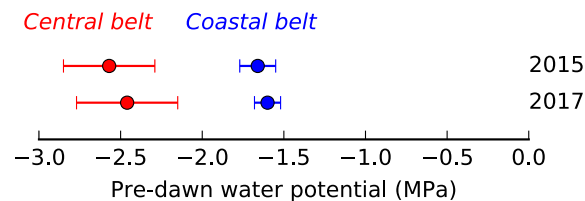


Figure 1.5: End-of-summer site-wide average and standard error tree pre-dawn water potential, a metric of relative plant water availability in the subsurface and internal plant water stress. Although the two sites are different (see details in Chapter 3), no detectable difference exists between years with very different total winter precipitation (2015: approximately 1600 mm; 2017: approximately 3500 mm).

not produce greater water storage. These observations are consistent with catchment-scale observations at Sagehorn’s Dry Creek, and at Rivendell’s Elder Creek. Running mass balances of catchment-wide storage, inferred from rainfall inputs and evapotranspiration and runoff outputs, indicate that storage increases at the start of the wet season, but then levels off, with further rain causing runoff but not greater storage [Dralle et al., 2018; Hahm et al., 2019b]. These observations suggested that—in this rain dominated Mediterranean environment—variations in total annual precipitation do not translate into variations in the amount of stored water between years, but instead cause differences in total winter runoff.

The final clue came from the trees themselves: we observed little mortality or foliage die-back at either site. Furthermore, end-of-summer predawn water potentials—a metric of subsurface water availability and plant water stress—while different between sites were indistinguishable at a given site between very wet years and relatively dry years (Figure 1.5).

Collectively, these observations indicated that the water storage capacity is ‘capped’ by the subsurface weathering profile structure, and, at these North Coast sites, is much lower than the average annual rainfall. This situation is depicted in the cartoon of Figure 1.6.

Hence, the final study presented here directly addresses the question of when a shortage of precipitation becomes a shortage of water supply to plants. Chapter 4 proposes—counter to common wisdom—that *low* water storage capacity in Earth’s critical zone (which includes soil and weathered bedrock) relative to average rainfall can decouple plant community productivity and water use from rainfall variability, and conversely that relatively large storage capacity increases plant sensitivity to annual swings in rainfall totals. A simple model and analysis of watersheds in winter wet, summer dry climates in California reveal that where it consistently rains much more than the subsurface can store, a similar amount of water is stored belowground in both relatively wet and dry years, with excess rainfall leaving as runoff. This results in the hypothesis that storage-capacity limitation would result in similar year-to-year summer plant water availability, in spite of highly variable winter rainfall. Satellite observations revealed that summer plant greenness was insensitive to swings in precipitation at these storage-capacity-limited sites. Contrary to predictions based primarily on tree density and rainfall deficits, these sites did not experience widespread mortality in

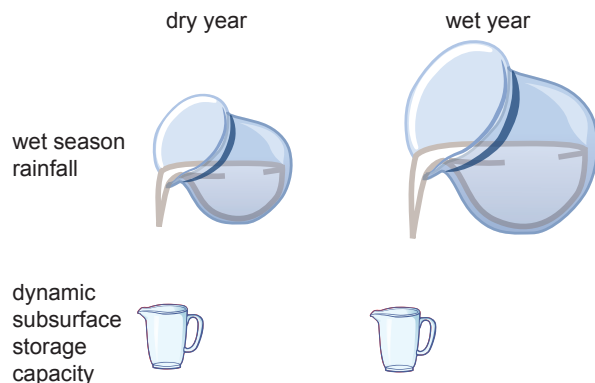


Figure 1.6: Cartoon depicting a relatively small subsurface water storage capacity, in the form of the cups below, which will be filled in both dry (left) and wet (right) years, because the average rainfall (above) is so much larger.

the 2011–2016 extreme drought.

Open questions and future directions

The work presented here raises many unanswered questions, which I describe here as starting points for future work:

—How can subsurface water storage capacity be predicted at large spatial scales? Addressing this question is central to incorporating more accurate ecohydrologic parameters (including, importantly, storage capacity in weathered bedrock below the soil) into Earth system models. Two avenues appear particularly promising: 1) mass-balance methods for tracking actual dynamic water storage over seasonal cycles (with geophysical methods such as the GRACE satellites or GPS-determined surface deformation due to the mass loading of water), and 2) using plants as “sensors” to detect how sensitive plants are to year-to-year precipitation variability; the latter is being explored in collaboration with David Dralle for which a related manuscript is in preparation.

—What governs critical zone evolution and the subsurface architecture of weathered bedrock, which is argued here to have a primary control on the routing and storage of water in the subsurface? In Chapter 3 a tentative explanation for the relatively thin extent of weathering in the Central belt *mélange* is offered, and much more work could be done. Progress on this front both locally and globally requires significantly more exploration of the subsurface, in order to generate datasets that span lithologic, climatic, and uplift gradients which can be used to test predictions emerging from models of CZ evolution.

—How does *hillslope* tree water use (in contrast to riparian tree water use) in summer impact baseflow in seasonally dry environments? A common assumption at the center of most previous considerations is that tree water use and stream baseflow are drawn from the same subsurface reservoir, such that increased tree water use should therefore detract

from the reservoir that drives summer baseflow. An alternative hypothesis has emerged from studying catchments in the Eel River watershed, particularly from the Rivendell hillslope bordering Elder Creek, described in Chapters 3 and 4. There, a suite of evidence suggests that summer baseflow is primarily generated from groundwater, whereas hillslope tree water use is sourced from the overlying vadose zone in both weathered bedrock and the soil. We hypothesize that if the hillslope trees were removed, the vast majority of the water they use over the summer would essentially sit statically in the vadose zone, at a “field capacity”-like state, and drain at a negligible rate to the underlying groundwater. Thus, there would not be increased summer baseflow at a particular date in the middle of the summer dry season. There would, however, be a shorter lag time for runoff to increase in response to the first winter rains, not only because of decreased interception, but also because the vadose zone “sponge” would not have as great a storage deficit that requires replenishment before triggering drainage to the underlying saturated zone (e.g., Salve et al. [2012], where higher head gradients arise that increase runoff. This line of reasoning is closely related to the following questions.

—What would the seasonal rock moisture dynamic be in the absence transpiration by vegetation, which is largely responsible for the summer water drawdown of hillslope vadose zone water storage at Rivendell? This question is ripe for a paired-hillslope treatment experiment, wherein a network of boreholes are exploited via neutron and nuclear magnetic resonance logging to monitor the intra-hillslope vadose zone water storage dynamic before and after a forest clearing or girdling treatment (alongside a non-cleared/girdled control).

—What is the origin of diel oscillations in stream stage and groundwater tables in the Northern California Coast Ranges? Field investigations focusing on high precision measurements of seasonally changing phase lag and amplitude are being planned now, which should help reveal whether diel oscillations arise due to i) direct tapping of groundwater by hillslope and/or riparian trees; ii) diel reductions and (possible increases) in groundwater recharge from the saturated zone, and/or iii) a pressure wave transmission through the unsaturated zone to the water table.

—The storage-capacity limitation mechanism described in Chapter 4 provides a mechanism by which summer plant water availability in the dry season can be decoupled from year-to-year swings in rainfall variability in a Mediterranean climate. This result raises a closely related question: to what extent is summer baseflow in seasonally dry climates similarly decoupled from rainfall variability? Preliminary analysis is tractable with the existing USGS gauge network, but an in-depth look at this problem would benefit from greater hillslope-scale observations of unsaturated and saturated zone water storage dynamics across sites with varying ratios of subsurface water storage capacity to average annual rainfall.

Note: Some of the text in this Introduction is adapted from the plain language summaries of Hahm et al. [2019b] and Hahm et al. [2019a].

Chapter 2

Controls on the distribution and resilience of *Quercus garryana*: ecophysiological evidence of oak's water-limitation tolerance

2.1 Abstract

The composition of forests in Western North America is changing. The decline in the shade-intolerant Oregon white oak (*Quercus garryana* var. *garryana*) is attributed to increased competition with the tall-growing Douglas fir (*Pseudotsuga menziesii* var. *menziesii*) as a result of widespread fire exclusion. In a warmer, drier future, both species will experience increased water stress, and their distribution will depend on ecophysiological adaptations to water limitation, of which little is known for *Q. garryana*. Here, we report a suite of new ecophysiological observations to better understand the oak's water-limitation tolerance, in order to predict its fate in a changing climate. Our study site in the Central Belt of the Franciscan complex in the Northern California Coast Ranges receives almost no rain in the leaf-on growing season and has limited subsurface water storage capacity. In spite of low pre-dawn water potentials (Ψ ; to below -3.0 MPa), mature trees maintained high rates of sap flow. Sap flow continued due to a high Ψ gradient (-1.6 MPa on average) at mid-day between shoots and the subsurface (inferred from pre-dawn measurements) throughout the dry season. Depletion and recharge of stored water in stem tissue and leaves helped to sustain transpiration. Leaves experienced low Ψ (below -4 MPa), and declining hydraulic conductance yet remained functional. Pressure-volume curve analyses revealed that the maintenance of positive turgor pressures in leaves at low Ψ may be attributable to dynamic adjustment due to changes in cell wall elasticity. The turgor loss point may be of limited use in delineating ecophysiological limits to growth and reproduction, as transpiration and apparently normal physiological behavior continued after pre-dawn water potentials declined

below turgor loss limits inferred from rehydrated leaves. These findings indicate that *Q. garryana* is a water-limitation-tolerant tree species that maintains hydraulic function as subsurface water supply and atmospheric demand conditions exceed the ranges at which *P. menziesii* can operate. These observations can be used to explain *Q. garryana*'s extant species range and anticipate its likely resilience in a warmer climate.

This chapter is adapted from Hahm, W., Dietrich, W., and Dawson, T. (2018). Controls on the distribution and resilience of *Quercus garryana*: ecophysiological evidence of oak's water-limitation tolerance. *Ecosphere*, 9(5):e02218.

2.2 Introduction

The composition and function of ecosystems are undergoing rapid alteration [Foley et al., 2005; Marlon et al., 2008; Loarie et al., 2009]. Globally, tree species distributions depend primarily upon water availability [Holdridge, 1947; Woodward, 1987], which in turn depends on precipitation patterns, atmospheric demand for water, and, in seasonally dry climates, the capacity of the subsurface to store and release water to terrestrial ecosystems [Jones and Graham, 1993; Anderson et al., 1995; Porporato et al., 2001]. Warm dry periods can result in widespread mortality: In the state of California alone, the most recent drought resulted in the death of more than one hundred million trees [Asner et al., 2016; US Forest Service, 2016b], a vivid example of the limits of ecosystems to climate perturbations. These types of events have spurred research into understanding plant response to changing climate, with a particular emphasis on water-use strategies and species-level traits that prolong functioning in drought [McDowell et al., 2008; Allen et al., 2010; Bartlett et al., 2012; West et al., 2012].

Alteration of natural and historic fire regimes can interact with water limitation. In western North America, for instance, fire-intolerant conifers (primarily coast Douglas Fir, *Pseudotsuga menziesii* var. *menziesii*) have encroached upon oak habitat in the wake of post-Euro-American-contact fire exclusion—that is, the cessation of intentional burning and the active suppression of naturally ignited fires [Sprague and Hansen, 1946; Devine and Harrington, 2006; Pellatt and Gedalof, 2014]. The dominant oak along most of the Pacific west coastal mountains, *Quercus garryana* Dougl. ex. Hook. var. *garryana* (Oregon White or Garry oak), has experienced radical habitat loss yet has received relatively little research on its ecophysiology within its ecological context [exceptions include Phillips et al., 2003a; Davis, 2005; Kelly, 2016; Merz et al., 2017]. This information gap hinders our ability to predict and manage the oak's fate as climate warming accelerates [Smith et al., 2015]. The success of physiologically based mechanistic models of species-level sensitivity to climatic and subsurface water status relies on accurate parameterization of how key plant traits respond in concert to water limitation. Although individual traits have been studied [Phillips et al., 2003b; Davis, 2005; Meinzer et al., 2005, 2016; Johnson et al., 2009, 2012; Merz et al., 2017], the collective water relations of wild, mature *Q. garryana* have not been documented.

In seasonally dry Mediterranean climates, water availability is generally out of phase with solar energy supply. Plants develop strategies and traits to obtain water as the subsurface

progressively dries. As turgor (the pressure inside plant cells that provides rigidity) is generally required for hydraulic function, there is a tendency for species with low turgor loss points (TLPs) to be water-limitation tolerant, and plants with low TLP tend to be found in more xeric habitats [Bartlett et al., 2012; Meinzer et al., 2016]. Significant variability in the TLP exists among co-occurring or even sympatric species, however, and seasonal and daily plasticity of osmotic potential or cell wall elasticity can prolong turgor loss [Joly and Zaerr, 1987; Dawson and Bliss, 1989; Marshall and Dumbroff, 1999]. This indicates that the TLP alone is insufficient to adequately characterize a species' sensitivity to water limitation for many predictive purposes and highlights the need for a more comprehensive understanding of individual species' water-use strategies to predict resilience to climate change and inform management decisions.

Quercus garryana range

Within *Q. garryana*'s naturally occurring range (Figure 2.1), annual average precipitation increases more than tenfold, from <170 mm in the Tehachapi Mountains of southern California to >2000 mm in the Cascades of Oregon [Stein, 1990]. *Quercus garryana* has the largest north–south range of any west-coast oak and is the only native oak in Washington and British Columbia and the principal native oak in Oregon. At the northern end of *Q. garryana*'s range, oak woodlands appear to be concentrated in the relatively xeric microclimates induced by orographic shielding [Pellatt and Gedalof, 2014]. Such biogeographic associations and findings from Franklin and Dyrness [1973] led Minore [1979] to rank *Q. garryana* as the most drought-tolerant common tree species in the Pacific Northwest. *Quercus garryana*'s competitive advantage over faster-growing species in the wetter parts of its range derives in large part due to its adaptation to fire.

Quercus garryana and fire

Conservationists predict that status quo fire exclusion in western North America will continue to result in takeover of *Q. garryana* woodlands and savanna by *P. menziesii* [Reed and Sugihara, 1987]. This prediction is based on the assumption that throughout their mutual range (Figure 2.1) *Pseudotsuga menziesii* can outcompete *Q. garryana* in fire-excluded areas, and the observation that many *Q. garryana* woodlands and savannas persisted through the Holocene primarily due to the role of fire, whether anthropogenic or naturally ignited [Devine and Harrington, 2006; Pellatt and Gedalof, 2014]. Two centuries of fire exclusion, after millennia of intentional burning that promoted oak habitat, resulted in significant conversion of oak woodlands and savanna to conifer habitat on the west coast [Cole, 1977; Barnhart et al., 1996; Thysell and Carey, 2001; Sugihara et al., 2006; Christy and Alverson, 2011; Dunwiddie et al., 2011; Gilligan and Muir, 2011; McCune et al., 2013; Cocking et al., 2015, but see exceptions in Thilenius, 1968; Gedalof et al., 2006; McDadi and Hebda, 2008]. Unlike *Q. garryana*, *P. menziesii* is highly susceptible to fire, particularly when young [Engber and Varner, 2012]. As firs grow, they become more fire resistant and shade out *Q. garryana*,

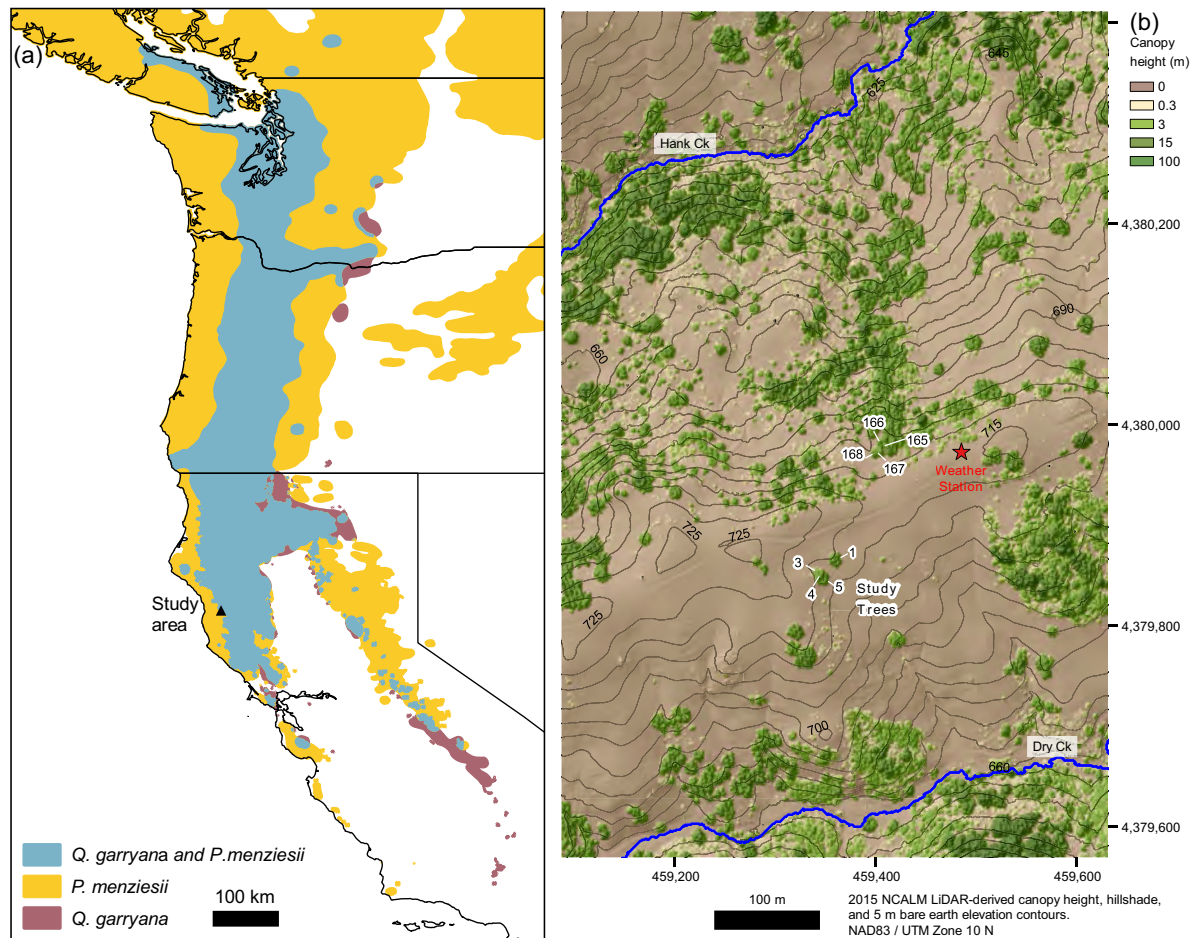


Figure 2.1: (a) Map showing distribution of *Quercus garryana* and *Pseudotsuga menziesii* in western North America and study area (black triangle). The *Q. garryana* range is almost entirely subsumed by *P. menziesii*, except at its western- and southern-most margins. Range maps were generated from the union of Little [1971] shapefiles provided by the USGS and scanned, georeferenced, and digitized maps by Griffin and Critchfield [1972] of the state of California, which include smaller, geographically isolated populations at higher spatial resolution. Study area map (b) created from semi-transparent canopy height raster draped over hillshade derived from first return lidar elevations. Elevation contour labels in meters above sea level; white-outlined numbers show the location of study trees (see Table 2.1)

reducing growth and ultimately resulting in mortality [Devine and Harrington, 2006; Gould et al., 2011]. Fire exclusion and the consequent loss of oak savanna and woodland adversely affect ecosystem biodiversity. *Quercus garryana* savanna and woodland host higher levels of species richness than any other terrestrial habitat in California and coastal British Columbia, including numerous at-risk species [California Department of Forestry, 1996; Erickson, 1996; Fuchs, 2001; Zack et al., 2005; Parks Canada, 2006b,a; Pellatt et al., 2015]. The great biodiversity in *Q. garryana* savanna and woodland ecosystems—and its disappearance under closed-canopy conifer forests—has prompted numerous managers and conservationists to begin manual conifer removal projects and/or prescribed fire treatments [Hastings et al., 1997]. This issue remains at the forefront of conservation efforts along the west coast [Miller, 2002; Thompson, 2007; Dunwiddie and Bakker, 2011].

To explore *Q. garryana*'s susceptibility to climate warming and its ability to compete with *P. menziesii* in a warmer future, we selected a field site in the Coast Ranges of Northern California where locally *Q. garryana* is common. Due to an extremely limited subsurface water storage capacity [Hahm et al., 2019b], the *Q. garryana* stands at our study site are not experiencing invasion by *P. menziesii* [Hahm et al., 2017b]. We propose that studying the water relations of *Q. garryana* at this site will inform the water-availability conditions that *Q. garryana* can tolerate but *P. menziesii* cannot. We further explored whether *Q. garryana* is more water-limitation tolerant than *P. menziesii* by comparing the water relations of *Q. garryana* to existing literature on the relatively better-studied *P. menziesii*, including a detailed water-use study in an area of essentially identical climate across a geologic contact where *P. menziesii* is the dominant canopy-emergent species [Link et al., 2014].

We hypothesized that, relative to *P. menziesii*, *Q. garryana* would (1) maintain a gradient between pre-dawn and mid-day Ψ longer into the dry summer growing season, (2) maintain higher late dry-season sap flow, reflecting continued water use and photosynthesis, (3) exhibit a lower leaf TLP, and (4) have less vulnerable hydraulic pathways. Our findings support all of these hypotheses. *Quercus garryana* is exceptionally water-limitation tolerant; it maintains sap flow at low water potentials (< -4 MPa in leaves), at times when neighboring *P. menziesii* exhibit marked declines, and exhibits a lower TLP and less vulnerable leaf hydraulic network than *P. menziesii*. These observations, in conjunction with paleo- and modern climate responses of the two species, suggest that extant *Q. garryana* woodlands and savanna will persevere as the west coast of North America continues to warm.

2.3 Methods

Site description

The study site, Sagehorn, is located in the main stem Eel River watershed in the Northern California Coast Ranges and is part of the National Science Foundation-supported Eel River Critical Zone Observatory (Figure 2.1). The site is ~ 25 km east of the Pacific Ocean at 700 m above sea level. This study complements ongoing ecohydrological efforts to understand

the influence of subsurface weathering profiles on hydrologic runoff pathways and regional forest distribution [Hahm et al., 2019b], oak water sourcing dynamics as inferred via stable isotopes [Hahm et al., 2017a], dynamic hillslope water storage [Dralle et al., 2018], and the extent of dry-season wetted stream channels [Lovill et al., 2018].

Climate, geology, and soils.—The site experiences a Mediterranean climate with hot, dry summers and cool, wet winters. Nearly all of the precipitation falls as rain between November and April. The annual average rainfall is ~ 1800 mm, and the average temperature is 13.3 °C (version M2; PRISM Climate Group, Oregon State University, <http://prism.oregonstate.edu>).

The site lies within the Central belt *mélange*, a chaotic metasedimentary belt of the Franciscan complex [Jayko et al., 1989; McLaughlin et al., 1994], which underlies $\approx 50\%$ of the Eel River watershed [Langenheim et al., 2013]. The matrix of the *mélange* is argillaceous and encompasses coherent blocks of greywacke, chert, and minor high-grade metamorphics and ultramafics [Blake and Jones, 1974; Cloos, 1982]. Formerly active earth flows are common at the site, but the study trees are situated close to the local topographic divide, above relict earthflow topography (Figure 2.1).

Soils at the site are classified as mollisols [Rittiman and Thorson, 2001]. Near the study trees, a typically 30 cm thick brown–black organic-rich granular mineral A horizon abruptly overlies a yellow-gray, massive 10–20 cm thick Bt horizon that has a sharp decrease in organic matter content and higher clay content. Below the Bt horizon lies a weathered-bedrock zone, and by ~ 2 –4 m depth, there is fresh, dense *mélange* with very low porosity that remains perennially saturated. Soil pits and hand augering revealed fine roots and fungal hyphae throughout the A and B horizons as well as the underlying weathered rock, to depths of at least 2 m. The A and B horizons are dilationally disturbed by roots and animal burrowing, leading to their progressive displacement downslope. Infiltrating rain collects in the pores of the weathered bedrock, and with sufficient rainfall, the pores become saturated throughout the subsurface, driving groundwater to the surface and promoting wide-spread saturation overland flow in the winter wet season (see descriptions in Hahm et al. [2019b] and Lovill et al. [2018]).

Vegetation and study trees.—The site is characterized by heterogeneous vegetation communities. Areas underlain by predominantly *mélange* matrix are commonly grassland–savannah (on south-facing slopes) and woodland (on north-facing slopes). The herbaceous groundcover is primarily annual and non-native. *Quercus garryana* is the dominant woodland/savannah species, with occasional California buckeye (*Aesculus californica*) and California black oak (*Quercus kelloggii*). Recruitment patterns inferred from an exploratory tree survey in the study area of >2800 individual trees indicated that stand species composition does not appear to be changing (e.g., juvenile and seedling *Q. garryana* are the dominant under the canopy of mature *Q. garryana*, and typically not found elsewhere; Hahm et al. [2017b]). Large sandstone blocks at the site support dense forests of Douglas fir and Pacific madrone (*Arbutus menziesii*). These vegetation assemblage patterns correlate with differences in seasonal water storage capacity controlled by the contrasting thickness and porosity of the subsurface weathered bedrock [Hahm et al., 2019b].

We chose small representative groups of monospecific stands of *Q. garryana* developed on the mélange for intensive study, and to account for possible effects of aspect, selected a stand from a savanna on a south-facing slope and from woodland on the paired north-facing slope (Figure 2.1). The trees ranged from 20 to 65 cm diameter at breast height (see Table 2.1). Canopy heights inferred from first vs. last return lidar (acquired by NCALM) and handheld impulse laser (Impulse 200 LR, Laser Technology, Englewood, Colorado, USA) ranged from 3.6 to 13.4 m. Mean canopy drip-line radii (calculated from the average of four cardinal directions) ranged from 3.0 to 7.4 m. Age determination from rings obtained via increment borers was not feasible due to the hardness of the heartwood; historical air photographs suggest that the study stands were established well before 1954, yielding a minimum age of 64 yr. The trees are situated on the sides of gently sloping hollows near channel heads (Figures 2.1, 2.2). The study trees, like most of the *Q. garryana* at the site, are variably colonized by evergreen American mistletoe (*Phoradendron leucarpum* subsp. *Tomentosum*).

Weather observations

In the spring of 2015, we installed a meteorological station in a grass-dominated area at the topographic divide between Hank and Dry creeks ~ 200 m east of the study trees (Figure 2.1). The station records precipitation (Hyquest TB4), temperature and relative humidity (Vaisala HMP50-L, Vantaa, Finland), wind speed and direction (RM YoungWind Monitor 05103-L), total solar radiation (Li-Cor LI200X-L Pyranometer Shortwave), and barometric pressure (Vaisala PTB110, Vantaa, Finland) every 5 min. We calculated the vapor pressure deficit (VPD), defined as the saturated vapor pressure of the air (e_s) minus the actual vapor pressure of the air (e_a), from the relative humidity and the temperature following Snyder [2005].

Tree water potential measurements

Shoot water potentials (Ψ) were measured with a Scholander-type pressure chamber (Model 1000 Pressure Chamber Instrument, PMS Instrument Company; Albany, Oregon, USA), following procedures in Boyer [1995]. We measured on a biweekly to monthly basis, from the end of the 2015 growing season to the end of the 2016 growing season. All shoots were collected between 1.5 and 2.5 m from the local ground surface. Immediately after excision, shoots were placed into sealed plastic bags in a dark container until measurement 5–60 min later. Pre-dawn Ψ samples were collected between 1.5 and 0.5 h before sunrise, and mid-day samples were collected between 11:00 and 14:30 hours, with two to three shoots collected from full to partial sun positions. We performed two averaging steps to report the pre-dawn and mid-day mean Ψ at a particular date, by first averaging all the shoots from an individual tree at a particular time of day, then averaging across all trees at the site. To highlight the seasonal evolution of the Ψ gradient from subsurface to shoot, indicative of stomatal control on mid-day Ψ and water acquisition strategy more generally, we also compare paired pre-dawn and mid-day Ψ for individual trees.

Table 2.1: Study tree characteristics.

Tree ID (tag #)	Slope aspect	Diameter at breast height (cm)	Average canopy radius (m)	Height (m; impulse laser- inferred)	Height (m; lidar- inferred)	UTM N (m)	UTM E (m)	Sap flow	Piston dendrometer	Pre-dawn & mid -day Ψ	Leaf K	Leaf pressure- volume curve
1	South	65.7	5.6	12.89	12.7	4,379,867.1	459,361.0	y	y	y	y	y
3	South	33.8	4.6	6.18	5.4	4,379,848.9	459,340.3	-	-	y	-	-
4	South	52.0	7.4	13.35	11.3	4,379,849.0	459,346.4	y	y	y	y	y
5	South	45.6	5.1	10.15	9.5	4,379,848.2	459,346.4	y	-	y	y	y
165	North	32.5	3.4	11.8	13.3	4,379,982.0	459,407.7	-	y	-	-	-
166	North	19.7	3.0	7.3	9.3	4,379,982.3	459,406.5	-	-	y	y	y
167	North	36.0	4.9	11.02	8.8	4,379,972.8	459,403.4	y	-	y	y	y
168	North	41.4	3.5	3.58	7.5	4,379,972.6	459,402.5	-	-	y	y	y

Notes: 'y' indicates that the designated measurement was made or sensor was installed on this tree. The dash denotes lack of measurement or sensor

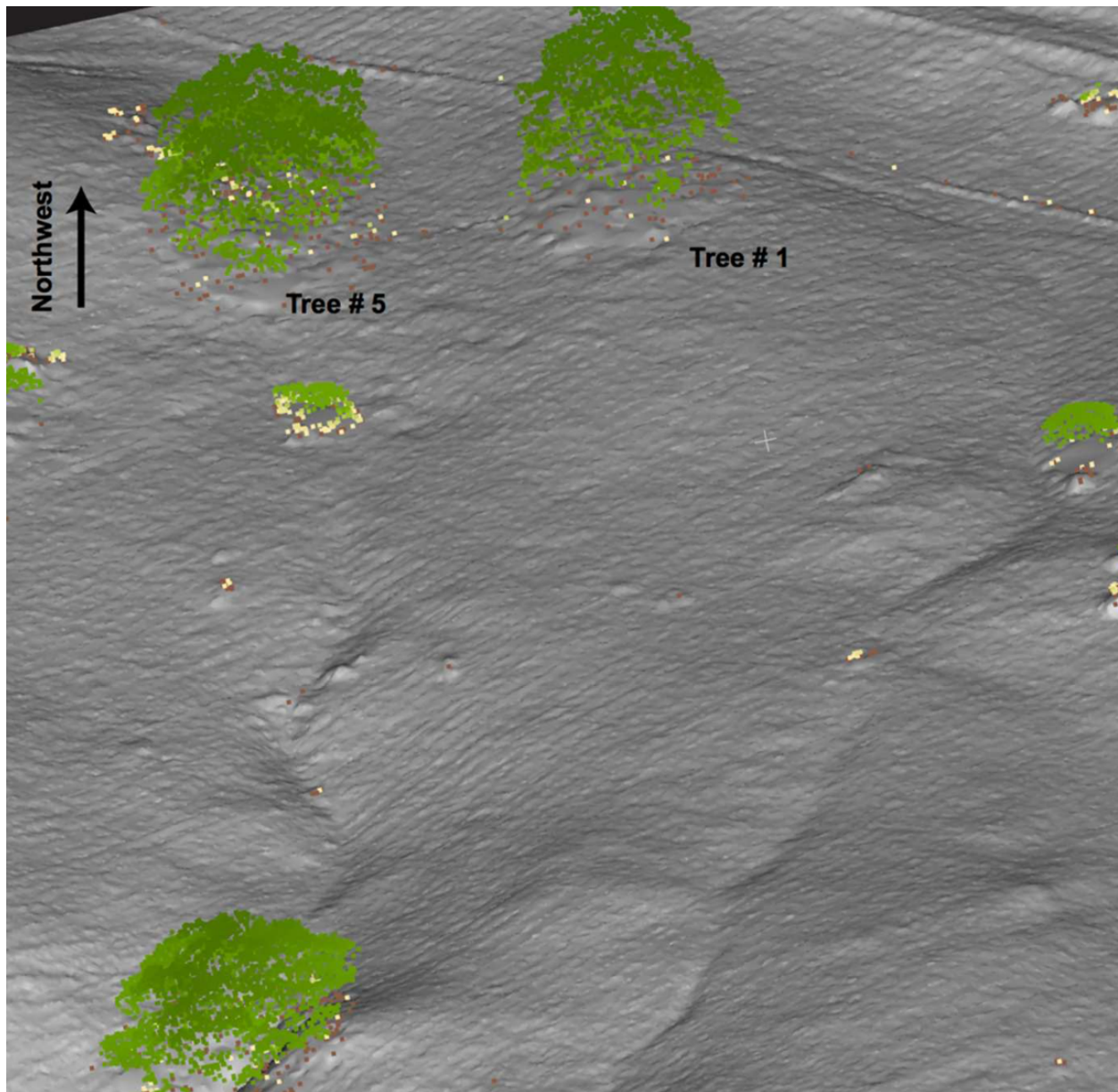


Figure 2.2: Perspective view of south-facing slope study trees, illustrating their geomorphic context (above first-order channel head) and savanna setting. First-return lidar point cloud above bare-earth hillshade shows density of data used to create canopy height in Figure 2.1. Points were clipped to include only those >1 m above the ground, brown-beige-green color scale shows increasing height above ground surface. Scale varies in this perspective view; Tree #1 is approximately 13 m tall.

Interpretation of pressure chamber values.—Pre-dawn Ψ is considered diagnostic of subsurface water availability within the rhizosphere, subject to two factors that tend to bias this interpretation in opposite directions: (1) to the extent that sap flow continues at night, due to nighttime transpiration and/or tissue rehydration [Donovan et al., 2003; Dawson et al., 2007], the pre-dawn tree Ψ will remain lower than the rhizosphere Ψ , and (2) pre-dawn tree Ψ is biased toward the higher Ψ (wetter) reservoirs in the rhizosphere, due to higher hydraulic conductance in these areas [Améglio et al., 1999]. Here, we adopt pre-dawn Ψ as the imperfect yet most physiologically relevant metric of subsurface water availability, and mid-day Ψ as the relevant metric impacting stomatal control and hydraulic limitations such as leaf turgor loss and hydraulic vulnerability of xylem.

Stem vs. leaf potential

In order to determine the magnitude of the Ψ drop between stem and leaf, we maintained individual leaves in Ψ equilibrium with their stems at mid-day by preventing transpiration. To accomplish this, we bagged single leaves in plastic before sunrise to promote 100% relative humidity and enclosed them with foil to exclude sunlight. At mid-day, when the leaves received full to partial sunlight, we excised the bagged leaves and opposite non-bagged leaves from the same shoot at the base of the petiole with a razor blade and measured them in a pressure chamber. A variation of this method was employed by Hellkvist et al. [1974] to determine the gradient of Ψ along trunks, and earlier by Begg and Turner [1970], who referred to this method in analogy to a tensiometer placed into the tree.

Pressure-volume relations

Recent analyses suggest that relative symplastic water content (RWC_{sym}) and Ψ at the TLP (MPa, also known as the wilting point) are primarily functions of the osmotic potential at full turgor (Ψ_{S100} , MPa) and the symplastic cell wall modulus of elasticity [ϵ , MPa; Bartlett et al., 2012]. These cell properties may adjust dynamically on both seasonal and diurnal timescales [Dawson and Bliss, 1989; Meinzer et al., 2014] to depress the TLP and maintain hydraulic function at low Ψ . Leaves are typically fully rehydrated to an initial $\Psi = 0$ MPa prior to determination of pressure-volume (PV) curves; however this rehydration may dynamically alter ϵ or Ψ_{S100} , and hence the inferred Ψ_{TLP} [see for example Meinzer et al., 1986]. One approach to identifying this plasticity is to establish PV curves for both rehydrated and non-rehydrated leaves (to capture short-term dynamics), at different times throughout the course of the year (to capture seasonal dynamics). We adopted this approach and collected shoots with 5–15 mature leaves at dusk or dawn, when water potentials were generally relaxed. To rehydrate samples, we excised leaves underwater near the petiole base with a razor blade and then left petioles in deionized water for >3 h in a dark cooler at $\approx 100\%$ relative humidity. We used a spreadsheet template designed by Cameron Williams (UC Berkeley/Franklin & Marshall College; see Williams et al. [2017]) to visually identify and remove over-hydrated

samples (the plateau effect) and determine all PV-curve parameters. Slopes and intercepts were determined via standardized major axis line fitting [Warton et al., 2006].

The principal metrics of interest were computed as follows: to estimate Ψ_{S100} , we plotted $-1/\Psi$ against $1-RWC$ (total relative water content) and extrapolated the linear (post-TLP) part of the curve to the ordinate. RWC is a derived parameter that requires the leaf dry mass and saturated water content mass, obtained by extrapolation to the abscissa-intercept on a plot of Ψ vs. leaf water mass (this enables the estimation of saturated water content when the first water potential measurement is below zero or when the plateau/over-hydration effect is present; Kubiske and Abrams [1990]). The apoplastic water fraction (AWF) is determined from the abscissa-intercept of $-1/\Psi$ vs. $1-RWC$ post-turgor loss. We calculate ε (the symplastic cell wall modulus of elasticity) by finding the slope on a plot of the pressure component of cell water potential (Ψ_P) against RWC_{sym} prior to turgor loss. At turgor loss, Ψ_P goes to zero, and the osmotic potential (Ψ_S) fully defines the total water potential. Ψ_{TLP} can then readily be determined from the abscissa-intercept in a plot of pre-turgor loss Ψ_P vs. Ψ_S . We calculated absolute area-normalized leaf capacitance C ($\text{mmol} \cdot \text{m}^{-2} \cdot \text{MPa}^{-1}$) as the mass of water in a fully rehydrated leaf multiplied by the slope of RWC vs. Ψ and divided by A and the molecular weight of water [Blackman and Brodribb, 2011].

Leaf hydraulic conductance

We estimated leaf hydraulic conductance (K) as a function of leaf Ψ using the leaf-as-a-capacitor method [Brodribb and Holbrook, 2003]. On 26 July 2016, between 06:00 and 06:30 hours, we collected branches with multiple shoots from six *Q. garryana* individuals (the same individuals instrumented with sap flow sensors and seasonally monitored for Ψ). Pressure-volume relations from leaves from these branches were determined, including pre-turgor loss C . The branches were recut under water and left to rehydrate with their cut ends in water in a dark cooler. On 27 July 2016, we removed the cut ends from water and allowed the branches to slowly dry on the laboratory bench. Prior to determining leaf Ψ , we sealed branches in dark coolers for at least 20 min to promote equilibration of water potential among leaves. We selected one leaf, measured its initial Ψ_0 with a pressure chamber, then cut its closest neighbor underwater, and allowed it to rehydrate through the petiole for 15–40 s. We then immediately determined the final Ψ_f . We calculate leaf K ($\text{mmol} \cdot \text{m}^{-2} \cdot \text{MPa}^{-1} \cdot \text{s}^{-1}$) via $K = C \ln[\Psi_0/\Psi_f]/t$, where t is time in seconds [Brodribb and Holbrook, 2003]. We used the pre-turgor loss C ($255 \text{ mmol} \cdot \text{m}^{-2} \cdot \text{MPa}^{-1}$) from rehydrated leaves for all measurements, even when the initial water potential was below the mean TLP of leaves collected that day. We opt for this method because most Ψ_0 and Ψ_f points were above or spanned the TLP.

Sap flow

We measured trunk sap flow every half hour from midsummer 2015 to fall 2016 on four trees (Table 2.1) with copper-constantan thermocouples at 12.5 mm depth into the sapwood (ICT International Pty, sensor model HRM30, Armidale, Australia; see Marshall [1958]).

All sensors were placed between 2.5 and 3.5 m above the ground along the main trunk below any photosynthetic tissue and secondary branches, in order to minimize interference from cattle, deer, elk, and black bear. Because probes are rarely perfectly spaced, at times of no flow a non-zero velocity may be inferred. To correct for this, following Link et al. [2014], we assume that no gradient in water potential to leaves is maintained during the three hours before sunrise when relative humidity is between 92% and 95%. At lower humidity, nighttime sap flow may occur due to non-negligible VPDs; at higher humidity, dew may condense on leaves, resulting in rehydration and sap flow toward roots. At these times, we take the median sap flow velocity for each sensor to be the true zero flow rate. We then employed the correction procedure for the heat-ratio method outlined in Burgess et al. [2001] to rescale all datapoints to the zero flow rate, assuming a thermal diffusivity of $2.5 \times 10^{-3} \text{ m}^2/\text{s}$. To compare trends in the seasonal and diurnal patterns in sap flow between trees in relation to subsurface water availability and leaf water potential, we normalized all sap flow velocities, following Link et al. [2014]. First, we identified outliers clearly attributable to sensor malfunction, which led us to trim the dataset to exclude values below -5 and above 50 cm/h . Occasional unphysical spikes or drops in sap flow were still present in the resulting datastream, which we eliminated by trimming the dataset again to exclude values below the 2.5 and above the 97.5 percentiles recorded for the entire time series of each individual sensor. We normalized the resulting dataset to the maximum value recorded by each individual sensor during its deployment. We present the entire datastream from each sensor, with a slight transparency to display the changing relative density of data. This time series highlights the daily maxima and minima sap flow throughout the measurement campaign in relation to environmental variables. We also determined the seasonality of total sap flow for each tree by summing normalized sap flow velocities by month, then averaging the resulting sums across all trees. When half-hourly data were missing due to equipment malfunction, we used linear interpolation to infill. We also sought to analyze seasonal changes in the diurnal sap flow pattern by averaging the normalized daily sap flow pattern by month, then averaging across all trees.

Piston dendrometers

To measure seasonal growth patterns and diurnal patterns of water storage, we installed point piston dendrometers (Natkon Model ZN11-T-WP, resolution of $\approx 1 \text{ }\mu\text{m}$; see Zweifel et al. [2006]) on trunks, adjacent to the sap flow probes. The dendrometers measured the combined radial displacement of inner bark, cambium, and sapwood relative to a heartwood frame of reference. Sapwood is the largest component volumetrically, typically composing 15% of stem basal area in *Q. garryana* [Meinzer et al., 2005]. We used a rolling median filter with a single timestep limit of $10 \text{ }\mu\text{m}$ to filter occasional sensor noise. We show the time series during the 2016 growing season of the three trees that did not experience sensor malfunction (#165, #1, and #4), and the average composite diurnal pattern by month of these same trees to highlight the daily patterns of growth and the magnitude of water storage and extraction.

2.4 Results

All terms, symbols, and units are defined in Table 2.2.

Weather

The rain gauge recorded 1976 mm of precipitation in the 2016 water year (Figure 2.3). This relatively wet winter was preceded by four years of drought that affected most of the state of California. No crown dieback was observed on any of the trees selected for this study at the end of the drought or in 2016 following the wetter winter, nor for that matter on any of the mature *Q. garryana* at the site. The last major winter storms of 2016 occurred in April, totaling 76 mm of precipitation, followed by minor storms in May (20 mm) and June (17 mm), with no measured precipitation in July, August, or September. Maximum daily summer temperatures routinely exceeded 30 °C, and during heat waves, nighttime minima did not fall below 20 °C. These high temperatures resulted in daytime VPDs above 4 kPa, and on warm nights, the VPD remained above 1 kPa.

Leaf phenology

Leaves on *Q. garryana* at Sagehorn emerge rapidly in late April through mid-May, and persist until mid- to late November, longer than co-occurring *Q. kelloggii*. *Quercus garryana* on south-facing slopes tend to keep their leaves 1–2 weeks longer than those inhabiting north-facing slopes. We did not observe drought-deciduous behavior in four years of observation (2014–2017); instead, most leaves typically fall after the first significant wet-season rains.

Table 2.2: Symbols, units, and terms.

Symbol	Units	Term
K	$\text{mmol} \cdot \text{m}^{-2} \cdot \text{MPa}^{-1} \cdot \text{s}^{-1}$	Leaf hydraulic conductance
C	$\text{mmol} \cdot \text{m}^{-2} \cdot \text{MPa}^{-1}$	Leaf hydraulic capacitance
TLP	MPA	Turgor loss point
Ψ	MPA	Water potential
Ψ_S	MPA	Osmotic potential
Ψ_{S100}	MPA	Osmotic potential at full turgor
Ψ_P	MPA	Pressure potential
ε	MPA	Symplastic cell wall modulus of elasticity
$\text{RWC}_{\text{total}}$	(decimal)	Total leaf relative water content
RWC_{sym}	(decimal)	Leaf symplastic relative water content
AWF	(decimal)	Apoplastic water fraction
A	cm^2	One-sided leaf area
SLA	m^2/kg	Specific leaf one-sided area
LMA	g/m^2	Leaf mass per one-sided area

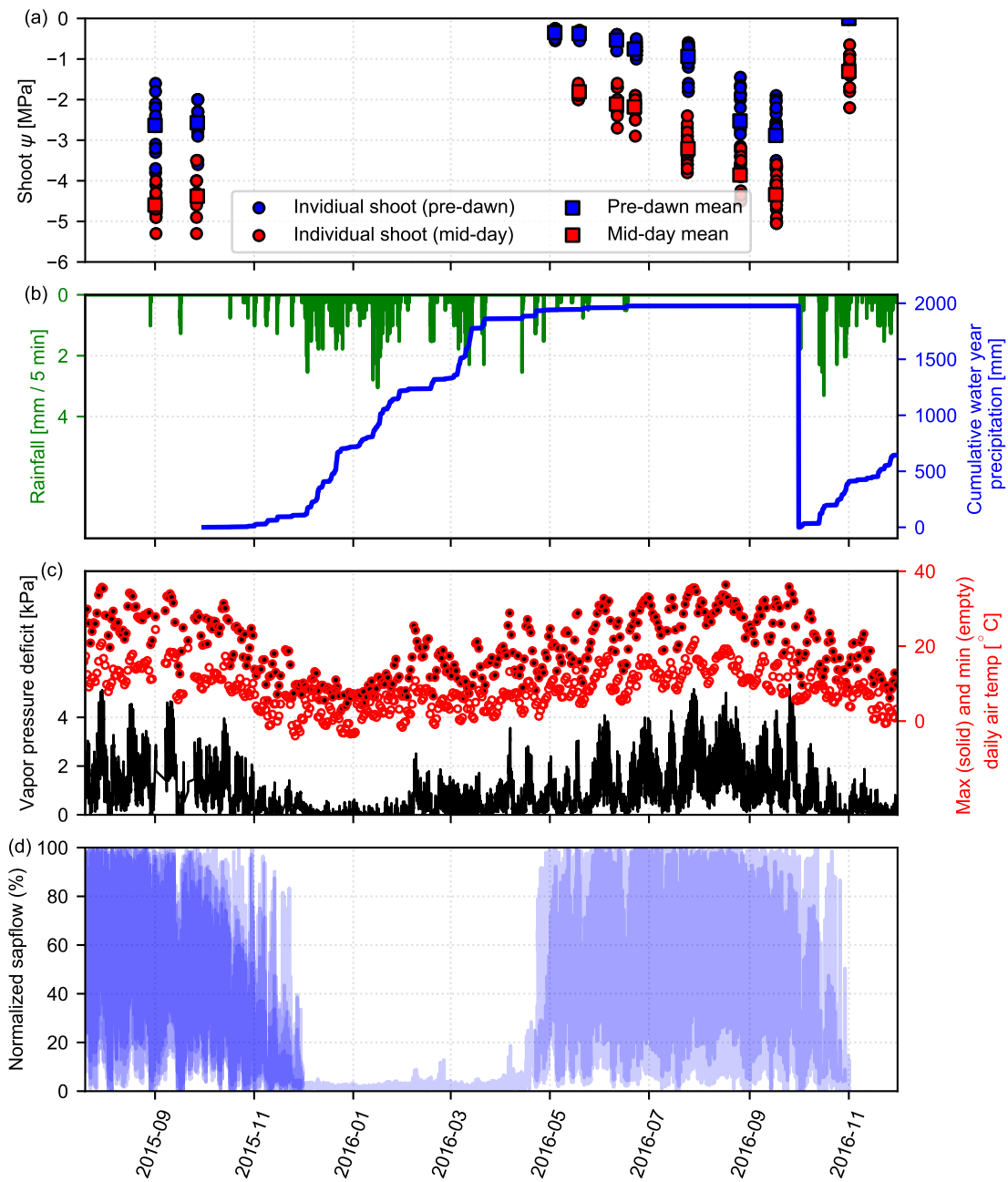


Figure 2.3: Time series of (a) pre-dawn and mid-day shoot Ψ , (b, c) climate, and (d) sap flow in mature *Quercus garryana*. Sap flow remains high in late summer (d) in spite of low subsurface water availability (low pre-dawn Ψ in a), and lack of summer precipitation (b). In (d), slight transparencies highlight the density of data. Cumulative water year precipitation in (b) is missing for 2015 due to incomplete record. Non-zero sap flow during winter when *Q. garryana* lacks leaves in (d) is attributable to evergreen mistletoe.

Table 2.3: Comparison of Ψ along the subsurface-plant-atmosphere continuum on two dry-growing season days.

Parameter	Ψ (–MPa, average \pm standard error of the mean)	
	25 July 2016	26 August 2016
Pre-dawn shoot	$0.94 \pm 0.14(n = 20)$	$2.53 \pm 0.33(n = 17)$
Mid-day stem	$2.38 \pm 0.10(n = 6)$	$3.03 \pm 0.23(n = 6)$
Mid-day shoot	$3.21 \pm 0.12(n = 21)$	$3.86 \pm 0.19(n = 15)$
Mid-day leaf	$3.66 \pm 0.09(n = 6)$	$4.14 \pm 0.19(n = 6)$

Tree water potential

Seasonal pattern.—Pre-dawn shoot Ψ declined throughout the 2016 growing season (Figure 2.3), from mid-May pre-dawn values of -0.38 ± 0.02 MPa, $n = 7$ (mean of individual tree mean \pm individual tree means standard error, $n =$ number of trees) and -1.81 ± 0.03 MPa, $n = 7$ (at mid-day) to mid-September pre-dawn values of -2.88 ± 0.34 MPa, $n = 6$, and mid-day values of -4.34 ± 0.22 MPa, $n = 6$. Two trees (#4 and #166) had average pre-dawn Ψ below -3.5 MPa by mid-September. With the return off fall rains in early November, pre-dawn Ψ rose to values indistinguishable from 0 MPa. Both intra-tree and inter-tree Ψ heterogeneity increased as the growing season progressed, with pre-dawn and mid-day values tightly clustered in May and exhibiting large scatter by September.

Time course of hydraulic gradient.—Figure 2.4 shows pre-dawn vs. mid-day shoot Ψ paired by individual tree on a particular sample day throughout the growing season. On average, a 1.6 MPa hydraulic gradient is maintained in spite of absolute declines in potential: The gradient at the start of the dry season, when pre-dawn Ψ was on average -0.4 MPa, was not markedly different than at the end of the dry season, when pre-dawn Ψ in some trees approached -4.0 MPa.

Stem, leaf, and shoot Ψ .—Figure 2.5 shows a sharp drop (~ 1.2 MPa) between leaf and stem Ψ at mid-day. Mid-day shoot Ψ lies between leaf and stem Ψ , and is closer to leaf Ψ than stem Ψ (Table 2.3), consistent with shoot Ψ representing a weighted average of leaf and stem. In late summer (26 August 2016), the Ψ drop between mid-day stem and mid-day leaf was larger than the Ψ drop between pre-dawn shoot and mid-day stem.

Leaf water relations inferred from pressure-volume curves

The pressure-volume curves exhibited high coefficients of determination ($R^2 > 0.95$) for linear relationships between pre-turgor loss Ψ_P vs. Ψ_S and post-turgor loss $1/\Psi$ vs. $1 - \text{RWC}$ (see example relations and graphical definitions of terms from one individual leaf in Figure 2.6; parameters for all leaves are summarized in Table 2.4). Curves with fewer than four pre-turgor loss measurement points were discarded. This resulted in the loss of three non-rehydrated leaves from the 17 September 2016 measurement campaign, which we infer were

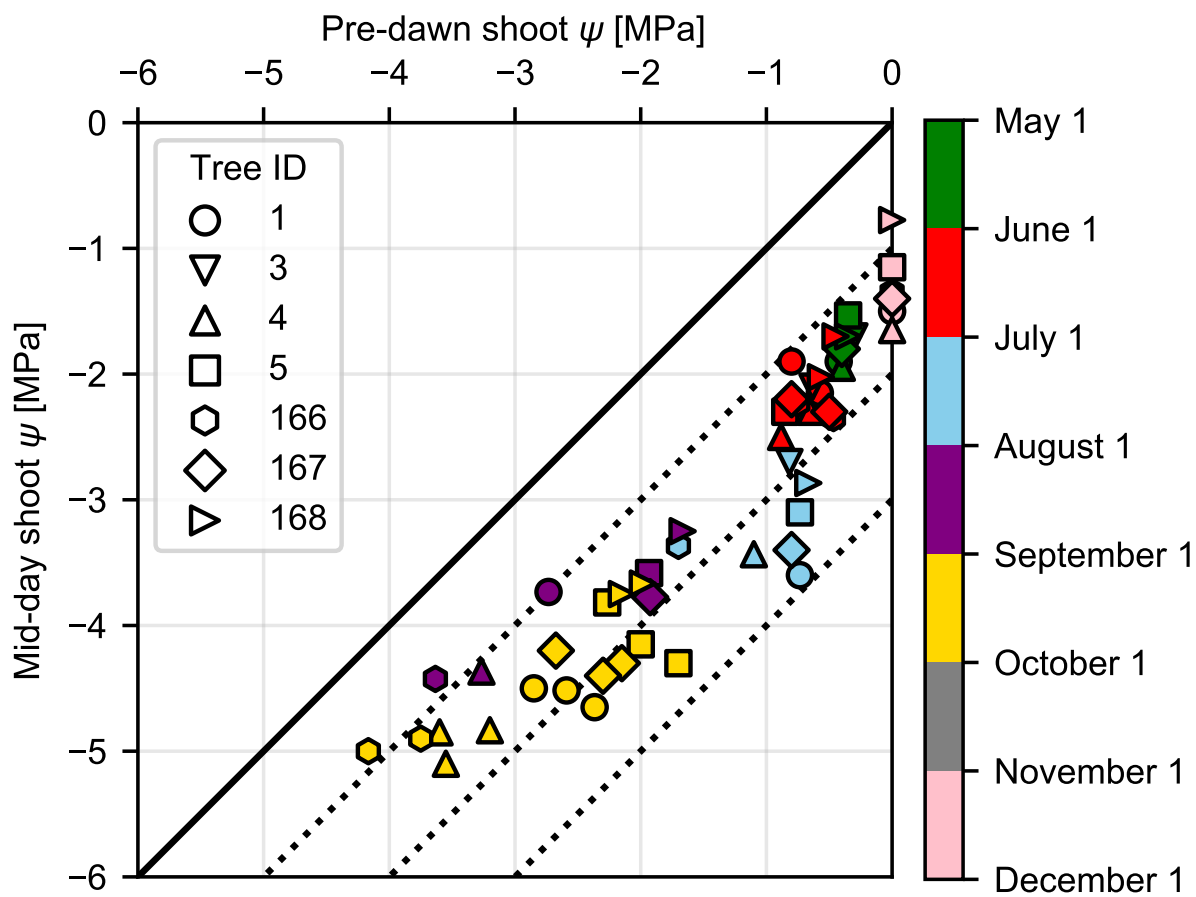


Figure 2.4: Pre-dawn vs. mid-day shoot Ψ of individual mature *Quercus garryana*, color-coded by measurement month in the 2015 and 2016 growing seasons. November measurements taken after return of wet-season rains in 2016. The diagonal dashed lines show -1 , -2 , and -3 MPa isopotential gradients for reference.

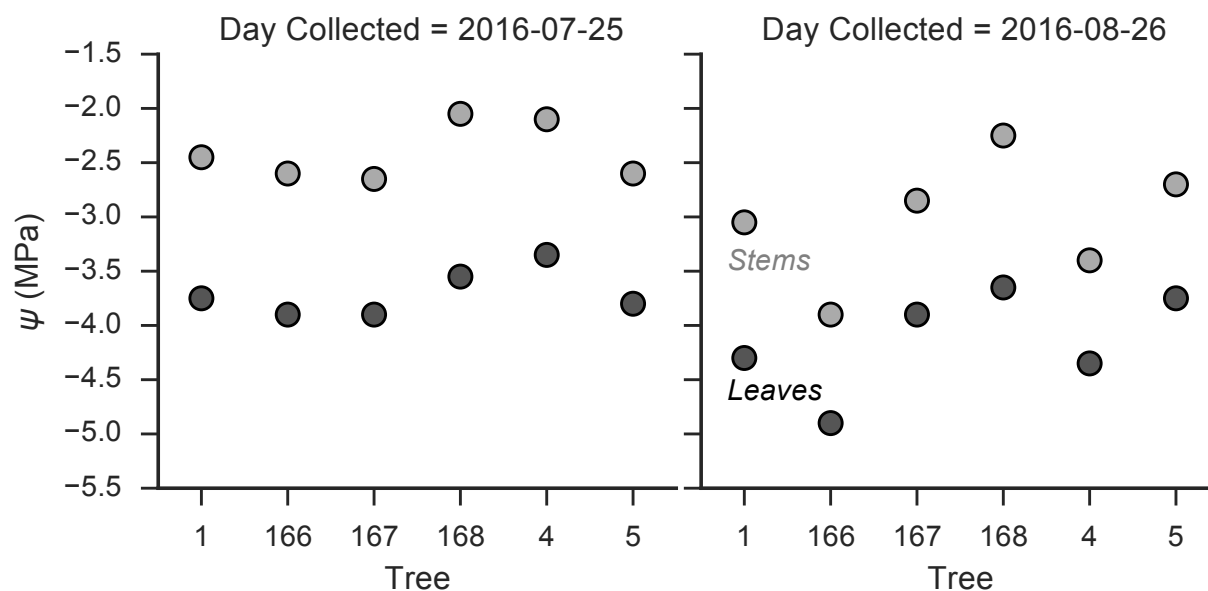


Figure 2.5: Comparison of stem and leaf Ψ from the same shoot at mid-day across two summer days shows consistent >1 MPa hydraulic gradient from stem to leaf. Numbers on horizontal axis refer to tree ID (see Table 2.1 and site map in Figure 2.1).

too close to the TLP at the start of measurement. The average TLP for all measurements was -3.61 MPa (Table 2.4) and varied by nearly 1 MPa across initial hydration status and dates, from a high of -3.28 MPa for rehydrated leaves on 26 July 2016 to a low of -4.26 MPa for non-rehydrated leaves on 17 September 2016. The TLP increased when leaves were rehydrated and generally decreased throughout the season. The average Ψ_{S100} for all measurements was -2.93 MPa, and Ψ_{S100} varied by a relatively smaller extent between initial hydration status and dates, from an average high of -2.74 MPa for rehydrated leaves to an average low of -3.17 MPa for non-rehydrated leaves. Ψ_{S100} decreased slightly on average throughout the season and tended to decrease with rehydration. Bulk tissue elastic modulus, ϵ varied little seasonally, but showed a strongest response to rehydration, approximately doubling on each date from values of ≈ 10 to ≈ 20 MPa, translating to much more rigid leaf tissue at higher initial water contents. RWC_{sym} at the TLP also varied systematically with initial hydration status but not season, with rehydrated leaves exhibiting much higher RWC_{sym} than non-rehydrated leaves. The size of leaves measured for PV curves did not vary systematically.

Leaf hydraulic conductance (K)

K decreased with decreasing leaf Ψ in a sigmoidal fashion (Figure 2.7). A Weibull-type vulnerability curve fit to the data indicates that the maximum K is $13.7 \text{ mmol} \cdot \text{m}^{-2} \cdot$

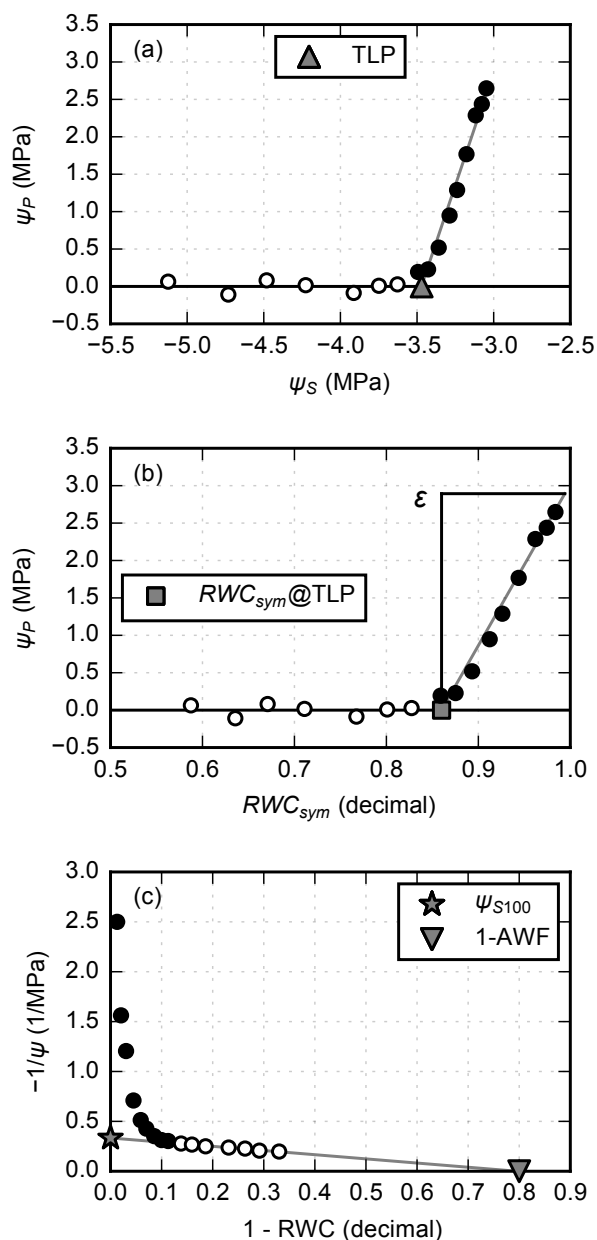


Figure 2.6: Example pressure-volume (PV) curve from a rehydrated *Q. garryana* leaf collected from tree #5 on September 17, 2016, showing pre- (filled) and post- (empty) turgor loss points. Plots (a)–(c) show graphical derivation of important leaf water relations metrics: the turgor loss point (TLP), cell wall symplastic modulus of elasticity (ϵ) and relative symplastic water content at turgor loss ($RWC_{sym}@TLP$), the osmotic potential at full turgor (Ψ_{S100}), and the apoplastic water fraction (AWF). All lines (grey) are determined with standardized major axis fitting.

Table 2.4: Leaf metrics derived from pressure-volume (PV) curve experiments on mature *Quercus garryana* individuals, across sampling days and hydration status.

Day and hydration status	n	Dry mass (g)	A (cm ²)	SLA (m ² /kg)	LMA (g/m ²)	TLP (MPa)	Ψ_{S100} (MPa)	ϵ (MPa)	AWF	RWC _{sym} @TLP
22 June 2016										
Rehydrated	7	0.45 ± 0.15	43.3 ± 18.9	9.40 ± 1.97	110.1 ± 21.1	-3.44 ± 0.32	-2.94 ± 0.35	20.0 ± 5.6	0.20 ± 0.16	0.85 ± 0.03
26 July 2016										
Non-rehydrated	5	0.40 ± 0.08	33.4 ± 9.3	8.30 ± 1.38	123.0 ± 18.3	-3.67 ± 0.44	-2.74 ± 0.21	10.5 ± 1.7	0.18 ± 0.04	0.75 ± 0.04
Rehydrated	5	0.36 ± 0.14	32.0 ± 9.1	9.38 ± 1.64	109.4 ± 19.8	-3.28 ± 0.52	-2.84 ± 0.46	21.6 ± 6.7	0.08 ± 0.24	0.86 ± 0.03
17 September 2016										
Non-rehydrated	2	0.42 ± 0.07	35.0 ± 5.7	8.25 ± 0.03	121.2 ± 0.4	-4.26 ± 0.25	-3.06 ± 0.52	10.4 ± 5.8	0.07 ± 0.03	0.72 ± 0.08
Rehydrated	5	0.45 ± 0.13	35.8 ± 10.5	7.95 ± 0.85	126.9 ± 13.8	-3.85 ± 0.23	-3.17 ± 0.10	17.9 ± 2.4	0.20 ± 0.02	0.82 ± 0.03
All leaves	24	0.42 ± 0.12	36.6 ± 12.8	8.77 ± 1.54	117.1 ± 18.2	-3.61 ± 0.45	-2.93 ± 0.34	17.1 ± 6.3	0.16 ± 0.14	0.81 ± 0.06

Notes: Mean ± 1 standard deviation. See Table 2.2 for abbreviations.

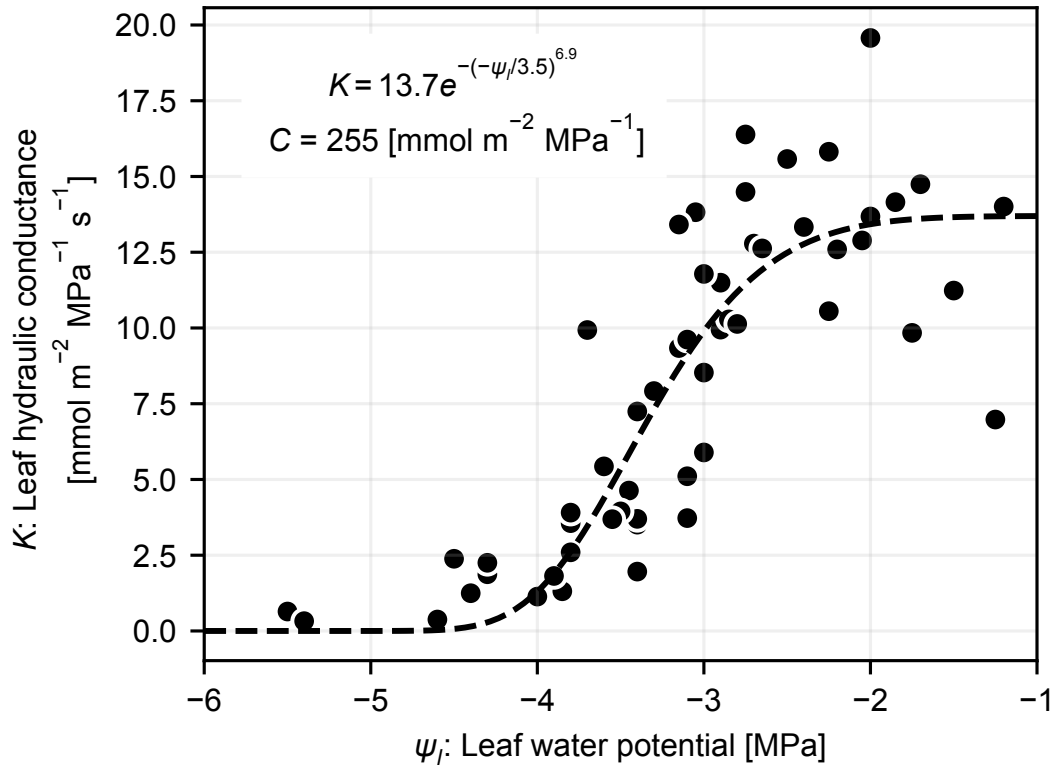


Figure 2.7: Leaf hydraulic vulnerability curve shows decline in the leaf hydraulic conductance (K) as leaf water potential (Ψ) declines.

$\text{MPa}^{-1} \cdot \text{s}^{-1}$. The midpoint (50% loss between maximum and minimum) occurs at a leaf Ψ of -3.35 MPa, and $>95\%$ of the loss occurred over a range of 2 MPa spanning this midpoint. K inferred at low Ψ would be approximately two times lower than presented values if the post-TLP capacitance was used in calculations.

Sap flow

Diurnal trends.—Sap flow exhibits a common diurnal pattern throughout the primary growing season (May–September; Figure 2.8 shows composite monthly averaged patterns across all trees). At pre-dawn sap flows in the trunk, from an April average of $\sim 5\%$ of the maximum, increasing to 12% during the driest, hottest month of the year. Sap flow increases rapidly and monotonically for four hours after sunrise, on average across all trees studied $\sim 60\%$ of the total range. A mid-day depression occurs, after which sap flow rebounds to a daily peak in the mid-afternoon in the summer months between 70% and 90% of the maximum recorded sensor value. With decreasing sunlight, sap flow declines at a lower rate than

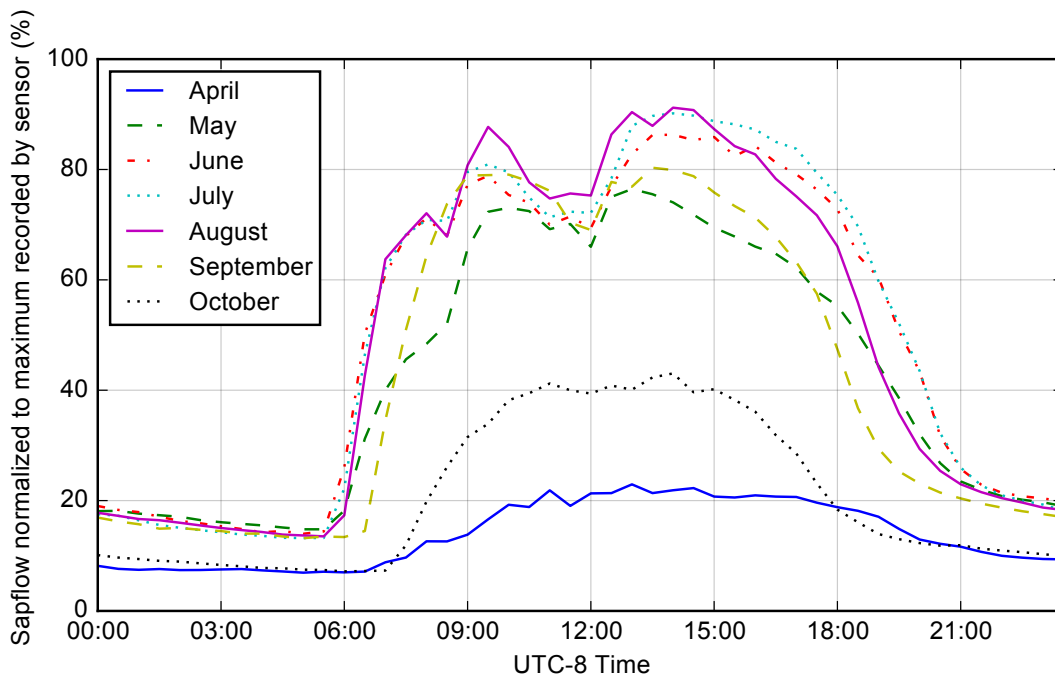


Figure 2.8: Average diurnal sap flow pattern across each month of the 2016 growing season. Sap flow is high in the dry-season summer months, continues at night, and exhibits a mid-day depression. Closer to the solstice, the onset of sap flow in the morning occurs earlier and the evening decline occurs later. Curves do not reach 0% or 100% as the monthly averaged behavior shown here averages across multiple trees and includes days when sap flow did not reach the minimum or maximum recorded.

the morning rise for five to six hours and at sunset is typically $\approx 25\%$ of the maximum value (a factor of ≈ 2 higher than the pre-dawn value). A slow monotonic decline continues until dawn. In April and October, which bookend the growing season, sap flow does not rise to midsummer highs. Nighttime flows are similarly reduced but remain positive pre-dawn.

Seasonal trends.—Phenological observations of leaf out and leaf loss indicate that the early-season (April–May) ramp-up of sap flow coincided with increasing leaf area, and late-season (October–November) declines in sap flow coincided with leaf loss. During the months of highest photosynthetically active radiation, from the beginning of May through mid-September, sap flow returned to near its maximum recorded value for each tree each day but declined in response to short-duration (1–3 d) storms (Figure 2.3). Total sap flow (which is directly correlated with total transpiration) reached a peak in midsummer (Figure 2.9), when atmospheric moisture demand was highest and subsurface water availability was low, as indicated in the VPD and pre-dawn Ψ time series (Figure 2.3). High sap flow throughout the dry-growing season occurred while shoots maintained hydraulic gradients with the subsurface of >1 MPa (Ψ difference between pre-dawn and mid-day), even as both pre-dawn and mid-

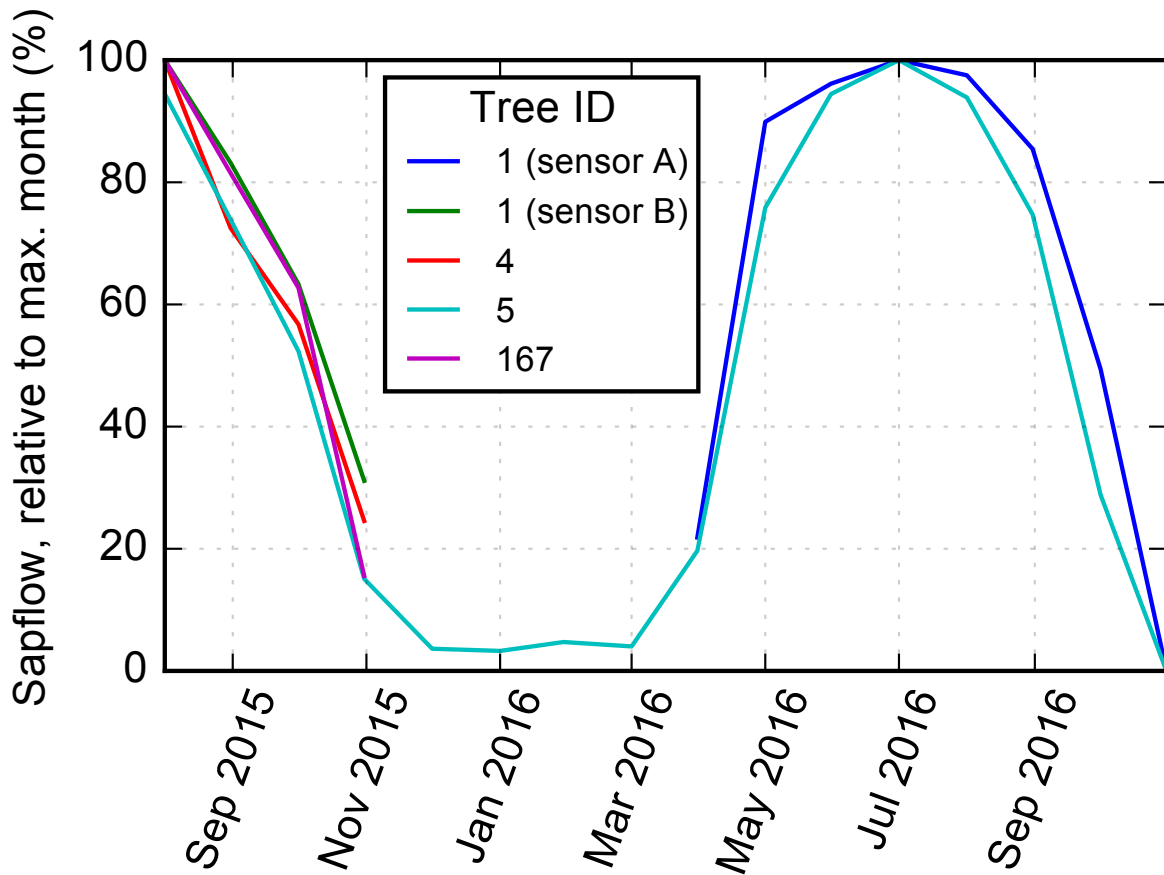


Figure 2.9: Total integrated sap flow per month, normalized to the maximum month recorded by each sensor. Sap flow peaks during the summer months with greatest insolation in spite of negligible precipitation.

day water potentials declined (Figure 2.4). In the winter wet season, sap flow continued on leafless trees parasitized with evergreen mistletoe on warm, dry days (Figure 2.3), indicating that some portion of the hydraulic pathway remained active throughout the year. We do not know the extent to which mistletoe accounts for total sap flow in summer, although its relatively small leaf area suggests its contribution should be minimal.

Piston dendrometers

Seasonal trends.—The sapwood, cambium, and inner bark increased in size radially in the early part of the growing season (April–July) by $\approx 1\text{--}3$ mm, then remained approximately constant in size during the latter half of the summer (July–September; Figure 2.10). Rain in April and May as well as October abruptly increased radial size, which then shrunk slowly

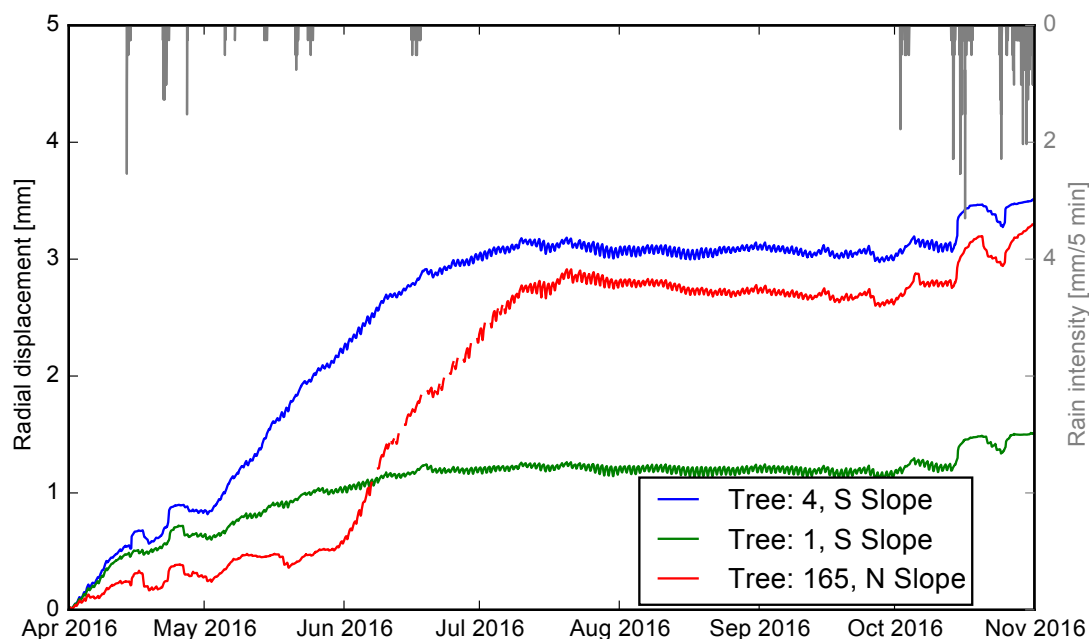


Figure 2.10: Radial displacement of sapwood, cambium, and inner bark away from the trunk in the 2016 growing season. Early growing season increase reflects sapwood growth. Smaller amplitude oscillations (see Figure 2.11) reflect diurnal water storage and release. Abrupt increases that decay after a period of days reflect rehydration of inner bark and sapwood due to rain (vertical gray lines, right y -axis).

over the course of a few days.

Diurnal trends.—Each day, the sapwood, cambium, and inner bark increase in size until early dawn, then begin to shrink as the sun rises, until late afternoon when they begin to increase again through the night (Figure 2.11). Net positive radial size increases of ≈ 20 $\mu\text{m}/\text{d}$ occur in the early (April–June) and late (October) months of the growing season, consistent with the seasonal observations of net positive displacement in Figure 2.10. The daily amplitude of radial size change increases from ≈ 10 μm in the early spring to ≈ 25 μm in the late summer months. The dendrometers recorded continual size changes, with no month exhibiting a time of day when radial size remained constant.

2.5 Discussion

Here, we discuss the interacting environmental and physiological factors that regulate *Quercus garryana*'s water relations. We contrast our findings with previously published reports

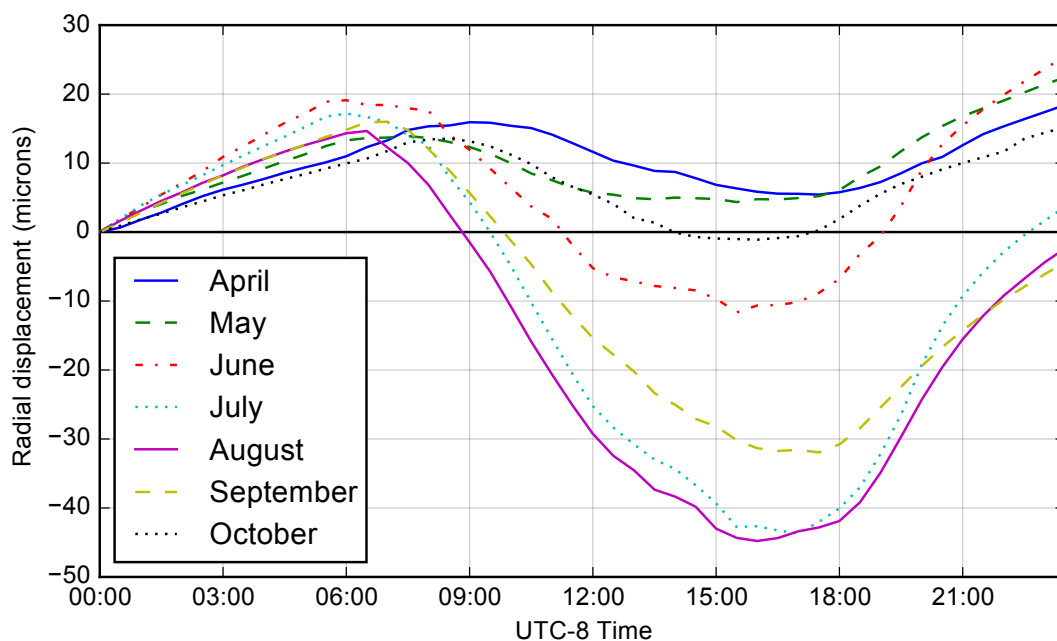


Figure 2.11: Average daily displacement of sapwood, cambium, and inner bark away from the trunk in a heartwood reference frame (positive is radially outward) across all instrumented trees each month of the 2016 growing season. The start of each 24-h period is fixed to zero to highlight inter-month dynamics. Spring–early summer months exhibit net positive daily displacement, reflecting sapwood growth, and the amplitude of displacement is highest in midsummer, reflecting greatest daily uptake and release of stored water.

on a variety of oaks and *Q. garryana*'s perceived competitor, *Pseudotsuga menziesii*. We then step back and juxtapose these individual observations with the effects of modern and paleoclimate shifts on these species' populations. Together, the data lead us to conclude that *Q. garryana* is an exceptionally water-limitation-tolerant species that will be favored in the increasingly arid climate.

Water potential

Relatively high and uniform pre-dawn Ψ in May likely reflect access to shallow groundwater. Pre-dawn Ψ slowly declined for three months from the beginning of May and remained above -1 MPa in late July on average (Figure 2.3). One month later, pre-dawn values were below -2.5 MPa. This precipitous drop is likely caused both by the declining availability of easily extracted groundwater [see also Hahm et al., 2017a] and an inflection point in the subsurface water characteristic curve, where at low volumetric water contents water potential may decrease rapidly during drying (we lack characteristic curve measurements to confirm this).

Site-wide average late-season (mid-September) 2016 Ψ values were similar to late-season (late September) 2015 Ψ values of -2.57 ± 0.28 MPa, $n = 5$ (pre-dawn; mean \pm standard error of the mean, number of trees), and -4.38 ± 0.22 MPa, $n = 5$ (mid-day), consistent with a common seasonal evolution of pre-dawn Ψ across years, in spite of confounding factors such as varied late spring rains, one week difference in sampling dates, and different total water year rains. This common evolution of Ψ may arise due to an upper limit on subsurface water storage at the site that is much less than mean annual precipitation, as explored in Hahm et al. [2019a].

The pre-dawn Ψ observed here is far lower than previous reports of mature *Q. garryana*. Late summer *Q. garryana* pre-dawn Ψ across a wide range of sites in Oregon was > -1.5 MPa on average in 60-yr-old, 13 m tall individuals [Kelly, 2016], ≈ -0.5 MPa in mid-late summer for ≈ 15 -yr-old individuals [Johnson et al., 2009], > -1.5 MPa for stump sprouts to 30-yr-old individuals [Davis, 2005], and > -1.0 MPa for 30 m tall individuals [Phillips et al., 2003a]. The Ψ we observed is higher, however, than the pre-dawn summer Ψ in mature *Q. douglasii* of ≈ -6.2 MPa in the foothills of the Sierra Nevada [Xu and Baldocchi, 2003]. Anderson and Pasquinelli [1984] found *Q. douglasii* replacing *Q. garryana* along a mesic-to-xeric moisture gradient in Sonoma County, and the *Q. douglasii* range generally extends into more xeric habitat, indicating that it is likely more water-limitation tolerant.

Seasonally declining mid-day Ψ to maintain sap flow indicates that in this particular environment stomata remain open, enabling carbon assimilation in desiccating conditions. This is consistent with the observation of greenhouse-grown *Q. garryana* seedlings maintaining positive carbon assimilation rates even after a 42-d period of drying when soil volumetric water content dropped below 2% [Merz et al., 2017]. Davis [2005] similarly plotted mid-day vs. pre-dawn Ψ of mature *Q. garryana* in Oregon [Davis, 2005: Figure 3.10] and found a steep slope across the range of pre-dawn Ψ observed (to approximately -1.5 MPa).

Meinzer et al. [2016] observed the Ψ evolution of *Q. garryana* seedlings subjected to drought in a greenhouse and also found large pre-dawn to mid-day $\Delta\Psi$ (> 1 MPa) at pre-dawn water potentials < -4 MPa. However, as their drought experiment continued, pre-dawn Ψ equaled mid-day Ψ at -6 MPa, indicating that there was no longer a gradient between root and shoot, consistent with stomatal closure (or hydraulic failure). This suggests that strict anisohydric behavior [sensu McDowell et al., 2008] does not apply to *Q. garryana*'s water-use regulation across the entire range of extreme dry conditions that may be encountered in nature, consistent with recent work that suggests that where plants map onto the anisohydry–isohydry continuum is likely contingent on intrinsic factors as well as the environmental conditions experienced [Meinzer et al., 2016; Martínez-Vilalta and Garcia-Forner, 2017].

Stem, leaf, and shoot Ψ .—The Ψ drop between root and stem, which occurs over a relatively long distance (order decameter), is of the same order of magnitude as that between stem and leaf (order decimeter; Table 2.3). Continuity of sap flow implies a large increase in resistance in the hydraulic pathway at the stem–leaf transition, due to either lower hydraulic conductivity or smaller functional xylem cross-sectional area, which reduce the hydraulic conductance (K). This indicates a much lower K in the leaf than in the roots, trunk, and distal stems. The leaf vulnerability curve is consistent with this finding: Leaf K drops

dramatically at low leaf Ψ (Figure 2.7). Stem hydraulic conductivities measured elsewhere in *Q. garryana* indicate that they may decline less in response to declining Ψ . Davis [2005] found relatively high rates of leaf-specific twig xylem hydraulic conductivity that did not change significantly throughout the growing season. Domec et al. [2007] found relatively high rates of trunk-specific conductivity, and Merz et al. [2017] observed that stem hydraulic conductivity losses remained below 50% to < -3.6 MPa in seedlings.

Leaf pressure-volume curves

Comparison of leaf parameters and dynamic adjustment.—The TLP (-3.61 MPa) and Ψ_{S100} (osmotic potential at full turgor; -2.93 MPa) measured in this study for *Q. garryana* are both below 95% of reported values in a global compilation of 248 (TLP) and 303 (Ψ_{S100}) species, spanning a broad range of climatic settings [Bartlett et al., 2012]. This is a first-order indication of the ability of *Q. garryana*'s leaves to maintain basic hydraulic function at the low water potentials encountered in the course of a dry season or drought. Three previous studies report TLP values for *Q. garryana* of ≈ -3.45 MPa [seedlings; Meinzer et al., 2016], ≈ -3.95 MPa [Johnson et al., 2009] and -3.2 to -3.6 MPa [Davis, 2005]. These values were all derived from rehydrated leaves from Oregon and fall within the range of values we measured for individual leaves, indicative of a general convergence in this trait across its geographic range.

Davis [2005] also reported Ψ_{S100} which was higher (between -2.00 and -2.75 MPa) than found in this study, suggesting that an environmental or genetic factor affects this leaf property. The comparable TLP of Davis [2005] in spite of higher Ψ_{S100} may be attributable to generally low ϵ (elasticity; ≈ 13.5 MPa). This is because a decrease in either Ψ_{S100} or ϵ lowers the TLP, as described by Bartlett et al. [2012]: $TLP = (\epsilon\Psi_{S100})/(\epsilon + \Psi_{S100})$ (depicted graphically by the contour plot in Figure 2.12). Bartlett et al. [2012] found that the TLP is more sensitive to changes in Ψ_{S100} than ϵ given the range of common plant values; that is, a 1 MPa decrease in Ψ_{S100} will typically depress the TLP much more than a 1 MPa decrease in ϵ . Furthermore, in a global meta-analysis of biomes associated with different water supplies, Bartlett et al. [2012] found that adjustments in Ψ_{S100} , and not ϵ , primarily explained adjustments in the TLP that conferred water-limitation tolerance to dry-biome species. The analytical expression of TLP from Bartlett et al. [2012] predicted the TLP we derived (see Figure 2.6), except at very low TLP (Figure 2.12 inset plot). Furthermore, an equivalent change in Ψ_{S100} has a much larger effect on TLP than ϵ across most of the leaves studied here. However, because ϵ varied much more ($\sim 100\%$ relative change) than Ψ_{S100} ($\sim 15\%$ relative change) across sample dates and initial hydration status, the *Q. garryana* TLP was also sensitive to ϵ , particularly as it approached values < 10 MPa (Figure 2.12). This effect was most pronounced between non-rehydrated and rehydrated leaves, with rehydrated leaves exhibiting a stiffening of the cell wall (increasing ϵ) and consequently a diminishing effect on TLP.

Sustained sap flow and stomatal opening at Ψ below the TLP.—We observed high sap flow in late summer (Figure 2.9) as pre-dawn shoot Ψ dropped below -3.6 MPa and mid-day

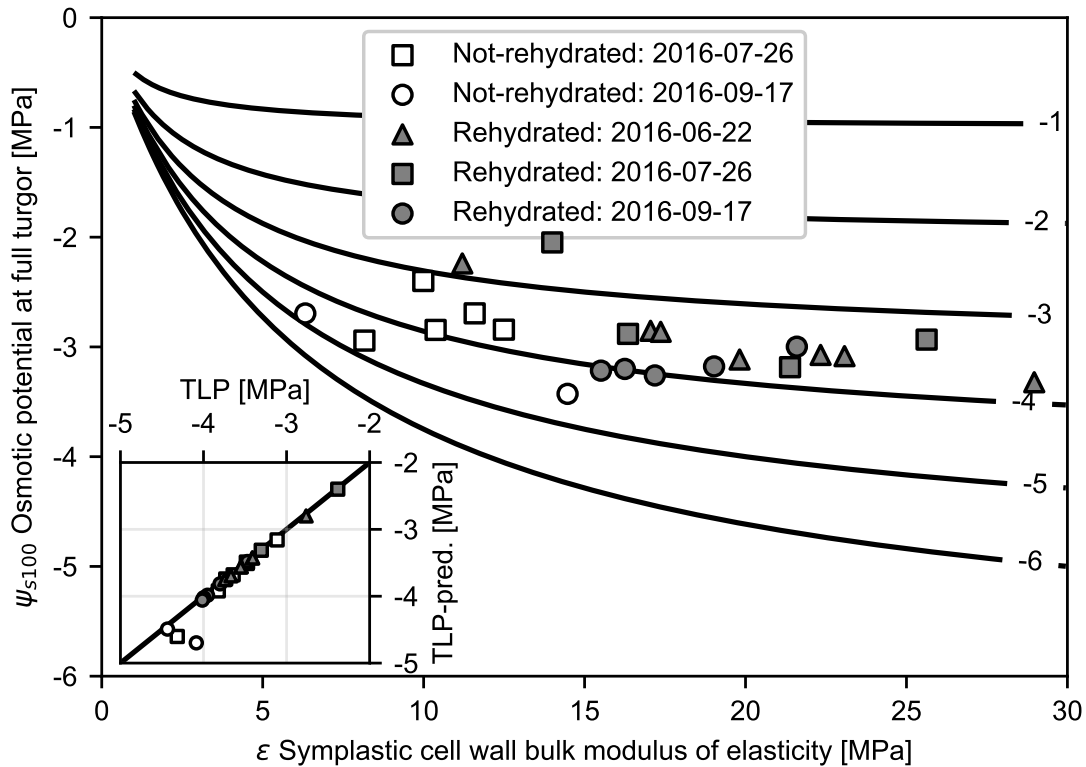


Figure 2.12: The turgor loss point (TLP; labeled contours) as a function of Ψ_{S100} and ϵ , based on the analytical formulation of Bartlett et al. [2012]. The TLP is more sensitive to Ψ_{S100} than ϵ for a given 1 MPa change in either term, but ϵ varies much more than Ψ_{S100} , and is lower for non-rehydrated leaves, illustrating a potential mechanism for TLP depression in leaves experiencing low Ψ . Inset shows TLP (x -axis) inferred as described in the *Methods* section and illustrated in Figure 2.6 compared to analytical prediction of Bartlett et al. [2012] as a function of Ψ_{S100} and ϵ .

shoot Ψ dropped below -4.5 MPa (Figure 2.4). Leaves experienced even lower Ψ (Table 2.3). Given the average TLP of -3.61 MPa, this indicates that stomata remained open during leaf turgor loss. Johnson et al. [2009] observed maximum daily stomatal conductance in *Q. garryana* coincident with daily minimum leaf Ψ at -3.6 MPa. Mitchell et al. [2008] observed pre-dawn leaf Ψ lower than the TLP inferred from PV curves of rehydrated leaves for species growing in a dry biome in southwest Australia, and Meinzer et al. [2016] documented *Q. garryana* seedlings with pre-dawn $\Psi < -4$ MPa and mid-day Ψ nearing -6 MPa [Meinzer et al., 2016's Figure S4], with a TLP of ≈ -3.45 MPa [Meinzer et al., 2016's Figure 4]. Farrell et al. [2017] concluded that water-limitation-tolerant plants can keep stomata open at Ψ lower than the TLP. Continued sap flow at Ψ lower than the TLP suggests that (1) leaf stomata remain open and sap flow continues post-turgor loss, (2) dynamic depression of the TLP occurs, and that this depression is poorly captured in traditional PV curves, (3) the TLP occurs at different Ψ for different cells in the leaf, with the PV curve inferred bulk leaf average TLP possibly higher than guard cell TLP, or (4) leaf Ψ lowers substantially between excision and measurement in the pressure chamber. While condition (4) must occur to some extent in *Q. garryana*, it seems unlikely to produce the large (>1 MPa) discrepancies noted above, especially at pre-dawn when stomata are shut and given the observation in obtaining PV curves that uncovered leaves lose water slowly at low Ψ . The most likely explanation for continued sap flow at pre-dawn Ψ below the TLP is a poorly captured dynamic adjustment of TLP in traditional PV curves. This explanation is also consistent with visual assessment of leaves in the field that remain healthy and turgid (Figure 2.13). Large changes occurred in important leaf metrics like $RWC_{\text{sym}}@TLP$ and ε between rehydrated and non-rehydrated leaves, suggesting that further, difficult-to-detect changes may occur as leaves near the TLP.

Leaf hydraulic conductance (K)

Reductions in K with declining leaf Ψ like those in Figure 2.7 are common in many species, but the precise mechanisms of K loss and recovery and the consequences for sap flow remain poorly understood. Johnson et al. [2009], employing the same method as this study, showed that K in leaves of *Q. garryana* from Oregon declined in a similar pattern with decreasing Ψ , with a slightly lower Ψ at 50% loss of K (-3.61 MPa [Johnson et al., 2009] vs. -3.35 MPa [this study]). We observed high rates of sap flow at the end of the dry season coincident with mid-day Ψ that would have resulted in significantly reduced leaf K . A large drop in Ψ occurs between the stem and leaf (Table 2.3), so that declining K may not inhibit leaf function due to the compensatory effect of a larger Ψ gradient across the leaf.

Sap flow dynamics

The *Q. garryana* studied here maintained high rates of sap flow even as pre-dawn Ψ dipped below -3 MPa and VPDs exceeded 4 kPa. This indicates that *Q. garryana* is water-limitation tolerant, leaving stomata open during the dry Mediterranean summer that coincides with high incoming photosynthetically active radiation, thereby promoting carbon



Figure 2.13: End-of-summer (mid-September) *Q. garryana* foliage and acorns, seen from below. Photo by Wendy Baxter.

acquisition. This behavior contrasts with the seasonal timing of transpiration of the codominant plant functional group at the site (annual grasses), which transpire the most in the wet spring and lose their green photosynthetic tissue by midsummer.

Fisher et al. [2007] observed high rates of sap flow during the summer in *Q. douglasii* (which is genetically similar to *Q. garryana*), with integrated sap flow similar to the seasonal cycle we observed (Figure 2.9). Fisher et al. [2007] also observed nighttime sap flow which they attributed to transpiration. That nighttime sap flow was strongly correlated with VPD, consistent with the observations in this study. Pre-dawn sap flow can remain at >20% of the maximum on nights when VPD remains high (Figure 2.3). The only other studies to our knowledge presenting time series of sap flow data in mature *Q. garryana* [Phillips et al., 2003a,b] showed similar daytime patterns and also found relatively minor differences in total daily water flux between early and late season in spite of declining pre-dawn Ψ . Phillips et al. [2003a,b] found that sap flow in *Q. garryana* approached zero pre-dawn, unlike the trees in this study.

Quercus spp. on the East coast of the United States in the Shale Hills CZO displayed re-

markably different responses to declining soil moisture and increases in VPD: In the summer, after a rain event, sap flow declined by 62% in *Quercus alba*, *Quercus prinus*, *Quercus rubra*, and *Quercus velutina* over a period of just five days [Gaines et al., 2016]. This is consistent with a heightened sensitivity to moisture declines in the very near surface: Rooting density was observed to be concentrated across all topographic positions within 50 cm of the surface, and the trees showed strong isotopic evaporative enrichment signals consistent with sourcing water from shallow, rapidly drying soils. In contrast, Devine and Harrington [2005] noted that half of the cross-sectional area of first-order lateral roots branching from the taproot of *Q. garryana* growing in a glacial outwash soil was found below 30 cm, and mats of fine roots were found in moist lenses below 150 cm. Ugolini and Schlichte [1973] found that *Q. garryana* commonly has deep taproots extending below the surface soil. These observations of deeper, subsoil rooting are also common in *Q. agrifolia* and *Q. douglasii* in California [Cannon, 1914; Lewis and Burgy, 1964; Griffin, 1973; Miller et al., 2010], and highlight a greater reliance of eastern oak species on frequent summer storms for delivery of water to surface soils, in contrast to the western oaks that are better adapted to the dry-growing season of Mediterranean climates.

Growth and water storage dynamics inferred from piston dendrometers

The radial changes in Figures 2.10 and 2.11 reflect seasonal growth and tissue water storage and release. Most of the radial increase occurs in the early part of the growing season, which we attribute to sapwood growth, consistent with observations elsewhere that *Q. garryana* rings show a continuously declining amount of latewood relative to earlywood as the tree grows [Lei et al., 1996], and dendrometer-band inferred diameter change in open-grown *Q. garryana* that exhibits a convex-up profile throughout the growing season [Gould et al., 2011]. This is a common trend in ring-porous species [Lei et al., 1996] and oaks from around the world [Maertens, 2008]. Sap flow remains high after sapwood growth stops (compare Figures 2.8 and 2.10), leading us to propose that assimilation efficiency may decrease or that a reallocation of photosynthates from sapwood to fruit production and roots occurs throughout the growing season. The October radial increase is due primarily to tissue rehydration, as the sapwood reaches its lowest potential at the end of the summer and swells in response to early wet-season rains.

The diurnal patterns in Figure 2.11 show sinusoidal shrinking and swelling of the sapwood, cambium, and inner bark. Recharge of stored water occurs when the radial size increases from late afternoon to pre-dawn, whereas depletion of stored water occurs as the radial size decreases from pre-dawn to late afternoon. This pattern leads to the inference that stored water supplements the transpiration stream during the day at times of high sap flow and low Ψ . Phillips et al. [2003b] similarly found that *Q. garryana* tissue between the bole and crown was a net source of water for transpiration in the late morning and early afternoon, during times of maximum solar radiation, and that in the late afternoon to early evening this region

was a net sink of water. They also found that the reliance on stored water approximately doubled from the early to late season, consistent with our observations in Figure 2.11 of increasing diurnal amplitudes.

Volumes of stored water in the tree

We can estimate minimum daily trunk water storage by assuming the ~ 60 μm average diurnal radial change in sapwood, cambium, and innerbark of trees (Figure 2.11) is entirely due to the gain and loss of liquid water. A trunk height of 5 m for a 20 cm diameter tree (similar to the smaller trees in this study) results in daily water gain and loss of 0.2, and 1.2 L for a 10 m tall trunk and a 65 cm diameter tree (approximately the largest in this study). This does not include trunk water gain and loss that does not result in a volumetric dilation or any heartwood water storage, and only roughly approximates the trunk volume and does not include the crown stem network. We can also calculate the daily stored water in leaves. We consider a 20 cm diameter tree, with a crown radius of 4 m and an assumed leaf area index of 3. The average leaf dry mass and leaf mass/area of Table 2.4 results in $\sim 40,000$ leaves. Given the average daily shoot Ψ change from pre-dawn to mid-day of 1.6 MPa (Figure 2.4, and we note that the diurnal leaf change would be higher), and an average leaf $\Delta H_2O_{\text{mass}}/\Delta\Psi$ before the TLP across all leaves of 0.019 g/MPa from the PV curves, we estimate a daily leaf water storage of 1.3 L. A tree with a 7 m crown radius and leaf area index of 4 would have 170,000 leaves that lose 5.2 L daily. Diurnal dehydration of leaves can therefore constitute a significant fraction of the stored water contribution to transpiration—in this case, comparable to our conservative estimate of trunk sapwood contribution. If all nighttime sap flow went exclusively to tissue rehydration rather than transpiration, stored water would contribute ~ 20 – 30% of the daily transpiration stream, based on the integral of diurnal sap flow curves in Figure 2.8. This rehydration–transpiration partitioning estimate is not unreasonable; in a study of *Q. douglasii*, Fisher et al. [2007] found that $\sim 70\%$ of nocturnal sap flow went to rehydration.

Implications for competition with P. menziesii

How will the *P. menziesii* that have invaded oak savanna and woodlands fare relative to *Q. garryana* under continued warming in the 21st century? *Q. garryana* resilience, or the ability to persist in the face of climatic perturbation, hinges strongly on its water-limitation tolerance relative to *P. menziesii*. Although there is some uncertainty in climate models, mean annual temperature is among the most reliably predicted outputs [Rupp et al., 2013]. Models predict that an atmospheric CO_2 concentration of ~ 750 ppm will globally raise average temperatures this century by 2.4–5.4 $^\circ\text{C}$ [Murphy et al., 2004], with Pacific Northwest regional models predicting similar rises [Mote and Salathé, 2010]. The mean temperature of the warmest month in Northwest California is expected to increase by 3 $^\circ\text{C}$ [Kueppers et al., 2005]. As dry-season temperatures increase, plants will experience greater VPDs in the growing season [Luce et al., 2016]. Our study site, inhabited by mature *Q. garryana*

experiencing extremely water-limited conditions that have also not been subject to significant *P. menziesii* invasion, may serve as a microcosm of a more water-limited future. We discuss the paleoclimatic and paleoecologic record, modern climate-distribution studies, and finally compare and contrast the ecophysiology of the species in light of the new findings in this study.

Paleoclimate and paleoecology

Regionally, Pinaceae pollen abundance is negatively correlated with *Quercus* pollen, and shifts in these two plant communities follow temperature changes throughout glacial and inter-glacial cycles [Heusser, 2000; Poore et al., 2000]. In the Quaternary, *Quercus* pollen abundance was lowest during glacial maxima, when temperatures were cool, and increased during warmer inter-glacial times [Mensing, 2006]. For example, in the Sierra Nevada, oak range expanded from 10000 to 5000 yr before present, coincident with a warming climate [Byrne et al., 1991], and in the Northern California Coast Ranges oaks reached a maximum extent between 6000 and 3500 yr before present at Clear Lake and 5000 yr before present at Tule Lake [Adam et al., 1981; West, 1982; Adam and West, 1983; Mensing, 2005]. Oaks reached a maximum extent in coastal British Columbia 7500 yr before present, when temperatures were 2–4 °C warmer [Pellatt et al., 2001; Walker and Pellatt, 2003]. Lucas and Lacourse [2013] show a rise of *Q. garryana* in the Gulf Islands of British Columbia between 7600 and 5500 yr before present, followed by cooler and moister conditions that coincided with the rise of modern *P. menziesii* forests. These findings are consistent with White et al.'s [2015] pollen and charcoal records in the latter half of the Holocene from the southern Cascade Range in Oregon. They found declining fire frequency and cooler, wetter conditions accompanied increases in mesophytic taxa including *Pseudotsuga*. In northern California and southern Oregon, Mohr et al. [2000] similarly found a peak in *Quercus* during the relatively warm and dry early Holocene, with subsequent dominance of *Pinaceae* in the cooler, wetter late Holocene. Thus, the paleoecologic and paleoclimatic record of western North America indicates that during early Holocene warming *Quercus* pollen in general and *Q. garryana* specifically became more abundant, with concomitant declines in *Pinaceae* in general and *P. menziesii* specifically.

Modern climate and ecology

Temperature in the 20th century increased by ~0.6–0.8 °C in the Pacific Northwest [Abatzoglou et al., 2014], resulting in detectable shifts in mortality and growth patterns. In Northwest California, temperature has increased even faster [~0.23 °C per decade; LaDochy et al., 2007]. Hember et al. [2017] found no sensitivity in the probability of mortality sensitivity of *Q. garryana* (from 373 plots) to higher reference evapotranspiration, whereas *P. menziesii* (5828 plots) exhibited strong positive sensitivity. McIntyre et al. [2015] found a 20th-century trend of declining large tree and increasing oak abundance across California that was primarily attributable to increases in climatic water deficit. Dynamic vegetation

models that incorporate biogeographical patterns, future climate change projections, and fire disturbance predict an expansion of northern oak woodlands into Douglas fir–tan oak forest in Northwestern California [Lenihan et al., 2003; Bodtker et al., 2009]. Such models have not yet included the role of deeper moisture [e.g., rock moisture; sensu Rempe and Dietrich, 2018], which is largely unquantified but may be important in mediating plant water stress. Although exact species-level mortality rates are difficult to ascertain, in general the Northern California Coast Range *Q. garryana* habitat experienced relatively little mortality and maintained higher leaf water content in the most recent California drought [Asner et al., 2016; Young et al., 2017].

Inter-annual variations in tree growth reveal finer-scale climatic sensitivity. Maertens [2008] analyzed a >100-yr climate and *Q. garryana* annual growth ring record at 18 sites spanning most of the species' geographic and climate range, and found that growth was positively correlated with moisture availability. Gildehaus et al. [2015] developed a crossdated 341-yr-long ring-width chronology of *Q. garryana*, near the center of its geographic range in the Willamette Valley of Oregon, and also observed higher growth with higher summer moisture availability. In contrast, Jordan and Vander Gugten [2012] found no significant correlation between *Q. garryana* growth rate and precipitation and temperature for most months preceding and within the growing season. Perhaps this is due to the confounding effect of greater water availability in the early growing season coinciding with water-logged or overcast conditions that would tend to limit growth. Only one study to our knowledge has looked at colocated *Q. garryana* and *P. menziesii* climate–growth interactions: Franks [2008] found that in general both species' growth responded positively to current year precipitation and negatively to temperature across the southern mainland and Vancouver Island of British Columbia. However, *P. menziesii* growth declined more with lower precipitation and higher temperature in the driest part of the growing season, suggesting that it was more prone to drought stress than *Q. garryana*.

Pseudotsuga menziesii ecophysiological comparison

Decline in *P. menziesii* growth rates in the past century throughout the western United States appears to be specifically attributable to temperature increases that increase VPD, resulting in stomatal closure and lower rates of carbon uptake [Restaino et al., 2016]. This regional pattern is consistent with high stomatal aperture sensitivity to VPD in juvenile *P. menziesii* [Meinzer, 1982] relative to *Q. garryana* [Merz et al., 2017]. Data from Johnson et al. [2009] and Woodruff et al. [2007] indicate that 50% loss of leaf *K* occurs ≈ 2 MPa higher for *P. menziesii* than for *Q. garryana*. At the neighboring site to this study, with relatively higher subsurface water availability [pre-dawn water potentials typically > -2 MPa; Hahn et al., 2019b], *P. menziesii* sap flow declines significantly in the dry season [Link et al., 2014], indicating greater sensitivity to high summer VPD and declining subsurface water availability, a common observation for *P. menziesii* [Granier, 1987; Moore et al., 2004]. Phillips et al. [2003b] also documented much larger relative sap flow declines in *P. menziesii* than *Q. garryana* through the dry season in Washington and Oregon.

In contrast to the *Q. garryana* behavior in this study and of juveniles in Meinzer et al. [2016], *P. menziesii* maintains similar mid-day water potentials as water availability declines in the dry season [Domec et al., 2008]. The TLP of *P. menziesii* [Jackson and Spomer, 1979; Ritchie and Shula, 1984; Woodruff et al., 2007; Johnson et al., 2009] is generally higher than the TLP of *Q. garryana* found in this study and others discussed previously. *Quercus garryana* has the highest wood specific gravity and shortest height at maturity of common Pacific Northwest tree species [Minore, 1979; Davis, 2005], suggesting that it may invest more in its hydraulic architecture than *P. menziesii*. Together, these differences in ecophysiological response to temperature and water availability are consistent with a suite of evolutionary tradeoffs, in which *Q. garryana* maintains hydraulic function in drier conditions than *P. menziesii*, likely at the cost of slower growth. Such a tradeoff would favor *P. menziesii* where atmospheric water demand is low and/or subsurface moisture supply is high, and *Q. garryana* in relatively xeric environments and/or where low-intensity fires are allowed to burn, limiting *P. menziesii* encroachment.

2.6 Conclusions

At our Sagehorn study site, thin soils and a shallow weathered-bedrock zone over an impermeable mélange bedrock lead to limited winter water storage and thus limited growing season water availability, despite annual precipitation of ~ 1800 mm. Our intensive field measurements of mature *Quercus garryana* in a seasonally dry savanna and woodland in Northern California indicate that the species maintains hydraulic function in the summer growing season at extremely low water-availability conditions. Sustained high water use at low water potential is possible due to a robust hydraulic architecture, with specific adaptations such as dynamic leaf adjustment to lower the TLP and diurnal water storage and release in sapwood and leaves to compensate for high atmospheric moisture demand. We observed transpiration well after pre-dawn water potentials declined below the inferred TLP. Consequently, the common measurement of turgor loss from pressure-volume curves of rehydrated leaves may be of inadequate in predicting functional ecophysiological limits.

In comparison with data from previous studies of *Pseudotsuga menziesii*, *Q. garryana* is significantly more water-limitation tolerant. This helps explain the lack of *P. menziesii* invasion into our water-limited study area and suggests that future warming of western North America may favor *Q. garryana* persistence. Paleoclimatic and paleoecologic records of forest community composition in the Quaternary, as well as *Q. garryana* and *P. menziesii* growth and mortality patterns in response to modern climate changes and land use also suggest this outcome. Taken together, the evidence points toward *Q. garryana*'s resilience in a changing climate, provided that its extant habitat is protected from detrimental land use and—in relatively wetter areas—from the effects of fire exclusion-assisted conifer invasion.

2.7 Acknowledgements

We gratefully acknowledge the generous land access and scientific enthusiasm provided by Marilyn and Jerry Russell and the Holleman family. Fieldwork could not have been completed without the help of Cameron Williams, Rikke Naesborg, Sky Lovill, Chris Wong, Collin Bode, Peter Steel, and Ilana Stein, and the work benefitted from input from David Dralle, members of the Dawson and Ackerly laboratories at UC Berkeley, and two reviewers. The National Center for Airborne Laser Mapping (NCALM) acquired the high-resolution elevation and vegetation point cloud data used in the study. This project was primarily funded by the National Science Foundation–Eel River Critical Zone Observatory (EAR 1331940), with additional support from the University of California Natural Reserve System Mathias Grant.

Chapter 3

Lithologically controlled subsurface critical zone thickness and water storage capacity determine regional plant community composition

3.1 Abstract

Explanations for distinct adjacent ecosystems that extend across hilly landscapes typically point to differences in climate or land use. Here we document—within a similar climate—how contrasting regional plant communities correlate with distinct underlying lithology and reveal how differences in water storage capacity in the critical zone (CZ) explain this relationship. We present observations of subsurface CZ structure and groundwater dynamics from deep boreholes and quantify catchment-wide dynamic water storage in two Franciscan rock types of the Northern California Coast Ranges. Our field sites have a Mediterranean climate, where rains are out of phase with solar energy, amplifying the importance of subsurface water storage for periods of peak ecosystem productivity in the dry season. In the deeply weathered (~ 30 m at ridge) Coastal Belt argillite and sandstone, ample, seasonally replenished rock moisture supports an evergreen forest and groundwater drainage sustains baseflow throughout the summer. In the Central Belt argillite-matrix *mélange*, a thin CZ (~ 3 m at ridge) limits total dynamic water storage capacity (100–200 mm) and rapidly sheds winter rainfall via shallow storm and saturation overland flow, resulting in low plant-available water (inferred from predawn tree water potential) and negligible groundwater storage that can drain to streams in summer. This storage limitation mechanism explains the presence of an oak savanna-woodland bounded by seasonally ephemeral streams, despite $>1,800$ mm of average precipitation. Through hydrologic monitoring and subsurface characterization, we reveal a mechanism by which differences in rock type result in distinct regionally extensive plant communities under a similar climate.

This chapter is adapted from Hahm, W. J., Rempe, D. M., Dralle, D. N., Dawson, T. E., Lovill, S. M., Bryk, A. B., Bish, D. L., Schieber, J., and Dietrich, W. E. (2019b). Lithologically controlled subsurface critical zone thickness and water storage capacity determine regional plant community composition. *Water Resources Research*, 55.

3.2 Introduction

Large-scale variations in the vegetation composition across landscapes are commonly explained by climatic gradients, which exert a primary control on water and energy availability [Holdridge, 1947; Stephenson, 1990; Whittaker, 1975]. However, within any particular climate, distinct plant communities may coexist, unexplained by regional temperature or precipitation. These vegetation mosaics may result from patterns of anthropogenic land use but can also arise from a variety of ecosystem processes, including herbivory, clustering, dispersal-limitation, or disturbance-induced succession [Aguiar and Sala, 1994; Bond, 2005; Dantas et al., 2016; Heinselman, 1981; Polis, 1999; Scanlon et al., 2007]. Variations in microclimate, such as those arising from hillslope aspect [Holland and Steyn, 1975; Parker, 1982], or contrasting underlying lithology, which can influence toxin or nutrient delivery to plants [Hahm et al., 2014; Kruckeberg, 2004], can similarly demarcate abrupt vegetation boundaries.

In water-limited environments, soil water storage capacity can influence plant-available water and the onset of plant water stress, impacting primary productivity and plant water use [Barkaoui et al., 2017; Branson et al., 1970; Laio et al., 2001; Porporato et al., 2001, 2004; Prentice et al., 1992; Smith et al., 1995]. Even in climates with ample precipitation, storage limitations below ground can result in water limitation, affecting the distribution of plants [Rodriguez-Iturbe et al., 2007]. This is likely common in Mediterranean climates, where the delivery of precipitation is out of phase with solar energy availability and atmospheric moisture demand. In these regions, the importance of the subsurface is amplified, due to its role in storing rainfall that falls in the wet season and releasing that water to ecosystems in summer.

Plants in upland landscapes with thin soils may survive on water extracted from the weathered bedrock from below the soil, exploiting either groundwater [e.g., Miller et al., 2010] or rock moisture [sensu Salve et al., 2012; Rempe and Dietrich, 2018] from tens of meters below the ground surface [e.g., Anderson et al., 1995; Arkley, 1981; Bales et al., 2011; Eliades et al., 2018; Jones and Graham, 1993; Lewis and Burgy, 1964; Miller et al., 2010; Rempe and Dietrich, 2018; Rose et al., 2003; Sternberg et al., 1996; Zunzunegui et al., 2018; Zwieniecki and Newton, 1996]. These and other previous studies in seasonally dry environments, however, have focused on local, site-specific plant water use and have not explicitly addressed larger-scale relationships between dominant vegetation patterns and the spatial availability of moisture beneath the soil.

Research in critical zone science now suggests that there may be predictable, lithologically controlled regional patterns of weathered bedrock thickness across landscapes [Riebe

et al., 2017]. The depth and extent of weathering and the associated porosity increase must control the potential for moisture storage [e.g., Klos et al., 2018], which, in turn, should affect the composition of above ground plant community assemblages, especially in seasonally dry environments. This leads to the hypothesis that bedrock weathering patterns and associated water storage capacity should have a profound—yet hitherto undocumented—effect on regional patterns of plant water use, productivity, and species distribution in seasonally dry climates. This emerging view has not yet been tested. It presents a challenge because the extent of bedrock weathering is difficult to measure (typically requiring drilling or geophysics), and therefore difficult to document at large spatial scales.

Here we explore whether differences in subsurface critical zone development associated with differences in lithology can provide an explanation for a dramatic regional-scale contrast in dominant vegetation assemblage that extends for over 200 km (Figures 3.1–3.3). Our study region is located along the unglaciated Northern California Coast Ranges, where adjacent landscapes, underlain by different lithologic units of the Franciscan complex, support strikingly different plant communities. To the west, a towering evergreen forest mantles the steep hillslopes of the Coastal Belt, comprised of turbidite sequences of argillite, sandstone, and minor conglomerate. Sharply juxtaposed to the east are the rolling hills of the Central Belt, which is a *mélange* of geochemically similar yet metamorphosed and pervasively deformed Coastal Belt material. In the Central Belt *mélange*, the vegetation is a sparse deciduous-oak annual-grass savanna- woodland (Figures 3.1–3.3). These differences in plant communities occur despite the fact that both landscapes experience essentially the same mean annual rainfall (>1,800 mm) and mean annual temperature (about 13 °C). As Figure 3.4 shows, 1,800 mm greatly exceeds the expected precipitation range of a grassland savanna. Simply put, why would grassland savanna be the dominant vegetation in such a wet environment?

To test the hypothesis that the subsurface critical zone water storage capacity controls regional-scale vegetation distribution, we combine an analysis of regional-scale geologic maps, remotely sensed land cover and plant characteristics with a field-based ‘unit hillslope’ approach at individual, intensively monitored sites. Landscapes are a collection of hillslopes bordered by channels that collect and drain watersheds. Rather than attempt to characterize the critical zone properties over a large area (which is presently very difficult to do), we focus on intensive measurements of properties and processes on what we estimate to be a representative (unit) hillslope within a given lithology. We assume that the commonality of topographic form between repeating adjacent hillslopes reflects a commonality in the underlying weathering zone structure. This is consistent with current theories for critical zone evolution that propose that subsurface properties vary systematically with hillslope topography and lithology [Riebe et al., 2017]. We then use the mechanistic understanding gained at the unit hillslope scale to interpret and explain watershed and regional-scale runoff, water budgets, and plant community assemblage dependence on critical zone properties.

Prior studies have generated extensive documentation of a unit hillslope (‘Rivendell’) in the forested-dominated Coastal Belt [Kim et al., 2014; Link et al., 2014; Oshun et al., 2016; Rempe and Dietrich, 2014, 2018; Salve et al., 2012]. We initiated a new unit hillslope

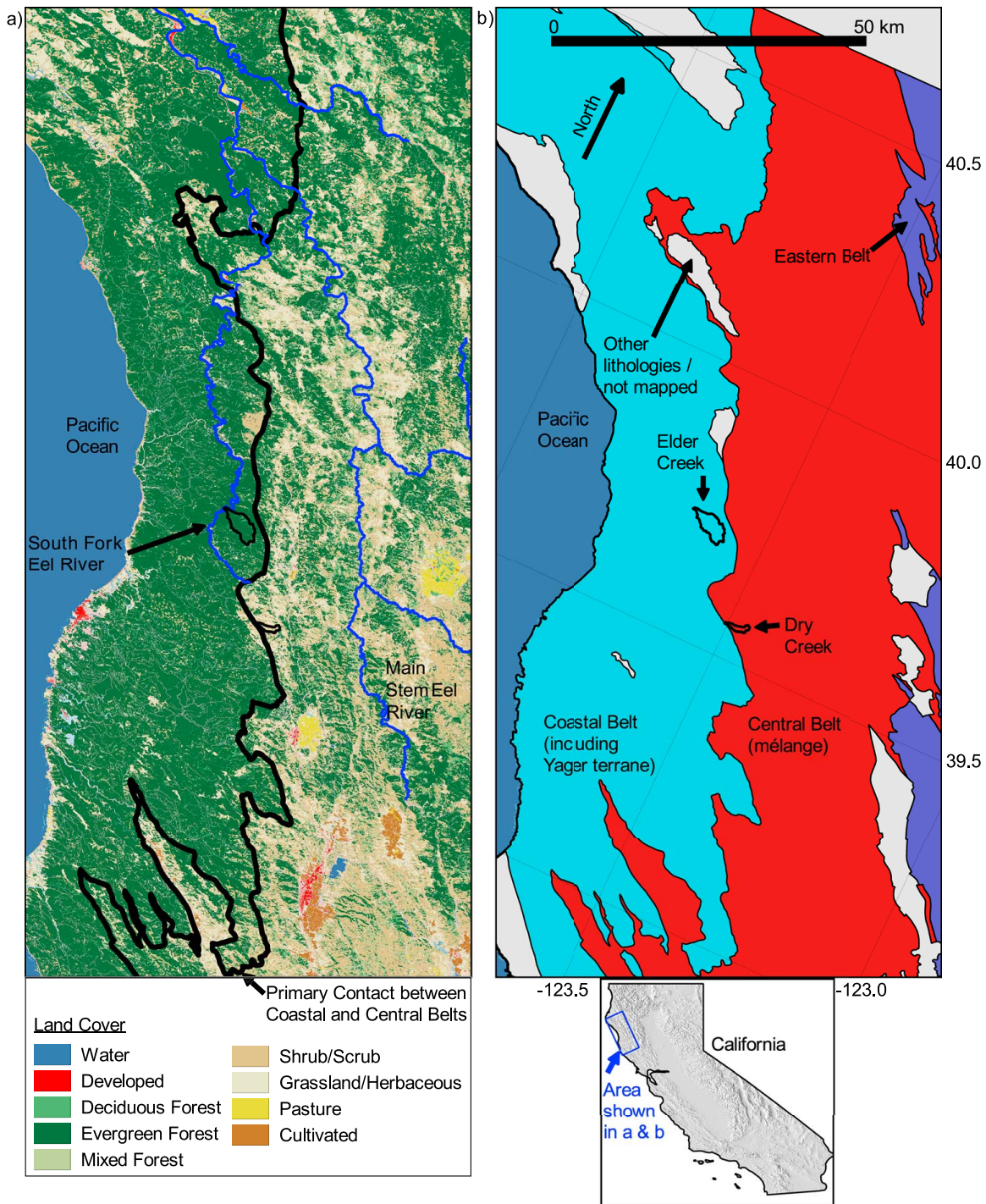


Figure 3.1: Comparison of land cover (a; 2011 National Land Cover Database [Homer et al., 2015]) and Franciscan bedrock geology (b; Langenheim et al. [2013]). Blue lines in (a) show primary forks of the Eel River. Map inspired by Figure 2 of Lovill et al. [2018].

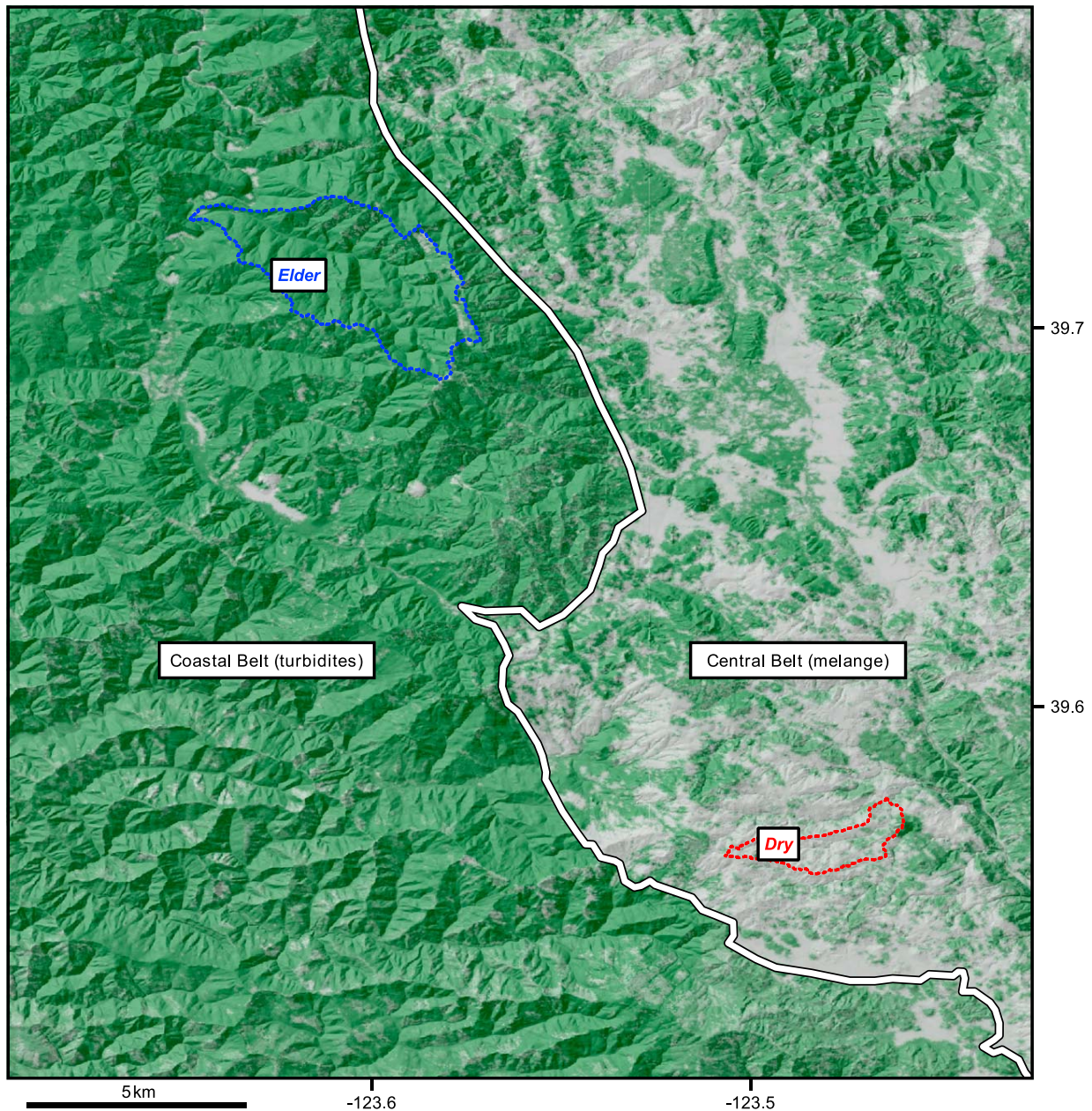


Figure 3.2: Tree canopy cover map of the field area shows the abrupt change in tree canopy cover at the geologic contact (white bold line) that separates the Coastal Belt (west) from the Central Belt (east) in the study area. Green (forested) patches in *mélange* are primarily on sandstone blocks. Study watersheds in each rock type are demarcated with dashed lines; gray = 0% canopy cover, darkest green = 100% canopy cover. Coordinates in WGS84; geologic contact after Jayko et al. [1989]. Canopy cover from the 2011 National Land Cover Database. Map inspired by Figure 2 of Dralle et al. [2018].



Figure 3.3: (a) Photo from headwaters of Elder Creek in the Coastal Belt, looking west, shows mixed broadleaf-needleleaf evergreen forest grading to chaparral on higher elevation, south-facing steep slopes. (b) Photo from northern ridge of Dry Creek watershed, looking north, shows annual-grass dominated, low-gradient hillslopes, with leafless winter-deciduous mistletoe-infested *Q. garryana* in foreground. The lumpy topography records relict earthflows. (c) Photo of south-facing tributary of Dry Creek during rainstorm (10 January 2017), showing extent of wetted channels and widespread saturation overland flow. Person for scale (170 cm tall); point in lower-right drains area of approximately 2 ha. (d) Panoramic photo between wells 503 and 500 at the Sagehorn Central Belt site along ridgetop on northern boundary of the Dry Creek catchment, showing complete saturation of the subsurface and overland flow in a winter rainstorm (190 cm tall person in yellow jacket for scale).

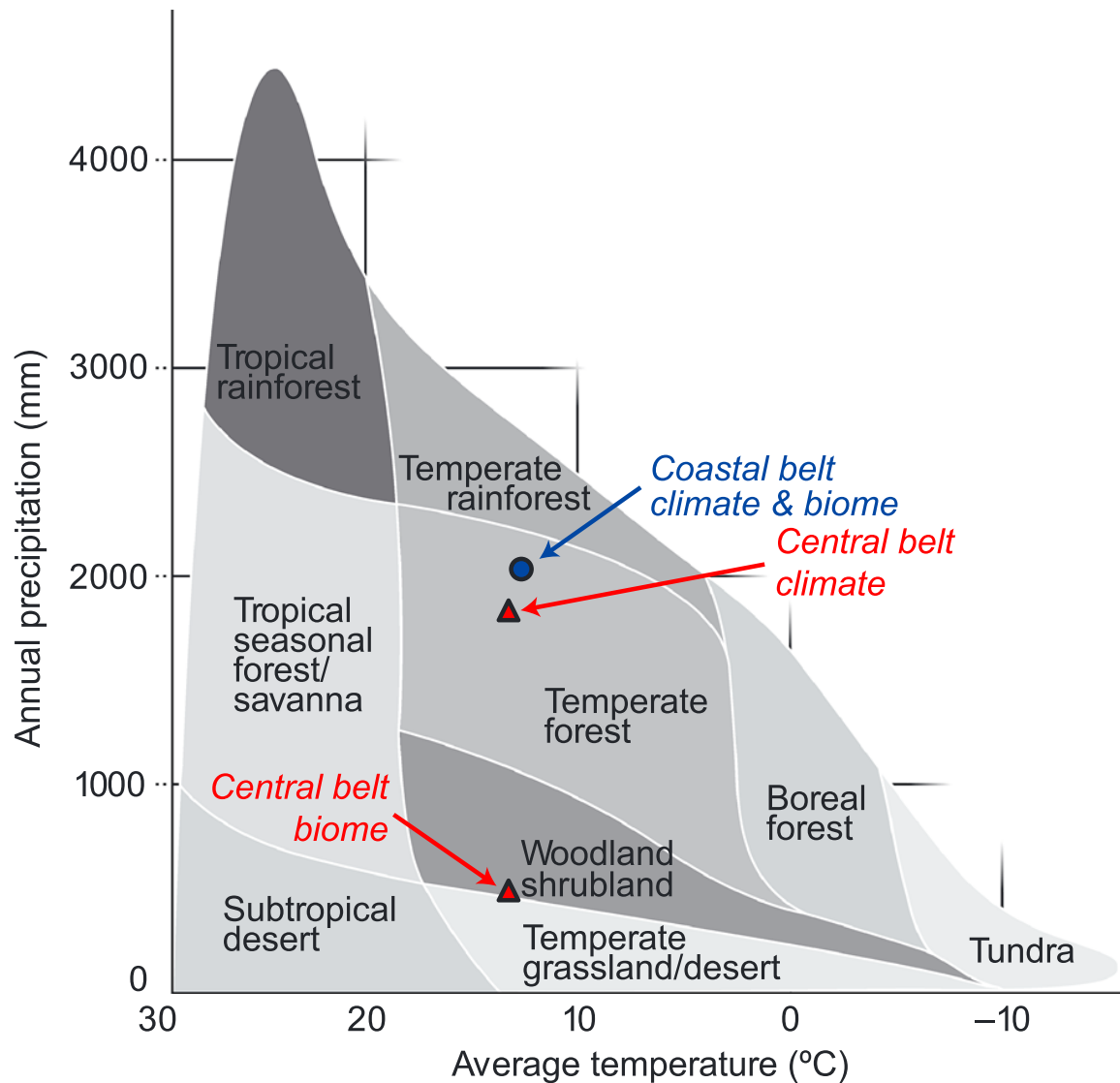


Figure 3.4: Global delineation of biome type as a function of mean annual precipitation and temperature. The average climate of the Coastal Belt (Angelo; blue circle) and Central Belt (Sagehorn; red triangle) study sites is associated with temperate forests, consistent with the ecosystem inhabiting the Coastal Belt. In contrast, the actual Central Belt biome is woodland/shrubland/grassland, denoted with the lower red triangle. Biome delineations based on Ricklefs [2008]; Whittaker [1975]. Greater interception at the Coastal Belt results in nearly identical precipitation at the ground surface, as discussed in text.

study in the Central Belt by exploring the subsurface with deep boreholes, establishing a network of monitoring wells, and monitoring weather and stream runoff. Here we report the results of this study, as well as new data for both sites on end-of-summer predawn tree water potentials, composite annual time series of remotely sensed vegetation indices, bulk mineralogy and geochemistry, and tree canopy cover. For the Central Belt site, we also report new cosmogenic nuclide-based erosion rates, dissolved oxygen concentrations in groundwater, scanning electron microscopy imagery of fresh bedrock, and historical air photo analysis.

3.3 Site description

Location and history

The two field sites, Angelo Coast Range Reserve (‘Angelo,’ in the Coastal Belt) and the Sagehorn-Russell Ranch (‘Sagehorn,’ in the Central Belt) form the core of the intensive monitoring sites in the Eel River Critical Zone Observatory. Angelo is part of the University of California Natural Reserve System and consists largely of steep-sloped, old-growth mixed broadleaf-needleleaf evergreen forest (see map in Figure 3.5). It contains the Elder Creek watershed (Table 3.1), a tributary to the South Fork Eel River, and Rivendell, an intensively instrumented hillslope that has been the site of numerous isotopic, geochemical, ecophysiological, and hydrologic studies [Dralle et al., 2018; Druhan et al., 2017; Kim et al., 2014; Link et al., 2014; Lovill et al., 2018; Oshun et al., 2016; Rempe and Dietrich, 2018; Salve et al., 2012; Simonin et al., 2014]. Rivendell (39.729° , -123.6451°) is ~ 15 km east of the Pacific Ocean, 430 m above sea level (a.s.l.).

Sagehorn, a privately owned ranch, contains the Dry Creek watershed (Table 3.1; see map in Figure 3.6), which is in the main stem Eel River watershed. The site is dominated by a deciduous oak savanna-woodland, with predominantly nonnative annual herbaceous ground cover. There are dispersed densely forested areas that more closely resemble the vegetation community of Angelo that are situated primarily on sandstone blocks within the *mélange*. The principal study hillslope (39.5678° , -123.4733°) lies along an east-west running ridge on the northern border of the east-flowing Dry Creek, ~ 25 km east of the Pacific Ocean and 700 m above sea level.

Climate

The field areas experience a Mediterranean climate, with warm, dry summers and wet (rain-dominated), cool winters. Although both sites are near the coast, fog blankets the Dry Creek catchment at Sagehorn in the Central Belt only a few days a year and rarely enters the Elder Creek catchment in the Coastal Belt due to strong topographic barriers. Historical climate data (summarized in Table 3.2) indicate that Angelo (in the Coastal Belt) received $\sim 2,000$ mm of annual precipitation on average over the past century, 10–30% more than Sagehorn (in the Central Belt), and is slightly ($\sim 1^\circ\text{C}$) cooler. However, due to greater interception

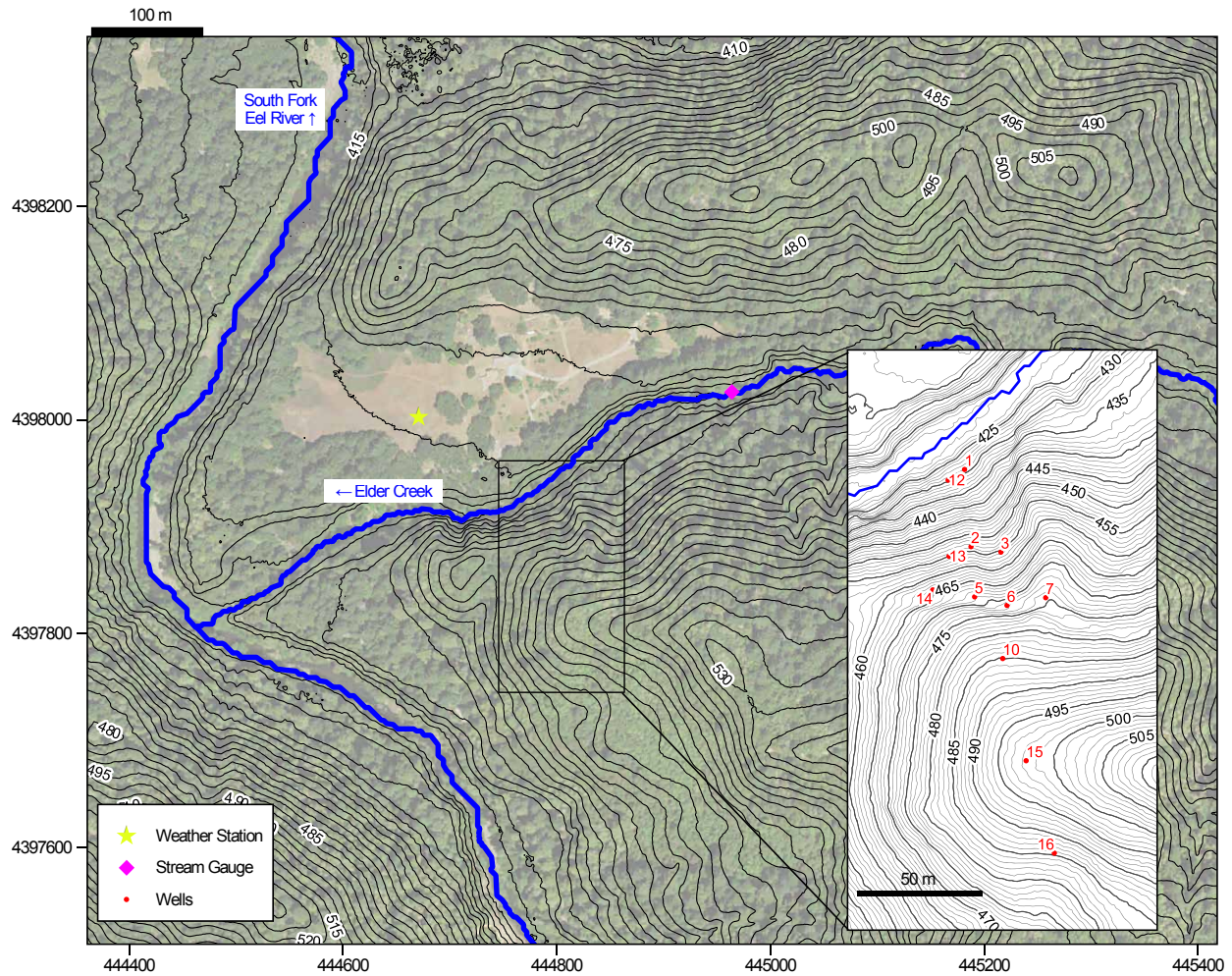


Figure 3.5: Map of study area in the Coastal Belt (‘Angelo’) highlighting evergreen forest community. Inset box shows expanded view of topography along intensively-studied hillslope (‘Rivendell’). Here only the location of wells drilled down to fresh bedrock are shown. Coordinates provided in NAD83/UTM Zone 10N. 1 (grey) and 5 (black) m ground surface elevation contours from 2014 lidar collected by NCALM. Background NAIP air photo from June 7, 2014

Table 3.1: Catchment physiographic and vegetation characteristics

	Elder Creek (Angelo; Coastal Belt)	Dry Creek (Sagehorn; Central Belt)
Catchment mouth location	39.7284°, -123.6477°	39.5754°, -123.4642°
Drainage area (km ²)	16.97	3.54
Elevation (max, mean, min; m.a.s.l.)	1,285, 849, 421	905, 733, 593
Geomorphic channel drainage density (km/km ²) ^a	7.9	16.9
Upslope contributing area at channel head (m ²) ^a	6,180	1,085
Canopy cover (mean, median ± 1 s.d.; %) ^b	89, 93 ± 12	21, 11 ± 19
Mean hillslope gradient (%) ^c	50.4	27.9
Lithology (See Table 3.3 for more detail)	Argillite (mudstone), greywacke (sandstone), minor conglomerate	Argillaceous-matrix chaotic mélange containing blocks of sandstone, chert, and various high-grade metamorphics
Erosion rate (mm/year)	0.2 (Holocene) ^d 0.4 (Pleistocene) ^d	0.12 ± 0.01 ^e (0.16 ± 0.02 in neighboring Hank Creek) ^e
Vegetation communities	Mixed broadleaf-needleleaf evergreen forest (north-facing slopes, valleys) ^f Woody plants: Douglas fir (<i>P. menziesii</i>), Tan oak (<i>N. densiflorus</i>), Live oak (<i>Q. chrysolepis</i> , <i>spp.</i>), Madrone (<i>A. menziesii</i>), California bay (<i>U. californica</i>) Understory: Poison oak (<i>T. diversilobum</i>), Oregon grape (<i>B. nervosa</i>), Huckleberry (<i>V. parvifolium</i>), Ferns (<i>spp.</i>) Riparian: Alder (<i>Alnus spp.</i>), Bigleaf maple (<i>A. macrophyllum</i>) Strath terraces: Oregon white oak (<i>Q. garryana</i>), Native perennial and invasive annual grasses Chaparral (south-facing slopes, higher elevations): Manzanita (<i>Arctostaphylos spp.</i>), Live oak (<i>Quercus spp.</i>), Chamise (<i>A. fasciculatum</i>), Ceanothus (<i>Ceanothus spp.</i>)	Annual grass deciduous oak savanna-woodland (mélange) ^g Woody plants: Oregon white oak (<i>Q. garryana</i>), Manzanita (<i>Arctostaphylos spp.</i>), Minor California black oak (<i>Q. kelloggii</i>) and buckeye (<i>A. californica</i>) Herbaceous cover: Slender oat (<i>A. barbata</i>), Foxtail barley (<i>H. murinum</i>), Filaree (<i>E. cicutarium</i>), Medusahead (<i>T. caput-medusae</i>), Velvet grass (<i>H. lanatus</i>), Italian thistle (<i>C. pycnocephalus</i>) Riparian: Oregon ash (<i>F. latifolia</i>), Bigleaf maple (<i>A. macrophyllum</i>) <i>Large sandstone blocks have similar vegetation community as Elder Creek</i>

Notes: ^aLovill et al. [2018]. ^bCalculated from National Land Cover analytical tree canopy cover data set. ^cCalculated from 1 m pixel-size NCALM lidar data set. ^dFuller et al. [2009]. ^eDetermined in this study using cosmogenic ²⁶Al; see section 3.4. ^fSee also Johnson [1979]. ^gSee also Hahm et al. [2017b] and Hahm et al. [2018].

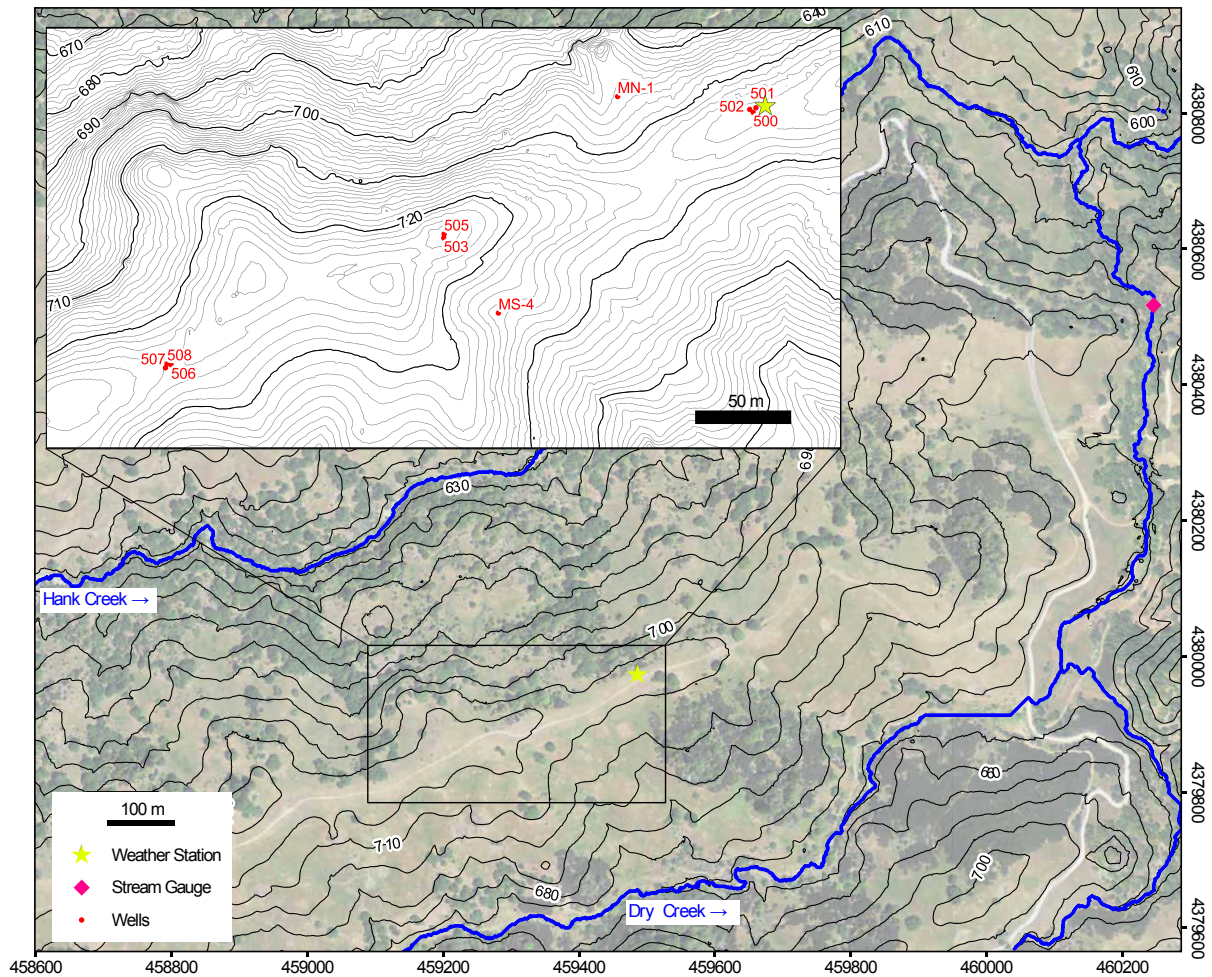


Figure 3.6: Map of study area in the Central Belt mélangé ('Sagehorn'), highlighting mixed woodland and savanna vegetation communities. Inset box shows expanded view of topography along intensively-studied hillslope. Coordinates provided in NAD83/UTM Zone 10N. 1 (grey) and 5 (black) m ground surface elevation contours from 2015 lidar collected by NCALM. Background NAIP air photo from May 29, 2012.

Table 3.2: Historical climate

Site	Mean annual precipitation (mm)	Mean annual temperature (°C)	Time range	Reference
Angelo	2,032		1900–1963	Rantz [1968]
	2,156		1946–1976	Johnson [1979]
	1,893		1985–2007	Peter Steel, pers. comm., 2016
Sagehorn	2,042	12.4	1981–2010	PRISM
	1,524–1,778		1900–1963	Rantz [1968]
	1,790		1961–1976	Interpolated COOP stations ^a
	1,811	13.3	1981–2010	PRISM

Notes: In the 15-year period from 1961 and 1976, two formerly active weather stations in Branscomb and Willits, CA, recorded 2,190 and 1,389 mm of average annual precipitation, respectively (data from NOAA.gov; COOP IDs: 041046 and 049684, elevations: 445 and 412 m, 25 km NW and 20 km SW of the site, respectively).

losses at Angelo [see discussion below and analysis by Dralle et al., 2018], the amount of rainfall arriving at the ground surface is nearly identical at both sites. Both sites experience high interannual precipitation variability resulting in periodic drought conditions (Dettinger et al. [2011] report that the regional coefficient of variation of annual water year precipitation between 1951 and 2008 was 0.3 to 0.4).

Geology

This area of the Northern California Coast Ranges is primarily underlain by the Franciscan complex (Table 3.3), which is divided into three generally north-south (coast-parallel) trending belts that are separated by fault contacts and decrease in age, subduction depth, and metamorphic grade to the west [Blake and Jones, 1974; Blake et al., 1985; Irwin, 1960; McLaughlin et al., 1994]. The Coastal and Central Belts underlie ~15% and ~50% of the Eel River watershed, respectively [Langenheim et al., 2013]. The Elder Creek watershed and our intensively studied hillslope, Rivendell, are underlain by Coastal Belt turbidites (which we group together with the lithologically similar and sometimes subdivided Yager terrane) and primarily consist of argillite with smaller amounts of interbedded sandstone (greywacke) and minor conglomerate [Jayko et al., 1989; Lovill et al., 2018].

Sagehorn is underlain by the Central Belt, which is locally interpreted to be a low-temperature, high-pressure tectonic flow mélange [Cloos, 1982]. The mélange matrix is primarily argillaceous (mudstone protolith) and has a scaly appearance [Blake and Jones, 1974]. The matrix grades over distances of tens of meters from fractured and folded but bedded mudstone into argillaceous material exhibiting “anastomosing fracture cleavage” [Cloos, 1983] that encompasses coherent blocks of widely varying sizes (10^{-2} to 10^4 m) of greywacke

Table 3.3: Franciscan geology of the Northern California Coast Ranges

	Coastal Belt	Central Belt
Lithology	Interbedded argillite, greywacke, minor conglomerate (‘broken formation’)	Argillite-matrix mélange with blocks (primarily greywacke, chert, minor greenstone, blueschist, eclogite, limestone)
Age	Paleocene to Eocene	Jurassic to Paleocene
Interpreted formation	Deformed turbidite sedimentary deposits	Subduction-complex flow mélange
Metamorphic facies	Zeolite	Pumpellyite
Approximate burial P - T	1 kbar, <175 °C	3–10 kbar, 100–250 °C
Mineralogy	Argillite: quartz, albite, illite, chlorite, muscovite, microcline, kaolinite, calcite, smectite, anatase, iron oxides, and pyrite Greywacke: feldspar, quartz, micas, lithics, and some prehnite <i>Abundant laumontite veins</i>	Mélange matrix: quartz, albite, microcline, muscovite, chlorite, illite, titanite, minor gypsum, pumpellyite and lawsonite, rare kaolinite, and locally aragonite/calcite <i>Lacks laumontite</i>
Notes	Argillite undergoes disaggregation upon wetting and drying cycles; open fractures above fresh bedrock	Mélange matrix deforms in near surface (‘blue goo’); tendency to seal fractures

Notes: References: this study; Cloos [1982]; Ernst and McLaughlin [2012]; Gu et al. [2016]; Jayko et al. [1989]; Kim et al. [2014].

(lithic-rich sandstone), chert, and minor high-grade metamorphics and ultramafics. At our site (and elsewhere within the Central Belt [Cloos, 1982]) greywacke is the most common block by exposed area [Lovill et al., 2018]. The mélange matrix is colloquially called *blue goo*, due its hue in a reduced state and its viscous-like rheology in the near surface. Previous mineralogical studies near the site indicated that the matrix is primarily quartz, albite, chlorite, and phengitic white mica with rare kaolinite, pumpellyite, and lawsonite [Cloos, 1983]. Although better known for its high-grade (blueschist) blocks, the pelitic matrix is the primary component of the Central Belt mélange [Cloos, 1983].

Soils

Soils at the Coastal Belt site are classified as alfisols [Rittiman and Thorson, 2001], consistent with our field observations. At Rivendell, the soil is thin where the slope steepens near the

channel and generally thicker (30–50 cm) toward the topographic divide [Oshun et al., 2016]. Augering and digging explorations indicate that the surface organic horizon is 5 cm thick. Below lies a massive or poorly sorted, yellow-brown layer rich in centimeter-scale colluvial fragments of argillite and sandstone that lacks clear horizonation. Rock fragments typically have red and brown oxide staining on their exteriors and on internal fracture surfaces. Visible macropores are common, most likely recording root casts and burrows by animals and insects. Despite originating from argillite bedrock, the soil does not experience seasonal deep cracking or other obvious shrink-swell features. The transition between this mobile soil and intact, physically immobile saprolite is typically abrupt and readily identifiable in road cuts or soil pits via poorly sorted colluvium overlying coherent argillite that exhibits through going networks of millimeter- and centimeter-scale fractures and occasional larger-scale bedding planes. Observed processes that collectively mix and transport soil at Rivendell include ground-wasp nesting, animal burrowing, tree throw, rain splash, and during colder winter days the formation of ice pedestals that loft particles downslope.

Soils within the savanna-woodland developed on mélange matrix at the Central Belt site are classified as mollisols [Rittiman and Thorson, 2001], in agreement with observations from ~30 pits and augered boreholes along the topographic divide within the oak-grassland areas. A ~30-cm-thick brown-black organic-rich granular mineral A horizon abruptly overlies a yellow-gray, massive 10- to 20-cm-thick Bt horizon with higher clay content. There is usually an increase in large rock fragments at the Bt–C horizon boundary, and the matrix and rock fragments become less yellow-red and more gray-black-blue in hue. It is not uncommon to find fragments of numerous lithologies (primarily greywacke, chert, and argillite) within a single soil pit at the topographic divide. Here, too, we observe no desiccation cracks on the ground surface in summer. Saturated hydraulic conductivity is high in the near surface (exceeding 10^4 cm/s and comparable to maximum hourly rainfall intensities observed since the deployment of a precipitation gauge in 2015) and decreases with depth, reaching lower values ($\sim 10^5$ cm/s) in the upper saprolite [Dralle et al., 2018]. Local soil transport occurs via gopher burrowing, wasp nesting, rainsplash, overland flow wash, and (accompanying Euro-American settlement) pig rooting.

Regional uplift and geomorphology

The northward migrating Mendocino Triple Junction was at the latitude of the study area approximately 3 Ma [Atwater and Stock, 1998], and fluvial-marine deposit transitions suggest that the land emerged from sea level at this time [Lock et al., 2006]. High regional uplift rates continue to drive rapid river incision in the Northern California Coast Ranges, creating ridge and valley topography. At the study watersheds, prominent local knickpoints (short, steep reaches) are present along the main stem channels [Lovill et al., 2018]. Rivendell lies below a major knickpoint on Elder Creek (in the Coastal Belt), which Seidl and Dietrich [1992] proposed originated at the junction with the South Fork Eel and propagated upslope. In contrast, our intensively studied hillslope at Sagehorn in the Central Belt lies above a major apparently stationary knickpoint interpreted to arise from a large resistant block

within the *mélange* encountered by the main stem during incision (as evidenced by a large continuous outcrop on the hillslope adjacent to the knickpoint). This may be one factor contributing to the generally gentler topography within Dry Creek (Central Belt) than in Elder Creek (Coastal belt; Table 3.1). Within Elder Creek, Holocene fluvial incision rates were ~ 0.2 mm/year, and during wetter conditions in the Pleistocene, landscape-averaged erosion rates were ~ 0.4 mm/year [Fuller et al., 2009]. Dry Creek’s basin-wide cosmogenic nuclide-inferred erosion rate (see section 3.4) is 0.12 ± 0.01 mm/year, about half that of Elder Creek, consistent with a decline in modeled regional rock uplift rates at the more southern location of Dry Creek [Lock et al., 2006] combined with lower erosion rates locally, above the prominent knickpoint [Lovill et al., 2018].

The generally weak bedrock of the Franciscan results in numerous earthflows within the Central Belt [Mackey and Roering, 2011; Roering et al., 2009, 2015] and deep-seated landslides and debris flows in the Coastal Belt [Stock et al., 2005]. The Dry Creek watershed exhibits widespread earthflow topography (lumpy, “melted ice cream” appearance [Kelsey, 1978]), yet few flows are presently active and the topography may be largely relict, perhaps due to reduced river incision upslope of the knickpoint. This would be consistent with the observations of Bennett et al. [2016], who noted the preponderance of active earthflows below knickpoints across the *mélange* and interpreted the relative lack of active earthflows above knickpoints to result in the preservation of relict terrain in headwater catchments of the Eel River watershed.

Vegetation

The vegetation communities across the two sites are starkly different (see species lists in Table 3.1, maps and photos in Figures 3.2 and 3.3, and early descriptions of the region in Clark [1937]). Angelo (in the Coastal Belt) is characterized by a mixed broadleaf-needleleaf evergreen forest that grades into chaparral at higher elevations and on some south-facing slopes. Douglas fir (*Pseudotsuga menziesii*) is the dominant canopy-emergent species on north-facing slopes and in tributary valleys on south-facing slopes and is typically associated with tan oak (*Notholithocarpus densiflorus*), live oaks (*Quercus chrysolepis* and *Quercus agrifolia*), Pacific madrone (*Arbutus menziesii*), and California bay laurel (*Umbellularia californica*). Coast Redwood (*Sequoia sempervirens*) is not present in the Elder Creek study watershed but is common elsewhere at Angelo and the Coastal Belt in areas more subject to fog. The spatial extent of the Douglas fir may partly be a relic of the practice of Native American burning, which reduced the extent of fir relative to the hardwood forests [Johnson, 1979].

In contrast, Sagehorn, in the Central Belt, is predominantly inhabited by winter deciduous oaks and annual grasses. The water limitation-tolerant Oregon white oak (also known as Garry oak; *Quercus garryana*) is the dominant species [Hahm et al., 2018] and is concentrated with higher density on north-facing slopes, occasionally forming woodlands with contiguous canopy. Dense evergreen forest areas without an herbaceous understory are found on large sandstone blocks, dominated by Pacific madrone and Douglas fir. California black

oak (*Quercus kelloggii*) is common along ecotones, which are typically abrupt between grassland and evergreen forest but diffuse between grassland and oak woodland. Rare ultramafic and high-grade metamorphic blocks (order 10 m across) outcrop as barrens devoid of soil and host rare endemic species.

3.4 Methods

Here we outline the methods employed to track water as it moves through the subsurface to streams, to document its storage within the subsurface in relation to the structure of the critical zone, and then to quantify plant community distribution and water availability.

Stream runoff

Stream runoff at the Coastal Belt site is measured by the U.S. Geological Survey (USGS Gauge 11475560, Elder Creek near Branscomb, CA; upstream area 16.8 km²), ~200 m upstream from the base of the Rivendell study hillslope near the confluence of the creek with the South Fork Eel River. During the study period, streamflow was gauged by the USGS 5–10 times per year, and the USGS estimates 5–10% accuracy for discharge. At the Central Belt *mélange* site, we measure stage in the channel of Dry Creek near its mouth (~1,400 m downstream from the base of the study hillslope; upstream area 3.46 km²) and calculate runoff from a rating curve established from >20 measurements spanning discharges of less than 0.001 to greater than 10 m³/s. Based on the quality of the rating curve and precision of the stage recorder (see below), we estimate 5–10% accuracy for the Dry Creek discharge record.

Precipitation and interception

Precipitation is measured with unshielded tipping-bucket rain gauges (Model TB4, Hyquest Solutions). The manufacturer-provided measurement accuracy is better than $\pm 3\%$ given the intensity of rainfall experienced at the site. We perform three adjustment procedures that account for (1) wind-induced undercatch [see supporting information and Allerup and Madsen, 1980; Sevruk, 1982; Yang et al., 1998, for more detail]; (2) horizontal variations in rainfall; and (3) data gaps prior to the deployment of gauges. For the Dry Creek catchment (Central Belt), we use one centrally located ridgetop rain gauge (Sagehorn, 715 m a.s.l.), and for the Elder Creek catchment (Coastal Belt), we average precipitation from a gauge located near the mouth (‘Angelo Meadow,’ 405 m a.s.l.) and the headwaters (‘Cahto Peak,’ 1,249 m a.s.l.). The Daymet V3 climate product (<https://daymet.ornl.gov/>) is used to extend the precipitation time series prior to 2015 at both sites.

To correct for the effects of wind at our weather station gauges [Allerup and Madsen, 1980; Sevruk, 1982], we use the wind speed correction factor specific to the gauge geometry to adjust recorded precipitation totals at each 5 minute interval following Yang et al. [1998].

This likely still underestimates total precipitation, as we exclude wetting losses, evaporation and splash. A few storms each winter may also fall as snow, which is generally more susceptible to aerodynamic losses than rain [Sevruk, 1982]. Across the 2016 and 2017 water years, this correction procedure resulted in a 5% increase in total precipitation for a relatively sheltered gauge in a lowland area with surrounding tall trees (‘Angelo Meadow’) and a 13% increase for a relatively exposed gauge on a grass-dominated ridgeline (‘Sagehorn’) due to high winds during precipitation events at the ridge.

Interception losses are calculated on a daily basis, based on site-specific wet-up losses [Laio et al., 2001]. We subtract 1 or 4 mm from daily rainfall totals respectively from the winter-deciduous oak annual grass savanna-woodland (Dry Creek catchment; Central Belt) or mixed needleleaf-broadleaf evergreen forest (Elder Creek catchment; Coastal Belt); when less rain falls than these thresholds no effective precipitation occurs. The result of this approach (13% precipitation reduction at Elder and 4% at Dry) is consistent with measured differences in rainfall totals found in the literature for the dominant species at our site [Krygier, 1971; Pypker et al., 2005], an under-canopy gauge at Rivendell in the Coastal Belt [Salve et al., 2012], and regional and global estimates of similar forest types [Miralles et al., 2010; Reid and Lewis, 2009].

The wind correction and interception accounting are only applied to the post 2015 rainfall record. For the historical data from 2002–2015 we assume the Daymet product is corrected for wind-induced losses. For this same time period, interception is interpreted to be included within the MODIS-derived ET dataset [Ryu et al., 2011]. Apparent discrepancies in the Elder Creek water year ET estimates presented here in the Budyko plot vs. in Rempe and Dietrich’s [2018] supplementary material are due to the fact that interception is not included in the precipitation term presented in the Budyko plot here, but is instead part of the MODIS-derived ET estimate. In contrast, interception is removed from P in Rempe and Dietrich [2018] prior to the estimation of ET from a water budget analysis.

We specify a canopy interception storage to account for an initial, event-based ‘wet-up’ period in which rain is captured by the canopy, after which throughfall is equal to the incoming rain intensity [see supporting information and Krygier, 1971; Laio et al., 2001; Miralles et al., 2010; Pypker et al., 2005; Reid and Lewis, 2009, for more detail]. The resulting effective precipitation available for storage, evapotranspiration, and runoff, P , is used in subsequent analyses.

Evapotranspiration and radiation

For each of the two study catchments, we compute potential evapotranspiration (PET) with the Hargreaves method [Hargreaves and Samani, 1982, 1985], which requires daily maximum, minimum, and mean temperatures obtained from the weather stations, as well as radiative forcing as a function of latitude and day of year, calculated with scripts from the PyETo Python package. PET calculated prior to 2015 relies on Daymet temperature records, which compare well with our local weather stations at both sites during times for which the two data sets overlap. Total solar radiation is measured at Angelo with a Li-Cor LI200X-L

Pyranometer. Using historical estimates of actual evapotranspiration (ET) from a process-based Moderate Resolution Imaging Spectroradiometer (MODIS)-derived data set described in Ryu et al. [2011] along with Daymet precipitation records, we also plot annual values for each catchment from 2002–2015 in the Budyko space: evaporative fraction (ET/P) versus aridity (PET/P). ET is difficult to quantify over large spatial scales (particularly when Q is lacking, as is the case at Dry Creek prior to our installation of a stream gauge there). The uncertainty of the ET data has been evaluated via intercomparison with annual basin water balance and flux tower estimates of ET by Ryu et al. [2011], yielding a root-mean-square error of 31% and 26%, respectively (these comparison data sets are also subject to their own inherent uncertainties). For the purposes of this study, we are primarily interested in how differences in subsurface water storage capacity between nearby sites manifest in distinct water balance regimes (and therefore location within the Budyko plot). For this purpose, the Ryu et al. [2011] ET data set, which relies on satellite-based greenness indices, is suitable for intersite comparison even if the absolute location of each catchment within the Budyko space is subject to uncertainty. This is based on the reasonable assumption that greenness scales with ET at each site (i.e., the remotely sensed ET signal is correct in relative if not in absolute magnitude). We fit curves to each site in the Budyko space using the analytical formulation of Yang et al. [2008]. A single fitting parameter (n) is used to describe the shape of the Budyko curve; low values of n correspond to catchments with low storage that transform precipitation into runoff efficiently; high values of n correspond to catchments with high storage that are able to store precipitation and return it to the atmosphere via evapotranspiration.

Catchment-integrated dynamic water storage

Catchment water budgets for the 2017 water year wet season were compared between the two study sites to quantify water storage. The seasonally dynamic water storage is calculated as the change in total catchment storage (ΔS) relative to an October 1 reference state [e.g., Sayama et al., 2011]. This date typically coincides with the end of the dry season when annual catchment water storage is at a minimum. Changes in dynamic storage result from gains due to effective precipitation (P) and losses to runoff (Q) and evapotranspiration, which in the wet season is assumed to be approximately equal to PET (we lack daily estimates of actual evapotranspiration for the 2017 water year). Using daily data, we plot cumulative running storage change as $\Delta S = \Sigma P - \Sigma Q - \Sigma PET$. We stop the analysis at the end of May, when the approximation $ET \approx PET$ —which assumes high wet season water availability (and an energy-limited state, as is typical in the area [Reid and Lewis, 2009])—becomes increasingly inaccurate. Hence, to the extent that $ET < PET$ in the wet season, the inferred dynamic storage is an underestimate of the actual dynamic storage. Small biased inaccuracies can compound in this running mass balance, requiring high-accuracy input data to produce reasonable dynamic storage estimates. Our analysis benefits from the small areas of the study catchments (which minimize horizontal variation in rainfall and PET) and is generally

corroborated by hillslope-scale measurements of dynamic storage capacity (discussed below). Dralle et al. [2018] further discuss this method of analysis and its uncertainty.

Boreholes and Well Casings

Boreholes were drilled during multiple field campaigns at both sites from 2007–2015 to depths typically below the transition from weathered to fresh bedrock (to a maximum of ~30 m). Recovered material was documented, where feasible, with respect to its color, texture, presence, or absence of minerals indicative of weathering fronts (e.g., pyrite and calcite), fracture density and fill, and water stable isotopic composition [see Hahm et al., 2017a; Oshun et al., 2016; Rempe and Dietrich, 2018]. These observations, together with groundwater dynamics and drilling rate-inferred material strength, are used to describe subsurface CZ structure. The depth to fresh bedrock is locally determined by a large increase in material strength, perennial saturation, and lack of mineral weathering. Boreholes were used to monitor groundwater and vadose zone moisture dynamics (see sections below)

Holes were drilled to 2", 3" or 4" diameter and cased with 2" or 3" schedule 40 PVC pipe, slotted along the entire length. The upper ~20 cm of wellheads are encased in concrete for stability and to prevent infiltrating near surface water from percolating along the casing.

SEM microstructure analysis, mineralogy, and bulk geochemistry

To study microstructures that control the porosity and permeability of the fresh mélange matrix of the Central Belt, we collected core on 25 September 2015 and analyzed a sample recovered from 15.3 m below the ground surface in borehole 501 (Figure 3.6) at the Indiana University Shale Research Lab [see Schieber, 2010, for more detail]. The sample was prepared for scanning electron microscope (SEM) analysis via argon ion milling and scanned at 15.0 kV and 70 Pa.

The mineralogy of both fresh and weathered material obtained from drilling at both sites was measured using X-ray powder diffraction at Indiana University, with quantitative phase determinations via the Rietveld method [see, e.g., Bish and Howard, 1988], normalized to 100%. The relative abundances of illite and smectite were separately estimated via fits to diffraction intensity and are expressed as point-bounded horizontal bars defining conservative concentration estimates; these phases are not included in the normalization.

To compare parent material bulk composition, we measured the geochemistry of fresh, unweathered bedrock at both sites after pulverization to 200 mesh and analysis via lithium-borate fusion inductively coupled plasma emission spectroscopy at the Bureau Veritas Mineral Laboratories (Vancouver, BC).

Erosion rates

We collected in-channel stream sediment from near the mouths of two creeks at Sagehorn (Dry and Hank, which bound the study ridge) within the Central Belt mélange to estimate

basin-wide cosmogenic-nuclide-inferred erosion rates [e.g., Granger et al., 1996]. In stream sediment samples were collected on 2017-04-23 near the mouths of Hank Creek (~300 m upstream from the Sherwood Road bridge) and Dry Creek (~70 m upstream from the Sherwood Road bridge). Because the basins are small (both <6 km²), we used their mean elevations and latitudes to determine basin-wide scaling factors. Due to the relatively gentle topography and lack of snow, we do not correct the scaling factor by any shielding term; topographic shielding is generally small [Vermeesch, 2007], and neglecting to account for it results in erosion rates that are slightly underestimated. We separated quartz from each sample following standard procedures and then isolated Al within the quartz. The concentration of cosmogenic ²⁶Al was measured at the PRIME lab at Purdue University. We then used the CosmoCalc program [Vermeesch, 2007] with Stone’s [2000] scaling relations to determine erosion rates (rates reported in Table 3.1). Analytical uncertainties from the accelerator mass spectrometer measurement were propagated and are reported with the erosion rate estimates. The original ²⁶Al atoms/g concentrations and uncertainties measured by the PRIME lab are included in the supplementary workbook (‘CosmoCalc-Dry_Hank.xlsx’) of Hahm et al. [2019b], which can be used to reproduce the erosion rate calculations when the CosmoCalc plugin [Vermeesch, 2007] is installed.

Groundwater dynamics

We deployed pressure transducers in wells to monitor groundwater table dynamics at Sagehorn in the Central Belt in 2015 (Rivendell’s 12 wells in the Coastal Belt were already instrumented before the start of this study). Most wells are outfitted with vented transducers that compensate for atmospheric pressure changes (models CS-450 and CS-451, Campbell Scientific); some are outfitted with offline, internal-battery powered pressure transducers (Solinst Levelogger) that are corrected for atmospheric pressure fluctuations with a nearby, similar-elevation barometric pressure sensor. In some boreholes that were not drilled to the fresh bedrock boundary (MN-1, MS-4, 505, and 508 at Sagehorn) the water table drops below the base of the wells during portions of the year. The accuracy of the Campbell and Solinst transducers are 3.5 and 5 mm, respectively.

Dissolved oxygen in groundwater

We measured dissolved oxygen content in groundwater at Sagehorn in the Central Belt with an optical luminescence sensor (YSI ProODO), with descending depth profiles through the entire undisturbed water column. We waited for readings to stabilize at each measurement depth, which typically took between 30 and 180 s. The instrument measures and adjusts dissolved oxygen percentages to temperature in the water and barometric pressure at the surface. We routinely calibrated the dissolved oxygen meter following manufacturer guidelines with two end-members: water-saturated air, achieved by equilibrating the sensor in a 100% relative humidity sleeve, and 0% dissolved oxygen solution, achieved by dissolving 8–10

g of sodium sulfite in 500 ml of water. The manufacturer provided accuracy when correctly calibrated is $\pm 1\%$.

Tree water potential

Predawn shoot water potentials were measured near topographic divides at the end of the summer dry season at both sites with a Scholander-type pressure-chamber apparatus [Boyer, 1995; Scholander et al., 1965] following the methods outlined in Hahm et al. [2018]; the instrument precision in field conditions is ± 0.1 MPa. These measurements are used to compare relative water stress between sites. At the Central Belt site, we measured *Q. garryana* and at the Coastal Belt site we measured three genera of hardwoods (*Q. chrysolepis*, *N. densiflorus*, and *A. menziesii*) as well as the conifer *P. menziesii*. Samples were collected from mature individuals (breast-height diameters typically >25 cm) within 2.5 m of the ground surface at the Central Belt. At the Coastal Belt site, approximately half of the trees sampled had canopies that were inaccessible from the ground, and climbing ropes were used to obtain shoots. These samples' predawn potentials were corrected for the gravitational component of water potential based on their collection height above the ground surface.

Remotely sensed vegetation analyses

Tree canopy cover and primary productivity.—To explore differences in the forest density between sites, we use the Landsat-derived 2011 analytical Tree Canopy Cover data set (0 to 100% tree canopy cover) provided by the National Land Cover Database [Homer et al., 2015]. We also accessed and aggregated the Landsat-derived Net Primary Production CONUS data set [Robinson et al., 2018] in the Google Earth Engine platform (30-m pixel size) to determine watershed average productivity across the two rock types.

MODIS EVI.—We analyzed time series of the MODIS enhanced vegetation index (EVI) MOD13Q1 product [Huete et al., 2002] to assess the impact of CZ water storage dynamics on plant community function and leaf phenology (250-m pixel size). We accessed and aggregated the data using the Google Earth Engine platform and extracted the median EVI pixel value within our study watersheds for the duration of the MODIS program, resulting in 16 complete water years of data. This effectively captured the leaf dynamics of the mixed broadleaf-needleleaf evergreen forest of the Coastal Belt and the herbaceous ground cover (with minor deciduous oak contribution) of the Central Belt [see, e.g., Huete et al., 2006]. To explore the seasonal dynamics of ecosystem function, we plot composite annual time series by averaging the median watershed EVI at the same date across all years.

Time series Landsat and historical air photos.—We created a cloud-free mosaicked video of the wider field area (Mendocino County, California) with all available Landsat natural color imagery in the Google Earth Engine platform (see the Movie S1 hosted online at the Hahm et al. [2019b] website) to visualize boundaries between vegetation types through time. We also analyzed historical air photos of the Central Belt site (provided by the UC

Santa Barbara Maps and Imagery library) and more recent orthoimagery from the National Agriculture Imagery Program.

3.5 Results

Results are organized around a description of subsurface critical zone structure, runoff pathways, and water storage at each site, followed by a comparison of plant community distribution, function, and water status. Some of the descriptions of subsurface structure and the hydrologic cycle, particularly for the Coastal Belt, synthesize many previously published works from the Eel River Critical Zone Observatory not previously collectively summarized. These descriptions (with appropriate citations) are combined together with new results here in order to provide a complete, stand-alone portrait of the site. They are then followed by a parallel description of the Central Belt. The common descriptions of both sites lay the foundation for the synthesis of subsurface weathering zone patterns, water storage, and surface ecosystems.

Coastal Belt (Rivendell unit hillslope and Elder Creek)

Subsurface critical zone structure.—The Coastal Belt is pervasively fractured and consists of turbidites—packages of interbedded mudstones, sandstones, and conglomerate—which are typically decimeters to meters thick. Extensive drilling shows that the weathering profile structure varies systematically across the landscape [Rempe and Dietrich, 2014, 2018; Salve et al., 2012]. Unweathered bedrock is exposed at the ground surface in Elder Creek and the South Fork Eel River. The depth to fresh bedrock increases from about 4 m just above the channel to ~ 30 m at the hillslope divide [Figure 3.7; Rempe and Dietrich, 2018]. Just below the soil, weathering has generated about 1 to 2 m of saprolite (a material with soil-like properties that retains relict-rock structure). A highly fractured and oxidized weathered bedrock zone lies between the saprolite and unweathered bedrock. Roots were observed to 16-m depth during drilling.

Runoff pathways and water storage.—At the start of the wet season, precipitation transits through the mixed broadleaf-needleleaf evergreen forest and then flows vertically as unsaturated flow through the highly conductive soil, saprolite, and weathered and fractured bedrock. A seasonal wetting front advances through the soil, saprolite, and weathered rock and replenishes a vadose zone storage deficit caused primarily by evapotranspiration in the preceding dry season [Rempe and Dietrich, 2018; Salve et al., 2012]. Across Rivendell, up to 60 ± 17 mm (avg. ± 1 s.d.) of water is seasonally stored within the soil, and 280 ± 140 mm is stored as rock moisture—exchangeable water stored in the unsaturated zone in weathered bedrock [which includes saprolite; Rempe and Dietrich, 2018].

At individual wells the annual maximum rock moisture content was the same in successive years, despite a wide range in precipitation [Rempe and Dietrich, 2018]. Total rock moisture content increases upslope, consistent with increasing weathered bedrock thickness upslope

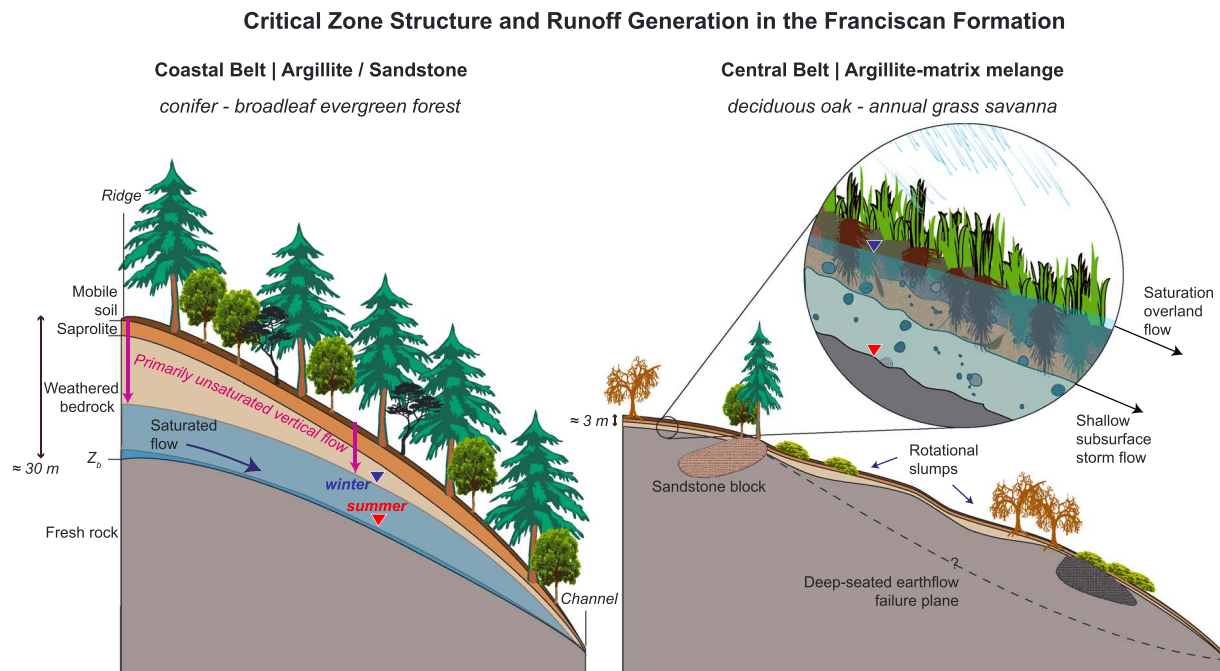


Figure 3.7: Schematic cross sections of hillslopes in the Coastal Belt (left) and Central Belt (right) of the Franciscan complex, highlighting contrasting critical zone structure, runoff pathways, vegetation distribution, and topography. End-of-winter and end-of-summer water table positions shown with inverted blue and red triangles, respectively. Runoff in Coastal Belt is generated from saturated flow through fractures in the deep, weathered rock zone that thickens toward the topographic divide. In the Central Belt, the subsurface CZ is approximately tenfold thinner at the topographic divide. Many winter storms completely saturate the subsurface, resulting in quick shallow subsurface storm flow through macropores and widespread saturation overland flow. Figure not to scale.

(Figure 3.7). Once the maximum storage capacity is reached, further rainwater inputs induce water transport deeper along fractures, recharging the underlying groundwater [Rempe and Dietrich, 2018]. Minor early wet season groundwater response occurs in some wells and has been interpreted to record local fracture flow that bypassed the rock moisture reservoir [Salve et al., 2012].

Low conductivity, perennially saturated fresh bedrock at the base of the weathering profile causes winter recharge to develop as a seasonal groundwater within the weathered bedrock [Salve et al., 2012]. As Figure 3.7 illustrates, the top surface of low-permeability fresh bedrock, defined as Z_b [sensu Rempe and Dietrich, 2014], slopes toward the adjacent channel, and groundwater flows laterally above it through a dense fracture network. Upslope, depending on the particular location and storm magnitude frequency, it takes between ~ 200 and 700 mm of cumulative water year rain for infiltrating water to elevate the rock moisture

and then pass water to the water table, causing a switch from its slow dry season decline to a more rapid wet season response [Rempe and Dietrich, 2018; Figure 3.8].

At the end of the wet season, groundwater recedes, exhibiting a slow decline through the dry summer (Figure 3.9). Drainage of groundwater from the weathered, fractured bedrock zone sustains perennial flow in Elder Creek [Lovill et al., 2018]: Runoff is low but persistent in the summer dry season (on average ~ 5 to 10 mm/month from June to September).

Catchment-wide seasonal dynamic water storage.—Figure 3.10 plots the 2017 water year catchment-integrated dynamic water storage as a residual of the balance between cumulative precipitation, runoff, and potential evaporation. The first major storms of the 2017 water year delivered ~ 250 mm of precipitation in early October to mid-October and produced minor stream runoff. *PET* at this time of year is minor and caused little moisture storage change before the arrival of subsequent storms. Subsequent precipitation continued to increase storage in the subsurface throughout the Elder Creek catchment, and the runoff response remained relatively muted until large storms in mid-December (recording the progressive increase in rock moisture storage). By January, increases in cumulative runoff closely tracked increases in the cumulative precipitation curve, and the cumulative storage curve leveled off between ~ 500 and 700 mm, with transient gains and losses in response to storms. Recession analysis indicates that the dynamic water storage at Elder consists primarily of “indirect” storage, which does not drive streamflow and is mainly held as water below a “field capacity”-like state in soils, saprolite, and weathered rock and is returned to the atmosphere via transpiration [Dralle et al., 2018; Rempe and Dietrich, 2018].

Central Belt (Sagehorn unit hillslope and Dry Creek)

General subsurface critical zone structure.—At Sagehorn in the Central Belt, fresh *mélange* matrix is often exposed in channels and drilling observations reveal that it is only 2 to 4 m below the surface at ridgetops. Hence, the subsurface CZ in the *mélange* is roughly 10 times thinner than in the Coastal Belt (Figure 3.7). Below the soil lies a ~ 50 -cm-thick, yellow-gray saprolite zone with soil-like texture that grades into a 1- to 2-m-thick, gray-black weathered rock zone. Observed rooting and hyphae depths are confined to the upper few meters. Recovered drill core and observations of fresh bedrock in stream channels indicate that unweathered *mélange* matrix has a characteristic blue-black unoxidized hue. Figure 3.11 reports mineral phases in depth profiles for a borehole at Sagehorn (Central Belt) and Rivendell (Coastal Belt). The uppermost two samples at Sagehorn (from 0.15 and 0.45 m below the surface) and the uppermost sample at Rivendell (from 0.6 m below the surface) were taken from within the mobile regolith (soil). At Sagehorn, the relatively unstable phase gypsum is gone from the soil but present above the fresh bedrock boundary, whereas calcite remains present in the near surface within the soil. There also appears to be a significant enrichment of quartz and depletion of muscovite and chlorite in the uppermost soil relative to the fresh underlying bedrock. Below the depth of the transition to fresh bedrock at Sagehorn (in the Central Belt), there is a higher concentration of chlorite and illite and lower concentration of kaolinite, relative to the mineralogy at Rivendell (in

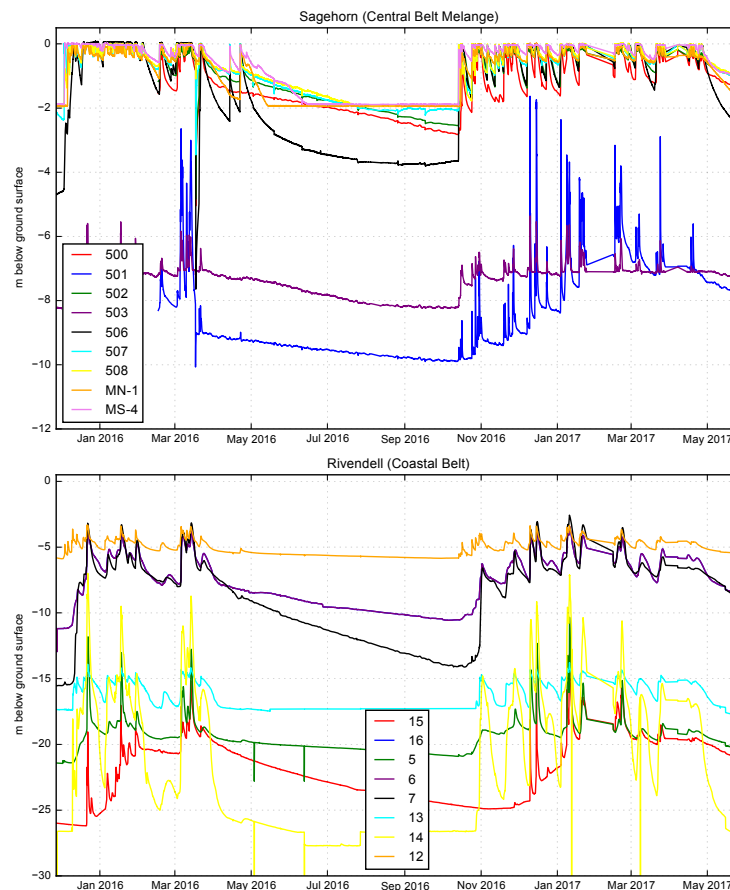


Figure 3.8: Timeseries of groundwater behavior inferred from pressure transducers in continuously slotted monitoring wells at Sagehorn (upper panel, Central Belt *mélange* site) and Rivendell (lower panel, Coastal Belt site). Groundwater elevation is referenced to the ground surface elevation at the location of each well. At Sagehorn, wells drilled into primarily *mélange* matrix (500, 502, 506, 507, 508, MN-1, and MS-4) exhibit flashy responses to winter rain events and rise to the ground surface frequently throughout the winter, receding to relatively shallow depths over the course of the dry season. Wells 501 and 503 are drilled into a crystalline-block complex and sandstone block, respectively, and have a deeper water table. Wells 500, 501, 502, and 503 are located along a topographic divide, wells 506, 507, and 508 along a slight topographic saddle, well MS-4 in the axis of a colluvial hollow, and well MN-1 along the side slope of a colluvial hollow (see Figure 3.6). Horizontal summer groundwater lines in wells 508, MN-1, and MS-4 reflect groundwater recession below pressure transducer depth. See Rivendell well locations in Figure 3.5. In all wells at both sites, periodic vertical negative excursions in summer reflect groundwater sampling events. Times when pressure transducers were removed for sampling were filtered from the timeseries with a median rolling filter with a 0.25 m threshold and 12 hour window, and gap-filled with linear interpolation. Straight lines in Feb., 2017, reflect missing, interpolated data.

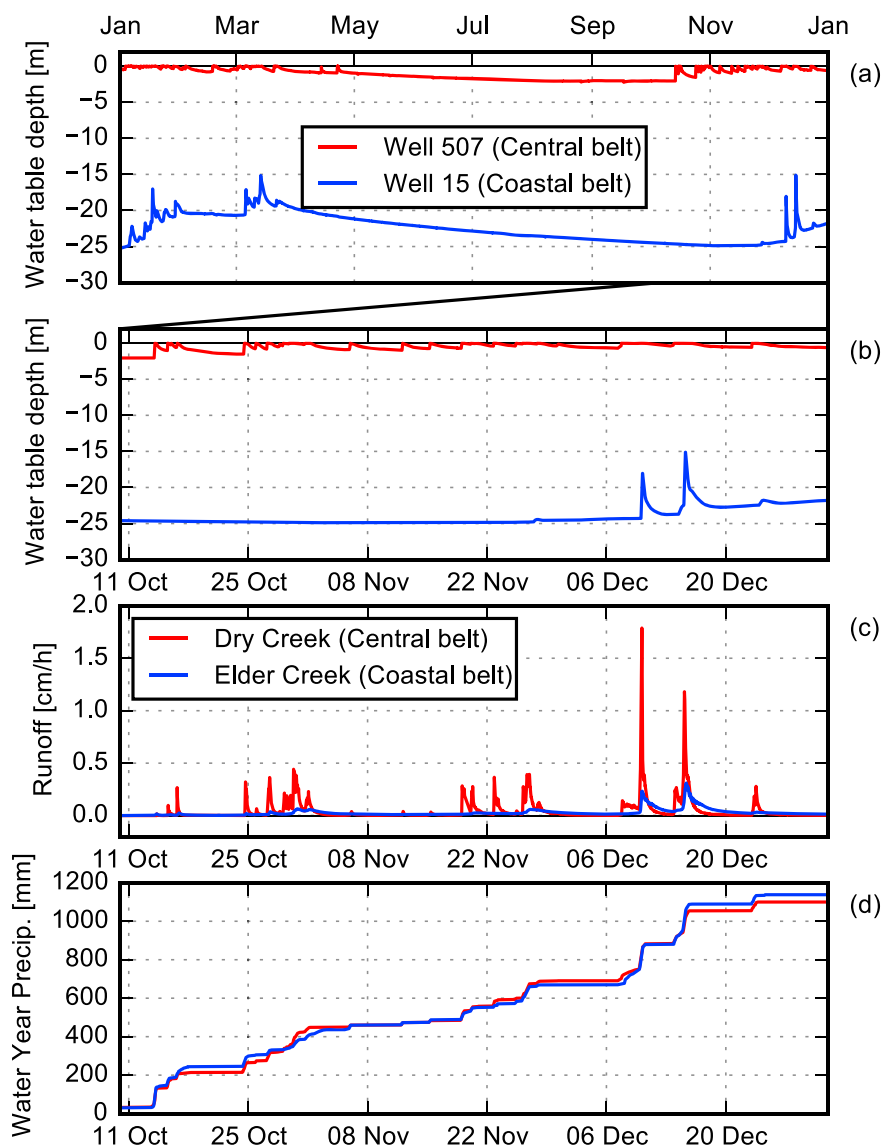


Figure 3.9: Contrasting groundwater (a, b) and stream (c) responses across sites with different depths to fresh bedrock, Z_b (blue = Coastal Belt; red = Central Belt) to similar precipitation input (d) in 2016. (a) Long dry season recession of groundwater at ridge after last winter rains to contrasting depths. (b) Expanded time series from (a) shows response of groundwater to first rains of wet season. Groundwater in Coastal Belt does not respond until ~ 700 mm of cumulative precipitation, whereas groundwater in Well 507 rises rapidly to ground surface in first major winter storm, indicating complete saturation of CZ in Central Belt, driving flashy runoff in Dry Creek (c). Variable maximum runoff in Dry Creek with saturated CZ indicates importance of saturation overland flow. Elder Creek response is muted in comparison, with longer recession.

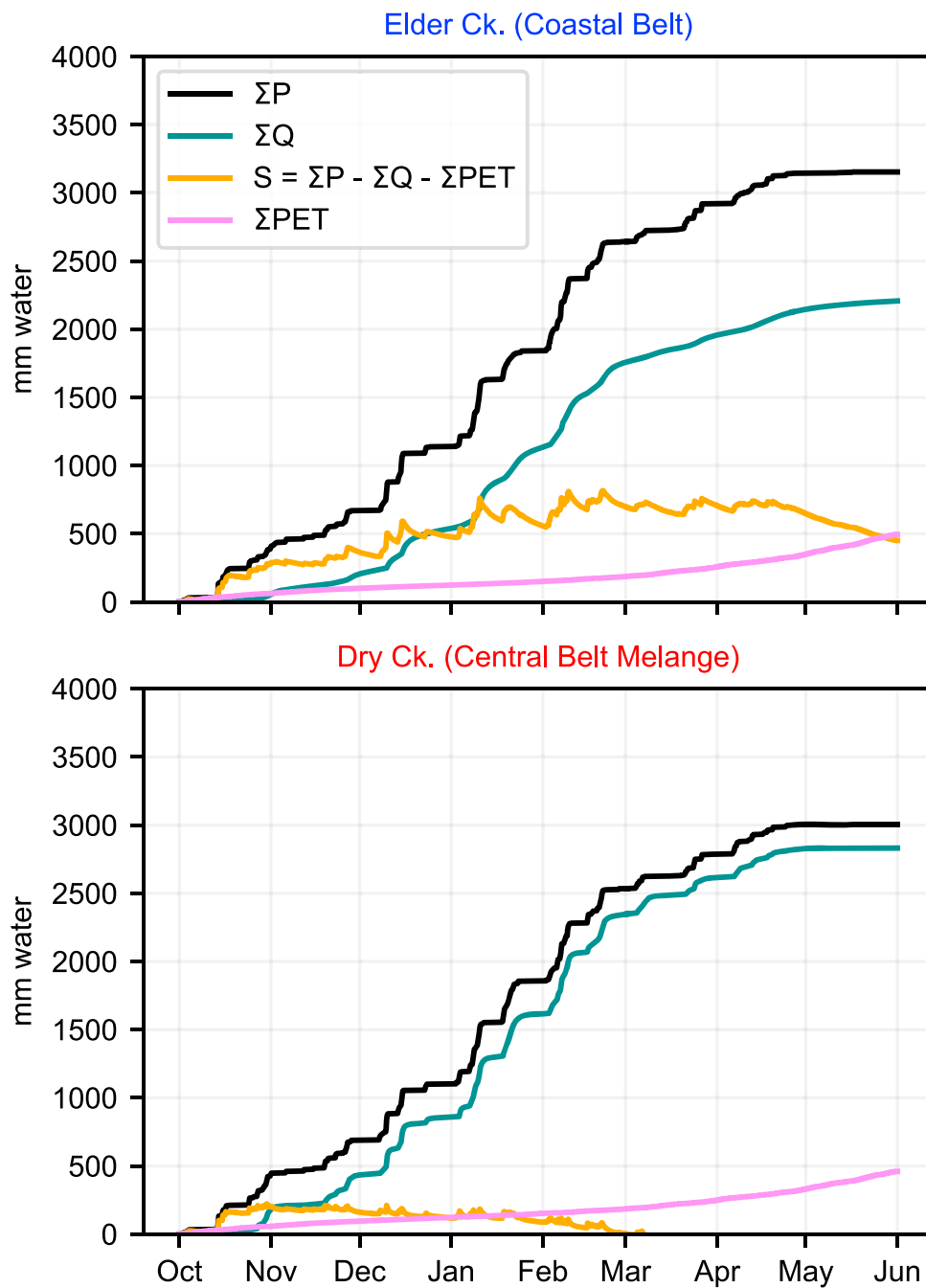


Figure 3.10: Cumulative precipitation (P), runoff (Q), potential evapotranspiration (PET), and inferred catchment-wide dynamic storage (S) in the 2017 water year. The Dry Creek watershed has a factor of approximately four lower catchment-wide dynamic storage than the Elder Creek watershed and reaches a maximum storage sooner into the wet season, resulting in a much higher runoff ratio.

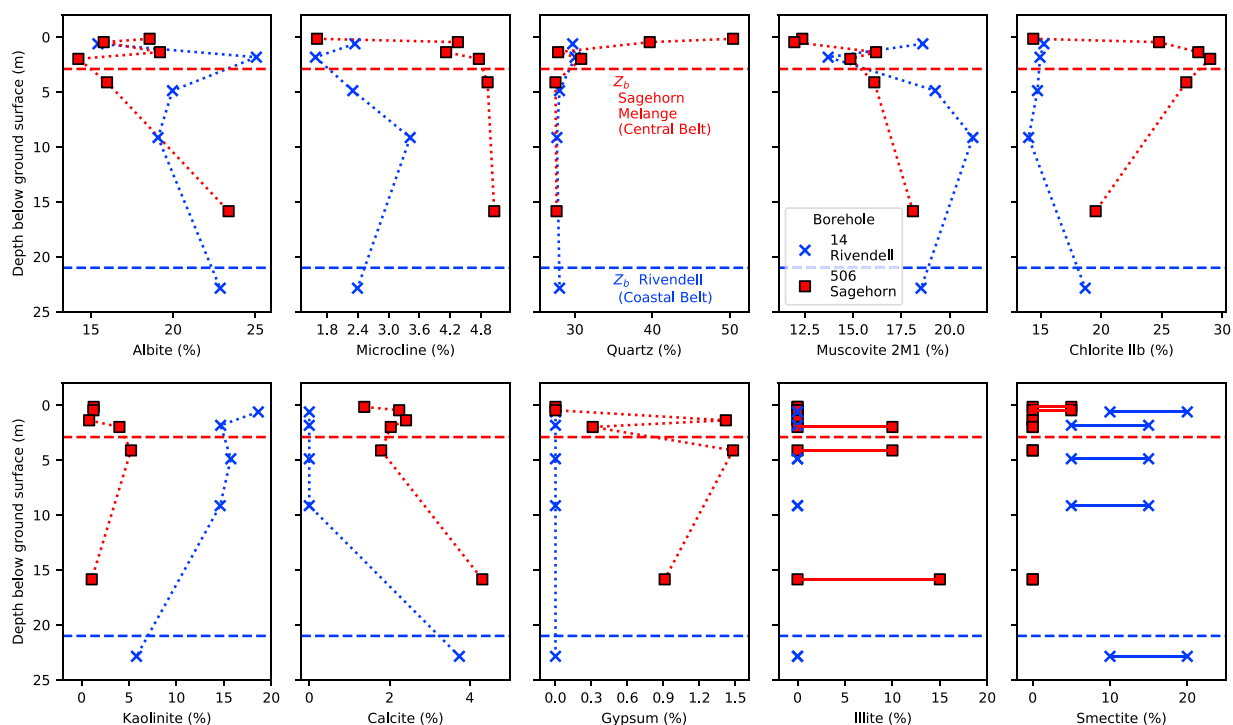


Figure 3.11: Depth profiles of XRD-determined mineral phases. Horizontal dashed lines indicate drilling-inferred transition to fresh bedrock (Z_b) at each borehole (14, blue, Coastal Belt; 506, red, Central Belt). Illite and smectite were separately estimated and not included in the normalization, resulting in some sums exceeding 100% (see section 3.4). Their concentrations are presented as likely ranges, as denoted by the horizontal lines.

the Coastal Belt). Two samples from Sagehorn (at 1.8–2.1 and 4.0–4.3 m in W506) also exhibited X-ray diffraction patterns consistent with the presence of regularly interstratified (R1) chlorite/smectite, which was not identified in the Rivendell samples. Determining the exact concentration of interstratified chlorite/smectite at Sagehorn is difficult and is not shown in Figure 3.11; however, it may be between 10% and 20%. Smectite is present throughout the Rivendell profile (in the Coastal Belt) but only appears in the soil at Sagehorn (in the Central Belt).

Subsurface structure, runoff pathways, and water storage.—Most rain falls directly on low (<20 cm tall) herbaceous ground cover. The soil has a wide distribution of macropores from roots, insects, and burrowing mammals that promote near-surface infiltration and (upon saturation) exfiltration. At the end of the dry season, the seasonally dynamic groundwater is absent: Only residual and essentially stagnant groundwater in the underlying fresh *mélange* remains at depths greater than 2 to 4 m below the surface (Figure 3.7). The first major winter storm increases the soil and rock moisture. Further rain leads to groundwater developing in the weathered bedrock zone above the fresh, perennially saturated *mélange*. Groundwater

tables in mélange-dominated wells respond after as little as 50 mm of cumulative precipitation and rise to within 20 cm of the ground surface after only ~ 100 to 200 mm, effectively saturating the CZ due to the presence of a capillary fringe, implying a dynamic porosity of only $\sim 5\%$ to 10% in the subsurface critical zone.

In contrast to the Coastal Belt, where groundwater remains >10 m below the ground surface at the topographic divide throughout the winter, in the Central Belt the groundwater table frequently reaches the surface during rainfall events (see Figure 3.9, for detailed dynamics of Well 507 and Figure 3.8 for time series of all wells at the site). Stream runoff is generated by subsurface storm flow and saturation overland flow, which quickly deliver water to channels from adjacent hillslopes (Figures 3.3c and 3.7). Field observations indicate that during times of sustained mean rainfall intensity exceeding ~ 1 cm/hr, which occurs in many winter storms, saturation overland flow extends to ridgetops across the landscape (see photo in Figure 3.3d).

In the spring, the seasonally dynamic groundwater levels rapidly decline (Figure 3.8). Rapid exhaustion of this shallow storage leads to a lack of baseflow in adjacent streams and a dry channel network in the appropriately named Dry Creek watershed. By 1 August, the water table in the ridgetop Well 507 in the Central Belt mélange has lowered to the fresh bedrock boundary, Z_b , and remains essentially static for the rest of the dry season (Figure 3.9a), indicative of very low saturated conductivity. The underlying saturated fresh bedrock does not drain significantly on a seasonal timescale and thus does not contribute measureable flow to channels. The dissolved oxygen content was indistinguishable from 0% throughout the groundwater column in Well 507 (except for near the water table surface, which exhibited higher oxygen concentrations) for measurement dates in the 2017 water year (Figure 3.12).

SEM imagery of a fresh, deep sample obtained via drilling reveals a heterogeneous fabric of sand-size metamorphic rock fragments, set in a finer-grained matrix composed of $<60\text{-}\mu\text{m}$ fine particles that are angular and very poorly sorted (Figure 3.13). These fine particles are themselves situated within a matrix-supported felted mass of phyllosilicates (likely chlorite) and lack obvious cleavage and foliation at this scale. Interparticle pores (i.e., framework pores) range in size from 10–20 nm, and larger particles may show intraparticle pores in the 10- to 100-nm size range. Due to its low intrinsic porosity, the low-viscosity epoxy resin that was used to stabilize the sample did not penetrate into the sample. Collectively, these observations and the reduced color (blue/gray) reveal the fresh mélange matrix to have very little porosity, likely extremely low saturated conductivity, and minimal groundwater flux—consistent with persistent saturation and low runoff, despite a relatively large hydraulic gradient (20% slope) from ridgetop to channel.

Subsurface heterogeneity results in contrasting hydrologic dynamics over relatively short spatial scales. For example, in the group of three deep wells near the weather station (500, 501, and 502; Figure 3.6), which are each ~ 2 m horizontally from each other and at similar ground surface elevations, a more-than-7-m vertical water table difference is maintained throughout the dry season (Figure 3.8) in these adjacent wells. The depth to the perennially saturated zone is 2 to 3 m below the ground surface in wells drilled to 6- to 8-m depth, and 9 to 10 m (Well 501) below the ground surface in a well drilled to 15-m depth. During drilling,

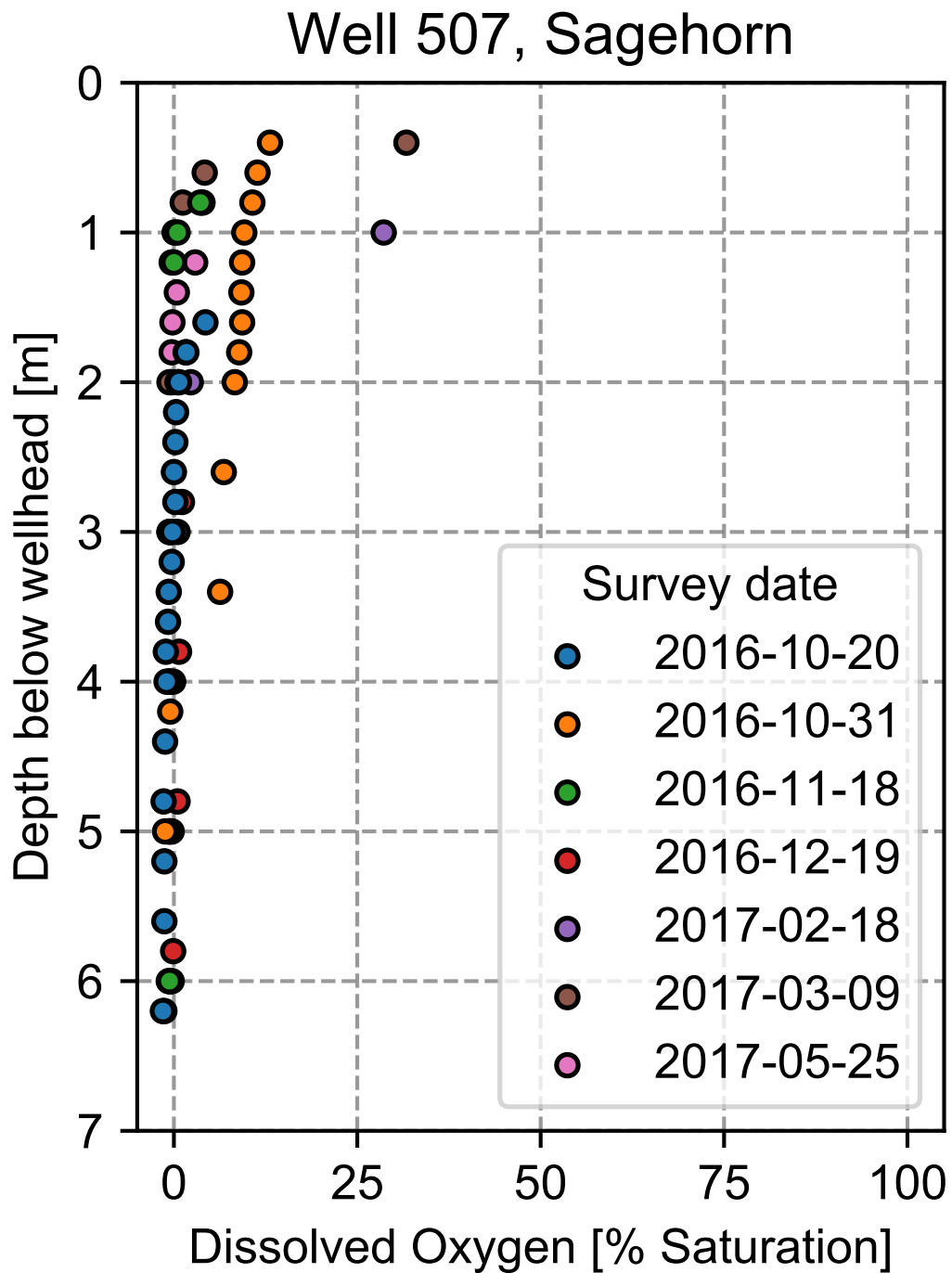


Figure 3.12: Depth-profiles of dissolved oxygen within groundwater in the Central Belt mélange in the 2017 water year. Measurements were made from the top of the groundwater table downward, in continuously slotted boreholes.

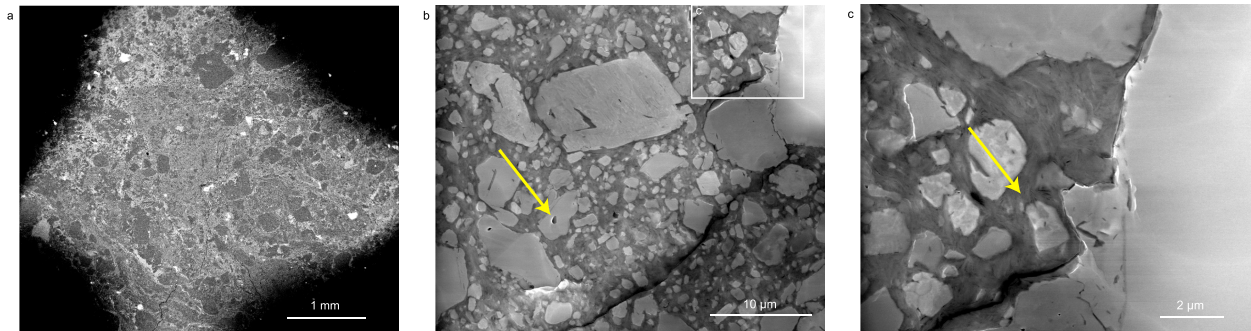


Figure 3.13: Scanning electron microscope images taken at increasing levels of magnification of fresh mélangé matrix. The uppermost image (a, low magnification), shows scattered larger (sand size) particles (mineral and rock fragments) that are suspended in a fine-grained matrix. At intermediate magnification (b), we see larger silt-size particles (also mineral and rock fragments) in a finer matrix. The larger particles may show intraparticle pores (yellow arrow). At highest magnification (c), the intraparticle matrix resolves as a felted mass of phyllosilicates (likely chlorite). This phyllosilicate matrix has some intrinsic porosity (interparticle framework pores, yellow arrow), but pores are small ($\sim 10\text{--}20$ nm) and not abundant, and thus permeability is low. Larger open spaces between phyllosilicate matrix and mineral grains are not pores but rather artifacts of sample preparation (beam heating causes shrinkage of phyllosilicate matrix).

we encountered repeated contrasts between soft mélangé matrix and hard blocks in this area, suggesting a chaotic subsurface block-in-matrix fabric with extremely low hydraulic conductivity (likely on the order of 10^{-10} cm/s, based on the lack of drainage between wells over the summer). In a sandstone block on the same ridgeline (Well 503; Figure 3.6), groundwater behaves in a manner more similar to the Coastal Belt, staying >5 m below the ground surface throughout the wet season and slowly receding throughout the summer (Figure 3.8).

Subsurface structure and catchment-wide seasonal dynamic water storage.—Similar to storage in the Elder Creek watershed, Dry Creek storage responds to early rainfall events and exhibits rapid dynamic storage increases as the first rains of the wet season infiltrate into the subsurface (Figure 3.10). However, after 250 mm of rain, storage (S) continues to increase at Elder Creek, whereas subsequent rain at Dry Creek produces only minor, transient increases in storage. Rain inputs rapidly trigger runoff in Dry Creek. As a result, the precipitation (ΣP) and runoff (ΣQ) curves are coupled (i.e., parallel). The total magnitude of maximum dynamic water storage at Dry Creek is approximately four times lower than Elder Creek, consistent with the differences inferred from the hillslope-scale groundwater and rock moisture storage dynamics. At its peak, the dynamic water storage at Dry Creek primarily occurs as groundwater (the entire subsurface is saturated). The seasonally dynamic storage becomes negative at Dry Creek in March, which is due to ΣPET overestimating actual

evapotranspiration as the site becomes water limited.

Cross-site comparison of forest density and productivity

The >200-km-long ecotone that separates mixed broadleaf-needleleaf evergreen forests (in the west) from oak savanna-woodland (in the east) in the Northern California Coast Ranges (Figure 3.1) generally coincides with the mapped geologic contact separating the Coastal (in the west) and Central (in the east) Belts of the Franciscan (geologic mapping by Jayko et al., 1989; Figure 3.2). This is consistent with our geologic surveys of the area, independent airborne magnetic surveys [Langenheim et al., 2013], and topography, which indicates a change from the steep-sloped Coastal Belt to gently sloped Central Belt. Across the Elder Creek watershed in the Coastal Belt, the tree canopy cover is 89, $93 \pm 12\%$ (mean, median ± 1 s.d.), compared to 21, $11 \pm 19\%$ in the Dry Creek watershed in the Central Belt. The average remotely sensed and modeled annual net primary productivity between 1986 and 2017 is about twice as high in the Coastal belt forests in the Elder Creek watershed (1.2 ± 0.064 kg C/m²; mean ± 1 s.d.) than in the Central Belt mélange savanna-woodland in the Dry Creek watershed (0.6 ± 0.037 kg C/m²).

The larger variance in the Central Belt is attributable to the mosaic of pure grassland and oak woodland, as well as distinct ‘islands’ of mixed broadleaf-needleleaf evergreen forest that abruptly rise from ‘seas’ of grassland and oak savanna. Our local reconnaissance geologic mapping has revealed that these evergreen forest communities occupy large (up to kilometers) blocks of sandstone within the Central Belt. Figure 3.14 shows one such island plant community assemblage near the mouth of Dry Creek, which has developed on a monolithologic block of lithic-rich sandstone (greywacke), a block type that is common throughout the Central Belt, according to Ernst and McLaughlin [2012], and also a significant constituent of the Coastal Belt. The intrinsic heterogeneity of the Central Belt mélange results in blocks of varying lithology and size being scattered across the landscape. These blocks, when composed of sandstone that is similar to the Coastal belt, are potentially capable of storing 100s of mm of seasonal plant-available water. It is difficult to determine the minimum size of these blocks necessary to support forests like those in the Coastal Belt, due in part to the difficulty in constraining the thickness and areal extent of the blocks and factors like seed dispersal limitation to isolated blocks. However, we have identified within the mélange (via on-the-ground mapping) dense Douglas fir and madrone stands inhabiting monolithologic greywacke blocks just ~ 100 m across (these blocks are visible as dense forested stands in the air-photo imagery of Figure 3.6 and Figure 3.15). More focused mapping (ideally supported by more groundwater monitoring wells) may reveal smaller block sizes than this that support Coastal Belt-like forests in the Central Belt.

Alternative possible drivers of vegetation patterns

Disturbance, in the form of anthropogenic landscape modification and fire, does not appear to control the distribution of the plant communities. Long-standing fence lines do not coincide



Figure 3.14: Perspective view near the mouth of Dry Creek at the Central Belt site. Red line denotes contact between sandstone block (covered with mixed broadleaf-needleleaf evergreen forest) and *mélange* matrix (with primarily annual herbaceous ground cover) from reconnaissance geologic mapping. Scale varies in this west-looking view; sandstone block is ~ 750 m across in W-E direction. Google Earth imagery date 30 May 2014, eye-altitude 1.5 km, $1.5\times$ vertical exaggeration.

with ecotones at our Central Belt site, indicating that preferential grazing does not give rise to the forest and grassland transitions. Native Americans practiced a fire management regime that included high-frequency, low-intensity burning to enhance acorn production, improve hunting grounds, and promote desired cultivars for millennia in the area [Johnson, 1979; Lightfoot and Parrish, 2009; Mensing, 2006]. However, the response of vegetation on each side of the geologic contact to disturbances like logging and fire indicates that the distribution of plants does not primarily reflect successional stages. Landsat surveillance shows repeated and widespread clearcutting across Mendocino County, CA, within the Coastal Belt forests around the Angelo Coast Range Reserve over the past three decades. The movie S1 available online accompanying Hahm et al. [2019b] shows that after a parcel is cut, forest canopy begins to return within years and does not revert to grassland. The 12,536-acre 2014 Lodge Lightning Complex fire that burned just north of Elder Creek (Coastal Belt) is also visible in the last frame of the Landsat video, and our on-the-ground post-fire recovery observations do not indicate a transition from forest to grassland. The extent of the herbaceous ground cover of the Central Belt has remained essentially static throughout the duration of the Landsat program, and historical air imagery dating from 1941 (Figure 3.15) also shows that ecosystem boundaries have remained largely unchanged, in spite of selective logging and a large fire that occurred at Sagehorn (in the Central Belt) in 1950 (the aftermath of which can be seen in the 1952 air photo in Figure 3.15b). The air imagery indicates that although forest abundance was higher across the Central Belt site prior to logging and fire, the spatial arrangement of forests do not appear to have shifted (cf. Figures 3.15a and 3.15c).

The bulk elemental chemistry of fresh rock samples from the two sites is broadly similar and consistent with typical compositions of fine-grained siliciclastic rock (Table 3.4). The Central Belt *mélange* tends to have higher Mg compared to the Coastal Belt, in agreement with the difference between the average compositions of shale and metamorphosed shale (Gromet et al., 1984; Table 3.4). Neither site has exceedingly high concentrations of elements associated with ultramafic toxicity [Kruckeberg, 2004], although the *mélange* does have higher Ni concentrations (~ 200 ppm) than the Coastal Belt (~ 60 ppm). Both sites have relatively abundant concentrations of the plant-limiting rock-derived nutrient phosphorus (>0.2 weight % P_2O_5 ; compare with concentrations of <0.05 weight % inferred to be limiting in Hahm et al., 2014). We therefore rule out the possibility that the sharp ecotones arise from historical land use, fire disturbance, or parent material geochemical composition.

After lithology, the second strongest apparent control on plant community distribution is hillslope aspect. At both sites, tree canopy cover is denser on north-facing (poleward) slopes. Within the Dry Creek watershed in the Central Belt, northfacing (315° to 45° azimuth) tree canopy cover is $25.9 \pm 20.5\%$ (mean ± 1 s.d.) and south facing (135° to 225°) is $12.6 \pm 13.0\%$. Within the Elder Creek watershed in the Coastal Belt north-facing canopy cover is $92.9 \pm 5.9\%$ and south-facing canopy cover is $81.3 \pm 19.4\%$. Poleward facing slopes are typically associated with lower solar radiation and evaporative demand, which lead to higher water availability. This could suggest that the higher tree canopy cover on north-facing slopes at both sites indicates that vegetation is more water limited than energy limited. However, fires were common at both sites [Hahm et al., 2018; Johnson, 1979], and drier vegetation on south-

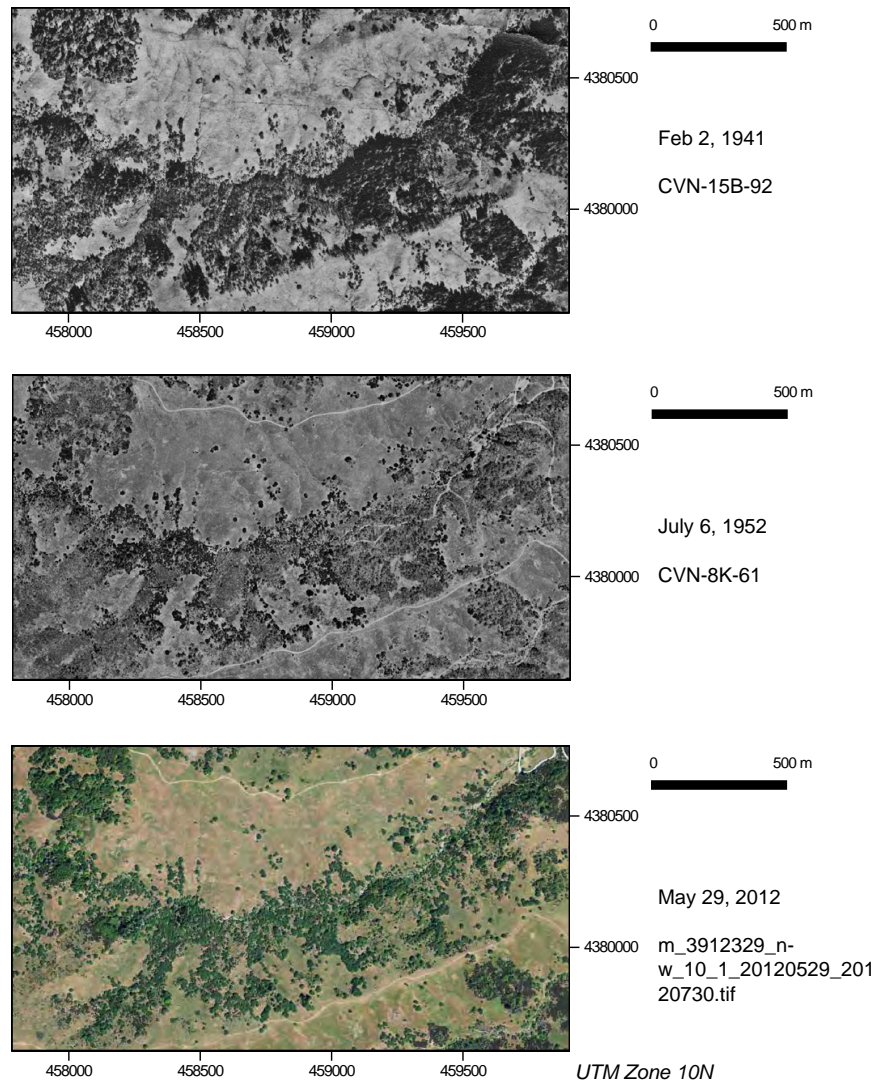


Figure 3.15: Time series of air photos of the Central Belt mélange site (groundwater monitoring wells are distributed along WSW–ENE running road in SE portion of photo; Dry Creek runs approximately NE from ‘459500’ to ‘4380000’ m UTM grid zone marks). The boundary between forest and grassland has remained essentially fixed in space for more than seven decades. The 1952 image shows the large reduction in woody canopy cover in aftermath of selective logging of *P. menziesii* and a large fire. Forested areas have regrown in the same locations, which coincide with the location of large sandstone blocks or north-facing hillslopes. The photo name is provided below the date each photo was taken; 1941 and 1952 photos provided by the Map and Imagery Laboratory at UC Santa Barbara; 2012 image from the USDA National Agriculture Imagery Program.

Table 3.4: Fresh rock bulk geochemistry

	Coastal Belt ($n = 12$)		Central Belt ($n = 4$)		North American shale composite ^a	Metamorphosed shale composite ^a
	mean	s.d.	mean	s.d.	mean	mean
SiO ₂	62.69	2.78	62.75	1.81	64.82	60.48
TiO ₂	0.84	0.07	0.78	0.11	0.80	0.91
Al ₂ O ₃	18.89	1.31	15.48	1.18	17.05	16.58
FeO	7.24	0.83	6.95	0.29	5.70	8.10
MnO	0.12	0.03	0.12	0.01	0.25	0.13
MgO	3.00	0.29	6.85	1.56	2.83	6.35
CaO	2.19	0.69	2.46	0.72	3.51	2.31
Na ₂ O	2.41	0.60	2.38	0.84	1.13	1.80
K ₂ O	2.40	0.44	2.03	0.24	3.97	3.17
P ₂ O ₅	0.22	0.03	0.21	0.03	0.15	0.17

Notes: Weight percent, normalized to 100%. ^aGromet et al. [1984].

facing slopes may have burned more readily, also potentially explaining the aspect-related canopy cover differences.

Plant ecosystem function in relation to energy and water availability.—Composite annual time series of the EVI highlight contrasting phenological patterns in the Central and Coastal Belts in response to similar climatic forcing (Figure 3.16). Radiation is approximately 5 times higher in the summer than the winter, due to the effects of longer days, higher solar angle of incidence, and lower cloud cover. In the Central Belt *mélange*, peak EVI occurs in early May, approximately 45 days before the summer solstice and peak incoming solar radiation. This typically coincides with the last significant wet season precipitation event. The subsequent summer decline in EVI is consistent with senescence of annual grasses and dormancy in perennial grasses, both of which also respond rapidly to the first winter rains in early October. The interannual variation in EVI (1 s.d. vertical bars in Figure 3.16) in the Central Belt is highest in the spring and fall, indicating sensitivity to high interannual variation in late and early wet season precipitation (Figure 3.16a). In contrast, at the Coastal Belt site, EVI peaks with the summer solstice and closely tracks incoming solar radiation throughout the year, reaching a minimum during the winter solstice (Figure 3.16). Unlike the Central Belt, the interannual variation is relatively constant throughout the year in the Coastal Belt.

The sustained evergreen transpiration within the Elder Creek watershed (Coastal Belt) results in an evaporative fraction (ET/P) that is consistently larger than the Dry Creek watershed (Central Belt) for similar values of aridity (PET/P ; Figure 3.17a). The corresponding distributions of water year total P , ET , and PET (Figure 3.17b) across multiple years (2002–2015) reveal that despite high annual variations in P , ET is relatively constant from year to year at both sites, in general agreement with the similar annual phenological patterns in Figure 3.16.

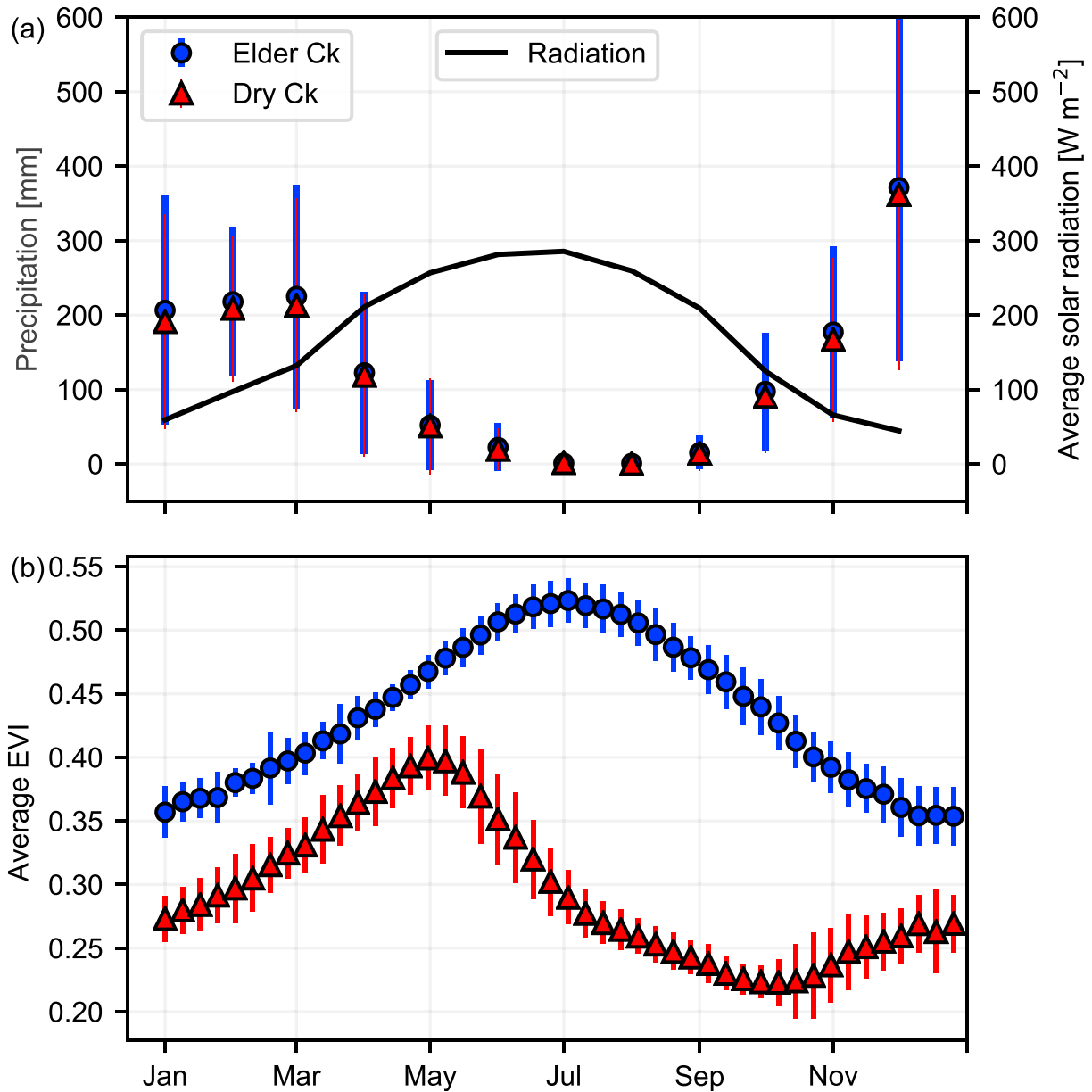


Figure 3.16: Composite annual time series of (a) energy (radiation measured at Angelo in the Coastal Belt) and water delivery reveal that in spite of similar climate, distinct subsurface CZ water storage capacity, and plant water availability result in distinct annual phenological trends, as shown via the enhanced vegetation index (EVI; b) from MODIS within the Elder Creek (Coastal Belt) and Dry Creek (Central Belt) watersheds. Vertical bars = 1 standard deviation.

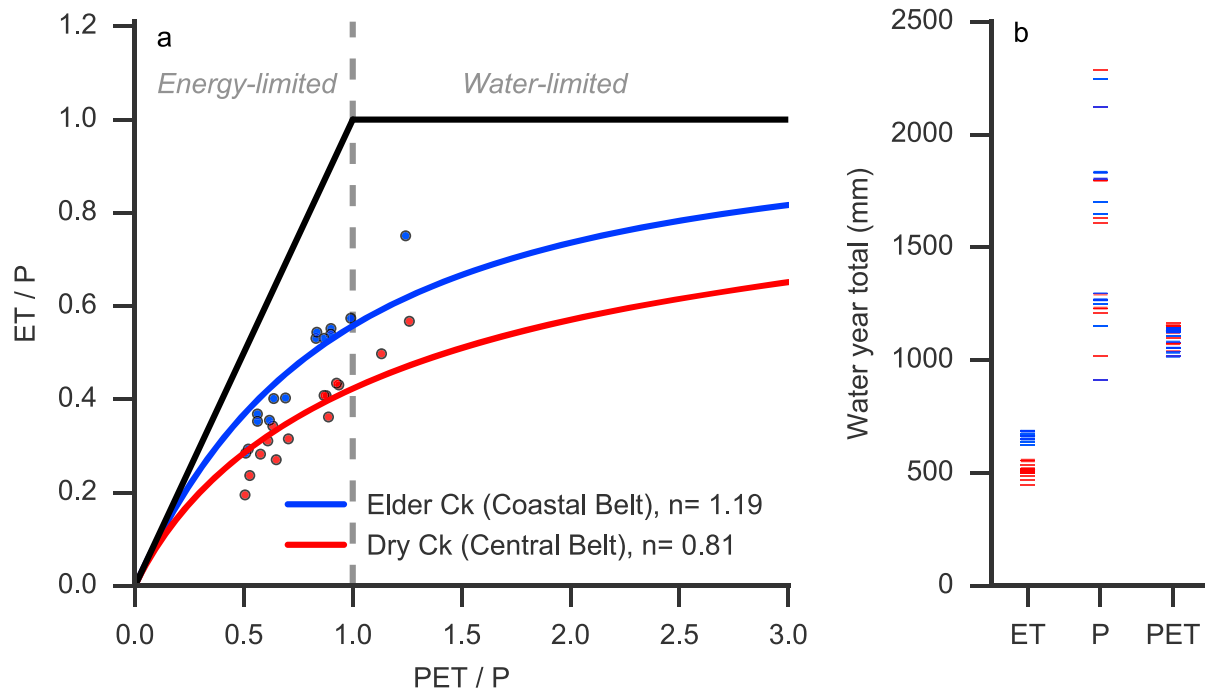


Figure 3.17: Energy and water balances of each site depicted within the traditional Budyko framework indicate that the Elder Creek catchment partitions more incoming precipitation into evapotranspiration (ET ; remotely sensed, and including interception losses; see Ryu et al., 2011) than Dry Creek, in spite of similar P and potential evapotranspiration (PET) between the sites. Each point (a) and horizontal line (b) represent a single water year, from 2002–2015. Lines fit (and reported parameter n) according to equation described in Yang et al. [2008].

End-of-summer subsurface water availability.—Predawn water potential in Douglas fir, live oak, madrone, and tan oak in upslope positions in the Coastal Belt in mid-September, 2017, was -1.60 ± 0.08 MPa; $n = 22$ (mean \pm s.e.m.; $n =$ number of trees), nearly 1 MPa higher than the Oregon white oak in the Central Belt (2.46 ± 0.31 MPa; $n = 6$; data for each individual tree are provided in the accompanying data set). This indicates that root zone water availability is much lower in the Central Belt than in the Coastal Belt. Hence, in spite of the much higher canopy density in the Coastal Belt than the Central Belt—and associated high transpiration demand—water potentials are higher in the Coastal Belt than the Central Belt, consistent with a higher amount of subsurface plant available water in the Coastal Belt.

3.6 Discussion

We found that two compositionally similar lithologies produce radically different subsurface critical zone thickness, water storage capacity, and, consequently, plant-available summer water availability. Here we discuss how these differences control plant assemblages and the partitioning of water between *ET* and runoff. We also explore possible mechanisms leading to thin versus thick subsurface critical zones in the two rock types.

Lithologic controls on plant communities: why a savanna occurs where it rains nearly 2 m per year

Climate monitoring indicates that the two sites receive similar rainfall, yet the Coastal belt supports an evergreen forest that is twice as productive as the annual grassland savanna found in the Central Belt. Climatic conditions are expected to favor temperate forests (Figure 3.4). Due to the deeper critical zone, hillslopes in the Coastal Belt store much more precipitation as plant-available rock moisture than the Central Belt (Figure 3.10), resulting in greater summer water availability and higher predawn water potential. At both sites, augering and drilling observations of roots, as well as repeat neutron probe measurements [Hahm et al., 2017c; Rempe and Dietrich, 2018], indicate that plants use soil and rock moisture. Sap flow rates in Oregon white oak in the Central Belt remain high throughout the summer dry season, declining to only 70–90% of their maximum with shorter day lengths in the autumn [Hahm et al., 2018]. In the Coastal Belt, madrone—and to a lesser degree live oak—similarly transpire at high rates in September, whereas Douglas fir exhibits greater decline during the summer [Link et al., 2014]. The continued transpiration results in progressive depletion of subsurface moisture storage and associated declines in water potential throughout the summer. The distinct predawn water potentials between the sites presumably reflect differences in both subsurface plant-available water as well as the ability of each plant community to draw down that water: The oaks that inhabit the *mélange* are able to pull harder, explaining their ability to persist in the water-limited subsurface critical zone of the Central Belt.

The low storage capacity at the Central Belt arises due to the relatively shallow depth of weathering, indicated by perennially saturated, fresh *mélange* matrix just a few meters from the ground surface. The shallow weathering in the Central Belt *mélange* results in a critical zone that quickly saturates and sheds most winter rainfall, and then becomes very dry in the summer, supporting only annual grasses that die in shortly after the wet season and scattered oaks that can continue to draw down moisture at extremely low water potentials.

A second factor that likely limits the establishment of forests at Sagehorn is the complete saturation of the Central Belt's thin subsurface CZ with each major winter storm event (Figure 3.9). This results in an upland landscape that is effectively flooded for almost half of the year (Figure 3.9). Saturation promotes an anoxic rhizosphere, due to the consumption of oxygen in respiration and the much lower diffusion coefficient of oxygen in liquid water relative to air [Armstrong, 1980], as observed in the winter groundwater of Well 507 at

Sagehorn in the Central Belt (Figure 3.12). *P. menziesii* seedlings (the widespread conifer within Elder Creek in the Coastal Belt) respond negatively to even short periods (1 day) of saturation [Minore, 1968; Zaerr, 1983]. This indicates that a recruitment bottleneck for *P. menziesii* due to wet season saturation likely exists in the Central Belt mélange in addition to low dry season water availability. The lack of conifers on poorly drained sheared mudstone with clay-rich argillic horizons in the Franciscan complex was noted by Popenoe et al. [1992], who also suggested that poor drainage would inhibit *P. menziesii* establishment.

Our observations suggest that vegetation inhabiting the Central Belt mélange must overcome the challenge of a CZ that is both very dry (in summer) and very wet (in winter). Species inhabiting this landscape need to be water limitation tolerant and flood tolerant or winter dormant. The annual grass life history strategy is adapted to these conditions; our observations also indicate that remaining native perennial bunchgrasses return year after year in spite of winter water logging [Biswell, 1956; Burcham, 1957; Danielsen and Halvorson, 1991; Davy, 1902; Frenkel, 1977; Gordon et al., 1989; Gordon and Rice, 1993; Hibbs and Yoder, 1993]. The dominant tree species inhabiting the mélange matrix, *Q. garryana*, is also well suited to these conditions. It is winter deciduous, with a leaf-off period that closely matches the sustained wet-season subsurface saturation [Hahm et al., 2018] and is known to inhabit riparian areas elsewhere prone to saturation [Stein, 1990]. *Q. garryana* is also extremely water limitation tolerant, capable of sustaining high rates of sap flow throughout the summer even as predawn water potentials drop to -3 MPa in some individuals [Hahm et al., 2018]. Sap flow is sustained via a low turgor loss point that dynamically adjusts to keep stomata open and investment in an embolism-resistant xylem network [Hahm et al., 2018]. These ecophysiological adaptations help to explain the abundance of *Q. garryana* within the mélange.

How long have the distinct plant communities across the lithologic persisted? Although there are many challenges in assessing Californias pre-historical vegetation patterns, particularly the distribution of grasslands and savannas [see, e.g., discussion in Frenkel, 1977; Biswell, 1956], Burcham's [1957] survey of early explorers' accounts indicates that savannas were widespread and interspersed with forest throughout Northwestern California, including areas now mapped as part of the Central Belt mélange. These early accounts also indicate that within the grasslands, there was a generally higher relative abundance of native perennial bunchgrasses [Burcham, 1957; Davy, 1902]. More recently (in the past two centuries), an added component of competition in the form of invasive annual grasses has played an important role in oak ecosystems, negatively affecting the recruitment of the endemic California oaks *Q. douglasii* and *Q. lobata*, which are closely related to the *Q. garryana* found at Sagehorn and across the Central Belt [Danielsen and Halvorson, 1991; Gordon et al., 1989; Gordon and Rice, 1993]. This occurs due to the tendency of the annual grasses to rapidly extract water in the shallow upper soil, hindering oak seedling growth (mature oaks fare better with annual grasses by extracting water from deeper within the CZ; for example, mature *Q. garryana* can have much higher pre-dawn water potential than collocated juveniles [Hibbs and Yoder, 1993]). The resulting increased water stress on seedlings is exacerbated on south-facing slopes, where there is a higher atmospheric moisture demand

due to increased radiative forcing. These effects may contribute to the relative dominance of grasses on south-facing slopes at Sagehorn and the confinement of contiguous oak woodlands to primarily north-facing slopes (e.g., Figure 3.14). This would also be consistent with the much higher recruitment densities of juvenile *Q. garryana* on north-facing slopes at Sagehorn [Hahm et al., 2017b].

An ecohydrologic framework for vegetation mosaics in seasonally dry environments

The patchy, heterogeneous distribution of ecosystems within areas of similar climate in both seasonally dry California and other Mediterranean climates globally has previously been interpreted to arise due to aspect, nutrient availability [e.g., Hahm et al., 2014], the presence of serpentine [e.g., Kruckeberg, 1985], or pyrodiversity [e.g., Bird et al., 2008; Martin and Sapis, 1991; Trauernicht et al., 2015]. Pyrodiversity is defined as “landscape heterogeneity and diverse biota that result from various stages of plant succession as those plants recolonize burned areas” [Lightfoot and Parrish, 2009]. Instead of reflecting topographic controls on energy supply, parent material toxins or nutrients, or fire-driven successional stages, we suggest that the diversity in ecosystem function and composition within an area of similar climate can also arise due to CZ-structure-mediated water storage capacity.

In a similar vein to our findings, previous studies have argued that lithologically controlled bedrock permeability can be responsible for differences in seasonal water storage [e.g., Pfister et al., 2017]. Ecohydrologic theory also suggests that differences in integrated porosity throughout the subsurface should translate into distinct plant-available water regimes [e.g., Laio et al., 2001; Porporato et al., 2001]. In line with this idea, Fellows and Goulden [2016] suggested that low summer plant water use in the high Sierra in glaciated areas may be due to limited subsurface water storage capacity. Studies have also highlighted the importance of soil water storage capacity in affecting water availability and partitioning [e.g., Heilman et al., 2014; Smith et al., 2011], yet there is increasing recognition of the ecohydrological importance and variability of the weathered bedrock below soils: Soils, in contrast to weathered bedrock, vary in thickness over a much smaller range and are commonly thin (<0.5 m) across upland landscapes [Amundson et al., 2015; Schwinning, 2010]. The difference in soil thickness—and presumably also the associated soil moisture—between our two sites is minor and not evidently responsible for the large differences in plant water availability. Instead, it is the great difference in the extent and depth of weathering in the underlying bedrock that results in the distinct plant communities.

Quantifying catchment-scale water storage—which we have found useful to scale between the unit hillslope to larger spatial scales—is an active research area in hydrology [McDonnell et al., 2018; McNamara et al., 2011; Tetzlaff et al., 2011]. However, we are unaware of studies that have paired these larger-scale catchment storage analyses with detailed subsurface investigation via boreholes to explain plant water availability and distribution. Our study exploits a unit hillslope approach, wherein detailed documentation of critical zone

hydrologic functions controlled by the degree and depth of bedrock weathering is used to explain regionally extensive (>100 km) contrasts in plant community distributions that covary with lithology. There are limits to the unit hillslope approach, to the extent that the site chosen for intensive study may not be an ideal representation of the larger landscape. However, given the current lack of methodologies to document the extent of the weathered zone and intra-hillslope hydrologic processes at large spatial scales, we suggest that study of a topographically and lithologically representative unit hillslope provides a useful proxy for understanding larger areas.

Figure 3.18 conceptually summarizes our interpretation that low dynamic water storage capacity arising from thin subsurface critical zones limits the supply of water to plants in the summer dry season. Rainfall is the same across the transect and is sufficient to support the mixed broadleaf-needleleaf evergreen forest found in the Coastal Belt. Where all else is hypothetically equal, a thin CZ with low storage becomes dominated by species that are winter saturation tolerant and more summer water limitation tolerant (at left in Figure 3.18). This would tend to manifest in lower leaf area, lower summer transpiration, and in general, a lower-productivity plant community. Although our two sites are presented here as general cases of relatively low and high storage capacity—associated with the Central Belt and Coastal Belt, and relatively low and high productivity ecosystems, respectively—the confluence of biota, climate, tectonics, and lithology that influence subsurface CZ structure presumably results in a spectrum of subsurface water storage capacity. Thus, as hypothesized in Figure 3.18, a subsurface water storage capacity control on ecosystem function may not only be important in creating vegetation mosaics in the Northern California Coast Ranges but in other water-limited seasonally dry environments as well. As the climate warms and habitable plant zones for particular species shift [e.g., Anderson and Ferree, 2010; Kelly and Goulden, 2008], rock type—through its impact on water storage capacity—will likely interact with the effects of climate change in setting future habitat compatibility in these regions.

Lithologic controls on the partitioning between evapotranspiration and runoff

When integrated over an annual cycle, water budgets for most years between 2002 and 2015 plot within the energy-limited side of the Budyko space (Figure 3.17a). This arises due to the temporal lag between water delivery and water demand in the Mediterranean climate of the study area [e.g., Milly, 1994]. This contrasts with the observation that the catchments are more water limited than energy limited in the summer: May–September *PET*, a metric of atmospheric moisture demand (based on the Hargreaves method) is on average 725 mm at Dry Creek (Central Belt) and 704 mm at Elder Creek (Coastal Belt), exceeding the maximum observed dynamic water storage volumes that could be returned to the atmosphere. This indicates that energy- versus water-limited descriptions for catchments determined from annual water budget analyses may not be useful descriptors of ecosystem water availability at subannual (i.e., seasonal) timescales in strongly seasonal climates, like

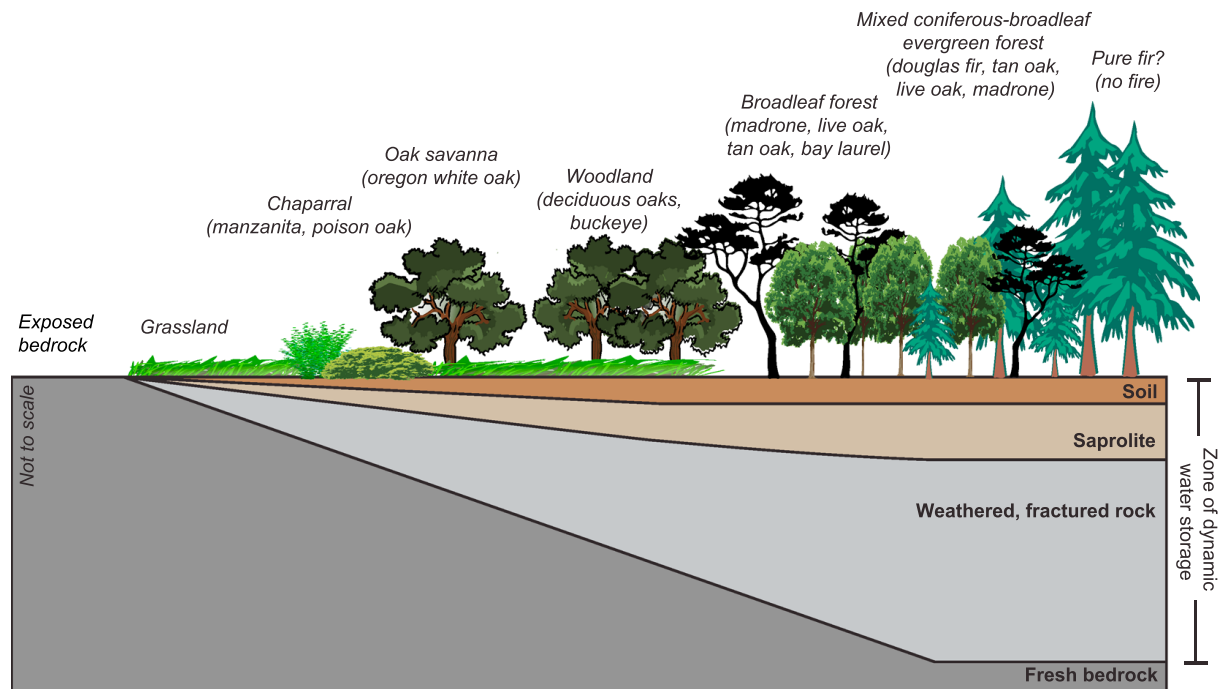


Figure 3.18: Conceptual cross section illustrating the hypothetical role of critical zone structure in governing water storage and ecosystem composition in the seasonally dry, Northern California Coast Ranges. Topographic position, rainfall, and evaporative demand are assumed constant: only the thickness and corresponding water storage capacity changes from left to right. Although shown as a horizontal surface, this analysis applies to well-drained hillslopes underlain by bedrock, not valley flats where thick colluvium or alluvium may accumulate and seasonal drainage may be poor. Plant variation at far right illustrates possible role of fire exclusion in promoting pure stands of Douglas fir [e.g., Schriver et al., 2018].

our Mediterranean study sites.

Variations in the vertical location of the Budyko line—or the amount of water that is returned to the atmosphere for a given dryness index—have been theorized to arise due to differences in subsurface moisture storage [e.g., Milly, 1994; Milly and Dunne, 1994; Porporato et al., 2004; Yang et al., 2008; Rouholahnejad Freund and Kirchner, 2017], but to our knowledge no empirical, comparative study in a seasonally dry climate has probed the entire depth of the critical zone with deep boreholes to show how lithologically controlled differences in bedrock weathering explicitly govern this water partitioning. Our catchment-wide analyses indicate that smaller dynamic storage volumes at Dry Creek (Central Belt) relative to Elder Creek (Coastal Belt) are likely the cause for lower values of ET/P at Dry Creek for the same value of PET/P (Figure 3.17a). This difference arises due to rock-type governed limitations on CZ water storage capacity.

The idea that subsurface CZ structure can limit dynamic water storage also has implications for the ET response to interannual variations in P . Excess P beyond that required to replenish the dynamic subsurface storage capacity runs off in the winter (as similarly found in and near the Eel River basin by Syvitski and Morehead, 1999, and Sayama et al., 2011, and suggested by Smith et al., 2011, in Idaho [in soils] and Fellows and Goulden, 2016, in the Sierra Nevada). Because it runs off, this excess P does not generate extra plant-available water storage for the following summer, as explored by Hahm et al. [2019a]. The result is that high year-to-year variations in P at both sites do not result in highly variable ET due to the storage-limited nature of the two study catchments (Figure 3.17b).

Development of the subsurface critical zone structure

Recent theories have identified the importance of tectonics, lithology, and climate in governing the development of the subsurface CZ [Anderson et al., 2013; Lebedeva and Brantley, 2013; Rempe and Dietrich, 2014; Riebe et al., 2017; St. Clair et al., 2015]. The thickness of the subsurface CZ is determined by the difference between the ground surface topography and the elevation of the transition from weathered to fresh bedrock. The slope of the fresh bedrock boundary that we observe at our Central Belt *mélange* site between the ridgetop wells and Dry Creek (Figure 3.6) is essentially the same as the slope of the topographic surface, and fresh bedrock outcrops in the channel (i.e., the subsurface CZ is thin relative to the hillslope lengthscale), whereas in the Coastal Belt, fresh bedrock also outcrops in the channel, but the fresh bedrock surface slope is considerably less than the average topographic slope, resulting in a thick CZ at the topographic divide. Motivated in part by observations in the Coastal Belt, Rempe and Dietrich [2014] propose that the slope of the fresh bedrock surface may represent the extent to which fresh bedrock can be drained of the chemically equilibrated, nearly stagnant fluid that resides within it as it is uplifted. They propose that channel incision couples the evolution of surface topography with the evolution of the subsurface weathering profile by setting the pace of hillslope erosion and by mediating the slow drainage of fresh bedrock. In their model, the slope of the fresh bedrock surface depends, in part, on the saturated hydraulic conductivity of the fresh bedrock. Other bedrock weathering models point to the intrinsic differences in porosity of different rock types: Bazilevskaya et al. [2013], for example, interpreted an approximately tenfold deeper weathering front in granite compared to diabase to arise from significant fracturing and interconnected porosity in the granite, enabling the advection of oxygen to fresh mineral surfaces.

At Sagehorn (in the Central Belt), the hummocky topography indicates that earthflows were active in the past and extended from the ridge to the major channels (Dry and Hank). This ridge-to-channel slope creates a sustained head gradient in the underlying saturated fresh *mélange* but appears to have caused insignificant drainage in this dense, likely very low saturated conductivity material: The depth to fresh saturated bedrock at the divide is only a few meters. Frequent saturation overland flow results in localized surface erosion and the development of small valley networks that have cut into the stagnant earthflow features, creating a dense channel system bordered by convex hillslopes with a local relief of about 20

m (Figures 3.3 and 3.19). Even these local ridges generate saturation overland flow in the winter, consistent with a shallow depth to fresh, low conductivity *mélange*, even in locally steeper areas.

We suggest that the *mélange* may represent an extreme end-member of low saturated conductivity, such that topographically driven head gradients are ineffective in causing drainage. Instead, given the shallow depths to fresh bedrock, water extraction—and thus weathering due to the introduction of oxygen and replacement of meteoric reactive water—may be driven only by transpiration and evaporation. In effect, the ‘bottom up’ control is so strong—preventing deep lateral drainage—that the weathering front can only advance from these surface-driven processes. If so, the weathering front is strongly tied to the vegetation. The ~ 3 -m depth to fresh bedrock in predominantly grassland areas may therefore reflect water extraction from previously widespread native perennial grasses, which have deeper roots than the present invasive annual grassland community [Dyer and Rice, 1999; Holmes and Rice, 1996].

Once drained, the Coastal Belt and Central Belt weather very differently. The shales of the Coastal Belt rapidly undergo slaking upon experiencing wetting and drying cycles, with rock disaggregating into millimeter- to centimeter-scale fragments once at the surface. This process is readily observable in previously saturated stream cobbles (Figure 3.20) as well as freshly incised bedrock channels and may, along with pyrite oxidation and mineral dissolution, create a network of fractures in the weathered rock zone that conveys water and holds a significant portion of the seasonally dynamic water storage. In contrast, augering observations and exposed stream cuts in the Central Belt suggest that weathered *mélange* matrix can deform in a manner that may tend to seal fractures, inhibiting the movement of water.

Together, these observations suggest that the distinct mineralogy and/or tectonic history between the Belts of the Franciscan result in different subsurface CZ structure in spite of similar bulk elemental composition, climate, and uplift history. The large differences in CZ structure have important ecohydrological consequences as they directly affect hillslope runoff pathways and seasonal water storage, and ultimately the composition and productivity of the ecosystems covering the landscape.

3.7 Conclusions

Adjacent plant communities and runoff patterns in the Northern California Coast Ranges vary strongly within a region of similar precipitation and temperature due to differences in the weathering of the underlying bedrock. Mixed broadleaf-needleleaf evergreen forests primarily inhabit the deeply weathered argillite and sandstones of the Coastal Belt, whereas a deciduous oak savanna-woodland with annual herbaceous ground cover inhabits the thinly weathered Central Belt *mélange*. Here we present direct evidence for lithologically controlled differences in bedrock weathering and water storage that explain these surface plant communities at regional (>100 -km) scales. At our two field sites, we employ a unit hillslope

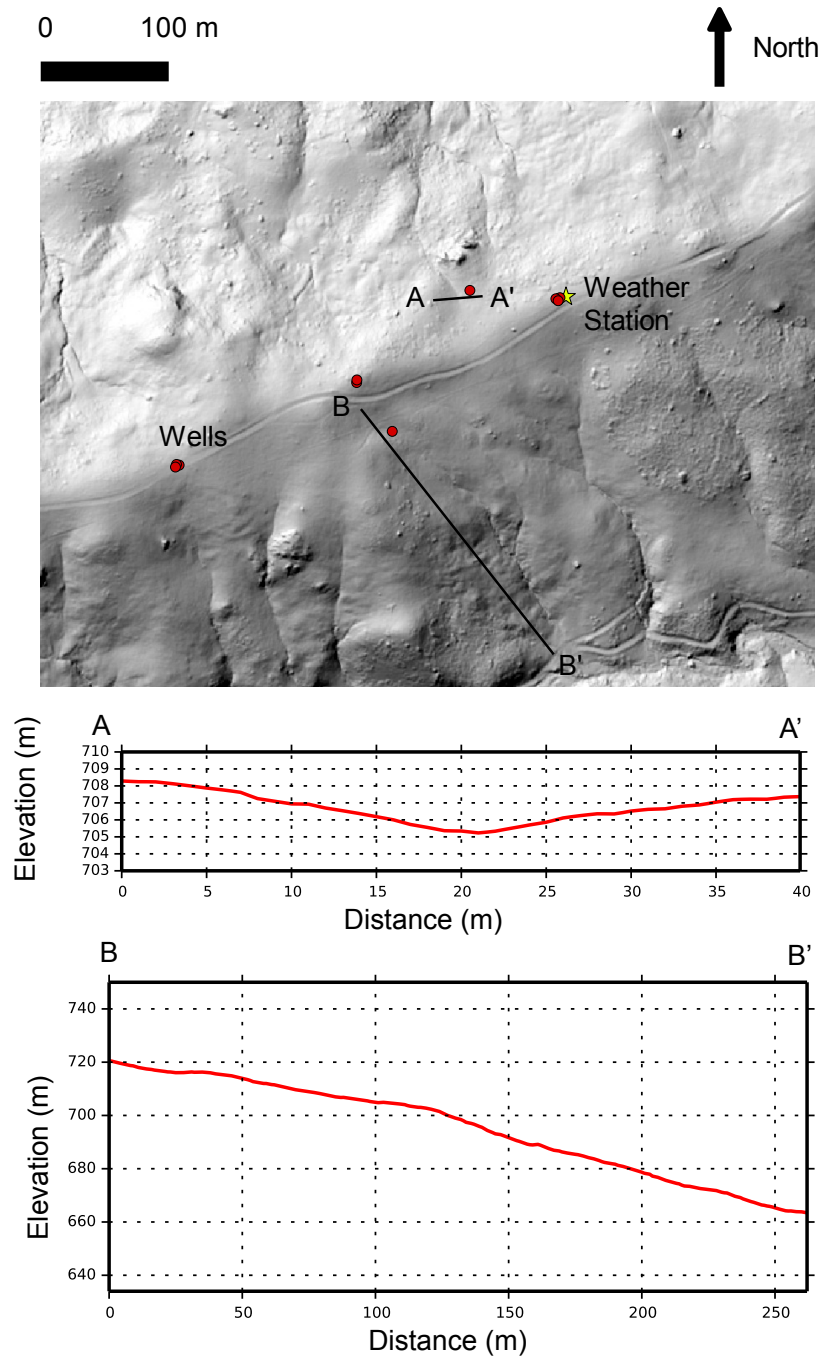


Figure 3.19: Lidar-derived shaded relief map of the Central Belt mélangé Sagehorn study site, in which the incised channel network has resulted in the development of both convex-up hillslopes (seen in the vertical elevation profile A–A') and gently undulating earthflow topography (B–B'). Also visible are prominent blocks within the mélangé matrix that disrupt the otherwise smooth, soil-mantled topography.



Figure 3.20: Photo of disaggregating shale cobble (approximately 20 cm across) resting on sandstone and conglomerate boulders in active stream bed, illustrating effect of wetting and drying cycles on the bedrock of the Coastal Belt. Photo courtesy Mary E. Power.

approach in which we intensively monitored ecohydrologic processes on a hillslope within each rock type to explain ecological, runoff, and water budget differences observed at the catchment and regional scale. We find that subsurface dynamic water storage capacity scales with the depth of weathering. The Coastal Belt has a deep weathered zone—up to 30 m at ridgetops—and stores approximately 4 times more water seasonally than the Central Belt mélange, where fresh, unweathered parent material is found just ~ 2 to 4 m below the surface. Forests are sustained by the relatively high water content held at physiologically accessible water potentials within the hillslopes of the Coastal Belt. In the Central Belt mélange, less than 200 mm of precipitation leads to saturation of the subsurface, prompting widespread saturation overland flow and flashy stream runoff. This arises due to minimal water storage capacity and results in dry channel networks in the summer. Low water storage capacity results in low plant water availability and a community dominated by annual grasses and oaks that can extract tightly held water despite receiving $\sim 1,800$ mm of annual precipitation. A further factor likely limiting the establishment of the needleleaf tree *P. menziesii* (Douglas fir) is a seedling recruitment bottleneck due to the seasonal ground saturation. The differences in plant-available water availability between the two sites would not have been apparent from a study of the soils alone; the large differences in plant-available water storage capacity stem primarily from differences in the depth and extent of weathering in the bedrock underlying the soils.

Both sites are in areas of active uplift and channel incision, which will tend to drain the fresh bedrock and advance the weathering front. The underlying fresh Central Belt mélange bedrock, however, remains undrained (and unoxidized) even as channel incision drives hillslope evolution. This observation supports a ‘bottom-up’ theory for control on depth to fresh bedrock. In the mélange, we propose that this control is so strong that the drainage and advance of the weathering front (and corresponding development of porosity and water storage capacity) is accomplished by evaporation and transpiration withdrawal of moisture from the bedrock. In this seasonally dry Mediterranean climate, the extent to which the subsurface CZ sheds or stores precipitation during the wet season dictates dry season water availability and therefore the composition and productivity of ecosystems. Subsurface CZ water storage capacity regulation of plant water availability and community composition is likely widespread in seasonally dry climates. Deep drilling, intensive hydrologic monitoring on unit hillslopes, and catchment-wide storage analysis will help provide greater insight into the role of weathered bedrock in determining vegetation assemblages.

3.8 Acknowledgements

We thank Marilyn and Jerry Russell and the Holleman family for generous land access, as well as the University of California Angelo Coast Range Reserve. Chris Wong, Colleen Murphy, Sami Cargill, Collin Bode, Peter Steel, Wendy Baxter, Anya Mikheicheva, and Zhiyang Li helped with field and lab work. We also thank three anonymous reviewers whose feedback improved the manuscript. This project was funded by the National Sci-

ence Foundation-supported Eel River Critical Zone Observatory (NSF EAR 1331940), the University of California Natural Reserve System Mildred E. Mathias Graduate Student Research Grant, the Carol Baird Fund for Graduate Field Science, and the UC Berkeley Larsen Grant. Data from the Eel River Critical Zone Observatory used in this publication are available at <https://sensor.berkeley.edu/> (meteorological data); https://github.com/daviddralle/indirect_storage/tree/master/data (Dry Creek runoff data), the USGS (Elder Creek runoff data), and six supplementary data sets ('FreshRockBulkGeochemistry.csv,' 'Pre-DawnWaterPotentials.csv,' 'DissolvedOxygen.csv,' 'BulkMineralogy.csv,' 'GroundwaterDepthsBelowSurface(m).csv,' and 'CosmoCalc-Dry_Hank.xlsx') within the accompanying compressed folder 'Hahm et al - Datasets.zip.'

Chapter 4

Low subsurface water storage capacity relative to annual rainfall decouples Mediterranean plant productivity and water use from rainfall variability

4.1 Abstract

Plant water stress in response to rainfall variability is mediated by subsurface water storage, yet the controls on stored plant-available water remain poorly understood. Here we develop a probabilistic water balance model for Mediterranean climates that relates the amount of water stored over the wet season to annual rainfall statistics and subsurface storage capacity in soil and weathered bedrock. This model predicts that low storage capacity—relative to winter rainfall—results in similar year-to-year summer water availability, as both relatively wet and dry winters replenish storage. Observed water balances in seven catchments in the Northern California Coast Ranges exhibited this dynamic. We hypothesized that plants would be decoupled from precipitation variability at these storage-capacity-limited sites and observed that summer productivity and water use (inferred from the enhanced vegetation index) were independent of winter rainfall totals. These areas emerged largely unscathed from recent extreme drought, despite widespread plant mortality elsewhere.

This chapter is adapted from Hahm, W. J., Dralle, D. N., Rempe, D. M., Bryk, A. B., Thompson, S. E., Dawson, T. E., and Dietrich, W. E. (2019a). Low subsurface water storage capacity relative to annual rainfall decouples Mediterranean plant productivity and water use from rainfall variability. Geophysical Research Letters.

4.2 Introduction

Recent droughts have dramatically altered plant communities throughout many of the world’s arid and mesic biomes [Hartmann et al., 2018], and climate models predict further increases in the frequency of extreme precipitation events [Swain et al., 2018]. Analyses of the drivers of plant response to drought, including die-off, have largely focused on physiological and pest responses to climatic proxies for plant water stress [Adams et al., 2017; Choat et al., 2018]. However, in rain-dominated Mediterranean climates—home to many of the world’s most biodiverse and threatened plant communities [Cowling et al., 1996]—plants generally rely on subsurface water storage to sustain transpiration during the dry season [e.g., Klos et al., 2018]. Storage dynamics should therefore be central in regulating plant response to climatic variability. Water storage dynamics have been shown to impact plant greenness, with numerous satellite-based studies showing that the spectral signatures of leaves correlate with water storage in the upper few centimeter of soil measured with microwaves [e.g., A et al., 2017] or with storage in the entire hydrosphere measured from gravity [e.g., Yang et al., 2014]. A major knowledge gap remains, however, in our knowledge of both the structure of Earth’s near-surface weathering profile, which sets the plant-available water storage capacity in the critical zone (CZ; Figure 4.1)—extending from the top of the vegetation canopy through the soil and down to fresh bedrock [Grant and Dietrich, 2017; Riebe et al., 2017]—and how this structure’s interaction with rainfall dynamics determines how much water is stored for plants through wet and dry periods. Improving our understanding of the nature of deeper hillslope plant-available water storage has been identified as a pressing research frontier and will improve the accuracy of Earth system models [Fan et al., 2019].

A common but often implicit hypothesis is that ample belowground water storage capacity buffers plants from interannual variations in precipitation. Here we explore instead whether low subsurface plant-available water storage capacity—relative to precipitation—can decouple plant water supply (and, consequently, plant productivity) from precipitation anomalies, including droughts. We exploit the strong seasonality of Mediterranean climates to test this hypothesis. We propose that where subsurface storage capacity is low relative to typical winter precipitation totals, winter precipitation will be sufficient to replenish storage in wet and dry years alike, resulting in similar year-to-year summer water availability. We call this condition “storage-capacity limitation” because the amount of stored water is limited by storage capacity rather than precipitation. Winter precipitation at storage-capacity limited sites that exceeds this capacity contributes to winter runoff rather than greater storage at the start of the dry season. Established plants adapted to a summer water supply capped by the storage capacity therefore may not experience diminished water availability and increased stress in anomalously dry years. Elements of this mechanism have emerged in ecohydrologic models and field studies [Fellows and Goulden, 2016; Hahm et al., 2019b; Link et al., 2014; Milly, 1994; Porporato et al., 2004; Rempe and Dietrich, 2018; Sayama et al., 2011; Smith et al., 2011; Stephenson, 1990; Zanardo et al., 2012], yet to our knowledge the role of storage-capacity limitation in mediating plant productivity and water use sensitivity to precipitation variability at landscape scales remains unexplored.

The critical zone (CZ)

$$S = P - ET - Q$$

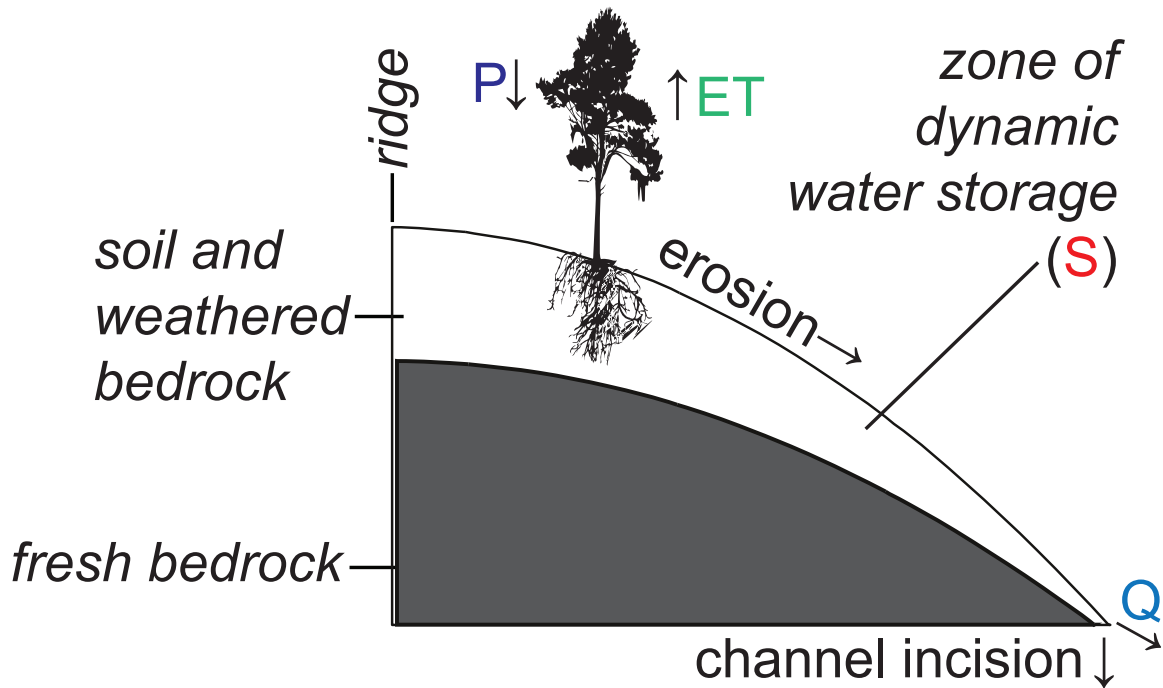


Figure 4.1: The critical zone (CZ) extends from treetops to the base of weathered bedrock. Channel incision and erosion bring fresh, low permeability bedrock into the near surface. Fresh bedrock can then be weathered to generate porosity and permeability, which mediate the partitioning of precipitation (P) into storage (S), evapotranspiration (ET) and runoff (Q).

Here we formulate a probabilistic hydrologic model for Mediterranean catchments to investigate whether dynamic storage capacity (S_{\max}) can decouple accumulated winter water storage (S) from winter precipitation (P) variability. We then use data from 26 rain-dominated catchments across California to test the hypothesis that where S is independent of P —diagnostic of storage-capacity limitation—summer plant productivity and water use, as measured by the enhanced vegetation index (EVI), are also uncorrelated with P . We apply a simple catchment water balance technique for estimating S [Dralle et al., 2018; Sayama et al., 2011], which is not limited to specifying storage capacity using mapped soil databases alone. These databases typically contain storage-capacity information only for shallow soils, while plants in Mediterranean climates are known to extract water in summer from both unsaturated and saturated weathered rock below the soil throughout the CZ (Figure 4.1)

to depths of tens of meters [Arkley, 1981; Jones and Graham, 1993; Rempe and Dietrich, 2018; Witty et al., 2003]. Both the modeling framework and empirical analysis support the notion that low storage capacity relative to winter precipitation can decouple summer plant productivity and water use from precipitation variability. Our method provides a simple approach for identifying subsurface controls on terrestrial ecosystem function. It also highlights a novel mechanism by which subsurface storage dynamics can shield plant communities from the potential ecohydrological risk associated with possible increased volatility of annual precipitation in Mediterranean climates globally.

4.3 Model development and catchment water balance methodology

Stochastic hydrological model

The hydrological model assumes that (1) a consistent minimum storage value is reached at the end of the dry season each year, that is, negligible interannual carryover of water occurs; (2) cumulative winter evapotranspiration (ET) is constant from year to year, includes interception losses, and is always less than P in the energy-limited winter; and (3) runoff (Q ; stream discharge normalized by catchment area) is generated only when dynamic storage reaches S_{\max} . The model does not distinguish between unsaturated and saturated storage. S for any given year is therefore piecewise defined:

$$S = P - ET \quad \text{if } P - ET < S_{\max}; \quad Q = 0 \quad (4.1a)$$

$$S = S_{\max} \quad \text{if } P - ET > S_{\max}; \quad Q = P - ET - S_{\max} \quad (4.1b)$$

Equation 4.1a represents a “precipitation-limited” condition, where S is limited by P . The inequality in Equation 4.1b signifies a “storage-capacity-limited” condition, in that S_{\max} limits S . Thus, summer plant water availability, to the extent that it scales with S , is limited by either precipitation (Equation 4.1a) or storage capacity (Equation 4.1b). Although this model omits some elements of the winter climate and hydrology, it provides a minimal description of the seasonal dependence of S on P and S_{\max} . Assumption (1) is reasonable to the extent that PET is typically much larger than ET across California in the summer dry season, indicating that each summer plants experience water-limited conditions. Assumptions (2) and (3) above are only present in the model; actual fluxes are tracked in the empirical catchment water balances described below, and the same variable names are used for consistency.

Small uncertainties in the water fluxes compound through the winter, distorting the running estimate of S . Error in reported Q (for example, due to rating curve or measurement uncertainty) is common, and Monte Carlo simulations (not shown) indicate that normally

distributed random errors with a mean of zero and a standard deviation equal to 5% of the observed value of Q can produce scatter in S comparable to that seen at Elder Creek (see data below). P and ET are similarly subject to random uncertainties and biases, which in some respects are only quantifiable in relation to each other. When Ryu et al. [2011] compared their MODIS-derived ET estimates to basin-annual water mass balance (precipitation – runoff), for example, they found a root mean square error of 168 mm/y across all basins. Tracking S over multiple years is therefore unfeasible and analysis is restricted to individual wet seasons. Nevertheless, at two of the storage-capacity-limited sites (Elder Creek and Dry Creek), multi-year intensive field campaigns have documented that end-of-summer hillslope water storage (inferred from repeat neutron probe surveys, groundwater dynamics, and pre-dawn water potential measurements) returns to a similar state year after year [Hahm et al., 2018; Rempe and Dietrich, 2018], implying limited interannual carryover, at least at the storage-capacity limited sites.

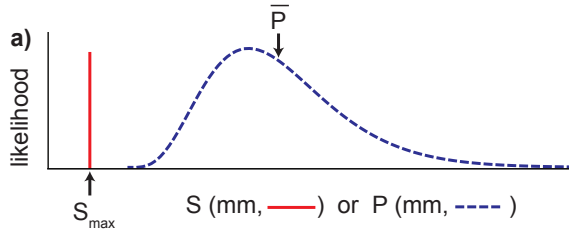
Remotely sensed vegetation indices are subject to uncertainties associated with background saturation. Our analysis of ranked correlations at individual sites, rather than comparison of absolute magnitudes between sites, however, minimizes the impact of these uncertainties. Data gaps due to, for example, cloudy periods, are also of concern, but are also minimized in this study, due to the fact that California is largely cloud-free in the summer dry season.

As input to the water-balance–storage relationships, we assume that annual P is a gamma distributed random variable [e.g., Abramowitz and Stegun, 1965; Ison et al., 1971], with a probability distribution function $f_P(p)$ that is defined by its mean (\bar{P}) and coefficient of variation (CV). CV captures the spread of the annual precipitation distribution, which may yield wet years and drought years. The theoretical distributions in the left column of Figure 4.2 conceptually show how Equation (4.1) maps values of P to values of S , for different values of S_{\max} (increasing downward from (a) to (c)). In case (a), S consistently reaches the relatively low S_{\max} , in spite of variable year-to-year winter precipitation. In case (c), S rarely reaches the relatively high S_{\max} , and the resulting variability in annual storage reflects variability in annual precipitation.

Across many years, P may take a range of values as determined by $f_P(p)$. The resulting strength of the relationship between P and S will determine the extent to which a watershed is precipitation-limited or storage-capacity-limited. This can be quantified by the nonparametric Spearman correlation coefficient, ρ , which is the Pearson correlation of the rank orders of P and S [Fieller et al., 1957]. As Equation (4.1) indicates, the correlation between P and S should be zero at a completely storage-capacity-limited site, as S is a constant S_{\max} from year to year, and therefore statistically independent of P . Conversely, ρ will be equal to 1 at a completely precipitation-limited site.

Idealized plots of S versus P and the corresponding value of ρ are shown in the center column of Figure 4.2 for five hypothetical water years. The right-hand side of Figure 4.2 illustrates the winter catchment water balance in wet and dry years corresponding to the precipitation and storage conditions illustrated in the first column. This shows how S_{\max} controls the partitioning of P between S , Q , and ET . Note that P and ET are the same in

Theoretical distributions:



Idealized observations and interpretation:

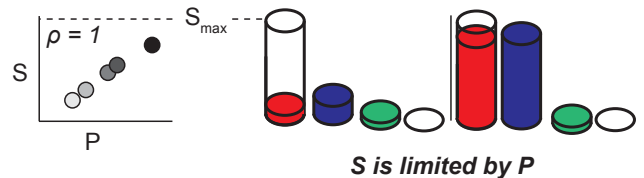
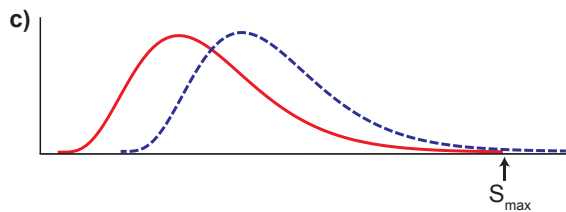
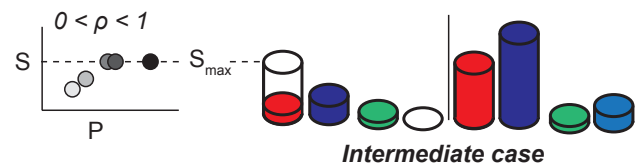
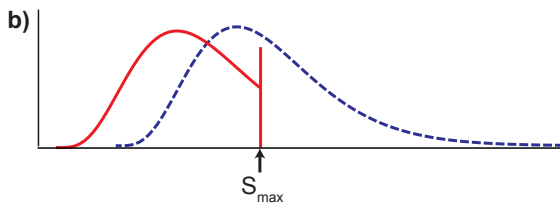
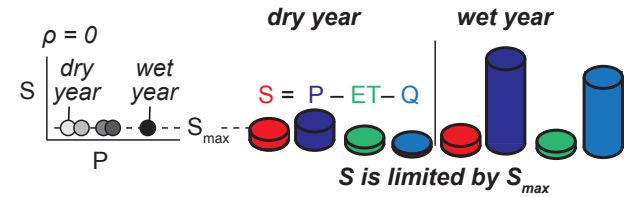


Figure 4.2: Conceptual diagram illustrating how the start-of-summer dynamic water storage (S), depends on winter precipitation (P) and subsurface critical zone water storage capacity (S_{\max}). Evapotranspiration (ET) is winter evapotranspiration (assumed constant here) and Q is the winter runoff. The three rows (a–c) show, for an increase in S_{\max} : (left column) the probability distribution of annual precipitation (P) relative to S_{\max} , and the resultant S distribution, shifted left due to ET ; (middle column) corresponding scatter plots of S versus P for five hypothetical years, along with the Spearman rank correlation coefficient (ρ) expressing the dependence of S on P ; (right column) relative water volumes, stylized as columns, of S , P , ET , and Q for an exemplary dry (left) and wet (right) year. In cases when $P < S_{\max} - ET$, the volume of S (colored red) is less than S_{\max} (the column’s wire frame).

each column, and when S is less than S_{\max} there is no predicted runoff.

Figure 4.3 plots contours of the Spearman coefficient, ρ , as a function of the CV of P and a dimensionless combination of the average winter precipitation (\bar{P}), S_{\max} , and ET , according to Equation (4.1) for gamma-distributed P . The storage-capacity-limited condition is approached (i.e., ρ approaches 0) for increasing $\bar{P}/(ET + S_{\max})$. Under these conditions, summer ET may be limited by neither energy nor annual precipitation [in the sense of Budyko, 1974], but by the storage capacity [e.g., Milly, 1994]. As CV increases along the horizontal axis in Figure 4.3, occasional dry years will not replenish the subsurface storage, resulting in a higher correlation between P and S .

The contours in Figure 4.3 are determined by assuming that total winter precipitation (P) is a random variable, and total winter evapotranspiration (ET) is approximately constant. Here we assume S is equal to its maximum plus or minus a small error term, $S_{\max} + \varepsilon$ when P exceeds $S_{\max} + ET$ (we assume a small random noise term (ε) that disallows ranked ties when $P - ET > S_{\max}$). This storage-capacity-limited condition occurs with probability $1 - x$. Otherwise, with probability x , a precipitation-limited condition prevails with $S = P - ET$. It is assumed that $P > ET$ in all years.

With these definitions, we can determine the expected Spearman rank correlation (ρ_{all}) between S and P as a function of annual mean of winter precipitation (\bar{P}), its coefficient of variation (CV), S_{\max} , and ET . The Spearman rank correlation is equal to the Pearson correlation between the ranked annual values of P and S (higher values denote stronger statistical dependence of S on P).

Given N years of precipitation and storage observations (S_i, P_i) for which $P_i \neq P_j$ and $S_i \neq S_j$ with $i, j \in \{1, 2, \dots, N\}$, the observations can be sorted by S_i or P_i and assigned ranks $\text{rank}(S_i)$ and $\text{rank}(P_i)$.

Assuming (by virtue of the small error term in $S_{\max} + \varepsilon$) that no two years have identical values of dynamic storage, the Spearman rank correlation between S_i and P_i is defined by Fieller et al. [1957]:

$$\rho_{\text{all}} = 1 - \frac{6 \sum_{i=1}^N d_i^2}{N(N^2 - 1)} \quad (4.2)$$

where d_i is the difference between the two ranks of each observation ($d_i = \text{rank}(S_i) - \text{rank}(P_i)$).

Assuming ε is unrelated to precipitation, the expected Spearman rank correlation between S and P among all storage-capacity-limited years ($P > S_{\max} + ET$) is zero ($\rho_{\text{capacity-limited}} = 0$). During precipitation-limited years ($P < S_{\max} + ET$), the rank correlation should be exactly 1 ($\rho_{\text{precip-limited}} = 1$). In limit of large N , there will be $n = N(1 - x)$ storage-capacity-limited years, and Nx precipitation-limited years.

By evaluating Equation 4.2 separately for these groups of years, the unknown terms pertaining to d_i can be determined in terms of the probability x :

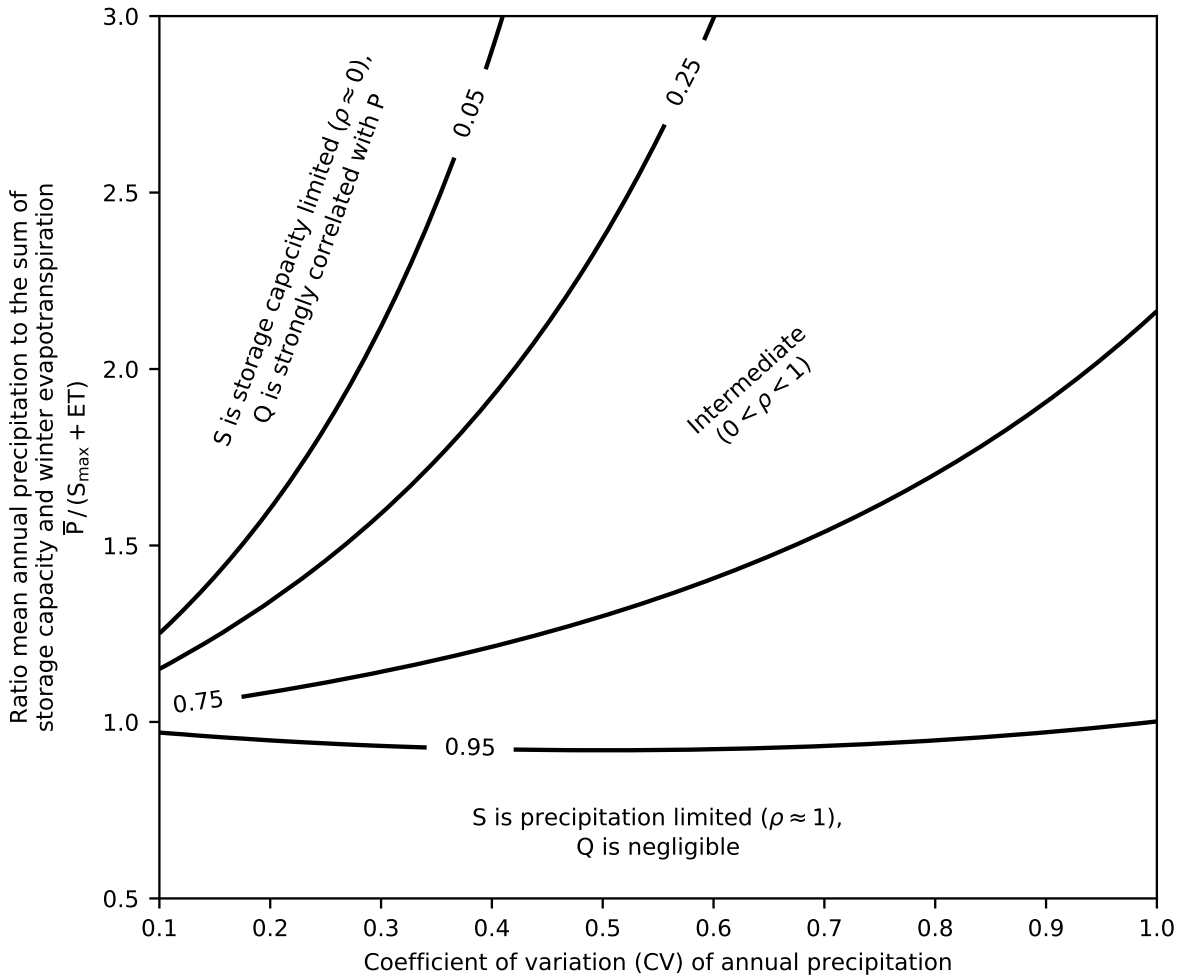


Figure 4.3: Storage sensitivity to precipitation depends on the coefficient of variation of winter precipitation and the ratio between average precipitation and storage capacity plus winter evapotranspiration. Contours represent the expected strength of correlation between stored water at the start of summer (S) and (gamma-distributed) cumulative winter precipitation (P) for varying S_{\max} , CV of P , and \bar{P} .

For storage-capacity-limited years:

$$\begin{aligned}\rho_{\text{capacity-limited}} = 0 &= 1 - \frac{6 \sum_{i=Nx+1}^N d_i^2}{n(n^2 - 1)} \\ \implies \sum_{i=Nx+1}^N d_i^2 &= \frac{n(n^2 - 1)}{6}\end{aligned}\quad (4.3)$$

For precipitation-limited years:

$$\begin{aligned}\rho_{\text{precip-limited}} = 1 &= 1 - \frac{6 \sum_{i=1}^{Nx} d_i^2}{Nx((Nx)^2 - 1)} \\ \implies \sum_{i=1}^{Nx} d_i^2 &= 0\end{aligned}\quad (4.4)$$

Combining the identities 4.3 and 4.4, the Spearman rank correlation for the full collection of N years is defined as:

$$\begin{aligned}\rho_{\text{all}} &= 1 - \frac{6 \sum_{i=1}^N d_i^2}{N(N^2 - 1)} \\ &= 1 - \frac{6}{N(N^2 - 1)} \times \left(\sum_{i=1}^{Nx} d_i^2 + \sum_{i=Nx+1}^N d_i^2 \right) \\ &= \frac{x(N^2(x^2 - 3x + 3) - 1)}{N^2 - 1}\end{aligned}\quad (4.5)$$

Taking the limit $N \rightarrow \infty$ in Equation 4.5 yields:

$$\rho_{\text{all}} = x^3 - 3x^2 + 3x \quad (4.6)$$

The challenge is now to define the probability x given knowledge of the probability distribution of the winter precipitation, S_{max} , and ET . We follow other authors [Ison et al., 1971] in assuming that annual winter precipitation P is a gamma distributed random variable (although a similar solution approach could be adopted for other distributions of P). We prescribe the mean winter precipitation as \bar{P} , and its standard deviation σ and coefficient of variation $CV = \sigma/\bar{P}$.

With these definitions, the cumulative probability distribution of the winter precipitation is:

$$F_P(p) = \frac{1}{\Gamma\left(\frac{1}{CV^2}\right)} \times \gamma\left[\frac{1}{CV^2}, \frac{p}{CV^2 \times \bar{P}}\right] \quad (4.7)$$

where Γ is the gamma function and γ is the lower incomplete gamma function [Abramowitz and Stegun, 1965]. A dimensionless precipitation $\tilde{P} = \frac{P}{S_{\text{max}} + ET}$, has its own CDF obtained

through a change of variables:

$$F_{\tilde{p}}(\tilde{p}) = F_p(\tilde{p} \times (S_{\max} + ET)) = \frac{1}{\Gamma\left(\frac{1}{CV^2}\right)} \times \gamma\left[\frac{1}{CV^2}, \frac{\tilde{p}}{CV^2 \times M}\right] \quad (4.8)$$

Where $M = \frac{\bar{P}}{S_{\max} + ET}$. The probability that a given year is precipitation limited (x) is found by evaluating $F_{\tilde{p}}(\tilde{p} = 1)$:

$$x = F_{\tilde{p}}(1) = \frac{1}{\Gamma\left(\frac{1}{CV^2}\right)} \times \gamma\left[\frac{1}{CV^2}, \frac{1}{CV^2 \times M}\right] \quad (4.9)$$

This expression for x can be substituted into Equation 4.6 to obtain the Spearman rank correlation between S and P for given values of the coefficient of variation of precipitation (CV) and the dimensionless ratio (M) of mean annual precipitation to the sum of storage capacity and winter evapotranspiration.

Selection of catchments and analysis of winter water balance and summer plant sensitivity

We tested whether rain-dominated Mediterranean sites in the U.S. exhibited storage-capacity-limited or precipitation-limited behavior by quantifying basin-wide storage dynamics. To calculate $S = P - ET - Q$, we rely on gridded precipitation (PRISM Climate Group, Oregon State University, <http://prism.oregonstate.edu>), a process-based ET model driven by remotely sensed data [Baldocchi et al., 2019; Ryu et al., 2011], and U.S. Geological Survey (USGS) runoff records. We queried the entire stream gauge network reported by the USGS to find suitable catchments that were winter wet, summer dry, unimpaired, rain-dominated, and relatively undisturbed (see Table 4.1 for complete criteria). Only 25 USGS-gauged catchments—all found within the state of California—met this selection criteria (we also include a non-USGS station at the Eel River Critical Zone Observatory (ERCZO), Dry Creek, which we classify as storage-capacity-limited based on intraseasonal storage dynamics; Dralle et al., 2018; Hahm et al., 2019b). The 26 sites span a large gradient in precipitation and biome, from mixed-coniferous-broadleaf evergreen forests to deciduous oak savanna, as well as underlying bedrock (marine sedimentary sequences to the granitic Sierra Nevada batholith; see table S2 online accompanying Hahm et al. [2019a] for more detail). A broader application of this empirical framework would likely register snow-dominated catchments as precipitation-limited, because higher precipitation typically results in higher storage as snowpack.

To test whether the subsurface storage dynamic governs plant community response to precipitation variability, we examined the correlation between catchment-wide mean summer EVI (derived from satellite observations [MOD13A1; Didan, 2015] between April and September) and winter precipitation. EVI is used here as a proxy for plant productivity and water use [Mu et al., 2007; Sims et al., 2006] and has been widely used as a metric of

Table 4.1: USGS Basin Filtering Criteria.

Rule	Rationale	Data source
0 dams upstream of gage ^a	Dams confound storage interpretation	
<20% of precipitation as snow	Restrict study to rain-dominated sites, to isolate role of belowground	GAGES-II: Geospatial Attributes of Gages for Evaluating Streamflow
<10% of precipitation falling between May 1–Sept. 31	Restrict study to winter-wet, summer-dry environments	(https://water.usgs.gov/GIS/metadata/usgswrd/XML/gagesII_Sept2011.xml)
Continuous daily runoff data over study period ^b	Data gaps preclude water balance	
Catchment area <1000 km ²	Limit spatial heterogeneity	
Cumulative clear cut or selective thinning logging 1997–present <20%	Logging confounds interpretation of EVI signal	California Timber Harvest Plans (ftp: ftp://ftp.fire.ca.gov/forest/Statewide_Timber_Harvest/)
Cumulative burned area from 1990–2014 <20%	Fire confounds interpretation of EVI signal	California Fire and Resource Assessment Program Fire Perimeters (http://frap.fire.ca.gov/data/frapgisdata-sw-fireperimeters_download)
Cumulative developed area <10%	Developed areas alter water balance	National Land Cover Database 2011 (https://www.mrlc.gov/nlcd2011.php)
Cumulative cultivated area <5%	Developed areas alter water balance (likely irrigated)	
No excessive water diversion upstream of gage	Alters water balance	USGS Water Year Summary Remarks and queries to USGS personnel

Notes: ^aSouth Fork Eel River at Leggett included as dam only active in summer, therefore does not interfere with winter storage tracking. ^bOccasional data gaps in the USGS runoff data that did not have an effect on determining the limitation classification were permitted (see, e.g., Miguelitos Creek). A complete dataset of winter runoff used is available at the code and data repository (https://github.com/daviddralle/storage_sensitivity/blob/master/data/winter_q.csv).

plant sensitivity to changes in measured subsurface water availability [e.g., Bai et al., 2019; A et al., 2017]. In our presentation of results, the annual summer EVI provided by the Moderate Resolution Imaging Spectroradiometer (MODIS) satellite program and obtained from the Google Earth Engine for each site is normalized by the site-specific mean across all study years. This allows for easy visual intercomparison between sites without affecting the rank correlation (ρ) between summer EVI and winter P . Nonnormalized data for each site are provided in Figure 4.4. In order to explore the role of summertime meteorological conditions on plant response, we also compared the sensitivity of summer EVI to summer potential evapotranspiration (PET ; calculated via the Hargreaves method [Hargreaves and Samani, 1982] with temperatures determined from PRISM).

We restricted the analysis to the 2002–2013 water years because (1) this marks the start of MODIS products that the ET data set relies on, (2) we wanted to limit the total number of

years studied to minimize trends in EVI associated with long-term plant community growth or succession that were distinct from the seasonal storage-climate signal we sought to isolate, (3) there was large variation in P across the sites during this time period, and (4) many trees across the state began to die at the end of this time period [US Forest Service, 2016a], which results in a step-change in the EVI signal, precluding our ability to detect the sensitivity of summer EVI to interannual variability in P .

4.4 Winter water balance and summer plant sensitivity to variable precipitation

The first row of Figure 4.5 illustrates annual storage dynamics from three sites spanning a gradient from storage-capacity-limited to precipitation-limited. The grey lines show the seasonal progression of S through multiple winters; the end-of-winter S value is shown with a colored point (evaluated from mass-balance between 1 October and 1 April). In each site, the same 12 years (water years 2002–2013) were selected. At Elder Creek, early winter rains steadily increase S . Storage eventually plateaus, however, and further precipitation instead results in runoff. Thus, across multiple years, end of winter S and P are largely uncorrelated, and ρ is not significantly different from zero (Figure 4.5a). The catchment is classified as storage-capacity-limited. At Los Gatos Creek, S increases with additional precipitation throughout the winter, consistent with precipitation limitation. Unlike Elder Creek, the seasonal storage traces do not plateau, and winter runoff is typically small (Figure S3). S and P are strongly correlated: $\rho = 1.0$ and is significant at $p < 0.05$. A strong positive correlation is guaranteed in this case, as small runoff results in the storage term being dominated by P ; this arises because precipitation is generally smaller than the storage capacity. San Lorenzo Creek is an intermediate case, where S increases with P during relatively dry years, but begins to plateau in wetter years.

The second row of Figure 4.5 illustrates the sensitivity of summer plant growth to the previous winter’s rainfall. At Elder Creek, there is no significant correlation between P and EVI, consistent with our hypothesis that storage-capacity limitation results in insensitivity of plant summer productivity and water use to year-to-year variability in total precipitation. In contrast, at Los Gatos Creek, EVI is strongly correlated with winter precipitation. In this precipitation-limited catchment, the EVI signal suggests that plants are more productive and return more water to the atmosphere in summers that follow wet winters.

Figure 4.6 summarizes the rank correlations between S , EVI, and P for all catchments. Six of the sites exhibited storage-capacity limitation, that is, insignificant correlation between S and P . At these sites (open symbols in Figure 4.6a) summer EVI was similarly insensitive to winter precipitation totals (open symbols in Figure 4.6b), as hypothesized. The storage-capacity-limited sites are found throughout the Northern California Coast Ranges (maps in Figure 4.6), indicating that storage-capacity limitation may be a widespread ecohydrologic phenomenon across an area with diverse plant communities, which have a large range in

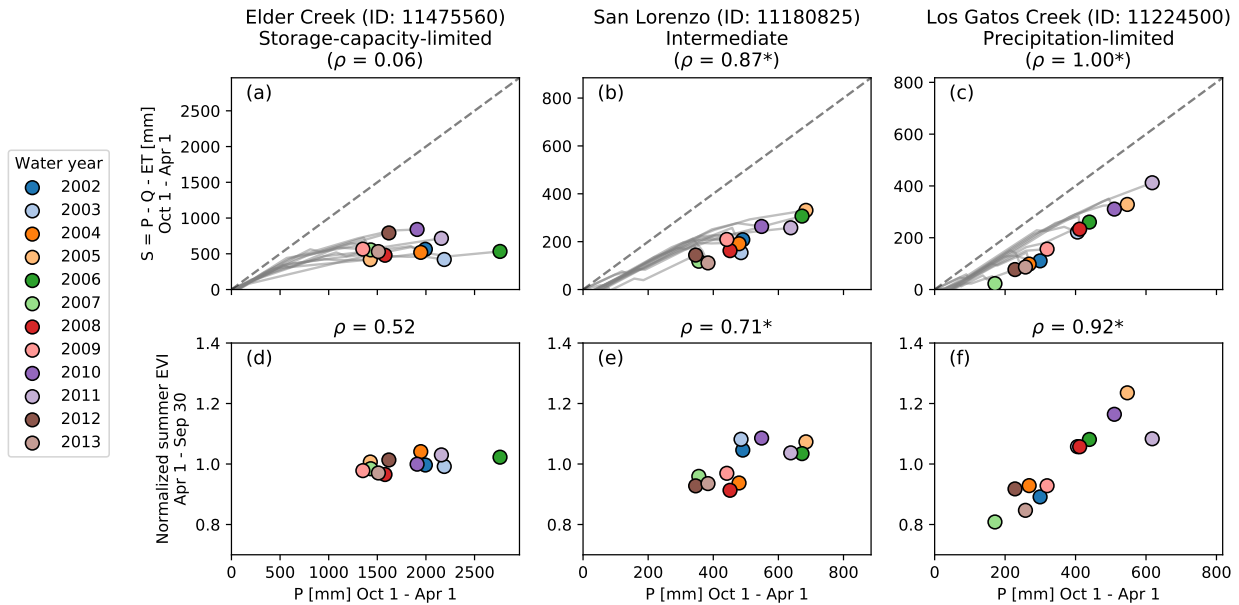


Figure 4.5: Winter storage (S) and the summer enhanced vegetation index as a function of winter precipitation (P). Plots (a–c) track the running catchment-wide S water balance (grey line traces) for each water year as a function of cumulative winter precipitation (up to 1 April). The dashed 1:1 lines reflect a reference case of no runoff (Q) or evapotranspiration. Plots (d–f) plot mean-normalized summer enhanced vegetation index between 1 April and 30 September, also as a function of total winter precipitation (P). ρ denotes the Spearman rank correlation for each scatter plot; asterisks denote significance at $p < 0.05$.

canopy cover (between ~ 20 and $\sim 90\%$; Figure 4.7) and absolute mean summer EVI (~ 0.32 to ~ 0.50 ; Figure 4.4). Sayama et al. [2011] also analyzed runoff from 17 small catchments, not monitored by the USGS, in Northern California Coast Range catchments and found behavior that we interpret as storage-capacity-limited (seasonal S traces plateau relatively early within the winter). This area also tends to have higher average annual rainfall (Figure 4.8); as the modeling framework predicts (Figure 4.3), locations with higher rainfall are more likely to be storage-capacity limited. At precipitation-limited sites, variations in P explain variations in S (filled symbols in Figure 4.6a), and summer EVI at most sites scales with winter precipitation (filled symbols in Figure 4.6b).

Figure 4.9 shows that in general the summer EVI signal has a weak negative correlation with summer PET across the state; however, at most sites the correlation is insignificant. We interpret this to indicate that if more energy is available for plant water use, vegetation is not necessarily able to use that energy to transpire more (i.e., the sites are water-limited in the summer). Furthermore, there is no apparent difference in the sensitivity of summer EVI to summer PET between storage-capacity-limited and precipitation-limited sites.

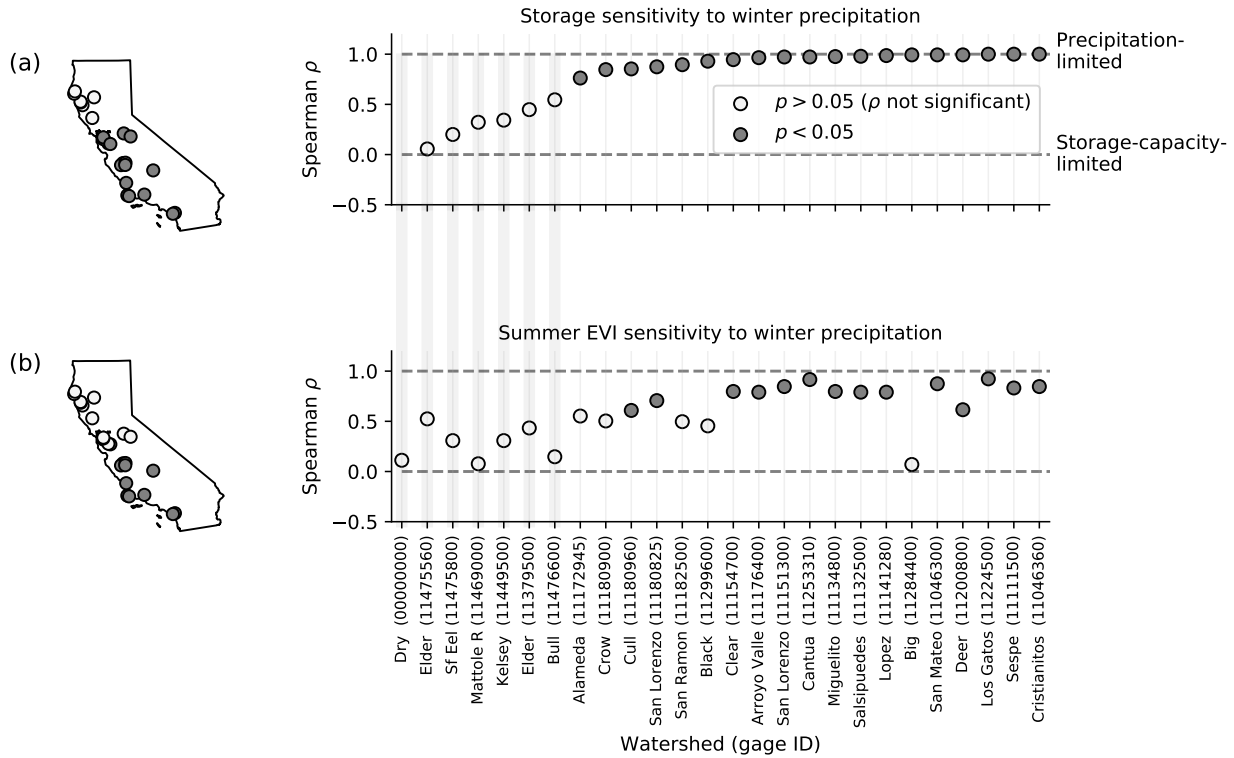


Figure 4.6: Winter storage and summer enhanced vegetation index (EVI) sensitivity to winter P . Spearman rank correlations between (a) S and winter precipitation and (b) summer EVI and winter precipitation. The filled symbols denote significance at $p < 0.05$. The grey-shaded vertical bars connect storage-capacity-limited sites between (a) and (b). Dry Creek lacks complete runoff record but is inferred to be storage-capacity-limited based on intensive hillslope-scale monitoring.

4.5 Discussion

Sites across California exhibit both precipitation-limited and storage-capacity limited behavior. Where the amount of water stored over the wet season is uncorrelated with rainfall, the storage capacity of the subsurface is inferred to be low relative to the winter rainfall, and correspondingly, the summer EVI is insensitive to variations in rainfall. This is consistent with our hypothesis that storage-capacity limitation can decouple plants from swings in rainfall, even when these swings are large: P varied more than twofold between years, and, in some cases, by more than 1,500 mm.

Similar to recent studies [e.g., Wang-Erlandsson et al., 2016], our analysis uses water flux tracking to estimate S independently of catchment physiographic features (e.g., soil characteristics). Considering only water storage in near-surface soils, all study sites would likely be storage-capacity-limited: the average plant-available water holding capacity in the

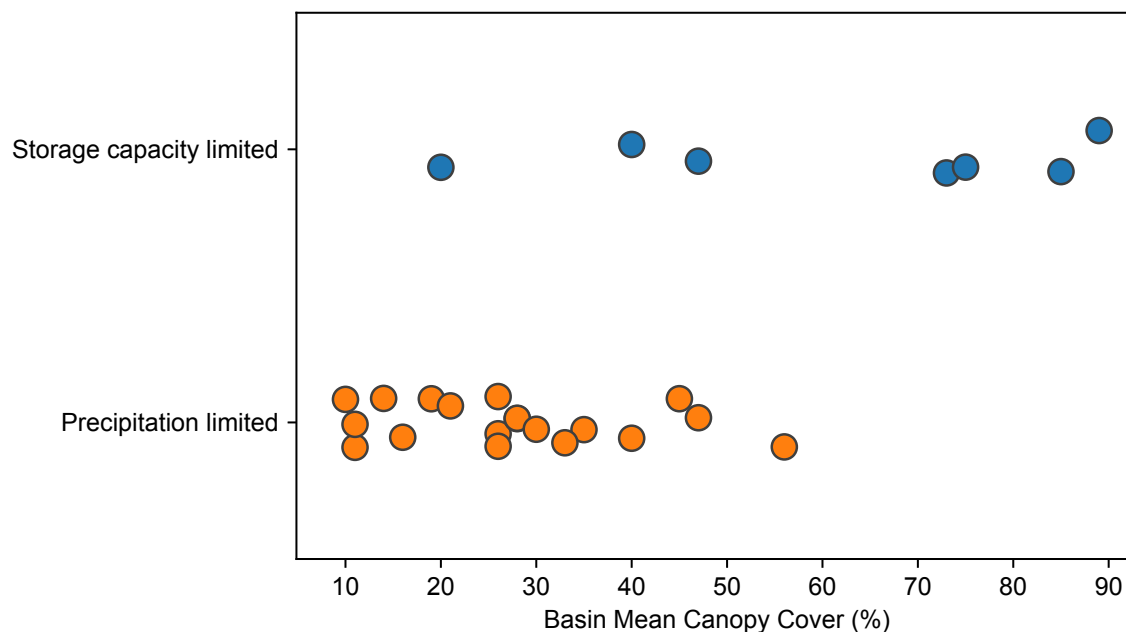


Figure 4.7: Distribution of mean canopy cover (jittered) by limitation category.

soil is about 100 mm based on querying the Soil Survey Geographic database [Soil Survey Staff, 2018]. Instead, most sites are precipitation-limited, indicating that the seasonal water storage likely extends well below the soil, consistent with large discrepancies between flux-tracked and soil survey-inferred storage capacities observed elsewhere [e.g., de BoerEuser et al., 2016]. Storage drawdowns in summer within Mediterranean climates are dominated by ET , not Q , and transpiration is the dominant (85–95%) component of summer ET at our sites [Martens et al., 2017]. This indicates that much of the water seasonally stored below the soil is plant-available, and that plants generate the below-soil storage deficit that is replenished by wet season rains. This deeper water occurs in saprolite or weathered bedrock as rock moisture [in the sense of Rempe and Dietrich, 2018] or groundwater.

The decoupling of summer plant greenness from winter precipitation variability

We considered additional mechanisms that could result in the decoupling of summer plant greenness from winter precipitation variability: (1) that some plant communities do not exhibit EVI variations in general and (2) that some plant communities do not exhibit EVI variations in response to changes in water availability. We rejected these explanations because (1) there are consistent, large seasonal swings in EVI at storage-capacity-limited sites

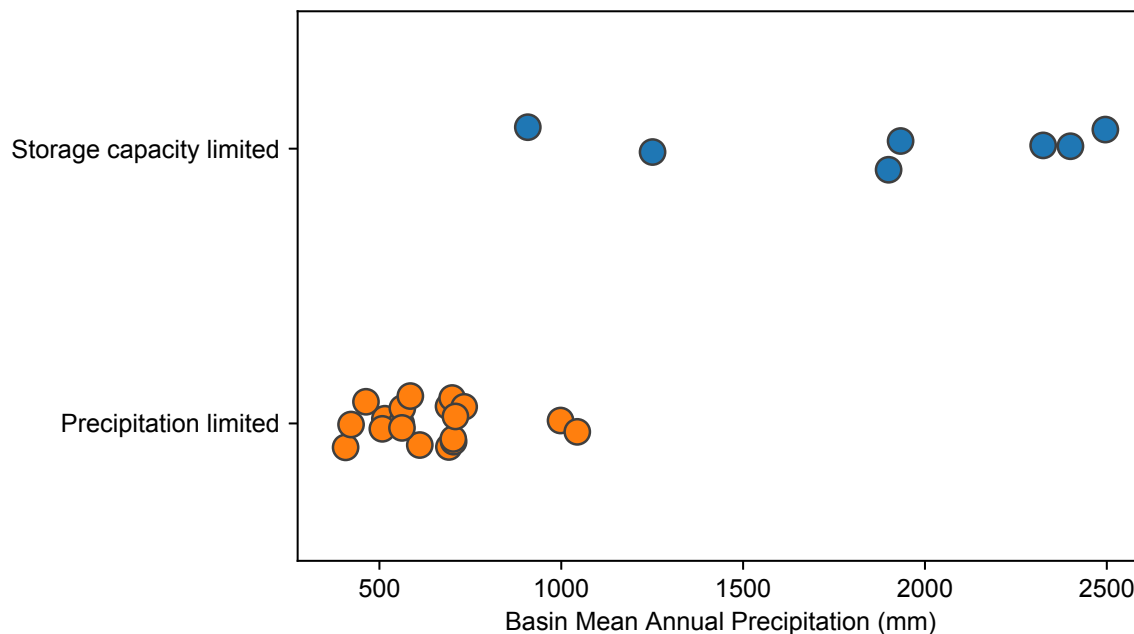


Figure 4.8: Distribution of mean annual precipitation (jittered) by limitation category.

with diverse plant communities [see Figure 11 of Hahm et al., 2019b], and (2) greenness across a wide range of plant communities has been shown to be significantly correlated with water storage [Yang et al., 2014]. There remain in our data set, however, five sites where precipitation limits S but is poorly correlated to summer EVI, contrary to our predictions. This may be due to storage capacity being met in some but not all years, significant inter-annual water storage carry-over, or S not scaling, as assumed, with plant available water, due to factors like interbasin flow that are not accounted for in our analysis.

Observations and hydrologic mechanisms of storage-capacity-limitation

Monitoring and drilling at two storage-capacity-limited catchments—Elder Creek and Dry Creek—in the Northern California Coast Range, within the ERCZO, illustrate how diverse CZ structures impose storage-capacity limitation. The subsurface CZ at Dry Creek consists of a shallow soil (~ 40 cm) developed on a relatively thin saprolite and weathered bedrock zone that transitions to low porosity, low conductivity fresh parent material at only ~ 2 -m depth [Dralle et al., 2018; Hahm et al., 2019b]). Here early winter rains (typically between 100 to 200 mm, or less than $1/10$ th of the local \bar{P}) saturate the CZ [Dralle et al., 2018]. Further precipitation generates widespread overland flow, and S does not increase, resulting

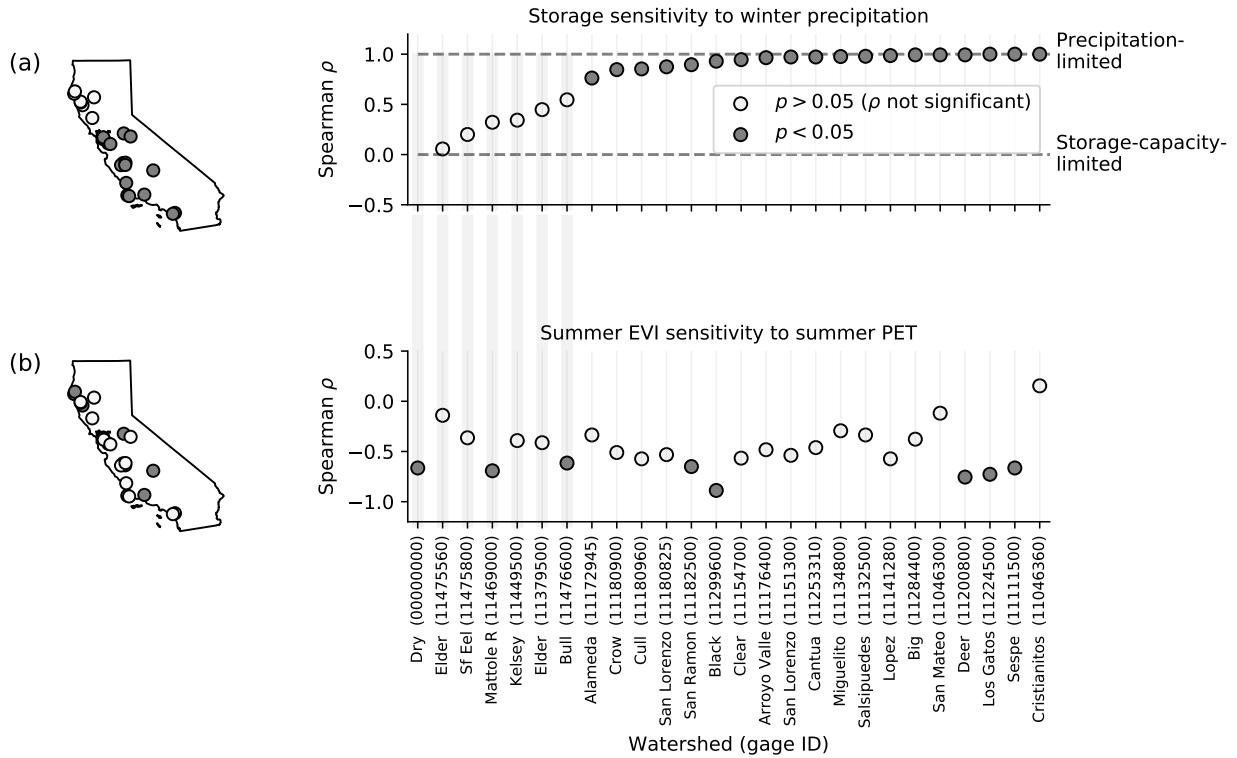


Figure 4.9: Winter storage sensitivity to P and summer EVI sensitivity to summer PET . Spearman rank correlations between S and winter precipitation (a), and summer EVI and summer PET (b), are shown for the 2002–2013 water years. Filled symbols denote significance at $p < 0.05$. Grey-shaded vertical bars connect storage-capacity-limited sites between (a) and (b).

in limited summer water availability in the summer. Despite an annual precipitation of $>1,800$ mm, a water-limitation tolerant oak savanna dominates [Hahm et al., 2018]. This can be explained by the subsurface CZ-structure imposed cap on plant-available water storage [Hahm et al., 2019b]. In contrast, the subsurface CZ at the densely forested Elder Creek (USGS gage #11475560) consists of a thin soil (typically <60 cm), underlain by a weathered bedrock layer which thickens upslope away from the channel, reaching depths of up to 30 m at the ridge [Oshun et al., 2016; Rempe and Dietrich, 2014; Salve et al., 2012]. The soil and weathered fractured rock progressively wet with early winter precipitation, until a field-capacity-like condition is reached in the vadose zone. Further precipitation triggers recharge to a seasonal groundwater table that develops above the fresh bedrock boundary that slopes toward the channels and drives relatively rapid runoff without completely saturating the subsurface [Rempe and Dietrich, 2018].

Differences in CZ structure at the two ERCZO sites correspond to different geologic units of the Franciscan complex [Hahm et al., 2019b]. Other lithological settings may influence

seasonal water storage through different runoff generation mechanisms. For example, at sites with low near-surface hydraulic conductivity where runoff generation is primarily via Horton overland flow or where shallow claypans promote shallow lateral subsurface flow [Swarowsky et al., 2011], greater winter precipitation (P) would not increase S but instead would increase runoff (Q), as suggested by Milly [1994]. Our empirical approach would register this catchment behavior as storage-capacity-limited, even though such sites may have ample subsurface porosity where water could be stored if, for example, winter precipitation events were less intense but more frequent.

Storage capacity limitation and drought resilience

More than 100 million trees died across California in the 2011–2016 drought [US Forest Service, 2016a]. However, we did not observe significant crown dieback or tree mortality at the two storage-capacity-limited ERCZO sites (Elder and Dry creeks), in spite of approximately twofold precipitation declines relative to long-term averages. Indeed, at five out of six storage-capacity-limited sites, summer EVI remained uncoupled from winter P even when years during and after the extreme drought are considered (2014–2016; Figure. 4.10; these years were not included in the analysis in Figure 4.6 in order to avoid the potential step-change in EVI signal due to dead trees at some sites; see discussion above). The site that shifted from storage-capacity limited to precipitation limited (Gage ID 11379500) likely did so because rainfall dropped low enough relative to storage capacity that it entered a precipitation-limited state in the drought, as predicted by the model and suggested by other intermediate cases (see, e.g., San Lorenzo in Figure 4.5). The storage-capacity limited sites are representative of much of the Northern California Coast Ranges, which avoided significant mortality compared to the Sierra and Southern California [US Forest Service, 2016a], and span a large gradient in ecosystem water-limitation tolerance, from grassland savanna to sclerophyllous shrubland to dense stands of Douglas Fir (*Pseudotsuga menziesii*). Although it rains more along the Northern California Coast Ranges compared to the rest of the state, the strong seasonal separation of water delivery to the landscape from water demand by plants results in summer water limitation in spite of annual P exceeding, in some years, PET .

Previous studies, in contrast to our hypothesis, concluded that these plant communities would suffer in the drought. For example, Choat et al. [2012] proposed that, in general, forests growing in relatively wet areas should be as susceptible to drought as those growing in dry environments, due to the tendency for trees to operate with narrow hydraulic safety margins within their water balance regime. Locally, relatively high canopy density and climatic water deficits resulted in model predictions of higher-than-observed mortality in the Northern California Coast Ranges in the drought [Young et al., 2017]. We propose that by decoupling summer water availability from year-to-year winter precipitation variability, storage-capacity limitation is a mechanism of drought resilience in this region. Plants were not spared from the drought here because the subsurface stored large quantities of water that were mined as the drought progressed; rather, plants survived because winter rains

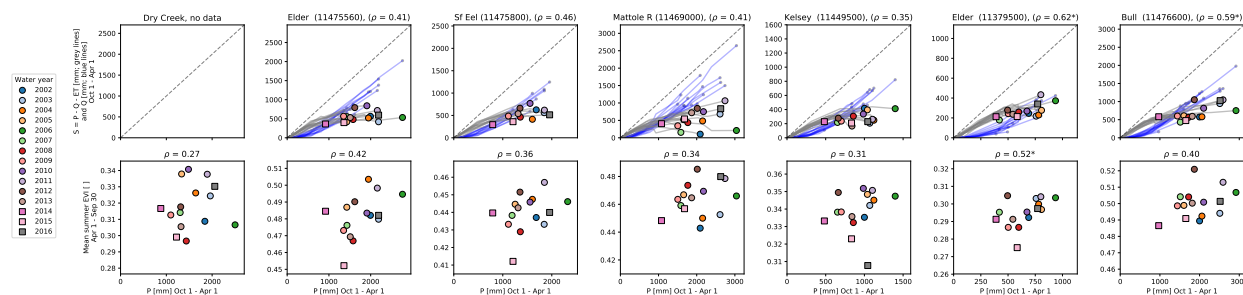


Figure 4.10: Plots of S and Q vs. winter P (top row) and mean summer EVI vs. winter P (bottom row), including extreme drought years, for sites classified as storage-capacity limited for the years 2002 to 2013. In the top row, lines trace the seasonal evolution of both the dynamic storage (S , grey) and the cumulative winter runoff (Q , blue). Points at the termini of the S traces are colored by the water year and are paired with the summer EVI in the bottom row. Squares denote water years after the start of extreme drought (2014, 2015, 2016, and 2017).

exceeded the subsurface storage capacity and replenished storage even in relatively dry years, consistent with intensive moisture monitoring campaigns throughout the CZ [Rempe and Dietrich, 2018]. At precipitation-limited sites (e.g., the Big Creek catchment included in this analysis), the patterns of mortality will depend on the severity of the meteorological drought and on plant physiological adaptations to water limitation [e.g., the varied ability of plants to avoid hydraulic failure and carbon starvation in anomalously dry years Adams et al., 2017].

The transition from rain to snow

As temperatures rise globally, mountains—including the Sierra Nevada in California—will receive less snow and more rain, likely elevating the role of subsurface storage in determining ecosystem response to climate variations. In areas where Pleistocene glaciation exposed fresh bedrock, low subsurface porosity [Klos et al., 2018] combined with loss of snowpack could lead to storage-capacity limitation. This would result in lower overall summer water availability that is also decoupled from winter precipitation variations, as similarly suggested by Smith et al. [2011] in snow-to-rain transitioning watersheds in Idaho. Thus, we would hypothesize that currently established plant communities adapted to relatively high summer water supplies afforded by snowpack may die off, and be replaced with plants that are adapted to lower summer water supplies capped by the subsurface storage capacity. Once established, this new community may be more resilient to fluctuating winter precipitation totals, due to the tendency for the limited subsurface storage capacity to be refilled in both wet and dry winters.

4.6 Conclusions

Hydrologic analysis of 26 relatively undisturbed basins within Mediterranean-climate areas of California revealed seven basins that showed a decoupling between annual rainfall and subsurface water storage. At these sites, annual rainfall variations do not impact storage because rainfall is typically in excess of subsurface storage deficits. As hypothesized, at each of these sites summer EVI did not vary with annual rainfall, highlighting a storage-capacity limitation mechanism that decouples plants from rainfall variability, including droughts.

Models rarely incorporate estimates of storage capacity beyond the soil, primarily due to lack of accurate, spatially distributed information about the deeper subsurface. Where water flux data are available, our modeling approach provides a means to quantify the sensitivity of plants in Mediterranean climates at catchment scales to rainfall variability and water storage capacity (including rock moisture and groundwater residing in weathered bedrock) without a priori or posteriori knowledge of that water storage capacity. This reduces the reliance on estimates of soil properties alone, and the assumption that soil is the only source of water for transpiration. Our conceptual model may enable identification of plant communities with a reduced risk of mortality under drought scenarios, and if climate change forecasts predict significant reduction in precipitation or increase in its variability, the model should also identify new areas of drought vulnerability.

4.7 Acknowledgements

We thank the managers and landowners of the ERCZO sites (the University of California Angelo Coast Range Reserve and Sagehorn), and Mary Power and Sky Lovill for helpful discussions. Primary funding came from the NSF CZO program (EAR 1331940), with additional support from the Mathias Graduate Student Research Grant, the Baird Fund for Graduate Field Science, and the Institute for the Study of Ecological and Evolutionary Climate Impacts. Data and Jupyter notebooks that reproduce the analyses are hosted at https://github.com/daviddralle/storage_sensitivity.

Bibliography

- A, G., Velicogna, I., Kimball, J. S., Du, J., Kim, Y., Colliander, A., and Njoku, E. (2017). Satellite-observed changes in vegetation sensitivities to surface soil moisture and total water storage variations since the 2011 Texas drought. Environmental Research Letters, 12(5):054006.
- Abatzoglou, J. T., Rupp, D. E., and Mote, P. W. (2014). Seasonal Climate Variability and Change in the Pacific Northwest of the United States. Journal of Climate, 27(5):2125–2142.
- Abramowitz, M. and Stegun, I. A. (1965). Handbook of Mathematical Functions: With Formulas, Graphs, and Mathematical Tables. Courier Corporation. Google-Books-ID: MtU8uP7XMvoC.
- Adam, D. P., Sims, J. D., and Throckmorton, C. K. (1981). 130,000-yr continuous pollen record from Clear Lake, Lake County, California. Geology, 9(8):373–377.
- Adam, D. P. and West, G. J. (1983). Temperature and Precipitation Estimates Through the Last Glacial Cycle from Clear Lake, California, Pollen Data. Science, 219(4581):168–170.
- Adams, H. D., Zeppel, M. J. B., Anderegg, W. R. L., Hartmann, H., Landhäusser, S. M., Tissue, D. T., Huxman, T. E., Hudson, P. J., Franz, T. E., Allen, C. D., Anderegg, L. D. L., Barron-Gafford, G. A., Beerling, D. J., Breshears, D. D., Brodrigg, T. J., Bugmann, H., Cobb, R. C., Collins, A. D., Dickman, L. T., Duan, H., Ewers, B. E., Galiano, L., Galvez, D. A., Garcia-Forner, N., Gaylord, M. L., Germino, M. J., Gessler, A., Hacke, U. G., Hakamada, R., Hector, A., Jenkins, M. W., Kane, J. M., Kolb, T. E., Law, D. J., Lewis, J. D., Limousin, J.-M., Love, D. M., Macalady, A. K., Martínez-Vilalta, J., Mencuccini, M., Mitchell, P. J., Muss, J. D., O'Brien, M. J., OGrady, A. P., Pangle, R. E., Pinkard, E. A., Piper, F. I., Plaut, J. A., Pockman, W. T., Quirk, J., Reinhardt, K., Ripullone, F., Ryan, M. G., Sala, A., Sevanto, S., Sperry, J. S., Vargas, R., Vennetier, M., Way, D. A., Xu, C., Yopez, E. A., and McDowell, N. G. (2017). A multi-species synthesis of physiological mechanisms in drought-induced tree mortality. Nature Ecology & Evolution, 1(9):1285–1291.
- Aguiar, M. R. and Sala, O. E. (1994). Competition, Facilitation, Seed Distribution and the Origin of Patches in a Patagonian Steppe. Oikos, 70(1):26–34.

- Allen, C. D., Macalady, A. K., Chenchouni, H., Bachelet, D., McDowell, N., Vennetier, M., Kitzberger, T., Rigling, A., Breshears, D. D., Hogg, E. H. T., Gonzalez, P., Fensham, R., Zhang, Z., Castro, J., Demidova, N., Lim, J.-H., Allard, G., Running, S. W., Semerci, A., and Cobb, N. (2010). A global overview of drought and heat-induced tree mortality reveals emerging climate change risks for forests. Forest Ecology and Management, 259(4):660–684.
- Allerup, P. and Madsen, H. (1980). Accuracy of Point Precipitation Measurements. Hydrology Research, 11(2):57–70.
- Améglio, T., Archer, P., Cohen, M., Valancogne, C., Daudet, F.-a., Dayau, S., and Cruiziat, P. (1999). Significance and limits in the use of predawn leaf water potential for tree irrigation. Plant and Soil, 207(2):155–167.
- Amundson, R., Heimsath, A., Owen, J., Yoo, K., and Dietrich, W. E. (2015). Hillslope soils and vegetation. Geomorphology, 234:122–132.
- Anderson, M., Graham, R., Alyanakian, G., and Martyn, D. (1995). Late summer water status of soils and weathered bedrock in a Giant Sequoia grove. Soil Science, 160(6):415–422. 00036.
- Anderson, M. G. and Ferree, C. E. (2010). Conserving the Stage: Climate Change and the Geophysical Underpinnings of Species Diversity. PLoS ONE, 5(7):e11554. 00120.
- Anderson, M. V. and Pasquinelli, R. L. (1984). Ecology and Management of the Northern Oak Woodland Community, Sonoma County, California. Thesis, Sonoma State University.
- Anderson, R. S., Anderson, S. P., and Tucker, G. E. (2013). Rock damage and regolith transport by frost: an example of climate modulation of the geomorphology of the critical zone. Earth Surface Processes and Landforms, 38(3):299–316. 00012.
- Anderson, S. P., Blum, J., Brantley, S. L., Chadwick, O., Chorover, J., Derry, L. A., Drever, J. I., Hering, J. G., Kirchner, J. W., Kump, L. R., Richter, D., and White, A. E. (2004). Proposed initiative would study Earth’s weathering engine. Eos, Transactions American Geophysical Union, 85(28):265–269. 00037.
- Arkley, R. J. (1981). Soil moisture use by mixed conifer forest in a summer-dry climate. Soil Science Society of America Journal, 45(2):423–427. 00078.
- Armstrong, W. (1980). Aeration in Higher Plants. In Woolhouse, H. W., editor, Advances in Botanical Research, volume 7, pages 225–332. Academic Press.
- Asner, G. P., Brodrick, P. G., Anderson, C. B., Vaughn, N., Knapp, D. E., and Martin, R. E. (2016). Progressive forest canopy water loss during the 2012–2015 California drought. Proceedings of the National Academy of Sciences, 113(2):E249–E255.

- Atwater, T. and Stock, J. (1998). Pacific-North America Plate Tectonics of the Neogene Southwestern United States: An Update. International Geology Review, 40(5):375–402.
- Bai, J., Shi, H., Yu, Q., Xie, Z., Li, L., Luo, G., Jin, N., and Li, J. (2019). Satellite-observed vegetation stability in response to changes in climate and total water storage in Central Asia. Science of The Total Environment, 659:862–871.
- Baldocchi, D., Dralle, D., Jiang, C., and Ryu, Y. (2019). How Much Water is Evaporated Across California?: A Multi-Year Assessment Using a Biophysical Model Forced with Satellite Remote Sensing Data. Water Resources Research.
- Baldocchi, D. D., Xu, L., and Kiang, N. (2004). How plant functional-type, weather, seasonal drought, and soil physical properties alter water and energy fluxes of an oakgrass savanna and an annual grassland. Agricultural and Forest Meteorology, 123(12):13–39. 00337.
- Bales, R. C., Hopmans, J. W., O’Geen, A. T., Meadows, M., Hartsough, P. C., Kirchner, P., Hunsaker, C. T., and Beaudette, D. (2011). Soil moisture response to snowmelt and rainfall in a Sierra Nevada mixed-conifer forest. Vadose Zone Journal, 10(3):786. 00039.
- Barkaoui, K., Navas, M.-L., Roumet, C., Cruz, P., and Volaire, F. (2017). Does water shortage generate water stress? An ecohydrological approach across Mediterranean plant communities. Functional Ecology, 31(6):1325–1335.
- Barnhart, S. J., McBride, J. R., and Warner, P. (1996). Invasion of Northern Oak Woodlands by *Pseudotsuga menziesii* (Mirb.) Franco in the Sonoma Mountains of California. Madroo, 43(1):28–45.
- Bartlett, M. K., Scoffoni, C., and Sack, L. (2012). The determinants of leaf turgor loss point and prediction of drought tolerance of species and biomes: a global meta-analysis. Ecology Letters, 15(5):393–405. 00129.
- Bazilevskaya, E., Lebedeva, M., Pavich, M., Rother, G., Parkinson, D. Y., Cole, D., and Brantley, S. L. (2013). Where fast weathering creates thin regolith and slow weathering creates thick regolith. Earth Surface Processes and Landforms, 38(8):847–858.
- Begg, J. E. and Turner, N. C. (1970). Water Potential Gradients in Field Tobacco. Plant Physiology, 46(2):343–346.
- Bennett, G. L., Miller, S. R., Roering, J. J., and Schmidt, D. A. (2016). Landslides, threshold slopes, and the survival of relict terrain in the wake of the Mendocino Triple Junction. Geology, 44(5):363–366.
- Bird, R. B., Bird, D. W., Coddling, B. F., Parker, C. H., and Jones, J. H. (2008). The fire stick farming hypothesis: Australian Aboriginal foraging strategies, biodiversity, and anthropogenic fire mosaics. Proceedings of the National Academy of Sciences, 105(39):14796–14801.

- Bish, D. L. and Howard, S. A. (1988). Quantitative phase analysis using the Rietveld method. Journal of Applied Crystallography, 21(2):86–91.
- Biswell, H. H. (1956). Ecology of California Grasslands. Journal of Range Management, 9(1):19–24.
- Blackman, C. J. and Brodribb, T. J. (2011). Two measures of leaf capacitance: insights into the water transport pathway and hydraulic conductance in leaves. Functional Plant Biology, 38(2):118–126.
- Blake, M. and Jones, D. L. (1974). Origin of Franciscan Melanges in Northern California. Special Publications of the Society of Economic Paleontologists and Mineralogists, (19 - Modern and Ancient Geosynclinal Sedimentation).
- Blake, Jr, M., Jayko, A. S., and McLaughlin, R. J. (1985). Tectonostratigraphic Terranes of the Northern Coast Ranges, California. 00084.
- Bodtker, K., Pellatt, M. G., and Cannon, A. (2009). A bioclimatic model to assess the impact of climate change on ecosystems at risk and inform land management decisions. Technical Report Report for the Climate Change Impacts and Adaptation Directorate, CCAF Project A718, Parks Canada.
- Bond, W. J. (2005). Large parts of the world are brown or black: A different view on the Green World hypothesis. Journal of Vegetation Science, 16(3):261–266.
- Boyer, J. S. (1995). Measuring the water status of plants and soils. Academic Press, Inc.
- Branson, F., Miller, R., and McQueen, I. (1970). Plant Communities and Associated Soil and Water Factors of ShaleDerived Soil in Northeastern Montana. Ecology, 51(3):391–407.
- Brodribb, T. J. and Holbrook, N. M. (2003). Stomatal Closure during Leaf Dehydration, Correlation with Other Leaf Physiological Traits. Plant Physiology, 132(4):2166–2173.
- Budyko, M. I. (1974). VI Climatic Factors of Geographical Zonality. In International Geophysics, volume 18 of Climate and Life, pages 317–370. Academic Press.
- Burcham, L. T. (1957). California range land: an historico-ecological study of the range resource of California. Division of Forestry, Department of Natural Resources, State of California.
- Burgess, S. S. O., Adams, M. A., Turner, N. C., Beverly, C. R., Ong, C. K., Khan, A. A. H., and Bleby, T. M. (2001). An improved heat pulse method to measure low and reverse rates of sap flow in woody plants. Tree Physiology, 21(9):589–598. 00294 PMID: 11390303.
- Byrne, R., Edlund, E., and Mensing, S. (1991). Holocene changes in the distribution and abundance of oaks in California. In Proceedings of the Symposium on Oak Woodlands and Hardwood Rangeland Management, pages 182–188.

- California Department of Forestry (1996). California Oak Woodland Community. Technical report, California Oaks.
- Cannon, W. A. (1914). Specialization in Vegetation and in Environment in California. The Plant World, 17(8):223–237.
- Choat, B., Brodribb, T. J., Brodersen, C. R., Duursma, R. A., López, R., and Medlyn, B. E. (2018). Triggers of tree mortality under drought. Nature, 558(7711):531–539.
- Choat, B., Jansen, S., Brodribb, T. J., Cochard, H., Delzon, S., Bhaskar, R., Bucci, S. J., Feild, T. S., Gleason, S. M., Hacke, U. G., Jacobsen, A. L., Lens, F., Maherali, H., Martínez-Vilalta, J., Mayr, S., Mencuccini, M., Mitchell, P. J., Nardini, A., Pittermann, J., Pratt, R. B., Sperry, J. S., Westoby, M., Wright, I. J., and Zanne, A. E. (2012). Global convergence in the vulnerability of forests to drought. Nature, 491(7426):752–755. 00449.
- Christy, J. A. and Alverson, E. R. (2011). Historical Vegetation of the Willamette Valley, Oregon, circa 1850. Northwest Science, 85(2):93–107.
- Clark, H. W. (1937). Association Types in the North Coast Ranges of California. Ecology, 18(2):214–230.
- Cloos, M. (1982). Flow melanges: Numerical modeling and geologic constraints on their origin in the Franciscan subduction complex, California. Geological Society of America Bulletin, 93(4):330–345. 00434.
- Cloos, M. (1983). Comparative Study of Melange Matrix and Metashales from the Franciscan Subduction Complex With the Basal Great Valley Sequence, California. The Journal of Geology, 91(3):291–306. 00063.
- Cocking, M. I., Varner, J. M., and Engber, E. A. . (2015). Conifer encroachment in California oak woodlands. In Gen. Tech. Rep. PSW-GTR-251. USDA Forest Service.
- Cole, D. (1977). Ecosystem Dynamics in the Coniferous Forest of the Willamette Valley, Oregon, U. S. A. Journal of Biogeography, 4(2):181–192.
- Cowling, R. M., Rundel, P. W., Lamont, B. B., Kalin Arroyo, M., and Arianoutsou, M. (1996). Plant diversity in mediterranean-climate regions. Trends in Ecology & Evolution, 11(9):362–366.
- Danielsen, K. C. and Halvorson, W. L. (1991). Valley oak seedling growth associated with selected grass species. In Proceedings of the Symposium on Oak Woodlands and Hardwood Rangeland Management, October 31–November 2, 1990, Davis, California, volume 126, page 9. US Department of Agriculture, Pacific Southwest Research Station.
- Dantas, V. d. L., Hirota, M., Oliveira, R. S., and Pausas, J. G. (2016). Disturbance maintains alternative biome states. Ecology Letters, 19(1):12–19.

- Davis, K. J. (2005). Comparison of the water relations characteristics of woody plants in western Oregon. PhD thesis, Oregon State University.
- Davy, J. B. (1902). Stock Ranges of Northwestern California, Notes on the Grasses and Forage Plants and Range Conditions. US Government Printing Office.
- Dawson, T. E. and Bliss, L. C. (1989). Patterns of water use and the tissue water relations in the dioecious shrub, *Salix arctica*: the physiological basis for habitat partitioning between the sexes. Oecologia, 79(3):332–343.
- Dawson, T. E., Burgess, S. S. O., Tu, K. P., Oliveira, R. S., Santiago, L. S., Fisher, J. B., Simonin, K. A., and Ambrose, A. R. (2007). Nighttime transpiration in woody plants from contrasting ecosystems. Tree Physiology, 27(4):561–575.
- de BoerEuser, T., McMillan, H. K., Hrachowitz, M., Winsemius, H. C., and Savenije, H. H. G. (2016). Influence of soil and climate on root zone storage capacity. Water Resources Research, 52(3):2009–2024.
- Dettinger, M. D., Ralph, F. M., Das, T., Neiman, P. J., and Cayan, D. R. (2011). Atmospheric Rivers, Floods and the Water Resources of California. Water, 3(2):445–478.
- Devine, W. D. and Harrington, C. A. (2005). Root system morphology of Oregon white oak on a glacial outwash soil. Northwest science, 79(2-3):179–188.
- Devine, W. D. and Harrington, C. A. (2006). Changes in Oregon white oak (*Quercus garryana* Dougl. ex Hook.) following release from overtopping conifers. Trees, 20(6):747–756.
- Didan, K. (2015). MOD13a1 MODIS/Terra Vegetation Indices 16-Day L3 Global 500m SIN Grid V006.
- Domec, J.-C., Lachenbruch, B., Meinzer, F. C., Woodruff, D. R., Warren, J. M., and McCulloh, K. A. (2008). Maximum height in a conifer is associated with conflicting requirements for xylem design. Proceedings of the National Academy of Sciences, 105(33):12069–12074.
- Domec, J.-C., Meinzer, F. C., Lachenbruch, B., and Housset, J. (2007). Dynamic variation in sapwood specific conductivity in six woody species. Tree Physiology, 27(10):1389–1400.
- Donovan, L. A., Richards, J. H., and Linton, M. J. (2003). Magnitude and Mechanisms of Disequilibrium Between Predawn Plant and Soil Water Potentials. Ecology, 84(2):463–470.
- Dralle, D. N., Hahm, W. J., Rempe, D. M., Karst, N. J., Thompson, S. E., and Dietrich, W. E. (2018). Quantification of the seasonal hillslope water storage that does not drive streamflow. Hydrological Processes, 32(13):1978–1992.

- Druhan, J. L., Fernandez, N., Wang, J., Dietrich, W. E., and Rempe, D. (2017). Seasonal shifts in the solute ion ratios of vadose zone rock moisture from the Eel River Critical Zone Observatory. Acta Geochimica, pages 1–4.
- Dunwiddie, P. W. and Bakker, J. D. (2011). The Future of Restoration and Management of Prairie-Oak Ecosystems in the Pacific Northwest. Northwest Science, 85(2):83–92.
- Dunwiddie, P. W., Bakker, J. D., Almaguer-Bay, M., and Sprenger, C. B. (2011). Environmental History of a Garry Oak/Douglas-Fir Woodland on Waldron Island, Washington. Northwest Science, 85(2):130–140.
- Dyer, A. R. and Rice, K. J. (1999). Effects of Competition on Resource Availability and Growth of a California Bunchgrass. Ecology, 80(8):2697–2710.
- Eliades, M., Bruggeman, A., Lubczynski, M. W., Christou, A., Camera, C., and Djuma, H. (2018). The water balance components of Mediterranean pine trees on a steep mountain slope during two hydrologically contrasting years. Journal of Hydrology, 562:712–724.
- Engber, E. A. and Varner, J. M. (2012). Predicting Douglas-fir Sapling Mortality Following Prescribed Fire in an Encroached Grassland. Restoration Ecology, 20(6):665–668.
- Erickson, W. R. (1996). Classification and interpretation of garry oak (Quercus garryana) plant communities and ecosystems in southwestern British Columbia. Thesis, University of Victoria.
- Ernst, W. G. and McLaughlin, R. J. (2012). Mineral parageneses, regional architecture, and tectonic evolution of Franciscan metagraywackes, Cape Mendocino-Garberville-Covelo 30 60 quadrangles, northwest California. Tectonics, 31(1):TC1001.
- Fan, Y., Clark, M., Lawrence, D. M., Swenson, S., Band, L. E., Brantley, S. L., Brooks, P. D., Dietrich, W. E., Flores, A., Grant, G., Kirchner, J. W., Mackay, D. S., McDonnell, J. J., Milly, P. C. D., Sullivan, P. L., Tague, C., Ajami, H., Chaney, N., Hartmann, A., Hazenberg, P., McNamara, J., Pelletier, J., Perket, J., Rouholahnejad-Freund, E., Wagener, T., Zeng, X., Beighley, E., Buzan, J., Huang, M., Livneh, B., Mohanty, B. P., Nijssen, B., Safeeq, M., Shen, C., Verseveld, W. v., Volk, J., and Yamazaki, D. (2019). Hillslope Hydrology in Global Change Research and Earth System Modeling. Water Resources Research.
- Farrell, C., Szota, C., and Arndt, S. K. (2017). Does the turgor loss point characterize drought response in dryland plants? Plant, Cell & Environment, 40(8):1500–1511.
- Fellows, A. W. and Goulden, M. L. (2016). Mapping and understanding dry season soil water drawdown by California montane vegetation. Ecohydrology, 10(1):e1772.
- Fieller, E. C., Hartley, H. O., and Pearson, E. S. (1957). Tests for Rank Correlation Coefficients. I. Biometrika, 44(3/4):470–481.

- Fisher, J. B., Baldocchi, D. D., Misson, L., Dawson, T. E., and Goldstein, A. H. (2007). What the towers don't see at night: nocturnal sap flow in trees and shrubs at two AmeriFlux sites in California. Tree Physiology, 27(4):597–610.
- Foley, J. A., DeFries, R., Asner, G. P., Barford, C., Bonan, G., Carpenter, S. R., Chapin, F. S., Coe, M. T., Daily, G. C., Gibbs, H. K., Helkowski, J. H., Holloway, T., Howard, E. A., Kucharik, C. J., Monfreda, C., Patz, J. A., Prentice, I. C., Ramankutty, N., and Snyder, P. K. (2005). Global Consequences of Land Use. Science, 309(5734):570–574.
- Franklin, J. and Dyrness, C. (1973). Natural vegetation of Oregon and Washington. Gen. Tech. Rep. PNW-GTR-008, USDA Forest Service.
- Franks, J. (2008). Competitive dynamics in a mixed Garry oak/Douglas-fir stand based on tree ring analysis. Master's thesis, University of Guelph (Canada), Canada.
- Frenkel, R. E. (1977). Ruderal Vegetation Along Some California Roadsides. University of California Press. Google-Books-ID: ill8s_V0SuwC.
- Fuchs, M. A. (2001). Towards a recovery strategy for Garry oak and associated ecosystems in Canada: ecological assessment and literature review. Environment Canada, Pacific and Yukon Region.
- Fuller, T. K., Perg, L. A., Willenbring, J. K., and Lepper, K. (2009). Field evidence for climate-driven changes in sediment supply leading to strath terrace formation. Geology, 37(5):467–470. 00048.
- Gaines, K. P., Stanley, J. W., Meinzer, F. C., McCulloh, K. A., Woodruff, D. R., Chen, W., Adams, T. S., Lin, H., and Eissenstat, D. M. (2016). Reliance on shallow soil water in a mixed-hardwood forest in central Pennsylvania. Tree Physiology, 36(4):444–458.
- Gedalof, Z., Pellatt, M., and Smith, D. J. (2006). From prairie to forest: three centuries of environmental change at Rocky Point, Vancouver Island, British Columbia. Northwest Science, 80(1):34–46.
- Gildehaus, S., Arabas, K., Larson, E., and Copes-Gerbitz, K. (2015). The Dendroclimatological Potential of Willamette Valley *Quercus garryana*. Tree-Ring Research, 71(1):13–23.
- Gilligan, L. A. and Muir, P. S. (2011). Stand Structures of Oregon White Oak Woodlands, Regeneration, and their Relationships to the Environment in Southwestern Oregon. Northwest Science, 85(2):141–158.
- Gordon, D. R., Menke, J. M., and Rice, K. J. (1989). Competition for soil water between annual plants and blue oak (*Quercus douglasii*) seedlings. Oecologia, 79(4):533–541.
- Gordon, D. R. and Rice, K. J. (1993). Competitive Effects of Grassland Annuals on Soil Water and Blue Oak (*Quercus Douglasii*) Seedlings. Ecology, 74(1):68–82.

- Gould, P. J., Harrington, C. A., and Devine, W. D. (2011). Growth of Oregon White Oak (*Quercus garryana*). Northwest Science, 85(2):159–171. 00008.
- Graham, R., Rossi, A., and Hubbert, R. (2010). Rock to regolith conversion: Producing hospitable substrates for terrestrial ecosystems. GSA Today, 20(2):4–9. 00040.
- Granger, D., Kirchner, J. W., and Finkel, R. (1996). Spatially averaged long-term erosion rates measured from in situ-produced cosmogenic nuclides in alluvial sediment. The Journal of Geology, 104(3):249–257.
- Granier, A. (1987). Evaluation of transpiration in a Douglas-fir stand by means of sap flow measurements. Tree Physiology, 3(4):309–320.
- Grant, G. E. and Dietrich, W. E. (2017). The frontier beneath our feet. Water Resources Research, 53(4):2605–2609.
- Griffin, D. and Anchukaitis, K. J. (2014). How unusual is the 20122014 California drought? Geophysical Research Letters, 41(24):2014GL062433.
- Griffin, J. R. (1973). Xylem Sap Tension in Three Woodland Oaks of Central California. Ecology, 54(1):152–159.
- Griffin, J. R. and Critchfield, W. B. (1972). The distribution of forest trees in California. Res. Paper PSW-RP-82. Berkeley, CA: Pacific Southwest Forest and Range Experiment Station, Forest Service, U.S. Department of Agriculture; 60 p, 082.
- Gromet, L. P., Haskin, L. A., Korotev, R. L., and Dymek, R. F. (1984). The North American shale composite: Its compilation, major and trace element characteristics. Geochimica et Cosmochimica Acta, 48(12):2469–2482.
- Gu, X., Rempe, D., and Brantley, S. L. (2016). Investigating the mechanisms of shale porosity development to understand hydrologic controls on hillslope scale weathering in a comparison across CZOs. In AGU Fall Meeting Abstracts, San Francisco, CA.
- Hahm, W., Dietrich, W., and Dawson, T. (2018). Controls on the distribution and resilience of *Quercus garryana*: ecophysiological evidence of oak’s water-limitation tolerance. Ecosphere, 9(5):e02218.
- Hahm, W. J., Dietrich, W. E., and Dawson, T. E. (2017a). Progressive depletion of stable isotopes recorded in a Mediterranean oak (*Q. garryana*) as a shallow saturated water source drains, leaving behind tightly held rock moisture. In Isotopes Switzerland 2017 Conference Proceedings, Mt. Verit, Ascona.
- Hahm, W. J., Dralle, D. N., Lovill, S., Rose, J., Dawson, T. E., and Dietrich, W. E. (2017b). Exploratory Tree Survey (2016 - Eel River Critical Zone Observatory - Sagehorn - Central Belt Melange, Franciscan Complex, Northern California Coast Ranges, USA), <http://dx.doi.org/10.4211/hs.7881821a5c0e4ae3822b96a59f4bf8b6>.

- Hahm, W. J., Dralle, D. N., Rempe, D. M., Bryk, A. B., Thompson, S. E., Dawson, T. E., and Dietrich, W. E. (2019a). Low subsurface water storage capacity relative to annual rainfall decouples Mediterranean plant productivity and water use from rainfall variability. Geophysical Research Letters.
- Hahm, W. J., Rempe, D. M., and Dietrich, W. E. (2017c). Direct measurements of seasonal groundwater and rock moisture storage in the deep Critical Zone reveal how lithology controls water availability and thus ecosystem characteristics in the Northern California Coast Ranges. In AGU-SEG Hydrogeophysics Workshop: Imaging the Critical Zone Abstracts, Stanford, CA.
- Hahm, W. J., Rempe, D. M., Dralle, D. N., Dawson, T. E., Lovill, S. M., Bryk, A. B., Bish, D. L., Schieber, J., and Dietrich, W. E. (2019b). Lithologically controlled subsurface critical zone thickness and water storage capacity determine regional plant community composition. Water Resources Research, 55.
- Hahm, W. J., Riebe, C. S., Lukens, C. E., and Araki, S. (2014). Bedrock composition regulates mountain ecosystems and landscape evolution. Proceedings of the National Academy of Sciences, 111(9):3338–3343. 00001 PMID: 24516144.
- Hargreaves, G. H. and Samani, Z. A. (1982). Estimating Potential Evapotranspiration. Journal of the Irrigation and Drainage Division, 108(3):225–230.
- Hargreaves, G. H. and Samani, Z. A. (1985). Reference crop evapotranspiration from temperature. Applied Engineering in Agriculture, 1(2).
- Hartmann, H., Moura, C. F., Anderegg, W. R. L., Ruehr, N. K., Salmon, Y., Allen, C. D., Arndt, S. K., Breshears, D. D., Davi, H., Galbraith, D., Ruthrof, K. X., Wunder, J., Adams, H. D., Bloemen, J., Cailleret, M., Cobb, R., Gessler, A., Grams, T. E. E., Jansen, S., Kautz, M., Lloret, F., and O'Brien, M. (2018). Research frontiers for improving our understanding of drought-induced tree and forest mortality. New Phytologist, 218(1):15–28.
- Hastings, M. S., Barnhart, S., and McBride, J. R. (1997). Restoration management of northern oak woodlands. In Proceedings of a symposium on oak woodlands: ecology, management, and urban interface issues, Gen. Tech. Rep. PSW-GTR-160. USDA Forest Service.
- Heilman, J. L., Litvak, M. E., McInnes, K. J., Kjølgaard, J. F., Kamps, R. H., and Schwinning, S. (2014). Water-storage capacity controls energy partitioning and water use in karst ecosystems on the Edwards Plateau, Texas. Ecohydrology, 7(1):127–138.
- Heinselman, M. L. (1981). Fire and Succession in the Conifer Forests of Northern North America. In Forest Succession, Springer Advanced Texts in Life Sciences, pages 374–405. Springer, New York, NY.

- Hellkvist, J., Richards, G. P., and Jarvis, P. G. (1974). Vertical Gradients of Water Potential and Tissue Water Relations in Sitka Spruce Trees Measured with the Pressure Chamber. Journal of Applied Ecology, 11(2):637–667.
- Hellmers, H., Horton, J. S., Juhren, G., and O’Keefe, J. (1955). Root systems of some chaparral plants in southern california. Ecology, 36(4):667. 00231.
- Hember, R. A., Kurz, W. A., and Coops, N. C. (2017). Relationships between individual-tree mortality and water-balance variables indicate positive trends in water stress-induced tree mortality across North America. Global Change Biology, 23(4):1691–1710.
- Heusser, L. E. (2000). Rapid oscillations in western North America vegetation and climate during oxygen isotope stage 5 inferred from pollen data from Santa Barbara Basin (Hole 893a). Palaeogeography, Palaeoclimatology, Palaeoecology, 161(34):407–421.
- Hibbs, D. E. and Yoder, B. J. (1993). Development of Oregon white oak seedlings. Northwest Science, 67(1).
- Holdridge, L. R. (1947). Determination of World Plant Formations From Simple Climatic Data. Science, 105(2727):367–368.
- Holland, P. G. and Steyn, D. G. (1975). Vegetational Responses to Latitudinal Variations in Slope Angle and Aspect. Journal of Biogeography, 2(3):179–183.
- Holmes, T. H. and Rice, K. J. (1996). Patterns of Growth and Soil-water Utilization in some Exotic Annuals and Native Perennial Bunchgrasses of California. Annals of Botany, 78(2):233–243.
- Homer, C. G., Dewitz, J. A., Yang, L., Jin, S., Danielson, P., Xian, G., Coulston, J., Herold, N. D., Wickham, J. D., and Megown, K. (2015). Completion of the 2011 National Land Cover Database for the conterminous United States-Representing a decade of land cover change information. Photogrammetric Engineering and Remote Sensing, 81(5):345–354.
- Huete, A., Didan, K., Miura, T., Rodriguez, E. P., Gao, X., and Ferreira, L. G. (2002). Overview of the radiometric and biophysical performance of the MODIS vegetation indices. Remote Sensing of Environment, 83(12):195–213.
- Huete, A. R., Didan, K., Shimabukuro, Y. E., Ratana, P., Saleska, S. R., Hutyrá, L. R., Yang, W., Nemani, R. R., and Myneni, R. (2006). Amazon rainforests green-up with sunlight in dry season. Geophysical Research Letters, 33(6).
- Irwin, W. P. (1960). Geologic reconnaissance of the northern Coast Ranges and Klamath Mountains, California, with a summary of the mineral resources. San Francisco. 00193.
- Ison, N. T., Feyerherm, A. M., and Bark, L. D. (1971). Wet Period Precipitation and the Gamma Distribution. Journal of Applied Meteorology, 10(4):658–665.

- Jackson, P. A. and Spomer, G. G. (1979). Biophysical Adaptations of Four Western Conifers to Habitat Water Conditions. Botanical Gazette, 140(4):428–432.
- Jayko, A. S., Blake, M. C., McLaughlin, R. J., Ohlin, H. N., Ellen, S. D., and Kelsey, H. M. (1989). Reconnaissance geologic map of the Covelo 30- by 60-minute Quadrangle, Northern California. Technical Report MF - 2001, United States Geological Survey. 00011.
- Johnson, D. M., McCulloh, K. A., Woodruff, D. R., and Meinzer, F. C. (2012). Evidence for xylem embolism as a primary factor in dehydration-induced declines in leaf hydraulic conductance. Plant, Cell & Environment, 35(4):760–769. 00039.
- Johnson, D. M., Woodruff, D. R., McCulloh, K. A., and Meinzer, F. C. (2009). Leaf hydraulic conductance, measured in situ, declines and recovers daily: leaf hydraulics, water potential and stomatal conductance in four temperate and three tropical tree species. Tree Physiology, 29(7):879–887.
- Johnson, S. (1979). The land-use history of the Coast Range Preserve, Mendocino County, California. Master's thesis, San Francisco State University.
- Joly, R. J. and Zaerr, J. B. (1987). Alteration of Cell-Wall Water Content and Elasticity in Douglas-Fir during Periods of Water Deficit. Plant Physiology, 83(2):418–422.
- Jones, D. P. and Graham, R. C. (1993). Water-Holding Characteristics of Weathered Granitic Rock in Chaparral and Forest Ecosystems. Soil Science Society of America Journal, 57(1):256–261.
- Jordan, D. A. and Vander Gugten, K. (2012). Dendrochronological Potential of *Quercus garryana*, Saltspring Island, British Columbia. Tree-Ring Research, 68(1):51–58.
- Kelly, A. E. and Goulden, M. L. (2008). Rapid shifts in plant distribution with recent climate change. Proceedings of the National Academy of Sciences, 105:11823–11826. 00303.
- Kelly, J. (2016). Physiological responses to drought in healthy and stressed trees: a comparison of four species in Oregon, USA. PhD thesis, Lund University.
- Kelsey, H. M. (1978). Earthflows in Franciscan melange, Van Duzen River basin, California. Geology, 6(6):361–364. 00051.
- Kim, H., Bishop, J. K. B., Dietrich, W. E., and Fung, I. Y. (2014). Process dominance shift in solute chemistry as revealed by long-term high-frequency water chemistry observations of groundwater flowing through weathered argillite underlying a steep forested hillslope. Geochimica et Cosmochimica Acta, 140:1–19. 00002.
- Klos, P. Z., Goulden, M. L., Riebe, C. S., Tague, C. L., OGeen, A. T., Flinchum, B. A., Safeeq, M., Conklin, M. H., Hart, S. C., Berhe, A. A., Hartsough, P. C., Holbrook, W. S., and Bales, R. C. (2018). Subsurface plant-accessible water in mountain ecosystems with a Mediterranean climate. Wiley Interdisciplinary Reviews: Water, 5(3):e1277.

- Kruckeberg, A. R. (1985). California Serpentes: Flora, Vegetation, Geology, Soils, and Management Problems. University of California Press. Google-Books-ID: 6OYD-NTs4dpgC.
- Kruckeberg, A. R. (2004). Geology And Plant Life: The Effects Of Landforms And Rock Types On Plants. University of Washington Press. 00147.
- Krygier, J. T. (1971). Project Completion Report on Comparative Water Loss of Douglas-fir and Oregon White Oak: Part of the Study of Hydrology of Water Yield Prediction. Water Resources Research Institute and School of Forestry, Oregon State University.
- Kubiske, M. E. and Abrams, M. D. (1990). Pressure-volume relationships in non-rehydrated tissue at various water deficits. Plant, Cell & Environment, 13(9):995–1000.
- Kueppers, L. M., Snyder, M. A., Sloan, L. C., Zavaleta, E. S., and Fulfroost, B. (2005). Modeled regional climate change and California endemic oak ranges. Proceedings of the National Academy of Sciences, 102(45):16281–16286.
- LaDochy, S., Medina, R., and Patzert, W. (2007). Recent California climate variability:: spatial and temporal patterns in temperature trends. Climate Research, 33(2):159–169.
- Laio, F., Porporato, A., Ridolfi, L., and Rodriguez-Iturbe, I. (2001). Plants in water-controlled ecosystems: active role in hydrologic processes and response to water stress: II. Probabilistic soil moisture dynamics. Advances in Water Resources, 24(7):707–723.
- Langenheim, V. E., Jachens, R. C., Wentworth, C. M., and McLaughlin, R. J. (2013). Previously unrecognized regional structure of the Coastal Belt of the Franciscan Complex, northern California, revealed by magnetic data. Geosphere, 9(6):1514–1529. 00001.
- Lebedeva, M. I. and Brantley, S. L. (2013). Exploring geochemical controls on weathering and erosion of convex hillslopes: beyond the empirical regolith production function. Earth Surface Processes and Landforms, 38(15):1793–1807.
- Lei, H., Milota, M. R., and Gartner, B. L. (1996). Between- and Within-Tree Variation in the Anatomy and Specific Gravity of Wood in Oregon White Oak (*Quercus Garryana* Dougl.). IAWA Journal, 17(4):445–461.
- Lenihan, J. M., Drapek, R., Bachelet, D., and Neilson, R. P. (2003). Climate Change Effects on Vegetation Distribution, Carbon, and Fire in California. Ecological Applications, 13(6):1667–1681.
- Lewis, D. C. and Burgy, R. H. (1964). The Relationship between oak tree roots and ground-water in fractured rock as determined by tritium tracing. Journal of Geophysical Research, 69(12):2579–2588.

- Lightfoot, K. G. and Parrish, O. (2009). California Indians and Their Environment: An Introduction. University of California Press. Google-Books-ID: 2qwMAQAAMAAJ.
- Link, P., Simonin, K., Maness, H., Oshun, J., Dawson, T., and Fung, I. (2014). Species differences in the seasonality of evergreen tree transpiration in a Mediterranean climate: Analysis of multiyear, half-hourly sap flow observations. Water Resources Research, 50(3):1869–1894. 00002.
- Little, E. L. (1971). Atlas of United States trees. Washington, D.C. : U.S. Dept. of Agriculture, Forest Service.
- Loarie, S. R., Duffy, P. B., Hamilton, H., Asner, G. P., Field, C. B., and Ackerly, D. D. (2009). The velocity of climate change. Nature, 462(7276):1052–1055.
- Lock, J., Kelsey, H., Furlong, K., and Woolace, A. (2006). Late Neogene and Quaternary landscape evolution of the northern California Coast Ranges: Evidence for Mendocino triple junction tectonics. Geological Society of America Bulletin, 118(9-10):1232–1246. 00045.
- Lovill, S., Hahm, W. J., and Dietrich, W. E. (2018). Drainage from the critical zone: lithologic controls on the persistence and spatial extent of wetted channels during the summer dry season. Water Resources Research, 54(8):5702–5726.
- Lucas, J. D. and Lacourse, T. (2013). Holocene vegetation history and fire regimes of *Pseudotsuga menziesii* forests in the Gulf Islands National Park Reserve, southwestern British Columbia, Canada. Quaternary Research, 79(3):366–376.
- Luce, C. H., Vose, J. M., Pederson, N., Campbell, J., Millar, C., Kormos, P., and Woods, R. (2016). Contributing factors for drought in United States forest ecosystems under projected future climates and their uncertainty. Forest Ecology and Management, 380:299–308.
- Mackey, B. H. and Roering, J. J. (2011). Sediment yield, spatial characteristics, and the long-term evolution of active earthflows determined from airborne LiDAR and historical aerial photographs, Eel River, California. Geological Society of America Bulletin, 123(7-8):1560–1576. 00031.
- Maertens, T. B. (2008). The growth-climate relationship of Oregon white oak (*Quercus garryana*). Master's thesis, University of Guelph (Canada), Canada.
- Marlon, J. R., Bartlein, P. J., Carcaillet, C., Gavin, D. G., Harrison, S. P., Higuera, P. E., Joos, F., Power, M. J., and Prentice, I. C. (2008). Climate and human influences on global biomass burning over the past twomillennia. Nature Geoscience, 1(10):697–702.
- Marshall, D. C. (1958). Measurement of Sap Flow in Conifers by Heat Transport. 1. Plant Physiology, 33(6):385–396.

- Marshall, J. G. and Dumbroff, E. B. (1999). Turgor Regulation via Cell Wall Adjustment in White Spruce. Plant Physiology, 119(1):313–320.
- Martens, B., Miralles, D. G., Lievens, H., van der Schalie, R., de Jeu, R. A. M., Fernandez-Prieto, D., Beck, H. E., Dorigo, W. A., and Verhoest, N. E. C. (2017). GLEAMv3: satellite-based land evaporation and root-zone soil moisture. Geosci. Model Dev., 10(5):1903–1925.
- Martin, R. E. and Sapis, D. B. (1991). Fires as agents of biodiversity: Pyrodiversity promotes biodiversity. In Proceedings of the Symposium on Biodiversity of Northwestern California, Santa Rosa, CA.
- Martínez-Vilalta, J. and Garcia-Forner, N. (2017). Water potential regulation, stomatal behaviour and hydraulic transport under drought: deconstructing the iso/anisohydric concept. Plant, Cell & Environment, 40(6):962–976.
- McCune, J. L., Pellatt, M. G., and Vellend, M. (2013). Multidisciplinary synthesis of long-term humanecosystem interactions: A perspective from the Garry oak ecosystem of British Columbia. Biological Conservation, 166:293–300.
- McDadi, O. and Hebda, R. J. (2008). Change in historic fire disturbance in a Garry oak (*Quercus garryana*) meadow and Douglas-fir (*Pseudotsuga menziesii*) mosaic, University of Victoria, British Columbia, Canada: A possible link with First Nations and Europeans. Forest Ecology and Management, 256(10):1704–1710.
- McDonnell, J. J., Evaristo, J., Bladon, K. D., Buttle, J., Creed, I. F., Dymond, S. F., Grant, G., Iroume, A., Jackson, C. R., Jones, J. A., Maness, T., McGuire, K. J., Scott, D. F., Segura, C., Sidle, R. C., and Tague, C. (2018). Water sustainability and watershed storage. Nature Sustainability, 1(8):378.
- McDowell, N., Pockman, W. T., Allen, C. D., Breshears, D. D., Cobb, N., Kolb, T., Plaut, J., Sperry, J., West, A., Williams, D. G., and Yezpe, E. A. (2008). Mechanisms of plant survival and mortality during drought: why do some plants survive while others succumb to drought? New Phytologist, 178(4):719–739.
- McIntyre, P. J., Thorne, J. H., Dolanc, C. R., Flint, A. L., Flint, L. E., Kelly, M., and Ackerly, D. D. (2015). Twentieth-century shifts in forest structure in California: Denser forests, smaller trees, and increased dominance of oaks. Proceedings of the National Academy of Sciences, 112(5):1458–1463.
- McLaughlin, R. J., Sliter, W. V., Frederiksen, N. O., Harbert, W. P., and McCulloch, D. S. (1994). Plate motions recorded in tectonostratigraphic terranes of the Franciscan complex and evolution of the Mendocino triple junction, northwestern California. Technical Report 1997, USGS.

- McNamara, J. P., Tetzlaff, D., Bishop, K., Soulsby, C., Seyfried, M., Peters, N. E., Aulenbach, B. T., and Hooper, R. (2011). Storage as a Metric of Catchment Comparison. Hydrological Processes, 25(21):3364–3371.
- Meinzer, F. C. (1982). The effect of vapor pressure on stomatal control of gas exchange in Douglas fir (*Pseudotsuga menziesii*) saplings. Oecologia, 54(2):236–242.
- Meinzer, F. C., Bond, B. J., Warren, J. M., and Woodruff, D. R. (2005). Does water transport scale universally with tree size? Functional Ecology, 19(4):558–565.
- Meinzer, F. C., Rundel, P. W., Sharifi, M. R., and Nilsen, E. T. (1986). Turgor and osmotic relations of the desert shrub *Larrea tridentata*. Plant, Cell & Environment, 9(6):467–475.
- Meinzer, F. C., Woodruff, D. R., Marias, D. E., McCulloh, K. A., and Sevanto, S. (2014). Dynamics of leaf water relations components in co-occurring iso- and anisohydric conifer species. Plant, Cell & Environment, 37(11):2577–2586.
- Meinzer, F. C., Woodruff, D. R., Marias, D. E., Smith, D. D., McCulloh, K. A., Howard, A. R., and Magedman, A. L. (2016). Mapping hydroscares along the iso- to anisohydric continuum of stomatal regulation of plant water status. Ecology Letters, 19(11):1343–1352.
- Mensing, S. (2005). The history of oak woodlands in California, part I: the paleoecologic record. California Geographer, 45(6).
- Mensing, S. (2006). The history of oak woodlands in California, part II: the native American and historic period. The California Geographer, 46(5).
- Merz, M., Donahue, R., and Poulson, M. (2017). Physiological Response of Garry oak (*Quercus garryana*) Seedlings to Drought. Northwest Science, 91(2).
- Miller, C. (2002). Management requirements for conservation of Garry oak and associated ecosystems in British Columbia. Master's thesis, Royal Roads University (Canada), Canada.
- Miller, G. R., Chen, X., Rubin, Y., Ma, S., and Baldocchi, D. D. (2010). Groundwater uptake by woody vegetation in a semiarid oak savanna. Water Resources Research, 46(10):W10503. 00059.
- Milly, P. C. D. (1994). Climate, interseasonal storage of soil water, and the annual water balance. Advances in Water Resources, 17(1):19–24.
- Milly, P. C. D. and Dunne, K. A. (1994). Sensitivity of the Global Water Cycle to the Water-Holding Capacity of Land. Journal of Climate, 7(4):506–526.
- Minore, D. (1968). Effects of artificial flooding on seedling survival and growth of six northwestern tree species. 00020.

- Minore, D. (1979). Comparative autecological characteristics of northwestern tree species literature review. Gen. Tech. Rep. PNW-GTR-087, USDA Forest Service.
- Miralles, D. G., Gash, J. H., Holmes, T. R. H., de Jeu, R. A. M., and Dolman, A. J. (2010). Global canopy interception from satellite observations. Journal of Geophysical Research: Atmospheres, 115(D16):D16122.
- Mitchell, P. J., Veneklaas, E. J., Lambers, H., and Burgess, S. S. O. (2008). Leaf water relations during summer water deficit: differential responses in turgor maintenance and variation in leaf structure among different plant communities in south-western Australia. Plant, Cell & Environment, 31(12):1791–1802.
- Mohr, J. A., Whitlock, C., and Skinner, C. N. (2000). Postglacial vegetation and fire history, eastern Klamath Mountains, California, USA. The Holocene, 10(5):587–601.
- Mooney, H. A., Parsons, D. J., and Kummerow, J. (1974). Plant Development in Mediterranean Climates. In Lieth, H., editor, Phenology and Seasonality Modeling, Ecological Studies, pages 255–267. Springer Berlin Heidelberg, Berlin, Heidelberg.
- Moore, G. W., Bond, B. J., Jones, J. A., Phillips, N., and Meinzer, F. C. (2004). Structural and compositional controls on transpiration in 40- and 450-year-old riparian forests in western Oregon, USA. Tree Physiology, 24(5):481–491.
- Mote, P. W. and Salathé, E. P. (2010). Future climate in the Pacific Northwest. Climatic Change, 102(1-2):29–50.
- Mu, Q., Heinsch, F. A., Zhao, M., and Running, S. W. (2007). Development of a global evapotranspiration algorithm based on MODIS and global meteorology data. Remote Sensing of Environment, 111(4):519–536.
- Murphy, J. M., Sexton, D. M. H., Barnett, D. N., Jones, G. S., Webb, M. J., Collins, M., and Stainforth, D. A. (2004). Quantification of modelling uncertainties in a large ensemble of climate change simulations. Nature, 430(7001):768–772.
- National Research Council (2012). Challenges and Opportunities in the Hydrologic Sciences. The National Academies Press, Washington, DC.
- Office of Governor, California (2015). Governor Brown Directs First Ever Statewide Mandatory Water Reductions (Newsroom). 00000.
- Oshun, J., Dietrich, W. E., Dawson, T. E., and Fung, I. (2016). Dynamic, structured heterogeneity of water isotopes inside hillslopes. Water Resources Research, 52(1):164–189. 00001.
- Parker, A. J. (1982). The Topographic Relative Moisture Index: An Approach to Soil-Moisture Assessment in Mountain Terrain. Physical Geography, 3(2):160–168.

- Parks Canada (2006a). Recovery Strategy for Multi-Species at Risk in Garry Oak Woodlands in Canada. Technical report, Parks Canada.
- Parks Canada (2006b). Recovery Strategy for Multi-Species at Risk in Maritime Meadows associated with Garry Oak Ecosystems in Canada. Technical report, Parks Canada.
- Pellatt, M. G. and Gedalof, Z. (2014). Environmental change in Garry oak (*Quercus garryana*) ecosystems: the evolution of an eco-cultural landscape. Biodiversity and Conservation, 23(8):2053–2067.
- Pellatt, M. G., Hebda, R. J., and Mathewes, R. W. (2001). High-resolution Holocene vegetation history and climate from Hole 1034b, ODP leg 169s, Saanich Inlet, Canada. Marine Geology, 174(14):211–222.
- Pellatt, M. G., McCoy, M. M., and Mathewes, R. W. (2015). Paleoecology and fire history of Garry oak ecosystems in Canada: implications for conservation and environmental management. Biodiversity and Conservation, 24(7):1621–1639.
- Pfister, L., Martínez-Carreras, N., Hissler, C., Klaus, J., Carrer, G. E., Stewart, M. K., and McDonnell, J. J. (2017). Bedrock geology controls on catchment storage, mixing, and release: A comparative analysis of 16 nested catchments. Hydrological Processes, 31(10):1828–1845.
- Phillips, N., Bond, B. J., McDowell, N. G., Ryan, M. G., and Schauer, A. (2003a). Leaf area compounds height-related hydraulic costs of water transport in Oregon White Oak trees. Functional Ecology, 17(6):832–840. 00047.
- Phillips, N. G., Ryan, M. G., Bond, B. J., McDowell, N. G., Hinckley, T. M., and Čermák, J. (2003b). Reliance on stored water increases with tree size in three species in the Pacific Northwest. Tree Physiology, 23(4):237–245.
- Polis, G. A. (1999). Why Are Parts of the World Green? Multiple Factors Control Productivity and the Distribution of Biomass. Oikos, 86(1):3–15.
- Poore, R. Z., Dowsett, H., Barron, J., Heusser, L., Ravelo, A., and Mix, A. (2000). Multi-proxy record of the last interglacial (MIS 5e) off central and northern California, U.S.A., from Ocean Drilling Program sites 1018 and 1020. USGS Numbered Series 1632, U.S. Geological Survey.
- Popenoe, J. H., Bevis, K. A., Gordon, B. R., Sturhan, N. K., and Hauxwell, D. L. (1992). Soil-Vegetation Relationships in Franciscan Terrain of Northwestern California. Soil Science Society of America Journal, 56(6):1951–1959.
- Porporato, A., Daly, E., and Rodriguez-Iturbe, I. (2004). Soil Water Balance and Ecosystem Response to Climate Change. The American Naturalist, 164(5):625–632.

- Porporato, A., Laio, F., Ridolfi, L., and Rodriguez-Iturbe, I. (2001). Plants in water-controlled ecosystems: active role in hydrologic processes and response to water stress. Advances in Water Resources, 24(7):725–744.
- Prentice, I. C., Cramer, W., Harrison, S. P., Leemans, R., Monserud, R. A., and Solomon, A. M. (1992). Special Paper: A Global Biome Model Based on Plant Physiology and Dominance, Soil Properties and Climate. Journal of Biogeography, 19(2):117–134.
- Pypker, T. G., Bond, B. J., Link, T. E., Marks, D., and Unsworth, M. H. (2005). The importance of canopy structure in controlling the interception loss of rainfall: Examples from a young and an old-growth Douglas-fir forest. Agricultural and Forest Meteorology, 130(1):113–129.
- Rantz, S. (1968). Average annual precipitation and runoff in north coastal California. USGS Numbered Series 298, USGS.
- Reed, L. J. and Sugihara, N. G. (1987). Northern oak woodlands: ecosystem in jeopardy or is it already too late? Technical report, AGRIS.
- Reid, L. M. and Lewis, J. (2009). Rates, timing, and mechanisms of rainfall interception loss in a coastal redwood forest. Journal of Hydrology, 375(34):459–470.
- Rempe, D. M. and Dietrich, W. E. (2014). A bottom-up control on fresh-bedrock topography under landscapes. Proceedings of the National Academy of Sciences, 111(18):6576–6581. 00000 PMID: 24760824.
- Rempe, D. M. and Dietrich, W. E. (2018). Direct observations of rock moisture, a hidden component of the hydrologic cycle. Proceedings of the National Academy of Sciences, 115(11):2664–2669.
- Restaino, C. M., Peterson, D. L., and Littell, J. (2016). Increased water deficit decreases Douglas fir growth throughout western US forests. Proceedings of the National Academy of Sciences, 113(34):9557–9562.
- Ricklefs, R. E. (2008). The Economy of Nature. W.H. Freeman. Google-Books-ID: nqFLj-ZLwKxIC.
- Riebe, C. S., Hahm, W. J., and Brantley, S. L. (2017). Controls on deep critical zone architecture: a historical review and four testable hypotheses. Earth Surface Processes and Landforms, 42(1):128–156.
- Ritchie, G. A. and Shula, R. G. (1984). Seasonal Changes of Tissue-Water Relations in Shoots and Root Systems of Douglas-fir Seedlings. Forest Science, 30(2):538–548.
- Rittiman, C. and Thorson, T. (2001). Soil Survey of Mendocino County. California, Western Part, Mendocino County Resource Conservation District. 00055.

- Robinson, N. P., Allred, B. W., Smith, W. K., Jones, M. O., Moreno, A., Erickson, T. A., Naugle, D. E., and Running, S. W. (2018). Terrestrial primary production for the conterminous United States derived from Landsat 30 m and MODIS 250 m. Remote Sensing in Ecology and Conservation, 4(3):264–280.
- Rodriguez-Iturbe, I., D’Odorico, P., Laio, F., Ridolfi, L., and Tamea, S. (2007). Challenges in humid land ecohydrology: Interactions of water table and unsaturated zone with climate, soil, and vegetation. Water Resources Research, 43(9):W09301.
- Roering, J. J., Mackey, B. H., Handwerger, A. L., Booth, A. M., Schmidt, D. A., Bennett, G. L., and Cerovski-Darriau, C. (2015). Beyond the angle of repose: A review and synthesis of landslide processes in response to rapid uplift, Eel River, Northern California. Geomorphology, 236:109–131. 00000.
- Roering, J. J., Stimely, L. L., Mackey, B. H., and Schmidt, D. A. (2009). Using DInSAR, airborne LiDAR, and archival air photos to quantify landsliding and sediment transport. Geophysical Research Letters, 36(19):L19402.
- Rose, K., Graham, R., and Parker, D. (2003). Water source utilization by *Pinus jeffreyi* and *Arctostaphylos patula* on thin soils over bedrock. Oecologia, 134(1):46–54. 00044.
- Rouholahnejad Freund, E. and Kirchner, J. W. (2017). A Budyko framework for estimating how spatial heterogeneity and lateral moisture redistribution affect average evapotranspiration rates as seen from the atmosphere. Hydrol. Earth Syst. Sci., 21(1):217–233.
- Rupp, D. E., Abatzoglou, J. T., Hegewisch, K. C., and Mote, P. W. (2013). Evaluation of CMIP5 20th century climate simulations for the Pacific Northwest USA. Journal of Geophysical Research: Atmospheres, 118(19):2013JD020085.
- Ryu, Y., Baldocchi, D. D., Kobayashi, H., van Ingen, C., Li, J., Black, T. A., Beringer, J., van Gorsel, E., Knohl, A., Law, B. E., and Rouspard, O. (2011). Integration of MODIS land and atmosphere products with a coupled-process model to estimate gross primary productivity and evapotranspiration from 1 km to global scales. Global Biogeochemical Cycles, 25(4):GB4017.
- Salve, R., Rempe, D. M., and Dietrich, W. E. (2012). Rain, rock moisture dynamics, and the rapid response of perched groundwater in weathered, fractured argillite underlying a steep hillslope. Water Resources Research, 48(11):W11528. 00021.
- Sayama, T., McDonnell, J. J., Dhakal, A., and Sullivan, K. (2011). How much water can a watershed store? Hydrological Processes, 25(25):3899–3908.
- Scanlon, T. M., Caylor, K. K., Levin, S. A., and Rodriguez-Iturbe, I. (2007). Positive feedbacks promote power-law clustering of Kalahari vegetation. Nature; London, 449(7159):209–12.

- Schieber, J. (2010). Common Themes in the Formation and Preservation of Intrinsic Porosity in Shales and Mudstones - Illustrated with Examples Across the Phanerozoic. In SPE Unconventional Gas Conference. Society of Petroleum Engineers.
- Scholander, P. F., Bradstreet, E. D., Hemmingsen, E. A., and Hammel, H. T. (1965). Sap Pressure in Vascular Plants: Negative hydrostatic pressure can be measured in plants. Science, 148(3668):339–346. 00000.
- Scholl, D. G. (1976). Soil Moisture Flux and Evapotranspiration Determined from Soil Hydraulic Properties in a Chaparral Stand 1. Soil Science Society of America Journal, 40(1):14–18.
- Schriver, M., Sherriff, R. L., Varner, J. M., Quinn-Davidson, L., and Valachovic, Y. (2018). Age and stand structure of oak woodlands along a gradient of conifer encroachment in northwestern California. Ecosphere, 9(10):e02446.
- Schwinning, S. (2010). The ecohydrology of roots in rocks. Ecohydrology, 3(2):238–245.
- Seidl, M. and Dietrich, W. E. (1992). The problem of channel erosion into bedrock. In Catena Supplement, volume 23, pages 101–124, Cremlingen. Verlag.
- Sevruk, B. (1982). Methods of correction for systematic error in point precipitation measurement for operational use. Secretariat of the World Meteorological Organization. Google-Books-ID: epgRAQAIAAJ.
- Simonin, K. A., Link, P., Rempe, D., Miller, S., Oshun, J., Bode, C., Dietrich, W. E., Fung, I., and Dawson, T. E. (2014). Vegetation induced changes in the stable isotope composition of near surface humidity. Ecohydrology, 7(3):936–949. 00005.
- Sims, D. A., Rahman, A. F., Cordova, V. D., ElMasri, B. Z., Baldocchi, D. D., Flanagan, L. B., Goldstein, A. H., Hollinger, D. Y., Misson, L., Monson, R. K., Oechel, W. C., Schmid, H. P., Wofsy, S. C., and Xu, L. (2006). On the use of MODIS EVI to assess gross primary productivity of North American ecosystems. Journal of Geophysical Research: Biogeosciences, 111(G4).
- Smith, S. D., Herr, C. A., Leary, K. L., and Piorkowski, J. M. (1995). Soil-plant water relations in a Mojave Desert mixed shrubcommunity: a comparison of three geomorphic surfaces. Journal of Arid Environments, 29(3):339–351. 00084.
- Smith, S. J., Edmonds, J., Hartin, C. A., Mundra, A., and Calvin, K. (2015). Near-term acceleration in the rate of temperature change. Nature Climate Change, 5(4):333–336.
- Smith, T. J., McNamara, J. P., Flores, A. N., Gribb, M. M., Aishlin, P. S., and Benner, S. G. (2011). Small soil storage capacity limits benefit of winter snowpack to upland vegetation. Hydrological Processes, 25(25):3858–3865.

- Snyder, R. (2005). The ASCE standardized reference evapotranspiration equation. Technical Report 173, ASCE.
- Soil Survey Staff (2018). Soil Survey Geographic (SSURGO) Database for California.
- Sprague, F. L. and Hansen, H. P. (1946). Forest Succession in the McDonald Forest, Willamette Valley, Oregon. Northwest science, 20(4):89–98.
- St. Clair, J., Moon, S., Holbrook, W. S., Perron, J. T., Riebe, C. S., Martel, S. J., Carr, B., Harman, C., Singha, K., and Richter, D. d. (2015). Geophysical imaging reveals topographic stress control of bedrock weathering. Science, 350(6260):534–538. 00001 PMID: 26516279.
- Stein, W. (1990). *Quercus garryana* Dougl. ex Hook. Oregon White Oak. In Burns, RM and Honkala, BH, tech. coords. Silvics of North America, Volume II: Hardwoods, volume 2 of Agricultural Handbook. USDA Forest Service, Washington, D.C.
- Stephenson, N. L. (1990). Climatic control of vegetation distribution: the role of the water balance. The American Naturalist, 135(5):649–670. 00430 ArticleType: research-article / Full publication date: May, 1990 / Copyright 1990 The University of Chicago.
- Sternberg, P. D., Anderson, M. A., Graham, R. C., Beyers, J. L., and Tice, K. R. (1996). Root distribution and seasonal water status in weathered granitic bedrock under chaparral. Geoderma, 72:89–98.
- Stock, G. M., Anderson, R. S., and Finkel, R. C. (2005). Rates of erosion and topographic evolution of the Sierra Nevada, California, inferred from cosmogenic ²⁶Al and ¹⁰Be concentrations. Earth Surface Processes and Landforms, 30(8):985–1006. 00052.
- Stone, J. O. (2000). Air pressure and cosmogenic isotope production. Journal of Geophysical Research: Solid Earth, 105(B10):23753–23759.
- Sugihara, N. G., van Wagtenonk, J., and Fites-Kaufman, J. (2006). Fire as an Ecological Process. In Fire in California's Ecosystems. University of California Press.
- Swain, D. L., Langenbrunner, B., Neelin, J. D., and Hall, A. (2018). Increasing precipitation volatility in twenty-first-century California. Nature Climate Change, 8(5):427–433.
- Swarowsky, A., Dahlgren, R. A., Tate, K. W., Hopmans, J. W., and O'Geen, A. T. (2011). Catchment-Scale Soil Water Dynamics in a Mediterranean-Type Oak Woodland. Vadose Zone Journal, 10(3):800–815. 00021.
- Syvitski, J. P. and Morehead, M. D. (1999). Estimating river-sediment discharge to the ocean: application to the Eel margin, northern California. Marine Geology, 154(14):13–28.

- Tetzlaff, D., McNamara, J. P., and Carey, S. K. (2011). Measurements and modelling of storage dynamics across scales. Hydrological Processes, 25(25):3831–3835.
- Thilenius, J. F. (1968). The Quercus Garryana Forests of the Willamette Valley, Oregon. Ecology, 49(6):1124–1133.
- Thompson, J. (2007). Move over, Douglas-fir: Oregon white oaks need room to grow. Technical Report 98, USDA Forest Service, Portland, OR, USA.
- Thysell, D. R. and Carey, A. B. . (2001). Quercus garryana communities in the Puget Trough, Washington. Northwest Science, 75(3):219–235.
- Trauernicht, C., Brook, B. W., Murphy, B. P., Williamson, G. J., and Bowman, D. M. J. S. (2015). Local and global pyrogeographic evidence that indigenous fire management creates pyrodiversity. Ecology and Evolution, 5(9):1908–1918.
- Ugolini, F. C. and Schlichte, A. K. (1973). The Effect Of Holocene Environmental Changes On Selected Western Washington Soils. Soil Science, 116(3):218–227.
- US Forest Service (2016a). 2016 Aerial Survey Results: California. Technical Report R5-PR-034, USDA.
- US Forest Service (2016b). New Aerial Survey Identifies More Than 100 Million Dead Trees in California. Technical report, USDA Office of Communications.
- Vermeesch, P. (2007). CosmoCalc: An Excel add-in for cosmogenic nuclide calculations. Geochemistry, Geophysics, Geosystems, 8(8).
- Walker, I. R. and Pellatt, M. G. (2003). Climate Change in Coastal British Columbia A Paleoenvironmental Perspective. Canadian Water Resources Journal / Revue canadienne des ressources hydriques, 28(4):531–566.
- Wang-Erlandsson, L., Bastiaanssen, W. G. M., Gao, H., Jägermeyr, J., Senay, G. B., vanDijk, A. I. J. M., Guerschman, J. P., Keys, P. W., Gordon, L. J., and Savenije, H. H. G. (2016). Global root zone storage capacity from satellite-based evaporation. Hydrol. Earth Syst. Sci., 20(4):1459–1481.
- Warton, D. I., Wright, I. J., Falster, D. S., and Westoby, M. (2006). Bivariate line-fitting methods for allometry. Biological Reviews, 81(2):259–291. 00819.
- West, A. G., Dawson, T. E., February, E. C., Midgley, G. F., Bond, W. J., and Aston, T. L. (2012). Diverse functional responses to drought in a Mediterranean-type shrubland in South Africa. New Phytologist, 195(2):396–407.

- West, G. J. (1982). Pollen analysis of sediments from Tule Lake: A record of Holocene vegetation/climatic changes in the Mendocino National Forest, California. In Proceedings, Symposium of Holocene Climate and Archeology of Californias Coast and Desert, San Diego, California.
- White, A., Briles, C., and Whitlock, C. (2015). Postglacial vegetation and fire history of the southern Cascade Range, Oregon. Quaternary Research, 84(3):348–357.
- Whittaker, R. H. (1975). Communities and Ecosystems. Macmillan Company, New York, 2 edition.
- Williams, C. B., Reese Næsborg, R., Dawson, T. E., and Cavaleri, M. (2017). Coping with gravity: the foliar water relations of giant sequoia. Tree Physiology, pages 1–15.
- Witty, J. H., Graham, R. C., Hubbert, K. R., Doolittle, J. A., and Wald, J. A. (2003). Contributions of water supply from the weathered bedrock zone to forest soil quality. Geoderma, 114(34):389–400.
- Woodruff, D. R., Mcculloh, K. A., Warren, J. M., Meinzer, F. C., and Lachenbruch, B. (2007). Impacts of tree height on leaf hydraulic architecture and stomatal control in Douglas-fir. Plant, Cell & Environment, 30(5):559–569.
- Woodward, F. I. (1987). Climate and Plant Distribution. Cambridge University Press. Google-Books-ID: 0Ld1h0MT3oIC.
- Xu, L. and Baldocchi, D. D. (2003). Seasonal trends in photosynthetic parameters and stomatal conductance of blue oak (*Quercus douglasii*) under prolonged summer drought and high temperature. Tree Physiology, 23(13):865–877. 00233 PMID: 14532010.
- Yang, D., Goodison, B. E., Metcalfe, J. R., Golubev, V. S., Bates, R., Pangburn, T., and Hanson, C. L. (1998). Accuracy of NWS 8” Standard Nonrecording Precipitation Gauge: Results and Application of WMO Intercomparison. Journal of Atmospheric and Oceanic Technology, 15(1):54–68.
- Yang, H., Yang, D., Lei, Z., and Sun, F. (2008). New analytical derivation of the mean annual water-energy balance equation. Water Resources Research, 44(3):W03410.
- Yang, Y., Long, D., Guan, H., Scanlon, B. R., Simmons, C. T., Jiang, L., and Xu, X. (2014). GRACE satellite observed hydrological controls on interannual and seasonal variability in surface greenness over mainland Australia. Journal of Geophysical Research: Biogeosciences, 119(12):2245–2260.
- Young, D. J. N., Stevens, J. T., Earles, J. M., Moore, J., Ellis, A., Jirka, A. L., and Latimer, A. M. (2017). Long-term climate and competition explain forest mortality patterns under extreme drought. Ecology Letters, 20(1):78–86.

- Zack, S., Chase, M. K., Geupel, G. R., and Stralberg, D. (2005). The Oak Woodland Bird Conservation Plan: A Strategy for Protecting and Managing Oak Woodland Habitats and Associated Birds in California. In Bird Conservation Implementation and Integration in the Americas: Proceedings of the Third International Partners in Flight Conference. 2002 March 20-24; Asilomar, California, Volume 1, Gen. Tech. Rep., pages 20–24. USDA Forest Service.
- Zaerr, J. B. (1983). Short-term flooding and net photosynthesis in seedlings of three conifers. Forest Science, 29(1):71–78. 00061.
- Zanardo, S., Harman, C., Troch, P., Rao, P., and Sivapalan, M. (2012). Intraannual rainfall variability control on interannual variability of catchment water balance: A stochastic analysis. Water Resources Research, 48(6).
- Zunzunegui, M., Boutaleb, S., Barradas, D., C, M., Esquivias, M. P., Valera, J., Juregui, J., Tagma, T., and Ain-Lhout, F. (2018). Reliance on deep soil water in the tree species *Argania spinosa*. Tree Physiology, 38(5):678–689.
- Zweifel, R., Zimmermann, L., Zeugin, F., and Newbery, D. M. (2006). Intra-annual radial growth and water relations of trees: implications towards a growth mechanism. Journal of Experimental Botany, 57(6):1445–1459.
- Zwieniecki, M. A. and Newton, M. (1996). Seasonal pattern of water depletion from soilrock profiles in a Mediterranean climate in southwestern Oregon. Canadian Journal of Forest Research, 26(8):1346–1352.